

COLLISIONAL GRANULAR FLOWS WITH AND
WITHOUT GAS INTERACTIONS IN MICROGRAVITY

A Dissertation

Presented to the Faculty of the Graduate School

of Cornell University

in Partial Fulfillment of the Requirements for the Degree of

Doctor of Philosophy

by

Haitao Xu

August 2003

© 2003 Haitao Xu

ALL RIGHTS RESERVED

COLLISIONAL GRANULAR FLOWS WITH AND WITHOUT GAS
INTERACTIONS IN MICROGRAVITY

Haitao Xu, Ph.D.

Cornell University 2003

We studied flows of agitated spherical grains in a gas. When the grains have large enough inertia and when collisions constitute the dominant mechanism for momentum transfer among them, the particle velocity distribution is determined by collisional rather than by hydrodynamic interactions, and the granular flow is governed by equations derived from the kinetic theory.

To solve these equations, we determined boundary conditions for agitated grains at solid walls of practical interest by considering the change of momentum and fluctuation energy of the grains in collisions with the wall. Using these conditions, solutions of the governing equations captured granular flows in microgravity experiments and in event-driven simulations.

We extended the theory to gas-particle flows with moderately large grain inertia, in which the viscous gas introduces an additional dissipation mechanism of particle fluctuation energy. When there is also a mean relative velocity between the gas and the particles, the gas gives rise to particle fluctuation energy and to mean drag. Solutions of the resulting equations compared well with Lattice-Boltzmann simulations at large to moderate Stokes numbers. However, theoretical predictions deviated from simulations at small Stokes number or at large particle Reynolds number.

Using a method analogous to the integral treatment of laminar boundary layers, we derived averaged equations to study the development of granular and gas-particle flows in rectangular channels. The corresponding predictions of the stream-wise evolution of averaged flow variables such as the mean particle velocity, the granular temperature, and the mean gas velocity agreed well with event-driven simulations.

Finally, we used our analyses to prescribe microgravity experiments in which to test theories for gas-particle interactions with large to moderate particle inertia and small gas inertia. We also predicted uncertainties in measuring the granular mean and fluctuation velocities from a computer vision analysis of video images of the flow.

BIOGRAPHICAL SKETCH

The author was born in April, 1974, in Suizhou, China. He received his B.E. in 1993 from Huazhong University of Science and Technology, China. In August, 1998, he joined the Sibley School of Mechanical and Aerospace Engineering of Cornell University. He was enchanted by “gorgeous” Ithaca and decided to stay at Cornell as a postdoc after graduation.

To my wife,
For her consistent love, understanding and support

ACKNOWLEDGEMENTS

I am grateful to Professor Michel Louge, the chairman of my special committee, for his advice, patience and constant help. His ideas initiated this work and his accessibility encouraged numerous discussions. I am also grateful to him for his help and valuable advice on my professional and personal development and for teaching me writing skills.

I am indebted to Professor James Jenkins and Professor Donald Koch, both served as members of my special committee, for their inspiring ideas and suggestions. I learned a lot from them.

I would also like to thank Professor Anthony Reeves for providing us the image analysis algorithm, and Steve Keast for building the shear cells that we used in the experiments.

Special thanks to Dr. Rolf Verberg, who generously provided us the result of his Lattice-Boltzmann simulations.

Finally, I would like to thank all of my friends at Cornell. Their friendship made my stay here a pleasant and memorable experience.

TABLE OF CONTENTS

1	Introduction	1
2	Boundary Conditions for Collisional Granular Flows	11
2.1	Smooth Bumpy Boundaries	13
2.2	Granular Flows of Disks interacting with Flat Frictional Walls . . .	23
2.3	Granular Flows of Disks interacting with Bumpy, Frictional Walls .	39
2.4	Three-Dimensional Flows of Spheres interacting with Bumpy, Frictional Walls	51
3	Solutions of the Kinetic Theory for Bounded Collisional Granular Flows	55
3.1	Flow of Identical Spheres	58
3.1.1	Conservation laws and constitutive relations	58
3.1.2	Comparison with simulations and experiments	61
3.2	Flow of Binary Mixtures	76
3.2.1	Exact theory	76
3.2.2	Simplified theory	82
3.2.3	Comparison of theory, simulations and experiments	85
3.3	Conclusion	94
4	Flow of Collisional Grains in a Viscous Gas	96
4.1	Governing Equations	97
4.2	Bounded Shear Flows	106
4.2.1	One-Dimensional Rectilinear Flow	106
4.2.2	Comparison with Lattice-Boltzmann Simulation	108
4.2.3	Effects of Stokes number	111
4.2.4	Two-Dimensional Rectilinear Flow	126
5	Flow Development of Bounded Collisional Granular Flows	136
5.1	Granular Flow in a Rectilinear Channel	137
5.1.1	Effects of flat side walls	145
5.1.2	Effects of section length	149
5.2	Granular Flow in an Axisymmetric Shear Cell	151
5.3	Granular Flow in a Shear Cell Shaped as a Race Track	158
5.4	Gas-particle Flow in an Axisymmetric Shear Cell	161
6	Measurement Errors in the Mean Velocity and Granular Temperature	170
6.1	Vision Algorithm	171
6.2	Measurement Errors	175
6.2.1	Imperfect Tracking	175
6.2.2	Finite Pixel Size	181

6.2.3	Collisions	185
6.2.4	Strip Statistics	188
6.3	Tradeoffs	191
7	Design of Experiments to Study Gas-particle Interaction in Microgravity	195
7.1	Experiment Objectives	196
7.1.1	Viscous dissipation experiments	196
7.1.2	Viscous drag experiments	200
7.2	Constraints on the design of experiments	201
7.2.1	Particle inertia	201
7.2.2	Gas inertia	202
7.2.3	Duration of microgravity	203
7.2.4	Quality of microgravity	208
7.2.5	Sphere properties	215
7.2.6	Continuum flow	217
7.2.7	Accuracy of gas flow rate	218
8	Conclusions and Recommendations	221
A	Collision Integrals	225
B	Approximations of Stresses and Heat Flux at Flat, Frictional Walls	227
C	Determination of Granular Pressure	231
C.1	Iteration Scheme	233
C.2	One Dimension	233
C.3	Two Dimensions	239
D	Expressions in the Exact Mixture Theory	245
E	Tentative Test Matrices	247
E.1	Viscous Dissipation Experiments	247
E.2	Viscous Drag Experiments	253
	Bibliography	275

LIST OF FIGURES

1.1	Categories of fluid-particle flow.	2
2.1	Geometry of the bumpy boundary.	14
2.2	Stress ratio and heat flux at smooth, bumpy boundaries: comparison of the present study (solid lines) and the results of Richman & Chou [105] (dashed lines). Top plot: stress ratio. Bottom plot: dimensionless heat fluxes. The circles are simulation data with $\sigma = d = 2, s = 0$; the squares are $\sigma = 2, d = 3.2, s = 0; e_w = 0.96$ in both cases.	21
2.3	Geometry of the flat boundary.	24
2.4	Distributions of the y -component of velocity.	31
2.5	Effects of the particle velocity distribution on the stress ratio and flux of fluctuation energy at flat, frictional walls. Dotted lines: twin- δ distribution; solid lines: Maxwellian distribution; dashed lines: Weibull distribution. Figures in the top row show stress ratios and heat fluxes with $\mu = 0.1$ and 0.3 , and fixed $e = 0.9$, and $\beta_0 = 0$. Figures in the middle row correspond to $e = 1$ and 0.7 , fixed $\mu = 0.3$ and $\beta_0 = 0$. Figures in the bottom row are for $\beta_0 = 0$ and 0.4 , fixed $e = 0.9$ and $\mu = 0.4$	34
2.6	Comparison of stress ratios and fluxes of fluctuation energy calculated in the two limits of “all-sticking” and “all-sliding” with the exact calculation assuming a twin- δ distribution. Solid lines: exact calculation; dashed lines: two-limit approximation. Figures in the top row show the stress ratio and heat flux corresponding to $\mu = 0.1$ and 0.3 with fixed $e = 0.9$, and $\beta_0 = 0$. Figures in the middle row correspond to $e = 1$ and 0.7 , fixed $\mu = 0.3$ and $\beta_0 = 0$. Figures in the bottom row are for $\beta_0 = 0$ and 0.4 , fixed $e = 0.9$ and $\mu = 0.4$	38
2.7	Geometry of a bumpy, frictional boundary of half-cylinders in “planar” granular flows.	40
2.8	Stress ratio S/N (top) and dimensionless flux of fluctuation energy $Q/N\sqrt{T}$ (bottom) for planar flows of spheres at a bumpy, frictional boundary. The dashed and dotted lines represent the respective contributions of bumps and friction. The solid lines show the total S/N or $Q/N\sqrt{T}$. The boundary parameters are $\sigma/d = 1, s/d = 1/2, e = 0.9, \mu = 0.1$, and $\beta_0 = 0$	49
2.9	Stress ratio S/N for 3-D flows of spheres at a bumpy, frictional boundary. Top plot: $\sigma = 2, d = 3.2, s = 0$; bottom plot: $\sigma = d = 2, s = 0$. Lines are the superposition Eq. (2.86), symbols are simulation results. Solid lines and squares: $\mu_w = 0.1$; dashed lines and circles: $\mu_w = 0.0$	52
3.1	Fully developed, steady flows in a rectilinear cell.	62

3.2	Mean and fluctuation velocities in the cross-section of a rectilinear cell. Top: mean velocity in x -direction made dimensionless with the velocity U of the top boundary. Bottom: fluctuation velocity made dimensionless with U . The symbols and lines represent, respectively, the results of the simulations and the predictions of the theory. Solid lines and squares are $y/H = 0$; dashed lines and upward triangles, $y/H = 1/3$; dash-dotted lines and circles, $y/H = 2/3$; dotted lines and downward triangles, $y/H = 1$	64
3.3	Transverse profiles of depth-averaged mean and fluctuation velocities made dimensionless with U for the conditions of Fig. 3.2. Symbols are simulation data averaged from side wall to side wall. Solid lines are the two-dimensional solutions of Fig. 3.2 averaged in the z -direction. Dashed lines are solutions from the depth-averaged Eqs. (3.25) and (3.26).	66
3.4	Effects of a streamwise body force on the mean and fluctuation velocities made dimensionless with U . Symbols are simulation data. Lines are solutions of Eqs. (3.25) and (3.26). Squares and solid lines denote $Fr = 0$, where $Fr \equiv g\sigma/U^2$ is a Froude number representing the relative magnitude of the body force g . Circles and dashed lines are $Fr = 0.005$. Conditions are otherwise those of Fig. 3.2.	69
3.5	Granular flows in the round section of a shear cell shaped as a race track. Actual dimensions of the shear cell are given in [80, 81]. Solid symbols are experimental data, open symbols are numerical simulations and solid lines are theoretical predictions. Top: dimensionless mean velocity profile $u(r)/U$. Bottom: dimensionless fluctuation velocities $w(r)/U$. Squares represent the component $T_{xx}^{1/2}/U$ along the x -direction, and circles are $T_{yy}^{1/2}/U$. Here, $y = 0$ at the stationary outer boundary and $y = H$ at the moving inner boundary.	71
3.6	A typical digital image of the curved region in the race-track Couette cell of Louge <i>et al</i> [81]. The top boundary is fixed while the bottom boundary moves from right to left. Persistent scratches on the window hide the moving boundary. Circles and lines are superimposed to indicate the location and trajectory of detected spheres.	73
3.7	Granular flows with $O(1)$ Knudsen number. The top and bottom graphs show dimensionless mean and fluctuation velocities, respectively. The simulations (symbols) are periodic in the z -direction and do not possess side walls. The lines are theoretical solutions. For squares and solid lines, $Kn = 0.75$; for triangles and dashed lines, $Kn = 0.30$; for circles and dash-dotted lines: $Kn = 0.15$. Conditions are $Y = 17.24$, $\sigma = d_0 = 2$, $d_1 = 3$, $s_0 = s_1 = 0$, $e = 0.95$, $\mu = 0.1$, $\beta_0 = 0.4$, $e_w = 0.85$, $\mu_w = 0.1$ and $\beta_{0w} = 0.4$	75

3.8	Flow of a binary mixture of grains with the same size, but different material densities in a Couette cell without flat side wall and with bumpy boundaries moving in opposite directions. (a) Mixture velocity u/U , (b) mixture fluctuation velocity w/U , (c) volume fraction of each species, (d) relative number fraction of each species. Symbols are simulation results. Solid and dashed lines are solutions of the exact and simplified theory, respectively. In (c) and (d), pluses and thick lines are for species A , while crosses and thin lines are for species B	87
3.9	Flow of a binary granular mixture with the same material density, but different sizes. See Figure 3.8 for cell geometry and impact properties. Parameters: $\rho_A = \rho_B$, $r_A = 1$, $r_B = 0.8$, $\bar{\nu} = 0.308$, $\bar{n}_A/\bar{n} = 0.339$	88
3.10	Flow of a binary granular mixture exhibiting no segregation. See Figure 3.8 for cell geometry and impact properties. Parameters: $\rho_A/\rho_B = 0.5842$, $r_A = 1.02$, $r_B = 0.8$, $\bar{\nu} = 0.344$, $\bar{n}_A/\bar{n} = 0.442$. . .	90
3.11	Flow of a granular mixture in a wide cell with $Y/r_{AB} = 25$. See Figure 3.8 for other dimensions and impact properties. The interior region in the range $0.1 \leq y/Y \leq 0.55$ has $\bar{\nu} = 0.28$ and $\bar{\nu}_A = 0.11$. .	91
3.12	Flow of a binary granular mixture in an axisymmetric Couette cell. The inner and the outer bumpy boundaries are moving at $0.2U$ and $-0.8U$, respectively, and the two flat side walls are stationary. Solid symbols are experimental data. In (a) and (b), open symbols are simulation results; squares and circles represent species A and B , respectively. For pluses, crosses and lines, see Figure 3.8. . . .	93
4.1	Change of R_{diss} with Re_T . The symbols are Lattice-Boltzmann data by Verberg & Koch [123]. Squares: $\nu = 0.1$, circles: $\nu = 0.2$, crosses: $\nu = 0.3$, pluses: $\nu = 0.4$. Lines are curve fits of Eq. (4.7). .	102
4.2	Bumpy boundary used in the Lattice-Boltzmann simulation of Verberg & Koch [123]. Boundaries normal to the x - and the z - directions are periodic. In the Lattice-Boltzmann simulations, the boundary spheres have a diameter $d = 5.84$ and the gap separating them is $s = 0.16$, so as to obtain a periodic array with $d+s = 6$ ‘‘lattice units’’. The flow spheres are of the same size as the boundary particles.	109
4.3	Variations of the granular temperature with Stokes number. Solid lines are results from Lattice-Boltzmann simulation [123]. Dashed lines are solutions of the continuum theory. Simulation parameters: $Y'/\sigma = 12$, $Re' = 0.1$, and overall particle volume fraction $\bar{\nu} = 0.3$. From top to bottom: $St' = 100, 50, 40, 30, 20, 15, 10$, and 5	112
4.4	Changes in the slip velocity at the solid boundary with Stokes number. Symbols are data from Lattice-Boltzmann simulations [123]. The line is the prediction of the theory.	114

4.5	<p>Transverse profiles at $St' = 20$ and $Re' = 0.1$. Solid lines are simulation results [123] and dashed lines are predictions of the theory. Top plot: mean particle velocity u_s^*; middle plot: granular fluctuation velocity, made dimensionless with $\Gamma\sigma/2$; bottom plot: particle volume fraction. For other simulation parameters, see Figure 4.3.</p>	116
4.6	<p>Shear stresses at $St' = 20$ and $St' = 100$. Symbols are results of the Lattice-Boltzmann simulations [123] and lines are predictions of the theory. Circles and solid lines: $St' = 100$; crosses and dashed lines: $St' = 20$. Top plot: shear stress in the particle phase, $\eta du_s/dy$; bottom plot: shear stress due to the viscous gas, $R_\mu\mu_g du_g/dy$. All stresses are made dimensionless with $\rho_s U^2$. For other simulation parameters, see Figure 4.3.</p>	118
4.7	<p>Effects of Reynolds number on the granular temperature at a fixed $St' = 100$. Solid lines are simulation results [123], and dashed lines are prediction of the theory. From top to bottom: $Re' = 0.1, 0.5, 1, 2,$ and 10. The simulation parameters are: $Y'/\sigma = 12$ and $\sigma = 5.84$ lattice units for $Re' = 0.1, 0.5, 1$ and 2; $Y'/\sigma = 12$ and $\sigma = 11.68$ lattice units for $Re' = 10$. In general, the simulation accuracy increases with the resolution, i.e., the sphere size in lattice units. The discrepancy between theory and simulation at $Re' = 1$ and $Re' = 2$ may be due to a low resolution in the simulation.</p>	119
4.8	<p>Comparison of transverse profiles with $St' = 100$ and $Re' = 10$, and with $St' = 20$ and $Re' = 0.1$. Symbols are LB simulation result [123] and lines are predictions of the theory. Pluses and solid lines: results for $St' = 100$ and $Re' = 10$, crosses and dashed lines: results for $St' = 20$ and $Re' = 0.1$. Top plot: mean particle velocity u_s^*; middle plot: granular fluctuation velocity w^*; bottom plot: particle volume fraction. Other simulation parameters: $Y'/\sigma = 12$ and $\bar{\nu} = 0.3$.</p>	121
4.9	<p>Shear stresses at $Re' = 0.1$ and $Re' = 10$ for a fixed $St' = 100$. Symbols are results from the Lattice-Boltzmann simulations [123] and lines are predictions of the theory. Circles and solid lines: $Re' = 0.1$; crosses and dashed lines: $Re' = 10$. Top plot: particle phase shear stress $\eta du_s/dy$; bottom plot: viscous gas shear stress $R_\mu\mu_g du_g/dy$. All stresses are made dimensionless with $\rho_s U^2$. For other simulation parameters, see Figure 4.7.</p>	122
4.10	<p>Effects of overall particle volume fraction on granular temperature (top) and volume fraction profiles (bottom) at fixed $St' = 30$ and $Re' = 0.1$, Symbols are simulation results [123] and lines are prediction of the theory. Dotted line and squares: $\nu = 0.1, Y'/\sigma = 12.7$; dash-dotted line and pluses: $\nu = 0.2, Y'/\sigma = 10$; solid line and circles: $\nu = 0.3, Y'/\sigma = 12$; dashed line and crosses: $\nu = 0.4, Y'/\sigma = 12$. All simulations are with $\sigma = 5.84$ lattice units.</p>	124

4.11	Effects of channel width Y on granular temperature (top) and particle volume fraction (bottom) at fixed $St' = 20$, $Re' = 0.1$, and $\bar{\nu} = 0.3$. Symbols are simulation results [123], thick lines are prediction of the theory. Solid line and circles: $Y'/\sigma = 12$; dashed line and crosses: $Y'/\sigma = 8$; dash-dotted line and triangles: $Y'/\sigma = 6$. Parameters in simulation: $\sigma = 5.84$ lattice units.	125
4.12	Theoretical solutions of mean solid velocity, gas velocity, and granular temperature in the cross-section. Parameters: $H/\sigma = W/\sigma = 11$, $St' = 30$, $Re' = 0.1$, lubrication cut-off $\varepsilon_m = 0.01$, and overall particle volume fraction is 0.3. Top and bottom boundary velocities are $U_t = 0.5U$ and $U_b = -0.5U$. The flat side walls are stationary. Impact parameters are $e = 1$, $\mu = 0$, and $\beta_0 = 0$ except for the flat side walls which have $\mu = 0.1$ and $\beta_0 = 0.4$. Top plot: profiles of mean solid velocity u_s^* and gas velocity u_g^* from side wall to side wall at different y/H . Thick lines: u_s^* , thin lines: u_g^* . Bottom plot: profiles of granular fluctuation velocity w^* at different y/H . Only granular temperature in $y/H \leq 1/2$ is shown because it is symmetrical about $y/H = 1/2$	130
4.13	Comparison of two-dimensional solution with one-dimensional integral solution. Parameters: $St' = 100$ and $R_\tau = 0.2$. All others are the same as in Figure 4.12. Impact parameters: for collisions between flow spheres and between a flow sphere and the boundary spheres: $e = 0.9$, $\mu = 0$, and $\beta_0 = 0$, for collisions between a flow sphere and the side walls: $e = 1$, $\mu = 0.1$, and $\beta_0 = 0.4$. Symbols are results from 2-D solution averaged from side wall to side wall, lines are results of the 1-D integral theory. Top plot: u_s^* (solid line and circles) and u_g^* (dashed line and squares). Middle plot: w^* . Bottom plot: ν	135
5.1	A sketch of the microgravity “race track” shear cell used by Louge <i>et al</i> [80].	138
5.2	Flow development in the straight section; comparison of theory and simulations. Top plot: $\nu(x^*)$, middle plot: $\bar{u}^*(x^*)$, bottom plot: $\sqrt{T^*}(x^*)$. Circles are simulation results. Solid lines are theoretical predictions; dash-dotted lines are predictions of a simplified theory that assumes a balance between shear production and inelastic dissipation at each cross section; dashed lines are predictions that ignore the working of the normal stress in the energy balance. Geometric parameters: $L = 420$, $H = 11.74$, $W = 8.85$, $\sigma = d_i = 3$, $d_o = 2$, and $s_i = s_o = 0$. Impact properties of flow spheres: $e = 0.95$, $\mu = 0.1$, $\beta_0 = 0.4$; bumpy boundaries: $e_w = 0.85$, $\mu_w = 0.1$, $\beta_{0,w} = 0.4$; flat side walls: $e_{sw} = 0.95$, $\mu_{sw} = 0$, $\beta_{0,sw} = 0$	146

5.3	Relative magnitude of the terms in the energy balance along the straight section. Thin solid line: shear production; dash-dotted line: total heat flux through both bumpy boundaries; dashed line: working of the normal stress; thick solid line: inelastic dissipation. All terms are made dimensionless by the inelastic dissipation in the fully developed region. Other terms in energy balance, i.e., conduction, convection, and total heat flux through the flat side walls, are very small and are not shown. For parameters and impact properties, see Figure 5.2.	147
5.4	Effects of flat side walls on flow development. Top plot: $\nu(x^*)$, middle plot: $\bar{u}^*(x^*)$, bottom plot: $\sqrt{T^*}(x^*)$. Symbols are simulation results and lines are theoretical predictions. Circles and solid lines: smooth side walls, $\mu_{sw} = 0$ and $W = 8.85$. Triangles and dashed lines: frictional side walls, $\mu_{sw} = 0.1$ and $W = 8.85$. Crosses and dash-dotted lines: a wider cell with frictional side walls, $\mu_{sw} = 0.1$ and $W = 36.86$. All other parameters are found in Figure 5.2.	148
5.5	Effects of straight section length on flow development. Top plot: $\nu(x^*)$, middle plot: $\bar{u}^*(x^*)$, bottom plot: $\sqrt{T^*}(x^*)$. Symbols are simulation results and lines are theoretical predictions. Circles and solid lines, $L/\sigma = 140$; triangles and dashed lines, $L/\sigma = 280$; crosses and dash-dotted lines, $L/\sigma = 560$. Other parameters, see Figure 5.2.	150
5.6	A sketch of the axisymmetric shear cell. Left: shear cell with two gas distributors separating the cell into a “co-flow” and a “counter-flow” region. Right: shear cell with three gas distributors. The third distributor creates an “iso-kinetic region” by maintaining $P_{D1} = P_{D3}$	152
5.7	Theoretical predictions and simulation data for the flow development in an axisymmetric cell with two gas distributors. Top plot: $\nu(\theta)$, middle plot: $\bar{u}^*(\theta)$, bottom plot: $\sqrt{T^*}(\theta)$. The abscissa represents the angle θ defined in Fig. 5.6 in multiples of π . The “co-flow” region lies in the range $0 \leq \theta \leq \pi$. Symbols and lines represent simulations and theory. Circles and solid lines: $Fr_{\theta,co} = 0.00083$; crosses and dashed lines: $Fr_{\theta,co} = 0.00017$. Eq. (5.28) provides the corresponding values for $Fr_{\theta,cf}$ in the counter-flow region. Simulation parameters: $R_i = 211$, $R_o = 224$, $W = 17.4$, $\sigma = d_o = 2$, $d_i = 3$, $s_i = s_o = 0$, $U_i = U$, $U_o = 0$, and $\theta_{D2} = \pi$. The overall loading is $\bar{\nu} = 0.33$, Impact properties of flow spheres: $e = 0.95$, $\mu = 0.1$, $\beta_0 = 0.4$; bumpy boundaries and flat side walls: $e_w = e_{sw} = 0.85$, $\mu_w = \mu_{sw} = 0.1$, and $\beta_{0,w} = \beta_{0,sw} = 0.4$	157
5.8	Effect of gas distributor separation on flow development in the axisymmetric cell for $Fr_{\theta,co} = 0.00083$. Circles and solid lines: gas distributor $D2$ at $\theta_{D2} = \pi$; crosses and dashed lines: $\theta_{D2} = \pi/2$. For other symbols and parameters, see Fig. 5.7.	159

5.9	Effect of boundary velocities on flow development in an axisymmetric cell for $Fr_{\theta,co} = 0.00083$ and $\theta_{D2} = \pi$. Circles and solid lines: $U_i = U$ and $U_o = 0$; crosses and dashed lines: $U_i = 0.75U$ and $U_o = -0.25U$. For other symbols and parameters, see Fig. 5.7.	160
5.10	Flow development in a race track over half the cell. Circles and solid lines: smooth side walls; crosses and dashed lines: frictional side walls with $\mu_{sw} = 0.1$. The dash-dotted line indicates the junction of the straight and curved sections. The latter is located to the right of this vertical line. For other symbols and parameters, see Fig. 5.7.	162
5.11	Predictions of gas-particle flows with different Stokes numbers in an axisymmetric cell with two distributors separated by π . Top plot: gas pressure $\frac{P_g - P_{D2}}{P_{D1} - P_{D2}}$, where P_{D1} and P_{D2} are the gas pressures at distributors $D1$ and $D2$, respectively. Middle plot: average solid velocity \bar{u}_s^* and gas velocity \bar{u}_g^* . Bottom plot: ν and $\sqrt{T^*}$. Solid lines: predictions for $St = 400$. Dashed lines: $St = 1000$. Simulation parameters: $R_i = 212$, $R_o = 226$, $W = 18$, $d = d_i = d_o = 2$, $s_i = 1$, $s_o = 0$, $\bar{\nu} = 0.3$, $R_{\tau,exp} = 0.008$. There are no leaks along the channel. Impact parameters for spheres: $e_{eff} = 0.85$; for all other impacts: $e = 0.85$, $\mu = 0.1$ and $\beta_0 = 0.4$	167
5.12	Predicted effects of gas leak on gas-particle flows in an axisymmetric cell with two distributors separated by π for a Stokes number $St = 400$. Top left: gas pressure $\frac{P_g - P_{D2}}{P_{D1} - P_{D2}}$, top right: dimensionless gas flow rate Q_g^* , middle left: \bar{u}_s^* , middle right: \bar{u}_g^* , bottom left: ν , bottom right: $\sqrt{T^*}$. Solid lines: predictions for a cell without leaks. Dashed lines: leak path length $L_l/R = 0.0688$ and clearance $\delta_l/L_l = 0.0133$. For all other parameters, see Fig. 5.11.	168
5.13	Predicted effects of the isokinetic region on the flow development in an axisymmetric cell with $St = 1000$. Top plot: gas pressure ratio $\frac{P_g - P_{D2}}{P_{D1} - P_{D2}}$, where P_{D1} and P_{D2} are pressures at the distributors for injection and withdrawal, respectively. Middle plot: average solid velocity \bar{u}_s^* and gas velocity \bar{u}_g^* . Bottom plot: particle volume fraction ν and fluctuation velocity $\sqrt{T^*}$. Solid lines: with three gas distributors, $D1$ at $\theta = 0$, $D2$ at π and $D3$ at $\frac{7}{4}\pi$. Dashed lines: with two distributors separated by π . For all other parameters, see Fig. 5.11.	169
6.1	A typical image acquired in microgravity experiments with 2 mm acrylic spheres. The top stationary boundary and bottom moving boundary are barely distinguishable. Lighting on both sides produces specular spots on most spheres.	173
6.2	Effects of tracking failure on measured mean velocity (a) and granular temperature profiles (b), all in the x -direction, made dimensionless with the relative speed U	180

- 6.3 Effects of finite pixel size on measured profiles of granular temperature in the x -direction. The abscissa is the corresponding relative error in T_{xx} . For the ordinate, see Fig. 6.2. The symbols are data from simulations in which grain centers are artificially repositioned to the center of a pixel before calculating grain velocities between two consecutive frames. The lines are predictions of the theory in Eq. (6.20). Circles and dashed lines: $F/F_0 = 1.85$; squares and solid lines: $F/F_0 = 3.70$. There are 384 pixels between the lines of bump centers on the two moving boundaries, which corresponds a ratio $d/p \approx 43$. See Fig. 6.2 for other simulation parameters. . . . 184
- 6.4 Effects of undetected collisions on the measured granular temperature in the x -direction. The abscissa is $\alpha \equiv f_{coll}\Delta t$. The ordinate is the measured granular temperature at the frame rate $F = 1/\Delta t$ relative to its actual value when $\Delta t \rightarrow 0$. The symbols are data derived from consecutive image realizations separated by Δt in simulations with $p = 0$ and $U_{tr} = \infty$. The solid line is the prediction of the theory in Eq. (6.30). Squares and circles: \tilde{T}_{xx}/T_{xx} ; triangles: \tilde{T}_{yy}/T_{yy} . Squares and up-triangles: at $y/H = 0.5$; circles and down-triangles: at $y/H = 0.8$. See Fig. 6.2 for other simulation parameters. 189
- 6.5 Theoretical prediction of the effects of camera frequency on the relative errors of granular temperature with $u_x/U = 0.5$, $T^{1/2}/U = 0.08$, and $\nu = 0.3$. The abscissa is the frame rate relative to F_0 in Eq. (6.21). The ordinate is the relative error in T_{xx} . The solid, dashed and dotted line represent the respective contributions of imperfect tracking, finite pixel resolution and collisions upon measurement errors. The horizontal dotted lines indicate $\pm 10\%$. Thus, if such an error level can be tolerated, one may adopt a frame rate in the range shown. In contrast, no camera frequency yields a relative error smaller than, for example, $\pm 5\%$ 193
- 6.6 Profiles of mean velocity u_x (a) and granular temperature T_{xx} (b) in the shear flow of Fig. 6.1(a) made dimensionless with U . In this experiment, the top boundary is moving at speed U and the bottom boundary is stationary. The solid lines are predictions of the numerical simulations. The symbols are experimental measurements. The dashed lines are simulation results corrupted by errors predicted by the theory, in which we assume that tracking is lost for displacements beyond $L_{tr} = d/4$ 194

7.1	Variations of the dimensionless fluctuation velocity $T^{1/2}/\Gamma\sigma$ with Stokes number in the simple shear flow of a gas-particle suspension. Solid line: solution given by the energy balance Eq. (7.4). Dashed line: limit of $St \rightarrow \infty$. Dash-dotted line: limit of small St . Parameters: $\nu = 0.3$, $e_{eff} = 0.8$, $\rho_g = 1.29 \times 10^{-3}$, $\rho_s = 6.71$, and lubrication cutoff $\varepsilon_m = 0.01$	199
7.2	Simulated evolution of the granular temperature in a shear flow between parallel, bumpy boundaries. The granular temperature is averaged across the cell and made dimensionless with U^2 . Simulation parameters: $H/\sigma = 6.4$, $d_i = 3$, $d_o = \sigma = 2$, $s_i = s_o = 0$, $\bar{\nu} = 0.33$, $\mu = 0.1$, $\beta_0 = 0.4$, and the coefficients of normal restitution shown in the figure.	206
7.3	Dimensionless relaxation time versus $[(1+4G)\sqrt{T_{ss}^*}]^{-1}$ evaluated at steady state. The circles, triangles and squares represent numerical simulations with conditions of Figure 7.2 at $\bar{\nu} = 0.23$, 0.33 and 0.43, respectively. For each volume fraction, the three data points correspond to $e = 0.75$, 0.85, and 0.95.	209
7.4	Increase in the mean granular velocity at the centerline with streamwise residual acceleration. Top plot: curve-fit of $c(\nu)$ in Eq. (7.37). Symbols are results from numerical integration of the conservation equations. The solid line is the least square fit Eq. (7.38). Bottom plot: variations of Δu_s^* with $Fr_x/\sqrt{T^*}$. Symbols are results from the numerical integration and lines are the simpler analysis Eq. (7.37) with $c(\nu)$ given by Eq. (7.38). Squares and thin solid line: $\nu = 0.05$, circles and dashed line: $\nu = 0.1$, up-triangles and dotted line: $\nu = 0.2$, down-triangles and dash-dotted line: $\nu = 0.3$, diamonds and thick solid line: $\nu = 0.4$	214
7.5	Variations of the gas volume flow rates due to a 20% change in R_{drag} . Symbols are numerical solutions of the 1 dimensional integral Eqs. (4.38), (4.40), and (4.41). Lines are the corresponding curve fits of Eq. (7.49). Squares: overall volume fraction $\bar{\nu} = 0.15$. Circles: $\bar{\nu} = 0.2$. Up-triangles: $\bar{\nu} = 0.3$. Down-triangles: $\bar{\nu} = 0.4$. Crosses: $\bar{\nu} = 0.45$. For other parameters, see Appendix E.	220
B.1	Two-limit approximation, with Maxwellian velocity distributions.	229
B.2	Two-limit approximation, with Weibull velocity distributions.	230
C.1	Curve fit of ν as a function of P^*/T^* . Top plot: ν vs. P^*/T^* ; symbols represent the exact function; the solid line is the curve fit of Eq. C.8. Bottom plot: relative error in the curve fit.	234

Chapter 1

Introduction

Flows involving a fluid and dispersed solid particles are ubiquitous, from sand storms that can travel thousands of kilometers to industrial flows in fluidized beds and transport lines. As Figure 1.1 suggests, such flows may be organized on a map featuring the Stokes and Reynolds numbers. The Stokes number $St \equiv \tau_v U / \sigma$ measures the relative importance of particle inertia and fluid viscosity. It does so by comparing the particle viscous relaxation time $\tau_v = \rho_s \sigma^2 / 18 \mu_f$ and a characteristic time U / σ for the flow. For example, in shear flows, the characteristic velocity U may be related to the mean strain rate γ using $U = \gamma \sigma$. The Reynolds number $Re \equiv \rho_f U \sigma / \mu_f$ compares the roles of inertia and viscosity in the fluid. In these expressions, ρ_s and ρ_f are the material density of the solid and the fluid, respectively, σ is the particle diameter, and μ is the gas viscosity.

The Stokes and Reynolds numbers are related through the ratio of fluid and solid material densities, ρ_f / ρ_s , which measures the relative importance of fluid and solid inertia. With a gas, this ratio is small enough that forces proportional to the fluid density, such as added mass and history forces, are negligible. In this work, we only consider flows where the system size L is much larger than a microscale l so that continuum descriptions of both the fluid and particle phases are possible. For the fluid, the microscale is the mean free path. For the particle phase, it is either the diameter σ of individual particles, or their own mean free path.

In many situations, the particle size is so small that the fluid inertia is negligible ($Re \ll 1$). Because the corresponding flows are locally governed by the Stokes equation, which is linear, these flows have been the subject of several theories and

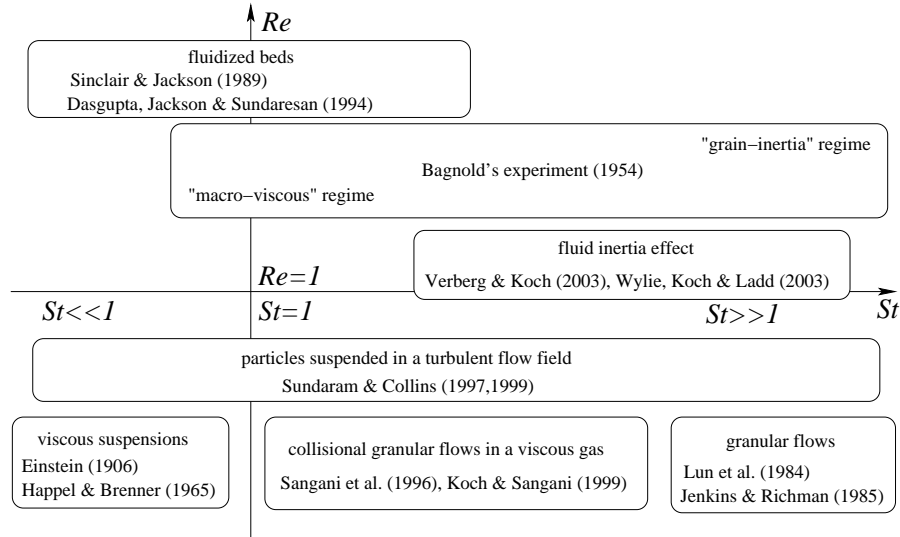


Figure 1.1: Categories of fluid-particle flow.

numerical simulations. Although the Reynolds number based on a macroscale such as the vessel size can be large enough for the mean flow to be turbulent, individual particles often react to the local flow field according to the Stokes equation [116, 117].

When particle inertia is small ($St \ll 1$), solid particles follow fluid streamlines closely. Since Einstein's classical work [31], such suspensions have been studied extensively [42] and are often treated as a single phase with an enhanced effective viscosity.

As particle inertia increases, collisional interactions between particles may transfer a significant amount of momentum. In his famous experiments with sheared suspension of neutrally buoyant spheres, Bagnold [9] identified three different flow regimes, which he distinguished by a dimensionless number that is directly proportional to the Stokes number. For small Bagnold numbers (small St), the suspension behaves as a Newtonian fluid, in which both shear and normal stresses

are proportional to the shear rate. Bagnold called this regime “macro-viscous”. For large Bagnold numbers (large St), Bagnold found a quadratic dependence of stresses on shear rate. In this “grain-inertia” regime, Bagnold argued that collisional interactions provide the main mechanism for momentum transfer. He attributed the quadratic dependence to the proportionality of both the collision rate and the momentum change during each collision to the shear rate. Between the two regimes, Bagnold identified a transition at moderate Bagnold number. Although Bagnold’s data have recently been challenged because of the questionable design of his experimental apparatus [47], his physical arguments were essentially correct and promoted the development of theories in fluid suspension and granular flow. Subsequent experiments by Savage & Sayed [109] verified the quadratic dependence of stresses on shear rate with dry granular materials.

For gas-particle flows with large particle Stokes number, the interstitial gas does not affect the particle motion. In such granular flows, two limiting regimes can be distinguished. The first is called “rapid” granular flow. Here, particles are violently agitated and the momentum is transferred entirely by collisional interactions. The second is a quasi-static regime, where particles are in contact with their neighbors at all times and the granular system behaves like a rate-independent plastic material. Between these two extremes is a slow and generally dense granular flow regime, where collisional interactions and longer-term contacts coexist.

The quasi-static regime is mainly the province of soil mechanics [131]. It is challenging to derive its constitutive equations because of non-local effects of the long-term contacts.

An intermediate regime between “rapid” flows and quasi-static assemblies appears to involve both long-term contacts and shorter-term impulses. In this regime,

some *ad hoc* theories [108, 75, 77] were proposed to take into account simultaneously the contribution from collisions and long-term contacts, but the determination of the corresponding constitutive equations from first principles remains an open problem.

Kinetic theory describes rapid granular flows successfully [87, 59, 62, 37, 111, 110, 36]. To do so, the theory exploits an analogy between agitated particles and the molecules of a dense gas. In this framework, the Boltzmann equation is solved approximately for the distribution of particle fluctuation velocity, and the transport coefficients are then calculated once the velocity distribution is known. This approach has been extended to granular flows with more than one constituents [57, 58, 6, 3].

To make the mathematical treatment tractable, all current theories assume “molecular chaos”, such that the velocities before a collision of any two colliding particles are uncorrelated. This assumption is expected to break down in dense flows, where particles mostly collide with their close neighbors. Another tacit assumption is the isotropy of the pair distribution function, which means that the probability to find another particle at a distance r from the center of the target particle depends only on r . In a shear flow, however, the presence of compression and extension directions in the flow field may cause a preferential distribution of particles and the pair distribution is expected to be anisotropic. Nonetheless, kinetic theories have been widely accepted for rapid granular flows, thanks in part to the agreement among theory, physical experiments [80, 81] and molecular dynamic simulations [78, 79, 81, 12], but also in anticipation of the difficulties involved in resolving these issues.

A key concept in kinetic theory is the “granular temperature”, $T \equiv \langle C^2 \rangle$

$/3$, where C is the particle velocity fluctuation and $\langle \rangle$ represents an ensemble average. As its name suggests, the granular temperature is the analog of the thermal temperature in molecular gases. It is related to the granular pressure and transport coefficients in a familiar way. However, unlike molecular gases, collisions in granular flows do not conserve kinetic energy because of the inelastic nature of the solid particles. Thus, an external forcing must be imposed on a granular flow in order to maintain its granular temperature. Because the forcing is generally applied through solid boundaries, energy losses in the interior of a typical flow often let the granular temperature decay away from these boundaries.

The concept of granular temperature can be extended to gas-particle systems where new mechanisms produce and dissipate particle fluctuation energy. For moderate particle Stokes number, the role of the viscous gas cannot be ignored. Sangani *et al* [107] studied the case where $Re \ll 1$ and St is large enough that the particle velocity distribution is still determined by inter-particle collisions, but the viscous drag on particle fluctuation causes additional dissipation of granular temperature. They also derived the constitutive equations for such a flow when the inelastic dissipation is small. Koch & Sangani [67] extended the theory to include the effect of relative mean velocity between the gas and the solid phase. They found that the gas velocity disturbance gives rise to viscous forces on the grains that create particle fluctuation kinetic energy.

When the particle Reynolds number increases, fluid inertia can no longer be ignored. Because the full Navier-Stokes equation must be invoked in this case [66], theoretical developments become more complicated. Verberg & Koch [123] extended the study of Sangani *et al* [107] to moderate particle Reynolds number and found that the viscous dissipation of particle fluctuation energy increases linearly

with the particle Reynolds number. In a similar work, Wylie *et al* [135] studied the effect of fluid inertia on both the energy dissipation and the mean drag. At present, however, there are no constitutive equations for gas-particle flows at moderate Reynolds number.

At small but finite particle Reynolds number, the Reynolds number based on a macroscale can be large enough that the mean flow becomes turbulent. In a turbulent flow, Sundaram & Collins [116, 117] studied clustering due to particle inertia and the effects of particles on the flow. To that end, they assumed that the drag on the solid particles is given by the Stokes law. Gas-particle flows at even higher particle Reynolds number, such as in industrial fluidized beds, are poorly understood because of the inherent instability of the homogeneous state of fluidization [119].

Computer simulations have become a valuable tool to understand the complex nature of fluid-particle flows and to lend insight to the derivation of theories. Several simulation techniques have thus been developed.

For granular flows, where the effect of gas can be neglected, the two most popular techniques are “hard-sphere” and “soft-sphere” simulations. In “hard-sphere” simulations, see for example Campbell & Brennen [18] and Luding & McNamara [85], collisions are assumed to be instantaneous. The occurrence of an upcoming collision is determined by maintaining a list of future such events and the simulation marches accordingly from one collision to the next. The discrete element model (DEM) proposed by Cundall and Strack [27] inspired Walton and Braun [127, 126] to develop a “soft-sphere” simulation, in which particles are allowed to deform during collisions. The principal advantage of this technique is to let the simulation capture long-lasting, as well as impulsive, granular interac-

tions. Here, detailed contact dynamics are resolved in small time steps typically much smaller than the time separating two successive collisions. As a variation of the “hard-sphere” simulation, Hopkins & Louge [44] used a “hard-sphere/overlap” simulation, in which collisions are also assumed to be instantaneous, but particles can overlap slightly with each other before detecting the occurrence of a contact. The simulation time increment is then adjusted to keep the mean overlap below a certain tolerance. This technique makes it redundant to maintain a collision list and facilitates simulations with complicated boundary geometry.

For gas-particle flows with $Re \ll 1$, several simulations take advantage of the linearity of the Stokes equation. These include, for example, the “Stokesian Dynamics” of Brady & Bossis [14] and the multipole expansion of Sangani & Mo [89, 106]. At moderate Reynolds number, numerical solutions of the suspension are more difficult because the full Navier-Stokes equations must be solved. For these flows, the Lattice-Boltzmann simulations [69, 70, 23] are a suitable choice. Unlike direct solutions of the Navier-Stokes equations, Lattice-Boltzmann simulations are relatively easy to program and are, at least in principle, more accurate because they solve directly the Boltzmann equation. Because the propagation speed of information along the lattice must be large compared with the mean flow velocity, the Lattice-Boltzmann method breaks down at high particle Reynolds numbers. In turbulent flows, it is generally preferable to use Direct Numerical Simulations [90, 116, 117].

In this work, we consider gas-particle flows with large particle inertia and small to moderate gas inertia. We first focus on rapid granular flows where the influence of the gas is negligible and particles interact with each other only through collisions. We solve the governing equations from the kinetic theory for bounded

granular flows. We compare our results with microgravity experiments and computer simulation data from “hard-sphere/overlap” simulations. We then extend the theory to gas-particle flows with large St but small to moderate Re . We solve the equations for averaged quantities in the particle and gas phase, and compare the results with recent Lattice-Boltzmann simulations by Verberg & Koch [123].

This thesis is organized as follows. Chapter 2 first focuses on boundary conditions. To use a continuum theory to analyze a granular flow, one must specify conditions at the solid walls that bound the flow. In particular, the mean granular velocity adjacent to the solid wall differs from the wall velocity. Given the exact boundary geometry and the impact parameters of the wall, boundary conditions may be derived from the collisional transfer of momentum and fluctuation energy at the wall [61, 50, 56]. Because previous conditions at bumpy boundaries were only valid for a small “slip velocity”, i.e., for a small relative velocity between the mean granular flow and the solid wall, we derive in Chapter 2 the stresses and flux of fluctuation energy at frictionless, bumpy walls over a large range of slip velocities. We also propose a simple superposition to calculate conditions at frictional, bumpy walls.

In Chapter 3, we solve the governing equations with appropriate boundary conditions for fully developed granular flows of a single constituent and binary mixtures. Comparisons of the predictions of continuum theory with molecular dynamic simulations and physical experiments in microgravity indicate that the kinetic theory and its boundary conditions produce accurate predictions of the principal flow variables.

When particle inertia decreases, the presence of an interstitial gas may affect both the momentum and the energy balance of the particle phase. In Chapter 4, we

consider the case in which particle inertia is large enough that the particle velocity distribution remains determined by collisions and the constitutive relations of the kinetic theory are still valid. However, the viscous gas causes additional dissipation of particle fluctuation energy [107, 123] and the mean relative velocity between the gas and the particle phase imposes a mean drag on the particle phase [67]. We thus introduce new terms in the governing equations for the granular phase and additional equations for the conservation of mass and momentum in the gas phase. Those equations are then solved with appropriate boundary conditions for each phase. Comparisons between the theory and recent Lattice-Boltzmann simulations reveal the smallest Stokes number for which the averaged equations still provide accurate results.

In Chapter 5, we use the governing equations invoked earlier to study the development of gas-particle flows in two types of bounded shear cells. The first is shaped as a racetrack and the second is axisymmetric. In these cells, the flow undergoes development because of the peculiar cell geometry or because of the presence of a streamwise body force. Using a method analog to the integral treatment of laminar boundary layers, we predict variations of cross-sectional averaged particle volume fraction, mean velocity, fluctuation velocity and mean gas velocity along the flow channel, and we verify these predictions with numerical simulations. The theory reveals the role of side walls on flow development, and it provides general insight on the presence of regions with nearly fully-developed flow in practical shear cells.

Chapter 6 turns to practical considerations for conducting experiments with the shear cells mentioned earlier. It focuses on the accuracy of digital cinematography in providing measurements of the principal flow variables. Photographical techniques are commonly used to record particle velocity in granular

flows [41, 132, 81, 10]. In these techniques, a sequence of digital images is analyzed by computer vision algorithms to identify and track particles, and, from the known image frequency, to infer their velocities. In Chapter 6, we predict errors that our imaging system will produce on the particle mean velocity and fluctuation velocity. These errors are associated with the failure of the vision algorithm to track fast-moving spheres, with uncertainties in determining the location of particle centers within a pixel, and with the possible occurrence of particle collisions between images. We check the predictions by simulating the shortcomings of the physical imaging system in our experiments. For a particular system and a certain error tolerance, we then prescribe the required capabilities of the digital camera.

In the last chapter, we propose a set of experiments to study gas-particle interactions in microgravity. Their goal is to measure the dissipation rate of particle fluctuation energy due to the presence of a viscous gas at small to moderate particle Reynolds number, and to quantify the role of particle agitation on the mean drag between gas and particles. We use the theories developed in the previous chapters to guide the design of experiments, to find out a practical range of conditions, and to estimate experimental errors.

Chapter 2

Boundary Conditions for Collisional Granular Flows

Unlike flows of ordinary fluids at normal pressure and temperature, in which the “no-slip” boundary condition applies, granular flows generally move with respect to solid boundaries. This phenomenon can be qualitatively explained by Maxwell’s classical work on a molecular gas. Maxwell showed that the slip velocity between a gas and a solid boundary is on the order of the product of the mean free path of gas and the gradient of the mean velocity at the boundary. Because the mean free path of an ordinary fluid is much smaller than characteristic length scales of the flow, the “no-slip” boundary condition is generally a good approximation. Collisional granular flows, however, are often driven by the surfaces that bound them. Because collisions among grains dissipate energy, the characteristic length scales of such flows are usually on the order of ten grain diameters. Thus, according to Maxwell’s argument, the slip velocity at the boundary cannot be neglected. Moreover, because granular flows have a relatively small thickness, their boundaries play a crucial role, which was clearly revealed in the experiments by Savage & Sayed [109], Hanes & Inman [40], and Craig et al [25] and in the computer simulations by Campbell & Gong [19].

The scope of this chapter is to derive the stresses and flux of fluctuation energy for the solid boundaries encountered in our experiments. Here, we are not concerned with conditions at interfaces between regions within a granular material, such as an “erodible” boundary between a solid-like and a fluid-like region (Jenkins & Askari [53]), or a free surface (Jenkins & Hanes [55]). Likewise, we do not

consider flows that involve long-lasting interactions between grains.

Boundary conditions for collisional granular flows at solid surfaces have been studied extensively. Hui et al [46] and Johnson & Jackson [63] proposed heuristic expressions, which depend upon adjustable constants that cannot be measured independently. Instead, consistent with the derivation of constitutive relations from the kinetic theory, our approach is to derive the stresses and flux of particle fluctuation energy at a solid boundary by averaging the collisional transfers of momentum and energy over all possible collisions between flow particles and the boundary. Calculations of this kind differ mainly in the choice of particle velocity distribution used in the averaging. To derive boundary conditions for granular flows of disks or spheres confined to a single plane, Pasquarell & Ackermann [102] and Pasquarell [101] approximated the distribution with a simple δ -function. Jenkins & Richman [61] employed a Maxwellian distribution to derive boundary conditions for flow of disks over a bumpy, frictionless wall. For the same geometry, Richman [104] and Richman & Chou [105] used the “dense-Maxwellian” velocity distribution found by Jenkins & Richman [59] and a more accurate definition of the location of the bumpy surface.

In this chapter, we derive conditions at solid surfaces using an approach similar to that proposed by Jenkins & Richman [61]. We calculate the stresses and heat flux at the wall by averaging over a continuous velocity distribution, but we relax the original assumption of small slip velocity that Jenkins & Richman invoked. An implication of their work is that there are no universal boundary conditions for collisional granular flows. Stresses and heat fluxes at solid boundaries depend on the detailed interactions between the flow particles and the wall. Different boundary conditions have to be derived for walls with different geometrical shapes.

In this section, we examine conditions for the following grains and wall geometry: first, we consider smooth spheres interacting with bumpy, frictionless walls up to relatively large slip velocity; second, we examine “planar” flows of circular disks or spheres confined to a single plane and colliding with a narrow flat, frictional wall; third, we focus on other planar flows of circular disks or spheres at bumpy, frictional walls; finally, we propose conditions for 3-dimensional flows of spheres at bumpy, frictional walls.

Our theory is limited to the slightly inelastic, moderately bumpy, and slightly frictional boundaries that we use in our experiments. We will later explain the significance of these restrictions.

2.1 Smooth Bumpy Boundaries

We analyze boundary interactions between granular flows of smooth, inelastic spheres and a bumpy, frictionless wall made of cylindrical bumps, as sketched in Figure 2.1. We consider cylindrical - rather than spherical - bumps, because the former are more straightforward to manufacture in actual experiments. This problem is very similar to that studied by Jenkins & Richman [61], Richman & Chou [105], and Richman [104]. Because in those earlier calculations the slip velocity was taken to be small compared with the granular fluctuation velocity, quadratic or higher order terms in the slip velocity were neglected in the expressions of the stresses and heat flux. In this section, we extend the results to larger slip velocities.

As illustrated in Fig. 2.1, the diameter of the flow spheres is σ , the diameter of the boundary cylinders is d , the separation between boundary cylinders is s . We define $\bar{\sigma} \equiv (d + \sigma)/2$ as the average of the two diameters. The mass of the flow

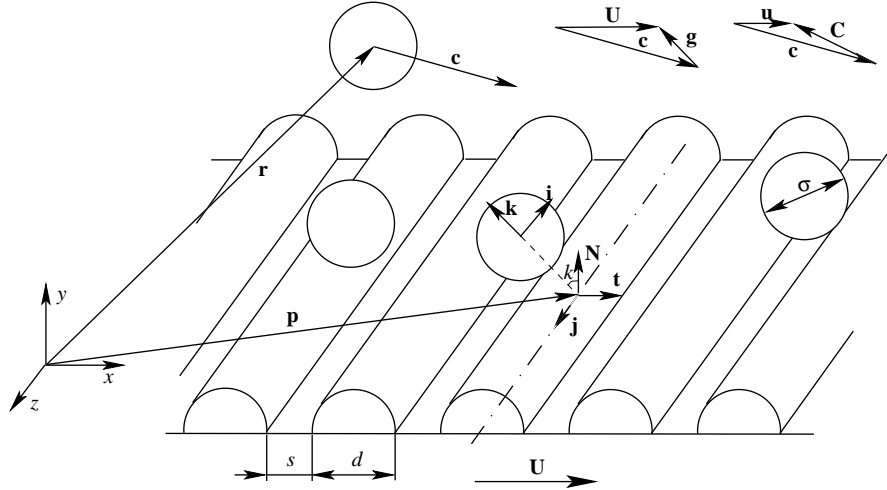


Figure 2.1: Geometry of the bumpy boundary.

sphere is m . The inward normal to the boundary is \mathbf{N} . The unit vector \mathbf{j} is parallel to the axes of the boundary cylinders. A unit vector \mathbf{t} is parallel to the wall but perpendicular to the boundary cylinders. \mathbf{N} , \mathbf{j} , and \mathbf{t} form the basis of the xyz coordinate system. A unit vector \mathbf{k} is defined in the plane passing through the center of a colliding sphere and perpendicular to the axis of the boundary cylinder involved in the collision. The direction of \mathbf{k} is pointing into the flow. The angle between \mathbf{k} and \mathbf{N} is k , and $\theta = \arcsin((d+s)/(d+\sigma))$ is the maximum value of k . \mathbf{r} is the position of the center of the flow sphere. \mathbf{p} is the position of the center of boundary cylinder. \mathbf{U} is the velocity of the boundary. \mathbf{c} is the velocity of the flow sphere before the collision. $\mathbf{g} = \mathbf{U} - \mathbf{c}$ is the relative velocity of the wall and the flow spheres. $f(\mathbf{c}, \mathbf{r})$ is the velocity distribution of the latter. By definition, the number density of flow spheres is given by

$$n(\mathbf{r}) = \int f(\mathbf{c}, \mathbf{r}) d\mathbf{c},$$

and the mean velocity of the flow is

$$\mathbf{u}(\mathbf{r}) = \frac{1}{n} \int \mathbf{c} f(\mathbf{c}, \mathbf{r}) d\mathbf{c}.$$

The fluctuation velocity is $\mathbf{C} = \mathbf{c} - \mathbf{u}$, and $\mathbf{v} = \mathbf{U} - \mathbf{u}$ is the wall velocity relative to the flow.

Because a smooth wall can only provide impulse in the direction normal to its surface, Jenkins & Richman [61] expressed the collisional rate of momentum production \mathbf{M} and the collisional dissipation rate D with the following integrals:

$$\mathbf{M} = \alpha \chi m (1 + e_w) \iint \mathbf{k} f(\mathbf{c}, \mathbf{p} + \bar{\sigma} \mathbf{k}) \bar{\sigma} (\mathbf{g} \cdot \mathbf{k})^2 d\mathbf{c} dk, \quad (2.1)$$

and

$$D = \frac{1}{2} \alpha \chi m (1 - e_w^2) \iint f(\mathbf{c}, \mathbf{p} + \bar{\sigma} \mathbf{k}) \bar{\sigma} (\mathbf{g} \cdot \mathbf{k})^3 d\mathbf{c} dk, \quad (2.2)$$

where χ is a factor that accounts for the effects of excluded area and collisional shielding on collision frequency, $\alpha = 1/(d + s)$ is the number of wall cylinders per unit length of the wall, and e_w is the coefficient of restitution for collisions between a flow sphere and the wall. To be consistent with the constitutive relations for granular flow, we assume that $1 - e_w$ is of order $\varepsilon \ll 1$. The integration is carried out for all $\mathbf{g} \cdot \mathbf{k} \geq 0$ and $-\theta \leq k \leq \theta$.

We employ the velocity distribution found by Jenkins & Richman [59] for slightly inelastic spheres. To the lowest order, their result is a corrected Maxwellian distribution:

$$f(\mathbf{c}, \mathbf{r}) = \frac{n}{(2\pi T)^{3/2}} \left[1 - \sqrt{\frac{2}{\pi}} \frac{\sigma B}{T^{3/2}} \mathbf{C} \cdot \hat{\mathbf{D}} \cdot \mathbf{C} \right] e^{-\frac{c^2}{2T}}, \quad (2.3)$$

where T is granular temperature at \mathbf{r} , $B(\nu) = \frac{\pi}{12\sqrt{2}}(1 + \frac{5}{8G})$ and $G(\nu) \equiv \frac{\nu(2-\nu)}{2(1-\nu)^3}$ are functions of the particle volume fraction ν that incorporate the Carnahan &

Starling [22] isotropic pair distribution function $(1 - \nu/2)/(1 - \nu)^3$, and $\hat{\mathbf{D}}$ is the deviatoric part of the symmetrical velocity gradient \mathbf{D} .

Following Richman & Chou [105], we expand $f(\mathbf{c}, \mathbf{p} + \bar{\sigma}\mathbf{k})$ about $\mathbf{p} + \bar{\sigma}\mathbf{N}$ and ignore terms involving $\sigma\nabla\nu$ and $\sigma\frac{\nabla T}{T}$, which are assumed to be of order ε . The resulting velocity distribution for colliding spheres is

$$f(\mathbf{c}, \mathbf{p} + \bar{\sigma}\mathbf{k}) = \frac{n}{(2\pi T)^{3/2}} \left\{ 1 + \frac{\bar{\sigma}}{T} [(\mathbf{k} \cdot \nabla - \mathbf{N} \cdot \nabla) \mathbf{u}] \cdot \mathbf{C} - \sqrt{\frac{2}{\pi}} \frac{\sigma B}{T^{3/2}} \mathbf{C} \cdot \hat{\mathbf{D}} \cdot \mathbf{C} \right\} e^{-\frac{c^2}{2T}}, \quad (2.4)$$

where all mean values are evaluated at $\mathbf{p} + \bar{\sigma}\mathbf{N}$. In this framework, the flow boundary is located at a distance $\bar{\sigma}\mathbf{N}$ from the flat base of the bumpy wall. Equations (2.1) and (2.2) can be written as

$$\mathbf{M} = \frac{1}{2}(1 + e_w)\rho\chi T \frac{1}{\sin\theta} \int \mathbf{k}\psi(\mathbf{k})dk, \quad (2.5)$$

and

$$D = \frac{1}{2}(1 - e_w^2)\rho\chi T^{3/2} \frac{1}{2\sin\theta} \int \phi(\mathbf{k})dk, \quad (2.6)$$

where

$$\psi(\mathbf{k}) = \frac{1}{T(2\pi T)^{3/2}} \int_{\mathbf{g} \cdot \mathbf{k} \geq 0} (\mathbf{g} \cdot \mathbf{k})^2 \Lambda e^{-\frac{c^2}{2T}} d\mathbf{C}, \quad (2.7)$$

$$\phi(\mathbf{k}) = \frac{1}{T^{3/2}(2\pi T)^{3/2}} \int_{\mathbf{g} \cdot \mathbf{k} \geq 0} (\mathbf{g} \cdot \mathbf{k})^3 \Lambda e^{-\frac{c^2}{2T}} d\mathbf{C}, \quad (2.8)$$

and

$$\Lambda \equiv 1 + \frac{\bar{\sigma}}{T} [(\mathbf{k} \cdot \nabla - \mathbf{N} \cdot \nabla) \mathbf{u}] \cdot \mathbf{C} - \sqrt{\frac{2}{\pi}} \frac{\sigma B}{T^{3/2}} \mathbf{C} \cdot \hat{\mathbf{D}} \cdot \mathbf{C}. \quad (2.9)$$

We first evaluate $\psi(\mathbf{k})$ and $\phi(\mathbf{k})$ by integrating over \mathbf{C} . Note that because $\mathbf{C} = \mathbf{v} - \mathbf{g}$ and \mathbf{v} is a constant, integrating over $\mathbf{g} \cdot \mathbf{k} \geq 0$ is the same as integrating over $-\mathbf{C} \cdot \mathbf{k} \geq -\mathbf{v} \cdot \mathbf{k}$. For any \mathbf{k} , we introduce another unit vector \mathbf{i} , which, together with \mathbf{k} and \mathbf{j} , forms a basis shown in Fig. 2.1. Then \mathbf{C} can be decomposed as

$$\mathbf{C} = -(\xi\mathbf{i} + \zeta(\mathbf{k} + z\mathbf{j})),$$

and $\mathbf{g} \cdot \mathbf{k}$ can be expressed as

$$\mathbf{g} \cdot \mathbf{k} = (-\mathbf{C} + \mathbf{v}) \cdot \mathbf{k} = -(\mathbf{C} \cdot \mathbf{k}) + (\mathbf{v} \cdot \mathbf{k}) = \zeta + (\mathbf{v} \cdot \mathbf{k}).$$

Then, the integrals (2.7) and (2.8) become

$$\begin{aligned} \psi(\mathbf{k}) = & \frac{1}{T(2\pi T)^{3/2}} \int_{\zeta=-(\mathbf{v} \cdot \mathbf{k})}^{\infty} \int_{\xi=-\infty}^{\infty} \int_{z=-\infty}^{\infty} \left\{ \left[\zeta^2 + 2(\mathbf{v} \cdot \mathbf{k})\zeta + (\mathbf{v} \cdot \mathbf{k})^2 \right] \right. \\ & \left[1 - \sqrt{\frac{2}{\pi}} \frac{\sigma B}{T^{3/2}} \left(D_{11}\xi^2 + D_{22}\zeta^2 + D_{33}z^2 + 2D_{12}\xi\zeta + 2D_{13}\xi z + 2D_{23}\zeta z \right) \right. \\ & \left. \left. - \eta_1\xi - \eta_2\zeta - \eta_3z \right] e^{-\frac{\xi^2 + \zeta^2 + z^2}{2T}} \right\} dz d\xi d\zeta \end{aligned} \quad (2.10)$$

and

$$\begin{aligned} \phi(\mathbf{k}) = & \frac{1}{T^{3/2}(2\pi T)^{3/2}} \int_{\zeta=-(\mathbf{v} \cdot \mathbf{k})}^{\infty} \int_{\xi=-\infty}^{\infty} \int_{z=-\infty}^{\infty} \left\{ \right. \\ & \left[\zeta^3 + 3(\mathbf{v} \cdot \mathbf{k})\zeta^2 + 3(\mathbf{v} \cdot \mathbf{k})^2\zeta + (\mathbf{v} \cdot \mathbf{k})^3 \right] \\ & \left[1 - \sqrt{\frac{2}{\pi}} \frac{\sigma B}{T^{3/2}} \left(D_{11}\xi^2 + D_{22}\zeta^2 + D_{33}z^2 + 2D_{12}\xi\zeta + 2D_{13}\xi z + 2D_{23}\zeta z \right) \right. \\ & \left. \left. - \eta_1\xi - \eta_2\zeta - \eta_3z \right] e^{-\frac{\xi^2 + \zeta^2 + z^2}{2T}} \right\} dz d\xi d\zeta \end{aligned} \quad (2.11)$$

where

$$\eta_i(\mathbf{k}, \mathbf{u}) = \frac{\bar{\sigma}}{T} \left[(\mathbf{k} \cdot \nabla - \mathbf{N} \cdot \nabla) \mathbf{u} \right] \cdot \mathbf{e}_i,$$

and

$$D_{ij} = \mathbf{e}_i \cdot \hat{\mathbf{D}} \cdot \mathbf{e}_j, \quad (i, j = 1, 2, 3),$$

with

$$\mathbf{e}_1 = \mathbf{i}, \mathbf{e}_2 = \mathbf{k}, \mathbf{e}_3 = \mathbf{j}.$$

Equations (2.10) and (2.11) can be integrated exactly by using the formulae

listed in Appendix A. The results are

$$\begin{aligned}
\psi(\mathbf{k}) = & \left(\frac{(\mathbf{v} \cdot \mathbf{k})^2}{2T} + \frac{1}{2} \right) \left(1 + \operatorname{erf} \left(\frac{\mathbf{v} \cdot \mathbf{k}}{\sqrt{2T}} \right) \right) \\
& + \frac{1}{\sqrt{\pi}} \frac{\mathbf{v} \cdot \mathbf{k}}{\sqrt{2T}} \exp \left(- \frac{(\mathbf{v} \cdot \mathbf{k})^2}{2T} \right) \\
& - \sqrt{2} \eta_2 T^{1/2} \left[\frac{\mathbf{v} \cdot \mathbf{k}}{\sqrt{2T}} \left(1 + \operatorname{erf} \left(\frac{\mathbf{v} \cdot \mathbf{k}}{\sqrt{2T}} \right) \right) + \frac{1}{\sqrt{\pi}} \exp \left(- \frac{(\mathbf{v} \cdot \mathbf{k})^2}{2T} \right) \right] \\
& - \frac{1}{\sqrt{2\pi}} B \frac{\sigma D_{22}}{T^{1/2}} \left(1 + \operatorname{erf} \left(\frac{\mathbf{v} \cdot \mathbf{k}}{\sqrt{2T}} \right) \right), \tag{2.12}
\end{aligned}$$

and

$$\begin{aligned}
\phi(\mathbf{k}) = & \frac{\mathbf{v} \cdot \mathbf{k}}{\sqrt{T}} \left(\frac{(\mathbf{v} \cdot \mathbf{k})^2}{2T} + \frac{3}{2} \right) \left(1 + \operatorname{erf} \left(\frac{\mathbf{v} \cdot \mathbf{k}}{\sqrt{2T}} \right) \right) \\
& + \sqrt{\frac{2}{\pi}} \left(\frac{(\mathbf{v} \cdot \mathbf{k})^2}{2T} + 1 \right) \exp \left(- \frac{(\mathbf{v} \cdot \mathbf{k})^2}{2T} \right) \\
& - \frac{6}{\sqrt{\pi}} B \frac{\sigma D_{22}}{T^{1/2}} \left[\frac{\mathbf{v} \cdot \mathbf{k}}{\sqrt{2T}} \left(1 + \operatorname{erf} \left(\frac{\mathbf{v} \cdot \mathbf{k}}{\sqrt{2T}} \right) \right) + \frac{1}{\sqrt{\pi}} \exp \left(- \frac{(\mathbf{v} \cdot \mathbf{k})^2}{2T} \right) \right] \\
& - 3\eta_2 T^{\frac{1}{2}} \left[\left(\frac{(\mathbf{v} \cdot \mathbf{k})^2}{2T} + \frac{1}{2} \right) \left(1 + \operatorname{erf} \left(\frac{\mathbf{v} \cdot \mathbf{k}}{\sqrt{2T}} \right) \right) \right. \\
& \left. + \frac{1}{\sqrt{\pi}} \frac{\mathbf{v} \cdot \mathbf{k}}{\sqrt{2T}} \exp \left(- \frac{(\mathbf{v} \cdot \mathbf{k})^2}{2T} \right) \right], \tag{2.13}
\end{aligned}$$

where $\operatorname{erf}(x)$ is the error function. Note that

$$\mathbf{v} \cdot \mathbf{t} = v, \quad \mathbf{v} \cdot \mathbf{k} = v \sin k, \quad \text{and } |\sin k| \leq \sin \theta.$$

We then treat $v/\sqrt{2T}$ as an $O(1)$ quantity, but regard $\sin \theta$ as a small quantity of order $\delta < 1$. We expand the error and exponential functions as power series in $\sin k$ and truncate them at the appropriate order. We further note that a term involving $\sin^n k$ in ψ (or ϕ) contributes a term of order $O(\delta^n)$ to \mathbf{M} (or D) because of the presence of the term $\bar{\sigma}\alpha = 1/2 \sin \theta$ in integrals. In this work, we focus our attention to boundaries with moderate bumpiness with $\delta = O(\varepsilon^{1/4})$ and ignore terms of order ε or higher.

Generally, a bumpy boundary with the geometry as shown in Fig. 2.1 is associated with nearly unidirectional granular flows, i.e., $\mathbf{u} = (u, 0, 0)$ and the variation in the flow direction is much smaller than the variation in the transverse direction. Therefore, we assume $\frac{\partial u}{\partial x} = \frac{\partial u}{\partial z} = 0$ and $\frac{\partial u}{\partial y} = u'$. Hence the expressions for η_2 and D_{22} can be simplified as

$$\eta_2 = \frac{\bar{\sigma} u'}{T} \sin k (\cos k - 1), \quad (2.14)$$

and

$$D_{22} = u' \sin k \cos k. \quad (2.15)$$

Upon substituting Eqs. (2.14) and (2.15) into Eqs. (2.12) and (2.13), and upon invoking the assumption that $\sigma u'/T^{1/2}$ is $O(\varepsilon^{1/2})$, we obtain the following simplified expressions for $\psi(\mathbf{k})$ and $\phi(\mathbf{k})$, up to an error of order ε ,

$$\begin{aligned} \psi(\mathbf{k}) = & \frac{1}{2} + \frac{2}{\sqrt{\pi}} \frac{v}{\sqrt{2T}} \sin k + \frac{v^2}{2T} \sin^2 k \\ & - \frac{2}{3} \frac{1}{\sqrt{\pi}} \left(\frac{v}{\sqrt{2T}} \right)^3 \sin^3 k - \frac{1}{\sqrt{2\pi}} B \frac{\sigma u'}{T^{1/2}} \sin k \cos k, \end{aligned} \quad (2.16)$$

and

$$\begin{aligned} \phi(\mathbf{k}) = & \sqrt{\frac{2}{\pi}} + \frac{3}{\sqrt{2}} \frac{v}{\sqrt{2T}} \sin k + 3 \sqrt{\frac{2}{\pi}} \frac{v^2}{2T} \sin^2 k \\ & - \sqrt{2} \left(\frac{v}{\sqrt{2T}} \right)^3 \sin^3 k - \frac{6}{\pi} B \frac{\sigma u'}{T^{1/2}} \sin k \cos k. \end{aligned} \quad (2.17)$$

With $\psi(\mathbf{k})$ and $\phi(\mathbf{k})$ given by Eqs. (2.16) and (2.17), integrals (2.5) and (2.6) become

$$\mathbf{M} = \frac{1}{2} (1 + e_w) \rho \chi T \left[\left(1 + \frac{v^2}{3T} \sin^2 \theta \right) \mathbf{N} + \sqrt{\frac{2}{\pi}} \frac{v}{\sqrt{T}} (\theta \csc \theta - \cos \theta) \mathbf{t} \right], \quad (2.18)$$

and

$$D = \frac{1}{2} (1 - e_w^2) \rho \chi T^{3/2} \sqrt{\frac{2}{\pi}} \left[\theta \csc \theta + \frac{3}{4} (\theta \csc \theta - \cos \theta) \frac{v^2}{T} \right]. \quad (2.19)$$

In numerical solution of granular flows, it is convenient to express the momentum boundary condition in the form of the ratio of shear to normal stresses at the wall. With Eq. (2.18), the stress ratio at a frictionless, bumpy boundary is

$$\frac{S}{N} = \frac{\sqrt{\frac{2}{\pi}}(\theta \csc \theta - \cos \theta) \frac{v}{\sqrt{T}}}{1 + \frac{v^2}{3T} \sin^2 \theta} \quad (2.20)$$

Upon carrying out an energy balance on a pillbox control volume and shrinking the thickness of the latter, Jenkins [50] showed that the flux of fluctuation energy through the wall is $Q = \mathbf{M} \cdot \mathbf{v} - D$. In our case,

$$Q = \frac{1}{2}(1 + e_w) \rho \chi T^{3/2} \sqrt{\frac{2}{\pi}} \left[(\theta \csc \theta - \cos \theta) \frac{v^2}{T} - \theta \csc \theta (1 - e_w) \right]. \quad (2.21)$$

By assuming moderate bumpiness and small slip, Richman & Chou [105] calculated a shear stress $S \equiv \mathbf{M} \cdot \mathbf{t}$ containing a term of order ε and, unlike our result, obtained a normal stress $N \equiv \mathbf{M} \cdot \mathbf{N}$ that is independent of slip velocity. In contrast, our expression for N increases with slip velocity. Consequently, while the ratio of shear to normal stress in the theory of Richman & Chou increases linearly with slip velocity, our stress ratio cannot exceed a maximum value for any bumpy boundary. This maximum depends only on the geometry of the boundary,

$$\left(\frac{S}{N} \right)_{\max} = \sqrt{\frac{3}{2\pi}} \frac{\theta \csc \theta - \cos \theta}{\sin \theta}, \quad (2.22)$$

and it occurs at

$$\frac{v}{\sqrt{T}} = \frac{\sqrt{3}}{\sin \theta}.$$

It is also worth noting that although the stress ratio decreases as the slip velocity increases, the shear stress itself increases monotonically with the slip velocity. In this sense, a bumpy boundary can always provide enough shear to balance external forces on granular flows.

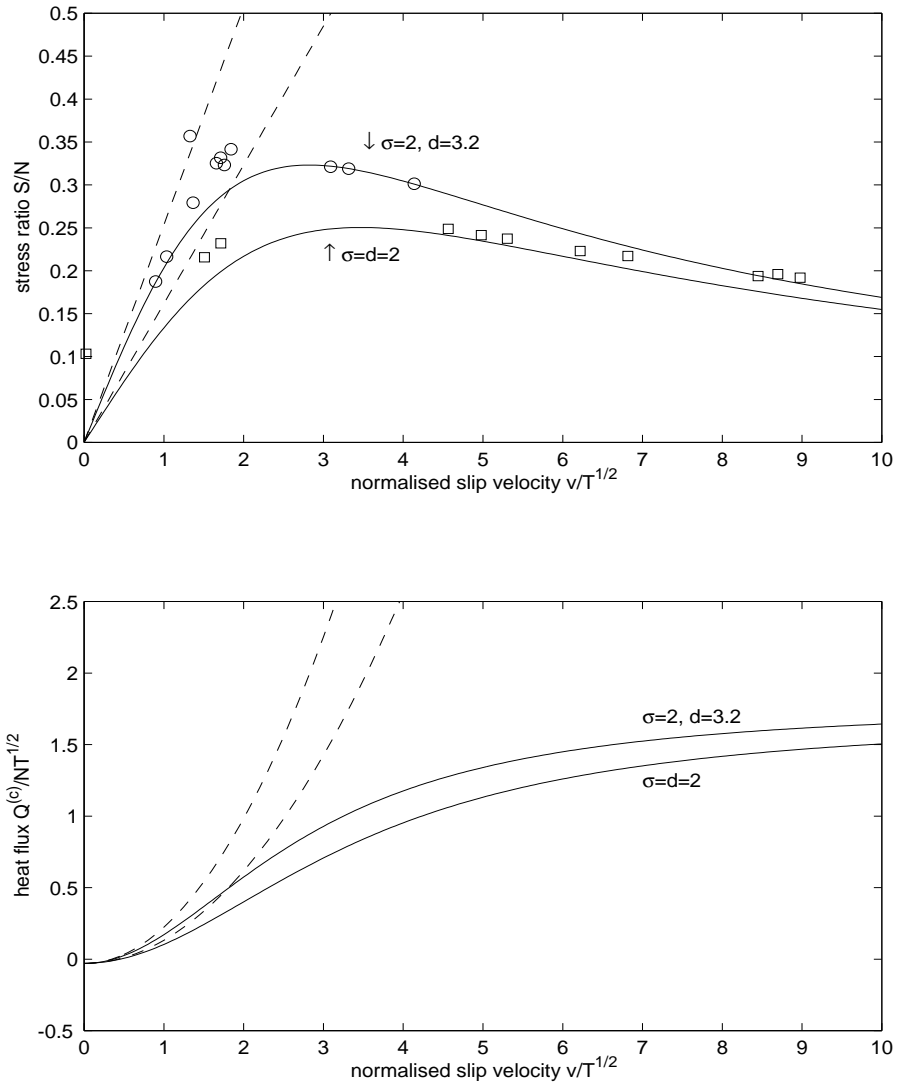


Figure 2.2: Stress ratio and heat flux at smooth, bumpy boundaries: comparison of the present study (solid lines) and the results of Richman & Chou [105] (dashed lines). Top plot: stress ratio. Bottom plot: dimensionless heat fluxes. The circles are simulation data with $\sigma = d = 2, s = 0$; the squares are $\sigma = 2, d = 3.2, s = 0$; $e_w = 0.96$ in both cases.

Because the normal stress grows with the slip velocity, the dimensionless heat flux through a bumpy boundary approaches a finite maximum, once again contradicting the linear calculation of Richman & Chou [105],

$$\left(\frac{Q}{N\sqrt{T}}\right)_{\max} = 3\sqrt{\frac{2}{\pi}} \frac{\theta \csc \theta - \cos \theta}{\sin^2 \theta}. \quad (2.23)$$

However, Eq. (2.23) must be used with caution. This is because when the slip velocity becomes large, our assumption of $v/\sqrt{2T}$ of order $O(1)$ eventually breaks down, and terms containing higher order powers of $\sin k$ can no longer be neglected.

Our predictions for the stress ratio and heat flux are plotted in Figure 2.2 along with the linear boundary condition of Richman & Chou and data from molecular dynamic simulations. As the Fig. shows, our calculation agrees with simulations over a wide range of slip velocity, while the linear boundary conditions can only be used for small slip velocities.

Jenkins & Richman [61] also derived boundary conditions in the small slip regime for bumpy boundaries that are made of randomly distributed spheres. Similar to the boundary we considered earlier this chapter, boundaries consisted of spheres can be characterised by the average bumpiness $\sin \theta$. It is then straightforward to carry out a similar analysis as we did in this section to find out the transfer of momentum and energy at the boundary by collisional interactions for dimensionless slip velocity $v/\sqrt{2T}$ of order $O(1)$. The results are

$$\frac{S}{N} = \frac{\sqrt{\frac{2}{\pi}} \frac{2}{3} \left(\frac{2}{1+\cos \theta} - \cos \theta \right) \frac{v}{\sqrt{T}}}{1 + \frac{1}{4} \sin^2 \theta \frac{v^2}{T}}, \quad (2.24)$$

and

$$\frac{Q}{N\sqrt{T}} = \frac{S}{N} \frac{v}{\sqrt{T}} - \frac{\frac{2}{\sqrt{\pi}} \frac{2}{1+\cos \theta}}{1 + \frac{1}{4} \sin^2 \theta \frac{v^2}{T}} (1 - e_w). \quad (2.25)$$

In many collisional granular flows, the dimensionless slip velocity v/\sqrt{T} is not very large. In this case, the boundary conditions derived by assuming a small slip



are good approximations, see for example Jenkins & Richman [61] and Richman & Chou [105]. In contrast, flows involving large slip at boundaries require the boundary conditions derived in this chapter. Large boundary slip can be caused by streamwise body forces (Section 3.1.2) or flows of agitated particles in a viscous gas with a large gas pressure gradient (Section 4.2.4).

2.2 Granular Flows of Disks interacting with Flat Frictional Walls

Boundary conditions for frictionless walls can be derived for various geometries using an approach similar to that used in the last section. In reality, grains and the surfaces bounding them are frictional. The additional momentum and energy transfer associated with friction can make the problem significantly more complicated. Jenkins [50] derived boundary conditions for flowing spheres interacting with a flat, frictional wall. In that case, the coupling between the velocity components that are tangential and perpendicular to the wall prohibited his derivation of expressions in closed form, but instead yielded analytical expressions for wall stresses and heat fluxes in two limiting cases only.

Such difficulty is not present in two dimensions. In this section, we consider the interaction between flowing disks (or planar flows of spheres) and a flat, frictional wall, which is possibly the simplest problem of this kind. We are then able to examine some of the assumptions that Jenkins [50] employed in his theory.

As shown in Figure 2.3, \mathbf{n} is the outward normal of the flat wall, \mathbf{t} is a unit vector tangent to the wall, \mathbf{U} is the velocity of the wall, \mathbf{u} is the mean velocity of the flow, $\mathbf{v} \equiv \mathbf{u} - \mathbf{U}$ is the slip velocity at the wall. m , σ , and ω are the mass,

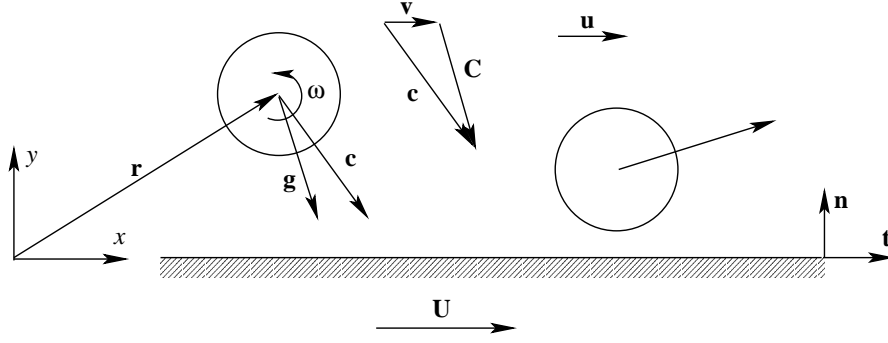


Figure 2.3: Geometry of the flat boundary.

diameter, and angular velocity of flowing disks, respectively. \mathbf{c} is the instantaneous velocity of a disk approaching the wall, and $\mathbf{C} \equiv \mathbf{c} - \mathbf{v}$ is its fluctuation velocity. $f(\mathbf{C}, \omega, \mathbf{r})$ is the velocity distribution of flow disks at position \mathbf{r} ; its integration over velocity space gives the number density n of flow disks

$$n(\mathbf{r}) = \iint f(\mathbf{C}, \omega, \mathbf{r}) d\mathbf{C} d\omega$$

The average value of any particle property ψ is defined by

$$\langle \psi \rangle = \frac{1}{n} \iint \psi(\mathbf{C}, \omega) f(\mathbf{C}, \omega, \mathbf{r}) d\mathbf{C} d\omega$$

where the dependence of $\langle \psi \rangle$ on \mathbf{r} is to be understood. For example, the mean relative velocity of flow disks is $\mathbf{v} = \langle \mathbf{c} \rangle$.

The velocities of a colliding disk before and after collision are related to the collisional impulse \mathbf{J} by

$$m(\mathbf{c}' - \mathbf{c}) = \mathbf{J}, \quad (2.26)$$

and

$$I(\omega' - \omega) = -\frac{\sigma}{2} \mathbf{n} \times \mathbf{J}, \quad (2.27)$$

where primes denote post-collision velocities and $I = \frac{1}{8} m \sigma^2$ is the moment of inertia for disks of uniform density.

For convenience, we introduce the relative velocity \mathbf{g} at the point of contact,

$$\mathbf{g} = \mathbf{c} - \frac{\sigma}{2}\boldsymbol{\omega} \times \mathbf{n}.$$

The change of total kinetic energy per collision is related to the collision impulse as

$$\Delta K = \mathbf{g} \cdot \mathbf{J} + \frac{1}{2m}\mathbf{J} \cdot \mathbf{J} + \frac{1}{m}(\mathbf{n} \times \mathbf{J}) \cdot (\mathbf{n} \times \mathbf{J}). \quad (2.28)$$

As Jenkins [50] showed, the rate of supply of linear momentum per unit area of the wall \mathbf{M} and the rate of energy dissipation per unit area D are

$$\mathbf{M} = \Theta[\mathbf{J}] \quad (2.29)$$

and

$$D = \Theta[-\Delta K], \quad (2.30)$$

where the operator Θ is defined as

$$\Theta[\psi] \equiv -\chi \iint_{\mathbf{C} \cdot \mathbf{n} \leq 0} \psi f(\mathbf{C}, \boldsymbol{\omega})(\mathbf{C} \cdot \mathbf{n}) d\mathbf{C} d\boldsymbol{\omega}.$$

In this expression, the factor χ accounts for the effects of the presence of the flat wall on the particle number density, and the integration is over all collisions. Jenkins also derived expression for the flux of fluctuation energy through the flat wall into the flow, Q , as

$$Q = -\mathbf{g}_0 \cdot \mathbf{M} - D, \quad (2.31)$$

where \mathbf{g}_0 is the mean relative velocity at the contact point,

$$\mathbf{g}_0 = \mathbf{v} - \frac{\sigma}{2} \langle \boldsymbol{\omega} \rangle \times \mathbf{n}$$

For simplicity, we follow Jenkins [50] in ignoring the fluctuation in particle spin, i.e., $\boldsymbol{\omega} = \langle \boldsymbol{\omega} \rangle$. Then

$$\mathbf{g} = \mathbf{g}_0 + \mathbf{C}. \quad (2.32)$$

Note that with this assumption, $f(\mathbf{C}, \omega)$ in any integrals may be replaced with $f(\mathbf{C})$.

Substituting Eqs. (2.28)–(2.30) and (2.32) into Eq. (2.31), we find that Q can be expressed as

$$Q = \Theta[q], \quad (2.33)$$

where

$$q = \mathbf{C} \cdot \mathbf{J} + \frac{1}{2m} \mathbf{J} \cdot \mathbf{J} + \frac{\sigma^2}{8I} (\mathbf{n} \times \mathbf{J}) \cdot (\mathbf{n} \times \mathbf{J}). \quad (2.34)$$

Walton [124] proposed a three-parameter model to characterize collisions, in which the normal component of \mathbf{g} before and after collision are related by the coefficient of restitution e with

$$\mathbf{g}' \cdot \mathbf{n} = -e(\mathbf{g} \cdot \mathbf{n}). \quad (2.35)$$

To determine the tangential component of \mathbf{g} after collision, we distinguish two kinds of collisions. If the contact point relative to the wall does not slide, the point of contact is deemed to “stick”, and the tangential component of \mathbf{g} before and after the collision are related by a tangential coefficient of restitution β_0 using

$$\mathbf{g}' \cdot \mathbf{t} = -\beta_0(\mathbf{g} \cdot \mathbf{t}). \quad (2.36)$$

In a collision that involves sliding, the tangential and normal components of the impulse are related by Coulomb friction,

$$\mathbf{J} \cdot \mathbf{s} = -\mu(\mathbf{J} \cdot \mathbf{n}). \quad (2.37)$$

where μ is the coefficient of friction, \mathbf{s} is a unit vector in the direction of relative velocity,

$$\mathbf{s} \equiv \frac{\mathbf{g} \cdot \mathbf{t}}{|\mathbf{g} \cdot \mathbf{t}|} \mathbf{t}.$$

Foerster, et al. [33] verified experimentally the validity of Walton's impact model in Eqs. (2.35)–(2.37) for a variety of homogeneous spheres impacting a flat plate or each other. However, there are instances for which Walton's assumption of constant impact coefficients fails. Louge & Adams observed anomalies in the apparent coefficients of normal restitution and friction [74] for hard spheres impacting a softer elastoplastic plate. Zener [137] outlined a theory for the broadcasting of waves in thin plates that leads to a dependence of normal restitution coefficients on plate thickness. More recently, Calsamiglia, et al. [15] confirmed the model for disks, but also revealed anomalies in the normal restitution coefficients in two dimensions. Despite these occasional difficulties, we adopt Walton's model for disks. In this case, the collision impulse is,

$$\mathbf{J}^{(1)} = -m(1+e) \left[(\mathbf{n} \cdot \mathbf{g})\mathbf{n} + \frac{\mu}{\bar{\mu}_0} (\mathbf{t} \cdot \mathbf{g})\mathbf{t} \right] \quad (2.38)$$

for collisions that do not slide. For those that do,

$$\mathbf{J}^{(2)} = -m(1+e)(\mathbf{n} \cdot \mathbf{g})(\mathbf{n} - \mu\mathbf{s}), \quad (2.39)$$

where $\bar{\mu}_0$ is a normalised friction coefficient,

$$\bar{\mu}_0 \equiv \left(\frac{m\sigma^2}{4I} + 1 \right) \frac{1+e}{1+\beta_0} \mu.$$

For disks of uniform density, $\bar{\mu}_0 = \frac{3(1+e)}{1+\beta_0} \mu$. Sticking occurs as long as the tangential component of impulse \mathbf{J} is smaller than $\mu|\mathbf{J} \cdot \mathbf{n}|$, i.e., when

$$|\mathbf{g} \cdot \mathbf{t}| \leq \bar{\mu}_0 |\mathbf{g} \cdot \mathbf{n}|.$$

Upon substituting Eqs. (2.38) and (2.39) into Eq. (2.34) and using $\mathbf{n} \cdot \mathbf{g} = \mathbf{n} \cdot \mathbf{C}$, we find for sticking collisions,

$$q^{(1)} = -\frac{1}{2}m(1+e) \left\{ (1-e)(\mathbf{C} \cdot \mathbf{n})^2 + \frac{\mu}{\bar{\mu}_0} \left(g_0 + (\mathbf{C} \cdot \mathbf{t}) \right) \left[(1-\beta_0)(\mathbf{C} \cdot \mathbf{t}) - (1+\beta_0)g_0 \right] \right\}, \quad (2.40)$$

and for sliding collisions

$$q^{(2)} = -\frac{1}{2}m(1+e)\left\{\left[(1-e) - \mu\bar{\mu}_0(1+\beta_0)\right](\mathbf{C}\cdot\mathbf{n})^2 + 2\mu(\mathbf{C}\cdot\mathbf{n})(\mathbf{C}\cdot\mathbf{t})\right\}, \quad (2.41)$$

where $g_0 \equiv \mathbf{g}_0 \cdot \mathbf{t}$. For convenience, we denote $x \equiv \mathbf{C} \cdot \mathbf{t}$ as the tangential component of the fluctuation velocity and $y \equiv \mathbf{C} \cdot \mathbf{n}$ as the normal component of the fluctuation velocity. The sticking and sliding regime are distinguished using

$$\begin{aligned} \mathbf{J} &= \mathbf{J}^{(1)}, \quad q = q^{(1)} && \text{if } \bar{\mu}_0 y - g_0 \leq x \leq -\bar{\mu}_0 y - g_0; \\ \mathbf{J} &= \mathbf{J}^{(2)}, \quad q = q^{(2)} && \text{otherwise;} \end{aligned}$$

where we have noted that particles collide with the flat wall if and only if $y = \mathbf{C} \cdot \mathbf{n} \leq 0$.

For the distribution of the pre-collisional linear velocity, we assume that the particle velocity component in the direction perpendicular to the wall is uncorrelated to the component parallel to the wall. Then the velocity distribution can be expressed as

$$f(\mathbf{C}) = nX(x)Y(y),$$

where $X(x)$ and $Y(y)$ are functions of x and y satisfying

$$\int_{-\infty}^{\infty} X(x)dx = \int_{-\infty}^{\infty} Y(y)dy = 1,$$

and

$$\int_{-\infty}^{\infty} xX(x)dx = \int_{-\infty}^{\infty} yY(y)dy = 0.$$

Granular temperatures are defined as the second moments of the velocity distribution,

$$\int_{-\infty}^{\infty} x^2 X(x)dx = T_{xx}, \quad \text{and} \quad \int_{-\infty}^{\infty} y^2 Y(y)dy = T_{yy}.$$

If the flow is isotropic, then $T_{xx} = T_{yy}$.

For flows near a flat wall, it is reasonable to assume that the x -component of velocity obeys a Maxwellian distribution,

$$X(x) = \frac{1}{\sqrt{2\pi T_{xx}}} e^{-\frac{x^2}{2T_{xx}}},$$

from which we evaluate $\Theta[\mathbf{J}]$ and $\Theta[q]$ to find the surface traction \mathbf{M} and heat flux Q at the flat wall. After some manipulation, the results can be written

$$N = \mathbf{M} \cdot \mathbf{n} = \rho\chi(1+e) \int_{-\infty}^0 y^2 Y(y) dy, \quad (2.42)$$

$$\begin{aligned} S = -\mathbf{M} \cdot \mathbf{t} = \rho\chi(1+e) & \left\{ \frac{\mu}{2} \int_{-\infty}^0 \left[\operatorname{erf}(r+ay) + \operatorname{erf}(r-ay) \right] y^2 Y(y) dy \right. \\ & + \frac{\mu}{2\bar{\mu}_0} g_0 \int_{-\infty}^0 \left[\operatorname{erf}(r+ay) - \operatorname{erf}(r-ay) \right] y Y(y) dy \\ & \left. + \frac{\mu}{\bar{\mu}_0} \sqrt{\frac{T_{xx}}{2\pi}} \int_{-\infty}^0 \left[e^{-(r+ay)^2} - e^{-(r-ay)^2} \right] y Y(y) dy \right\}, \quad (2.43) \end{aligned}$$

and

$$\begin{aligned} Q = \frac{1}{2} \rho\chi(1+e) & \left\{ \left[(1-e) - \mu\bar{\mu}_0(1+\beta_0) \right] \int_{-\infty}^0 y^3 Y(y) dy \right. \\ & + \frac{1}{2} \mu\bar{\mu}_0(1+\beta_0) \int_{-\infty}^0 \left[\operatorname{erf}(r-ay) - \operatorname{erf}(r+ay) \right] y^3 Y(y) dy \\ & - \mu(1+\beta_0) \sqrt{\frac{T_{xx}}{2\pi}} \int_{-\infty}^0 \left[e^{-(r+ay)^2} + e^{-(r-ay)^2} \right] y^2 Y(y) dy \\ & - \frac{\mu}{2\bar{\mu}_0} \left[(1+\beta_0)g_0^2 - (1-\beta_0)T_{xx} \right] \int_{-\infty}^0 \left[\operatorname{erf}(r-ay) - \operatorname{erf}(r+ay) \right] y Y(y) dy \\ & \left. - \frac{\mu}{\bar{\mu}_0} (1+\beta_0)g_0 \sqrt{\frac{T_{xx}}{2\pi}} \int_{-\infty}^0 \left[e^{-(r-ay)^2} - e^{-(r+ay)^2} \right] y Y(y) dy \right\}, \quad (2.44) \end{aligned}$$

where $a \equiv \bar{\mu}_0/\sqrt{2T_{xx}}$ is a constant, $r \equiv g_0/\sqrt{2T_{xx}}$ is the dimensionless slip velocity at the contact point. If the distribution $Y(y)$ is known, Eqs. (2.42)–(2.44) can be used to find the final expressions for S , N , and Q .

In his treatment of flows of spheres over a flat, frictional wall, Jenkins [50] assumed an isotropic velocity distribution consisting of twin δ functions. In his

numerical simulations of spheres interacting with a flat, frictional wall, Louge [76] instead observed that, while $X(x)$ is well-represented by a Maxwellian, $Y(y)$ in fact resembles a Weibull function [130]. We assume that Louge's result for spheres also applies to disks.

A more consistent theoretical approach would be to derive the velocity distribution near the wall by solving the Boltzmann equation with an appropriate collision operator. Recently, Kumaran [68] proposed an asymptotic velocity distribution for simple shear flows near a flat wall. However, because Kumaran used a different method than our kinetic theory derivation, it is not clear how to incorporate his result into our theoretical framework. For comparison, we consider three distributions for $Y(y)$,

1. twin δ -functions:

$$Y(y) = \frac{1}{2} \left[\delta(y + \sqrt{T_{yy}}) + \delta(y - \sqrt{T_{yy}}) \right];$$

2. a Maxwellian distribution:

$$Y(y) = \frac{1}{\sqrt{2\pi T_{yy}}} e^{-\frac{y^2}{2T_{yy}}};$$

3. a Weibull distribution:

$$Y(y) = \frac{|y|}{T_{yy}} e^{-\frac{y^2}{T_{yy}}}.$$

These distributions are shown in Figure 2.4. Because they are all symmetric in y ,

$$\int_{-\infty}^0 y^2 Y(y) dy = \frac{1}{2} T_{yy},$$

they all share the same expression for normal stress,

$$N = \frac{1}{2} \rho \chi (1 + e) T_{yy}, \tag{2.45}$$

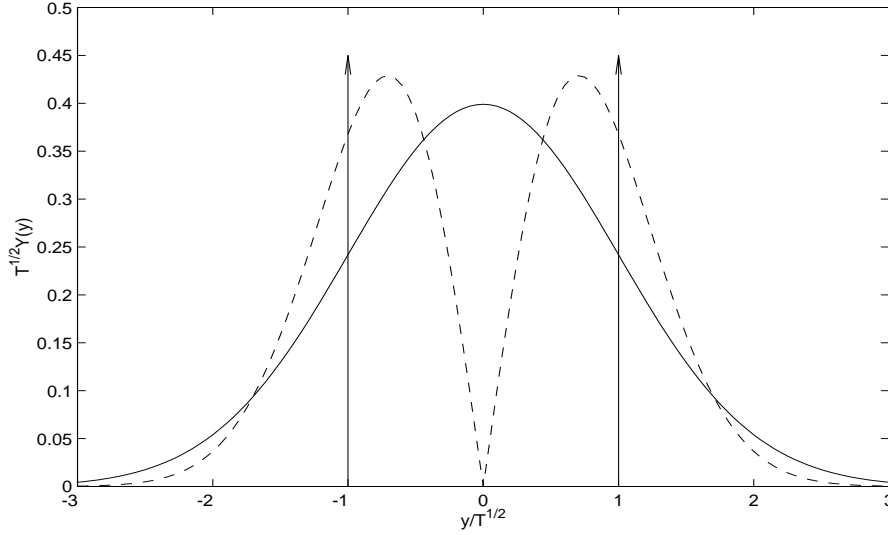


Figure 2.4: Distributions of the y -component of the velocity. The solid line is the Maxwellian distribution; the dashed line is the Weibull distribution; the arrows indicate twin δ -functions.

but they differ in the stress ratio S/N and the dimensionless heat flux $Q/NT_{yy}^{1/2}$.

For the twin δ -functions,

$$\begin{aligned} \frac{S}{N} = & \frac{\mu}{2} \left[\operatorname{erf}(r + \gamma) + \operatorname{erf}(r - \gamma) \right] + \frac{\mu}{2\gamma} r \left[\operatorname{erf}(r + \gamma) - \operatorname{erf}(r - \gamma) \right] \\ & + \frac{\mu}{2\sqrt{\pi}\gamma} \left[e^{-(r+\gamma)^2} - e^{-(r-\gamma)^2} \right], \end{aligned} \quad (2.46)$$

and

$$\begin{aligned} \frac{Q}{NT_{yy}^{1/2}} = & \frac{1}{2} \left[\mu\bar{\mu}_0(1 + \beta_0) - (1 - e) \right] + \frac{1}{4} \mu\bar{\mu}_0(1 + \beta_0) \left\{ \right. \\ & \frac{1}{\gamma^2} \left[r^2 - 1 - \frac{1}{2} \frac{1 - \beta_0}{1 + \beta_0} \right] \left[\operatorname{erf}(r + \gamma) - \operatorname{erf}(r - \gamma) \right] \\ & - \frac{1}{\gamma\sqrt{\pi}} \left[e^{-(r+\gamma)^2} + e^{-(r-\gamma)^2} \right] \\ & \left. - \frac{1}{\sqrt{\pi}} \frac{r}{\gamma^2} \left[e^{-(r+\gamma)^2} - e^{-(r-\gamma)^2} \right] \right\}, \end{aligned} \quad (2.47)$$

where

$$\gamma \equiv \frac{\bar{\mu}_0}{\sqrt{2}} \sqrt{\frac{T_{yy}}{T_{xx}}},$$

is a constant. For a Maxwellian distribution,

$$\begin{aligned} \frac{S}{N} = & \mu \frac{2}{\sqrt{\pi}} \left\{ \left[\text{Ierf}(r; 2, \sqrt{2}\gamma) + \text{Ierf}(r; 2, -\sqrt{2}\gamma) \right] \right. \\ & + \frac{r}{\sqrt{2}\gamma} \left[\text{Ierf}(r; 1, \sqrt{2}\gamma) - \text{Ierf}(r; 1, -\sqrt{2}\gamma) \right] \\ & \left. + \frac{1}{\sqrt{2\pi}\gamma} \left[\text{Iexp}(r; 1, \sqrt{2}\gamma) - \text{Iexp}(r; 1, -\sqrt{2}\gamma) \right] \right\}, \end{aligned} \quad (2.48)$$

and

$$\begin{aligned} \frac{Q}{NT_{yy}^{1/2}} = & \sqrt{\frac{2}{\pi}} \left[\mu \bar{\mu}_0 (1 + \beta_0) - (1 - e) \right] + \sqrt{\frac{2}{\pi}} \mu \bar{\mu}_0 (1 + \beta_0) \left\{ \right. \\ & \left[\text{Ierf}(r; 3, -\sqrt{2}\gamma) - \text{Ierf}(r; 3, \sqrt{2}\gamma) \right] \\ & - \frac{1}{\gamma \sqrt{2\pi}} \left[\text{Iexp}(r; 2, \sqrt{2}\gamma) + \text{Iexp}(r; 2, -\sqrt{2}\gamma) \right] \\ & + \frac{1}{2\gamma^2} \left[r^2 - \frac{1}{2} \frac{1 - \beta_0}{1 + \beta_0} \right] \left[\text{Ierf}(r; 1, \sqrt{2}\gamma) - \text{Ierf}(r; 1, -\sqrt{2}\gamma) \right] \\ & \left. + \frac{1}{2\sqrt{\pi}} \frac{r}{\gamma^2} \left[\text{Iexp}(r; 1, \sqrt{2}\gamma) - \text{Iexp}(r; 1, -\sqrt{2}\gamma) \right] \right\}, \end{aligned} \quad (2.49)$$

where

$$\text{Iexp}(r; n, a) \equiv \int_{-\infty}^0 t^n e^{-t^2} e^{-(r+at)^2} dt$$

and

$$\text{Ierf}(r; n, a) \equiv \int_{-\infty}^0 t^n e^{-t^2} \text{erf}(r + at) dt$$

are functions of r having n and a as parameters. For a Weibull distribution,

$$\begin{aligned} \frac{S}{N} = & \mu \left\{ \left[\text{Ierf}(r; 3, \gamma) + \text{Ierf}(r; 3, -\gamma) \right] \right. \\ & + \frac{r}{\gamma} \left[\text{Ierf}(r; 2, \gamma) - \text{Ierf}(r; 2, -\gamma) \right] \\ & \left. + \frac{1}{\gamma \sqrt{\pi}} \left[\text{Iexp}(r; 2, \gamma) - \text{Iexp}(r; 2, -\gamma) \right] \right\}, \end{aligned} \quad (2.50)$$

and

$$\begin{aligned}
\frac{Q}{NT_{yy}^{1/2}} = & \frac{3\sqrt{\pi}}{8} \left[\mu\bar{\mu}_0(1 + \beta_0) - (1 - e) \right] + \mu\bar{\mu}_0(1 + \beta_0) \left\{ \right. \\
& \left[\text{Ierf}(r; 4, -\gamma) - \text{Ierf}(r; 4, \gamma) \right] \\
& - \frac{1}{\gamma\sqrt{\pi}} \left[\text{Iexp}(r; 3, \gamma) + \text{Iexp}(r; 3, -\gamma) \right] \\
& + \frac{1}{\gamma^2} \left[r^2 - \frac{1}{2} \frac{1 - \beta_0}{1 + \beta_0} \right] \left[\text{Ierf}(r; 2, \gamma) - \text{Ierf}(r; 2, -\gamma) \right] \\
& \left. + \frac{1}{\sqrt{\pi}} \frac{r}{\gamma^2} \left[\text{Iexp}(r; 2, \gamma) - \text{Iexp}(r; 2, -\gamma) \right] \right\}. \quad (2.51)
\end{aligned}$$

The above calculations for disks can be extended to flows of a monolayer of spheres interacting with a perpendicular, narrow, flat frictional base. In the corresponding experiment, the spheres may be constrained to reside in a narrow channel bounded by two flat plates and the narrow base of interest. Because the moment of inertia of homogeneous spheres of mass m and diameter σ is $I = \frac{1}{10}m\sigma^2$, Equations 2.46 to 2.51 can be extended to such flows by replacing $\bar{\mu}_0$ with

$$\bar{\mu}_0 \equiv \frac{7(1 + e)}{2(1 + \beta_0)}\mu.$$

Figure 2.5 shows the stress ratio and heat flux in terms of dimensionless slip velocity $g_0/\sqrt{T_{xx}}$ for various impact parameters e , μ and β_0 . In this Fig., the functions Iexp and Ierf are evaluated numerically, and we plot a normalized stress ratio

$$R \equiv \frac{\bar{\mu}_0}{\mu} \frac{S}{N}$$

instead of S/N to magnify the effects of e and β_0 on the ratio.

As Fig. 2.5 indicates, the stress ratio is nearly independent of the assumed velocity distribution. This is particularly true at large slip velocities $g_0/\sqrt{T_{xx}}$, where S/N nearly equals the coefficient of friction. In contrast, the dimensionless heat

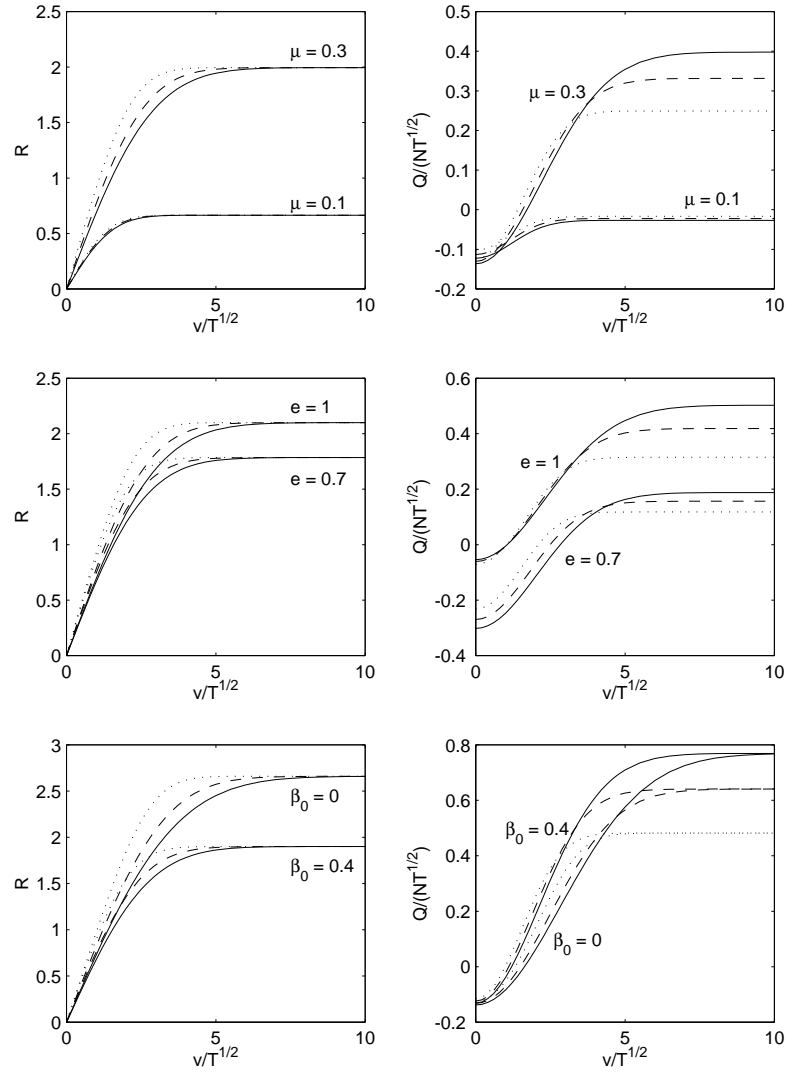


Figure 2.5: Effects of the particle velocity distribution on the stress ratio and flux of fluctuation energy at flat, frictional walls. Dotted lines: twin- δ distribution; solid lines: Maxwellian distribution; dashed lines: Weibull distribution. Figures in the top row show stress ratios and heat fluxes with $\mu = 0.1$ and 0.3 , and fixed $e = 0.9$, and $\beta_0 = 0$. Figures in the middle row correspond to $e = 1$ and 0.7 , fixed $\mu = 0.3$ and $\beta_0 = 0$. Figures in the bottom row are for $\beta_0 = 0$ and 0.4 , fixed $e = 0.9$ and $\mu = 0.4$.

flux is sensitive to the velocity distribution. To choose an appropriate expression for the latter near the flat wall, we must wait for data from numerical simulations or for more sophisticated theories that allow the coupling of particle velocity distribution and the interaction between particles and the wall.

In an attempt to improve the agreement in heat flux between Jenkins' theory [50] and Louge's numerical simulation data [76] for 3D flows of spheres over a flat, frictional wall, Jenkins & Louge [56] proposed that the normal and tangential components of pre-collisional velocities are correlated. An evidence of the correlation is that the dimensionless heat flux in the simulations depends on the coefficient of restitution of binary collisions between flowing grains. It is true that, at least in the sliding case, the two components of the post-collisional velocities are correlated. This correlation could survive after several collisions within the flow, and last until the next collision between the same grain and the flat wall. Jenkins & Louge [56] assumed that, in sliding collisions with the wall, the pre-collisional correlation is related to its post-collisional counterpart by a simple function of the coefficient of restitution of binary collisions between flowing grains. By fitting their simulation data, these authors improved their expression for heat flux in the large slip regime. However, as Fig 2.5 shows, the velocity distribution also affects the heat flux in that regime. The reality may involve both effects, namely the persistence of a velocity component correlation before and after a collision, and a significant departure of the velocity distribution from the twin δ -functions that Jenkins & Louge assumed. An advanced theory informed with detailed simulation data is needed to reveal the complicated interactions between colliding spheres and a frictional wall.

In his treatment of 3D flows of spheres, Jenkins [50] calculated the stress ratio

and the heat flux in two limiting regimes. Here, we calculate the corresponding expressions in 2D. By comparing the results with the exact expressions, we determine the range of impact parameters where the simplified two-limit expressions is a good approximation.

In the “small-friction/all-sliding” regime, the dimensionless slip velocity is so large that almost all collisions involve sliding, thus $\mathbf{J} = \mathbf{J}^{(2)}$ and $q = q^{(2)}$ for all collisions. Similarly, $\mathbf{J} = \mathbf{J}^{(1)}$ and $q = q^{(1)}$ for all collisions in the “small-slip/all-sticking” regime that Jenkins [50] considered. In this section, we only quote results with the twin δ -function distribution of the normal velocity component. Expressions with the Maxwellian and Weibull distributions are given in Appendix B. After evaluating the integrals in Eqs. (2.29) and (2.33) with appropriate expressions for \mathbf{J} and q , we find that, in the “all-sticking” regime,

$$\frac{S}{N} = \frac{\mu}{\gamma} r = \sqrt{2} \sqrt{\frac{T_{xx}}{T_{yy}}} \frac{\mu}{\bar{\mu}_0} \frac{g_0}{\sqrt{2T_{xx}}}, \quad (2.52)$$

$$\begin{aligned} \frac{Q}{N\sqrt{T_{yy}}} &= \frac{1}{2\gamma^2} \mu \bar{\mu}_0 (1 + \beta_0) r^2 - \frac{1}{4\gamma^2} \mu \bar{\mu}_0 (1 - \beta_0) - \frac{1}{2} (1 - e) \\ &= \frac{\mu}{\bar{\mu}_0} (1 + \beta_0) \frac{T_{xx}}{T_{yy}} \left(\frac{g_0^2}{2T_{xx}} \right) - \frac{1}{2} \frac{\mu}{\bar{\mu}_0} (1 - \beta_0) \frac{T_{xx}}{T_{yy}} - \frac{1}{2} (1 - e), \end{aligned} \quad (2.53)$$

and in the “all-sliding” regime

$$\frac{S}{N} = \mu \operatorname{erf} \left(\frac{g_0}{\sqrt{2T_{xx}}} \right) \approx \mu, \quad (2.54)$$

$$\begin{aligned} \frac{Q}{N\sqrt{T_{yy}}} &= \frac{1}{2} \mu \bar{\mu}_0 (1 + \beta_0) - \frac{1}{2} (1 - e) - \sqrt{\frac{2}{\pi}} \mu \frac{T_{xx}}{T_{yy}} e^{-\frac{g_0^2}{2T_{xx}}} \\ &\approx \frac{1}{2} \left[\mu \bar{\mu}_0 (1 + \beta_0) - (1 - e) \right], \end{aligned} \quad (2.55)$$

where we have used $\operatorname{erf}(x) \approx 1$ and $e^{-x^2} \approx 0$ when $x \gg 1$.

Alternately, the stress ratio and the heat flux in the small-slip and large-slip limits can be obtained by assuming $r \ll \gamma$ and $r \gg \gamma$ in Eqs. (2.46) and (2.47).

The results in the “small-slip” regime are

$$\frac{S}{N} = \frac{\mu}{\gamma} \operatorname{erf}(\gamma)r, \quad (2.56)$$

$$\begin{aligned} \frac{Q}{N\sqrt{T_{yy}}} &= \frac{1}{2\gamma^2}\mu\bar{\mu}_0(1+\beta_0)\operatorname{erf}(\gamma)r^2 - \frac{1}{4\gamma^2}\mu\bar{\mu}_0(1-\beta_0) - \frac{1}{2}(1-e) \\ &\quad + \frac{1}{2}\mu\bar{\mu}_0(1+\beta_0)\left[1 - \operatorname{erf}(\gamma) - \frac{1}{\sqrt{\pi}\gamma}e^{-\gamma^2}\right], \end{aligned} \quad (2.57)$$

and in the “all-sliding” regime

$$\frac{S}{N} = \mu \operatorname{erf}\left(\frac{g_0}{\sqrt{2T_{xx}}}\right) \approx \mu, \quad (2.58)$$

$$\frac{Q}{N\sqrt{T_{yy}}} = \frac{1}{2}\mu\bar{\mu}_0(1+\beta_0) - \frac{1}{2}(1-e). \quad (2.59)$$

Since $\mu/\bar{\mu}_0$ is independent of μ , the stress ratio and heat flux in the small-slip case calculated from the simplified “all-sticking” assumption in Eqs. (2.52) and (2.53) are independent of the coefficient of friction. On the other hand, the small-slip limit obtained from the exact expressions in Eqs. (2.56) and (2.57) depend on μ through their dependence on γ . Figure 2.6 shows the exact calculation Eqs. (2.46)-(2.47) and the simplified approximation Eqs. (2.52)-(2.55) for various impact parameters. Both Eqs. (2.56)-(2.59) and Fig. 2.6 show that the two-limit approximation agrees with the exact calculation for large slip but deviates from the latter for small slip unless γ is large i.e., unless μ or e are large, and/or β_0 is small.

Finally, to use these boundary conditions in a continuum representation, we need a prediction of $\langle\omega\rangle$ to calculate g_0 . A common assumption is that the mean spin is half the vorticity of the flow,

$$\langle\omega\rangle = \frac{1}{2}\nabla \times \mathbf{u}. \quad (2.60)$$

The numerical simulations of Campbell [19] and Louge [76] show that, while this assumption is valid in the interior of the flow, it breaks down near the boundary.

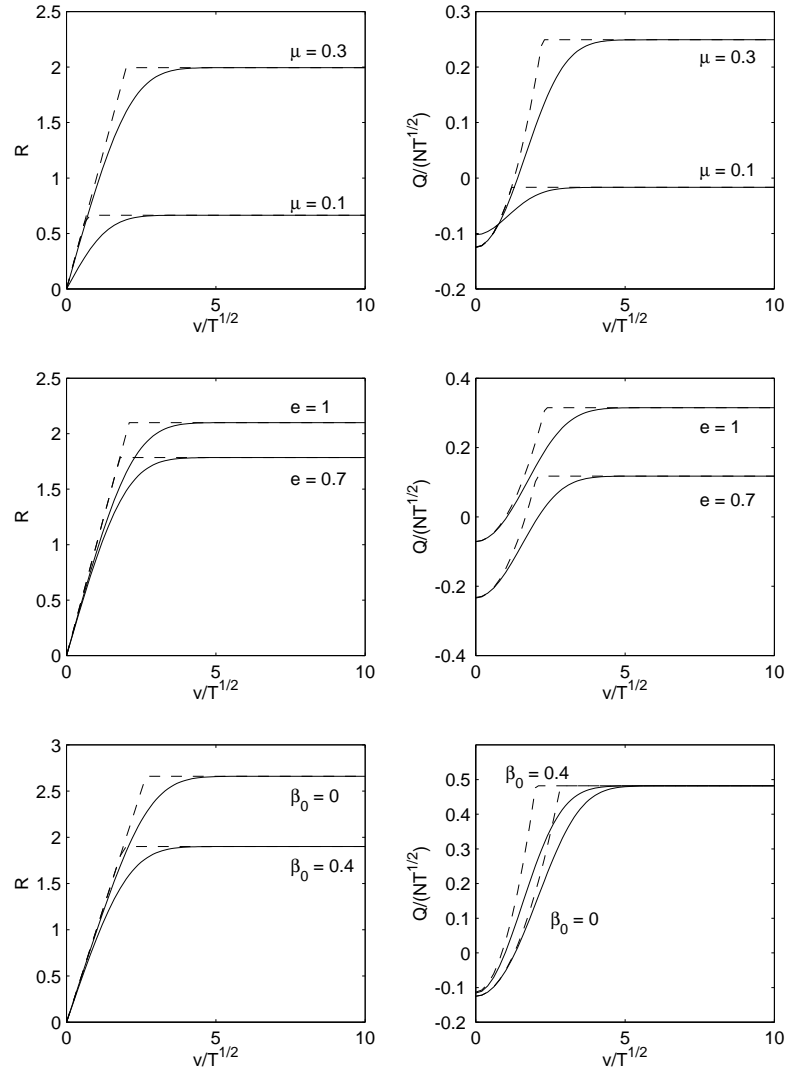


Figure 2.6: Comparison of stress ratios and fluxes of fluctuation energy calculated in the two limits of “all-sticking” and “all-sliding” with the exact calculation assuming a twin- δ distribution. Solid lines: exact calculation; dashed lines: two-limit approximation. Figures in the top row show the stress ratio and heat flux corresponding to $\mu = 0.1$ and 0.3 with fixed $e = 0.9$, and $\beta_0 = 0$. Figures in the middle row correspond to $e = 1$ and 0.7 , fixed $\mu = 0.3$ and $\beta_0 = 0$. Figures in the bottom row are for $\beta_0 = 0$ and 0.4 , fixed $e = 0.9$ and $\mu = 0.4$.

However, our experience is that the contribution of particle spin on the mean relative velocity at the contact point is small in practical situations [75].

2.3 Granular Flows of Disks interacting with Bumpy, Frictional Walls

In the previous two sections, we derived the stress ratio and heat flux at smooth, bumpy boundaries and at flat, frictional walls. However, because real bumpy walls are also frictional, an analytical derivation of their boundary conditions is much more difficult in the general case and, consequently, simplifying assumptions must be invoked.

For such calculation, Cao *et al* [20] assumed that all collisions involve Coulomb friction. Following Richman & Chou [105], they assumed that the dimensionless slip velocity v/\sqrt{T} is a small quantity on the order of $\varepsilon^{1/2}$. Except for a small correction to the energy dissipation, their results implied that friction has almost no effect on boundary conditions, which is counter-intuitive. In our present calculations, we show that the conclusions of Cao *et al* [20] only hold for very bumpy boundaries with $\delta \equiv \sin \theta \sim O(1)$, while for boundaries with moderate bumpiness, such as what we considered in section 2.1, friction does contribute to both the wall stress and the heat flux. In addition, Cao *et al* [20] ignored particle spin and argued that the rotational energy is much smaller than its translational counterpart (see Appendix A of Cao *et al* [20]). However, because the ratio of the *change* of rotational energy to the *change* of translational energy in a collision is proportional to $\mu^2/(1-e)$, particle rotation cannot be ignored if, as Cao *et al* assumed, μ is on the order of $\varepsilon^{1/2}$.

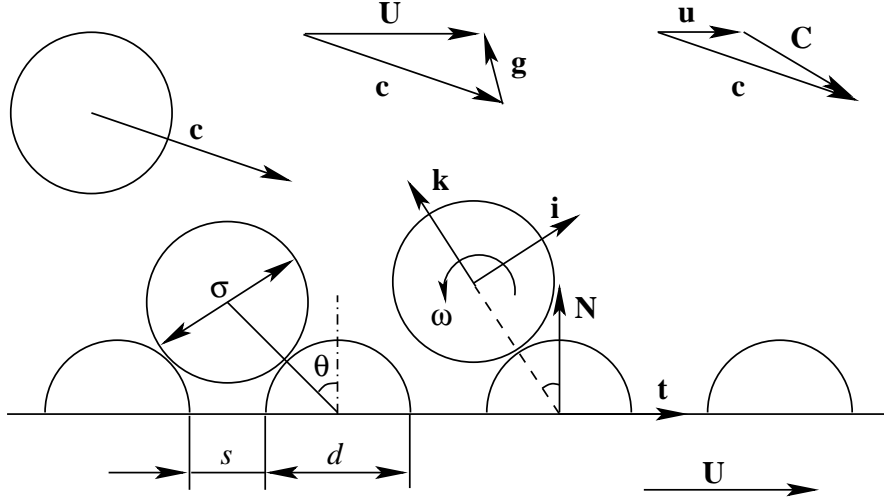


Figure 2.7: Geometry of a bumpy, frictional boundary of half-cylinders in “planar” granular flows.

In this section, we first show that the contribution to wall stress and energy dissipation from friction is on the same order as the contribution from bumpy features, even in the regime of small slip that Cao *et al* considered. We then extend our analysis to large slip velocities $v/\sqrt{T} \sim O(1)$.

To make the analytical derivation tractable, we consider planar granular flows, such as the disk flows or the flows of a monolayer of spheres considered in the previous section. The boundary geometry is illustrated in Figure 2.7. For convenience, we use the same notation as in section 2.1 wherever possible. For example, \mathbf{U} is the velocity of the moving boundary, \mathbf{u} is the mean velocity of the flow, \mathbf{C} is the fluctuation velocity, $\mathbf{v} = \mathbf{U} - \mathbf{u}$ is the slip velocity, and $\mathbf{g} = \mathbf{v} - \mathbf{C}$ is the velocity of the wall relative to the flow particles. The only new variable is the angular velocity ω of the flow particle. The traction and the energy dissipation at the wall are expressed as

$$\mathbf{M} = \mathbb{C}[\mathbf{J}],$$

and

$$D = \mathbb{C}[-\Delta K],$$

where the operator \mathbb{C} is defined as

$$\mathbb{C}[\psi] = \alpha\chi \iiint_{\mathbf{g}, \mathbf{k} \geq 0} \psi \bar{\sigma}(\mathbf{g} \cdot \mathbf{k}) f(\mathbf{c}, \omega, \mathbf{p} + \bar{\sigma}\mathbf{k}) d\mathbf{c} d\omega dk,$$

\mathbf{J} is the impulse and ΔK is the change of kinetic energy in a collision between a particle and the wall.

For collisions with Coulomb friction, the collisional impulse and change of kinetic energy are derived as in section 2.2,

$$\mathbf{J} = m(1+e)(\mathbf{g} \cdot \mathbf{k})(\mathbf{k} - \mu\mathbf{l}), \quad (2.61)$$

and

$$\Delta K = \frac{1}{2}m(1+e) \left\{ (\mathbf{g} \cdot \mathbf{k})^2 \left[\mu\mu_0 - (1-e) \right] + 2\mu(\mathbf{g} \cdot \mathbf{k}) \left[\left(\mathbf{g} + \frac{\sigma}{2}\boldsymbol{\omega} \times \mathbf{k} \right) \cdot \mathbf{l} \right] \right\}, \quad (2.62)$$

where \mathbf{l} is a unit vector in the direction of the relative velocity at the contact point,

$$\mathbf{l} = \begin{cases} \mathbf{i} & \text{if } \mathbf{g} \cdot \mathbf{i} \leq \frac{\sigma}{2}\boldsymbol{\omega} \times \mathbf{k} \cdot \mathbf{i} \\ -\mathbf{i} & \text{if } \mathbf{g} \cdot \mathbf{i} > \frac{\sigma}{2}\boldsymbol{\omega} \times \mathbf{k} \cdot \mathbf{i} \end{cases}$$

and μ_0 is defined as,

$$\mu_0 \equiv \left(\frac{m\sigma^2}{4I} + 1 \right) (1+e)\mu,$$

with $\mu_0 = 3(1+e)\mu$ for disks and $\mu_0 = \frac{7}{2}(1+e)\mu$ for spheres.

Following Jenkins [51], it is convenient to decompose the wall traction \mathbf{M} and heat flux D into separate contributions from the bumpy features and the friction,

$$\mathbf{M} = \mathbf{M}^B + \mathbf{M}^F, \quad (2.63)$$

and

$$D = D^B + D^F = D^B + D_1^F + D_2^F, \quad (2.64)$$

with

$$\mathbf{M}^B = m(1+e)\mathbb{C}[(\mathbf{g} \cdot \mathbf{k})\mathbf{k}] \quad (2.65a)$$

$$\mathbf{M}^F = -\mu m(1+e)\mathbb{C}[(\mathbf{g} \cdot \mathbf{k})\mathbf{1}] \quad (2.65b)$$

$$D^B = \frac{1}{2}m(1-e^2)\mathbb{C}[(\mathbf{g} \cdot \mathbf{k})^2] \quad (2.65c)$$

$$D_1^F = -\frac{1}{2}m(1+e)\mu\mu_0\mathbb{C}[(\mathbf{g} \cdot \mathbf{k})^2] = -\frac{\mu\mu_0}{(1-e)}D^B \quad (2.65d)$$

$$D_2^F = -\mu m(1+e)\mathbb{C}\left[(\mathbf{g} \cdot \mathbf{k})\left(\mathbf{g} + \frac{\sigma}{2}\boldsymbol{\omega} \times \mathbf{k}\right) \cdot \mathbf{1}\right] \quad (2.65e)$$

As in section 2.2, we neglect fluctuations in angular velocity i.e., $\boldsymbol{\omega} = \langle \boldsymbol{\omega} \rangle$, so that the operator \mathbb{C} can be simplified to

$$\mathbb{C}[\psi] = \alpha\chi \iiint_{\mathbf{g} \cdot \mathbf{k} \geq 0} \psi \bar{\sigma}(\mathbf{g} \cdot \mathbf{k}) f(\mathbf{c}, \mathbf{p} + \bar{\sigma}\mathbf{k}) d\mathbf{c} d\mathbf{k}.$$

For convenience, we define the rotational contribution to the linear velocity at the contact point as

$$v_r \equiv \frac{\sigma}{2}\mathbf{k} \times \langle \boldsymbol{\omega} \rangle \cdot \mathbf{i} = \frac{\sigma}{2} \langle \boldsymbol{\omega} \rangle \cdot$$

We assume that the velocity distribution of flow particles at the crest of the boundary bumps is the “dense-Maxwellian” described by Eq. (2.3). Because $\sigma\nabla\mathbf{u}/\sqrt{T} \sim O(\varepsilon^{1/2})$ in the regime of small slip with $v/\sqrt{T} \sim O(\varepsilon^{1/2})$, the velocity distribution (2.3) can be expanded at $\mathbf{p} + \bar{\sigma}\mathbf{k}$ as

$$f(\mathbf{c}, \mathbf{p} + \bar{\sigma}\mathbf{k}) = \frac{n}{2\pi T} \left\{ 1 + \frac{\mathbf{g} \cdot \mathbf{v}}{T} - \frac{\bar{\sigma}}{T} [(\mathbf{k} \cdot \nabla - \mathbf{N} \cdot \nabla)\mathbf{u}] \cdot \mathbf{g} - \sqrt{\frac{2}{\pi}} \frac{\sigma B}{T^{3/2}} \mathbf{g} \cdot \hat{\mathbf{D}} \cdot \mathbf{g} \right\} e^{-\frac{g^2}{2T}}. \quad (2.66)$$

It is at this stage that Cao *et al* [20] concluded that $\mathbf{M}^F = 0$ if $\mu \sim O(\varepsilon^{1/2})$. Their argument is as follows: because all terms except the first in the bracket of Eq. (2.66) are $O(\varepsilon^{1/2})$, and because \mathbf{M}^F involves the product of μ with these terms, their contribution to \mathbf{M}^F are on the order of ε and can be neglected. Because Cao

et al [20] ignored particle spin, the contribution to \mathbf{M}^F from the first term in the bracket in Eq. (2.66) vanishes, the unit vector \mathbf{l} is anti-symmetric about \mathbf{g} , and $\mathbb{C}[\mathbf{l}] = 0$.

In flows of spheres or disks confined to a plane, \mathbf{M} can be evaluated analytically from Eq. (2.63) with the velocity distribution in Eq. (2.66). The contribution of the bumpy nature of the boundary to the traction, \mathbf{M}^B , is the same as that found by Richman & Chou [105], while the frictional contribution, \mathbf{M}^F is

$$\begin{aligned} \mathbf{M}^F = & \frac{1}{2}\rho\chi(1+e)T\mu \left\{ -\operatorname{erf}\left(\frac{v_r}{\sqrt{2T}}\right)\mathbf{t} \right. \\ & + \frac{1}{\sqrt{2\pi T}} \left[(\mathbf{II} \cdot \mathbf{v}) \exp\left(-\frac{v_r^2}{2T}\right) - 2(\mathbf{IK} \cdot \mathbf{v}) \operatorname{erf}\left(\frac{v_r}{\sqrt{2T}}\right) \right] \\ & + \frac{\bar{\sigma}}{\sqrt{2\pi T}} \left[\left(\mathbf{II} \cdot (\nabla \mathbf{u})^T \cdot \mathbf{v} - \mathbf{IKI} : (\nabla \mathbf{u})^T \right) \exp\left(-\frac{v_r^2}{2T}\right) \right. \\ & \left. - 2 \left(\mathbf{IK} \cdot (\nabla \mathbf{u})^T \cdot \mathbf{v} - \mathbf{IKK} : (\nabla \mathbf{u})^T \right) \operatorname{erf}\left(\frac{v_r}{\sqrt{2T}}\right) \right] \\ & \left. - \sqrt{\frac{2}{\pi}} B \frac{\sigma}{T^{1/2}} \frac{2}{\pi} (\mathbf{IKI} : \hat{\mathbf{D}}) \exp\left(-\frac{v_r^2}{2T}\right) \right\}, \end{aligned} \quad (2.67)$$

where \mathbf{II} and \mathbf{IK} are 2nd-rank tensors and \mathbf{IKI} and \mathbf{IKK} are 3rd-rank tensors,

$$\begin{aligned} \mathbf{II} &= (\theta \csc \theta - \cos \theta)(\mathbf{nn}) + (\theta \csc \theta + \cos \theta)(\mathbf{tt}), \\ \mathbf{IK} &= -(\theta \csc \theta - \cos \theta)(\mathbf{nt}) + (\theta \csc \theta + \cos \theta)(\mathbf{tn}), \\ \mathbf{IKI} &= 2(\mathbf{tnt}) + \frac{2}{3}\sin^2\theta(\mathbf{nnn} - \mathbf{ntt} - \mathbf{ttn} - \mathbf{tnt}), \\ \mathbf{IKK} &= 2(\mathbf{tnn}) + \frac{2}{3}\sin^2\theta(\mathbf{ttt} - \mathbf{nnt} - \mathbf{ntn} - \mathbf{ttn}). \end{aligned}$$

If the flow is unidirectional and fully-developed, $\mathbf{u} = (u, 0)$, $\frac{\partial u}{\partial x} = 0$, and $\frac{\partial u}{\partial y} = u'$, then the frictional contribution to the normal and shear stresses can be expressed

as,

$$N^F = \mathbf{M}^F \cdot \mathbf{n} = \frac{1}{2}(1+e)\rho\chi T\mu\sqrt{\frac{2}{\pi}}\operatorname{erf}\left(\frac{v_r}{\sqrt{2T}}\right)\left\{(\theta\csc\theta - \cos\theta)\frac{v}{T^{1/2}} + \left[(\theta\csc\theta - \cos\theta) - \frac{2}{3}\sin^2\theta\right]\frac{\bar{\sigma}u'}{T^{1/2}}\right\}, \quad (2.68)$$

and

$$S^F = \mathbf{M}^F \cdot \mathbf{t} = \frac{1}{2}(1+e)\rho\chi T\mu\left\{-\operatorname{erf}\left(\frac{v_r}{\sqrt{2T}}\right) + \frac{1}{\sqrt{2\pi}}\exp\left(-\frac{v_r^2}{2T}\right)\left[(\theta\csc\theta + \cos\theta)\frac{v}{T^{1/2}} - \left((\theta\csc\theta + \cos\theta) - 2 + \frac{2}{3}\sin^2\theta - \frac{4}{\pi}\frac{\sigma}{\bar{\sigma}}B\left(2 - \frac{4}{3}\sin^2\theta\right)\right)\frac{\bar{\sigma}u'}{T^{1/2}}\right]\right\}. \quad (2.69)$$

The contribution of the bumpy character of the boundary to the normal and shear stresses are,

$$N^B = \mathbf{M}^B \cdot \mathbf{t} = \frac{1}{2}(1+e)\rho\chi T, \quad (2.70)$$

and

$$S^B = \mathbf{M}^B \cdot \mathbf{t} = \frac{1}{2}(1+e)\rho\chi T\sqrt{\frac{2}{\pi}}\left[(\theta\csc\theta - \cos\theta)\frac{v}{T^{1/2}} - \left((\theta\csc\theta - \cos\theta) - \frac{2}{3}\sin^2\theta - \frac{2}{3}\frac{\sigma}{\bar{\sigma}}B\sin^2\theta\right)\frac{\bar{\sigma}u'}{T^{1/2}}\right]. \quad (2.71)$$

For the moderate bumpiness $\delta \equiv \sin\theta \sim O(\varepsilon^{1/4})$ that we considered in section 2.1, $\theta\csc\theta - \cos\theta \sim O(\varepsilon^{1/2})$ but $\theta\csc\theta + \cos\theta \sim O(1)$. Therefore, S^F is on the same order as S^B , but N^F is negligible compared to N^B .

Our calculation above can be regarded as a correction to the results of Cao *et al* [20]. However, as Walton's impact model indicates [124], Coulomb friction occurs only at large relative velocities, thus contradicting the assumption of a small slip. In addition, collisional granular flows can involve large relative velocities with

the boundary. Therefore, we assume $v/\sqrt{T} \sim O(1)$ and calculate the boundary conditions using a method similar to that in section 2.1. However, for simplicity, like Jenkins [50] we do so in the two limiting cases of all-sliding and all-sticking. The all-sliding regime is the same as what we discussed earlier in this section but with a relaxed assumption of slip velocity. Therefore, the boundary traction \mathbf{M} and energy dissipation D are given by Eqs. (2.63) and (2.63), and the collisional impulse \mathbf{J} and energy change ΔK found in Eqs. (2.61) and (2.62). However, the velocity distribution in Eq. (2.66) is not valid. Instead, we use Eq. (2.4). For convenience, we re-write Eq. (2.65) as

$$\mathbf{M}^B = \frac{1}{2}(1+e)\rho\chi T \frac{1}{\sin\theta} \int \mathbf{k}\psi^B(\mathbf{k})dk \quad (2.72a)$$

$$\mathbf{M}^F = \frac{1}{2}(1+e)\rho\chi T \frac{\mu}{\sin\theta} \int \mathbf{i}\psi^F(\mathbf{k})dk \quad (2.72b)$$

$$D^B = \frac{1}{2}(1-e^2)\rho\chi T^{3/2} \frac{1}{2\sin\theta} \int \phi^B(\mathbf{k})dk \quad (2.72c)$$

$$D_1^F = -\frac{\mu\mu_0}{(1-e)}D^B \quad (2.72d)$$

$$D_2^F = \frac{1}{2}(1+e)\rho\chi T^{3/2} \frac{\mu}{\sin\theta} \int \phi^F(\mathbf{k})dk \quad (2.72e)$$

where

$$\begin{aligned} \psi^B(\mathbf{k}) &= \frac{1}{2\pi T^2} \int_{\mathbf{g}\cdot\mathbf{k}\geq 0} (\mathbf{g}\cdot\mathbf{k})^2 \Lambda e^{-\frac{c^2}{2T}} d\mathbf{C} \\ \psi^F(\mathbf{k}) &= \frac{1}{2\pi T^2} \int_{\mathbf{g}\cdot\mathbf{k}\geq 0} (-\mathbf{l}\cdot\mathbf{i})(\mathbf{g}\cdot\mathbf{k})^2 \Lambda e^{-\frac{c^2}{2T}} d\mathbf{C} \\ \phi^B(\mathbf{k}) &= \frac{1}{2\pi T^{5/2}} \int_{\mathbf{g}\cdot\mathbf{k}\geq 0} (\mathbf{g}\cdot\mathbf{k})^3 \Lambda e^{-\frac{c^2}{2T}} d\mathbf{C} \\ \phi^F(\mathbf{k}) &= \frac{1}{2\pi T^{5/2}} \int_{\mathbf{g}\cdot\mathbf{k}\geq 0} (\mathbf{g}\cdot\mathbf{k})^2 \left[(\mathbf{g} + \frac{\sigma}{2}\boldsymbol{\omega} \times \mathbf{k}) \cdot (-\mathbf{l}) \right] \Lambda e^{-\frac{c^2}{2T}} d\mathbf{C}, \end{aligned}$$

in which Λ is given in Eq. (2.9).

As in section 2.1, we decompose the fluctuation velocity \mathbf{C} as

$$\mathbf{C} = -(\xi\mathbf{i} + \zeta\mathbf{k}).$$

The unit vector \mathbf{l} tangential to bumps at the contact point is then

$$\mathbf{l} = \begin{cases} \mathbf{i} & \text{if } \xi \leq -(\mathbf{v} \cdot \mathbf{i} - v_r) \\ -\mathbf{i} & \text{if } \xi > -(\mathbf{v} \cdot \mathbf{i} - v_r) \end{cases}$$

Following the procedure of section 2.1 to evaluate the integrals, we find that $\psi^B(\mathbf{k}) = \psi(\mathbf{k})$ and $\phi^B(\mathbf{k}) = \phi(\mathbf{k})$, where $\psi(\mathbf{k})$ and $\phi(\mathbf{k})$ are given by Eq. (2.16) and Eq. (2.17). Then, to an error on the order of ε ,

$$\psi^F(\mathbf{k}) = \operatorname{erf}\left(\frac{g_0}{\sqrt{2T}}\right)\psi^B(\mathbf{k}),$$

and

$$\phi^F(\mathbf{k}) = \operatorname{erf}\left(\frac{g_0}{\sqrt{2T}}\right)\phi^B(\mathbf{k}),$$

where $g_0 \equiv \mathbf{v} \cdot \mathbf{i} - v_r = v \cos k - v_r$ is the relative velocity at the contact point.

When integrating ψ^F and ϕ^F , we approximate g_0 by its average over a bump,

$$g_0 \approx \bar{g}_0 \equiv \frac{1}{2 \sin \theta} \int_{-\theta}^{\theta} (v \cos k - v_r) dk = v - v_r \theta \csc \theta,$$

$$\operatorname{erf}\left(\frac{g_0}{\sqrt{2T}}\right) \approx \operatorname{erf}\left(\frac{\bar{g}_0}{\sqrt{2T}}\right).$$

For moderate bumpiness $\delta \sim O(\varepsilon^{1/4})$, the error associated with this approximation is less than $O(\varepsilon)$. With this approximation, the frictional contribution to \mathbf{M} and D are

$$S^F \equiv \mathbf{M}^F \cdot \mathbf{t} = \mu \operatorname{erf}\left(\frac{\bar{g}_0}{\sqrt{2T}}\right) N^B, \quad (2.73a)$$

$$N^F \equiv \mathbf{M}^F \cdot \mathbf{n} = -\mu \operatorname{erf}\left(\frac{\bar{g}_0}{\sqrt{2T}}\right) S^B, \quad (2.73b)$$

$$D_1^F = -\mu \bar{\mu}_0 \frac{(1 + \beta_0)}{(1 - e)} D^B, \quad (2.73c)$$

$$D_2^F = S^F \bar{g}_0. \quad (2.73d)$$

In these expressions, $N^B = \mathbf{M}^B \cdot \mathbf{n}$ and $S^B = \mathbf{M}^B \cdot \mathbf{t}$, \mathbf{M}^B is given by Eq. (2.18), and D^B derives from Eq. (2.19) as it did in section 2.1. The results of Eq. (2.73)

are expected because, in pure sliding, the component of the collisional impulse tangential to the contact line, which is due to the friction, is related to the normal component, which is due to the elasticity, by the friction coefficient. If relative velocities before the collision are all pointed in the same direction, then a simple decomposition of the two impulses leads to a relation similar to Eq. (2.19) namely, $N^F = -\mu S^B$, and $S^F = \mu N^B$. The factor $\text{erf}(\frac{\bar{g}_0}{\sqrt{2T}})$ in Eq. (2.19) betrays the fact that some collisions involve relative velocities in the opposite direction, so that the corresponding impulses, also in the opposite direction, produce smaller stresses than what the simple unidirectional argument would yield.

With \mathbf{M} and D given by Eq. (2.19), the contributions to the heat flux are

$$Q^B \equiv \mathbf{v} \cdot \mathbf{M}^B - D^B, \quad (2.74a)$$

$$\begin{aligned} Q^F &\equiv \bar{\mathbf{g}}_0 \cdot \mathbf{M}^F - D_1^F - D_2^F \\ &= \frac{1}{2} \rho \chi T^{3/2} \sqrt{\frac{2}{\pi}} \mu \mu_0 \theta \csc \theta, \end{aligned} \quad (2.74b)$$

and, therefore, Q^B is the same as in Eq. (2.21). The total heat flux is then

$$Q = Q^B + Q^F. \quad (2.75)$$

If we assume $\mu \sim O(\varepsilon^{1/2})$, then N^F is on the order of ε and can be neglected, since S^B is on the order of $\varepsilon^{1/2}$. Hence, to an error of $O(\varepsilon)$, $N = N^B$. Then the stress ratio at a bumpy, frictional boundary is,

$$\frac{S}{N} = \frac{S^B + S^F}{N^B} = \frac{S^B}{N^B} + \mu \text{erf} \left(\frac{\bar{g}_0}{\sqrt{2T}} \right). \quad (2.76)$$

We can also replace the $\theta \csc \theta$ in Eq. (2.74b) by 1 because $\mu(\theta \csc \theta - 1) \sim O(\varepsilon)$.

In section 2.2, we derived boundary conditions for granular flows of disks or spheres confined to a plane and interaction with a flat, frictional wall. We found

that in the regime of “all-sliding”, the stress ratio for an isotropic flow is

$$\left(\frac{S}{N}\right)^F = \mu \operatorname{erf}\left(\frac{g_0}{\sqrt{2T}}\right),$$

and the heat flux purely due to friction (without inelastic dissipation) is

$$Q^F = \frac{1}{2}\rho\chi T^{3/2}\sqrt{\frac{2}{\pi}}\mu\bar{\mu}_0(1+\beta_0) = \frac{1}{2}\rho\chi T^{3/2}\sqrt{\frac{2}{\pi}}\mu\mu_0,$$

where, to be consistent with the assumed velocity distribution in Eq. (2.4), we employ the result in Appendix B corresponding to a Maxwellian distribution in the normal direction.

Therefore, we conclude that in the “all-sliding” regime, the stress ratio (or heat flux) for a bumpy, frictional boundary can be approximated by the sum of the stress ratio (or heat flux) of a frictionless, bumpy boundary and that of a flat, frictional, elastic boundary. A slight correction is that the average relative velocity at the contact point \bar{g}_0 should be used to account for the effects of bumps.

Next, we evaluate the stresses and heat flux at a bumpy, frictional boundary with “sticking” collisions only. Because the calculation resembles what we presented earlier around Eqs. 2.75 – 2.76, we just outline it here briefly. The collisional impulse is

$$\mathbf{J} = m(1+e)\left[(\mathbf{g}\cdot\mathbf{k})\mathbf{k} + \frac{\mu}{\bar{\mu}_0}(\mathbf{g}\cdot\mathbf{i} - v_r)\mathbf{i}\right],$$

and the energy change during a collision is

$$\Delta K = -\frac{1}{2}m(1+e)\left[(1-e)(\mathbf{g}\cdot\mathbf{k})^2 + \frac{\mu}{\bar{\mu}_0}(1-\beta_0)(\mathbf{g}\cdot\mathbf{i} - v_r)^2\right],$$

where $\bar{\mu}_0$ is defined in section 2.2. The contributions \mathbf{M}^B and D^B from the boundary’s bumpiness are the same as in the “all-sliding” case. The frictional contributions are

$$\mathbf{M}^F = \frac{1}{2}(1+e)\rho\chi T\frac{\mu}{\bar{\mu}_0\sin\theta}\int\mathbf{i}\psi^F(\mathbf{k})d\mathbf{k}, \quad (2.77)$$

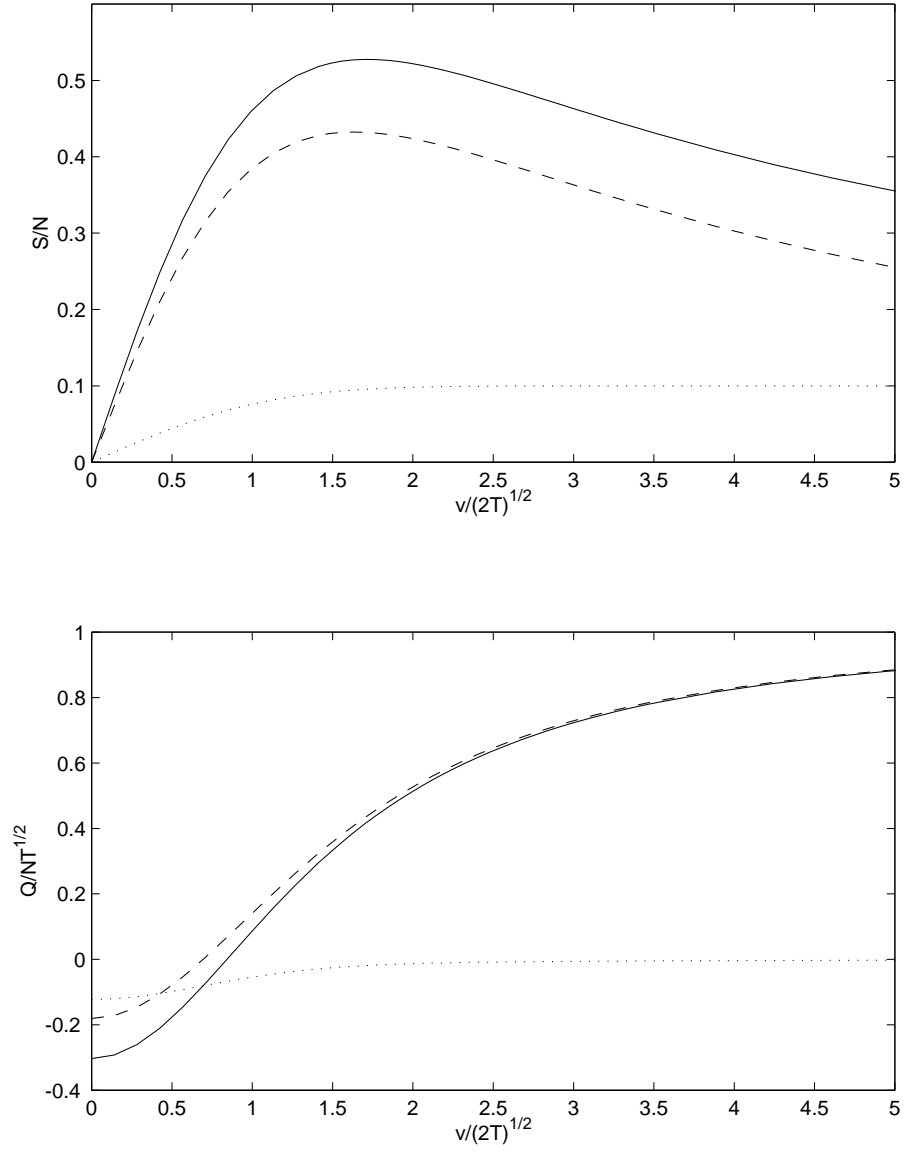


Figure 2.8: Stress ratio S/N (top) and dimensionless flux of fluctuation energy $Q/N\sqrt{T}$ (bottom) for planar flows of spheres at a bumpy, frictional boundary. The dashed and dotted lines represent the respective contributions of bumps and friction. The solid lines show the total S/N or $Q/N\sqrt{T}$. The boundary parameters are $\sigma/d = 1$, $s/d = 1/2$, $e = 0.9$, $\mu = 0.1$, and $\beta_0 = 0$.

and

$$D^F = \frac{1}{2}(1+e)\rho\chi T^{3/2} \frac{\mu}{\bar{\mu}_0} (1-\beta_0) \frac{1}{2\sin\theta} \int \phi^F(\mathbf{k}) d\mathbf{k}, \quad (2.78)$$

where

$$\begin{aligned} \psi^F(\mathbf{k}) &= \frac{1}{2\pi T^2} \int_{\mathbf{g}\cdot\mathbf{k}\geq 0} (\mathbf{g}\cdot\mathbf{i} - v_r)(\mathbf{g}\cdot\mathbf{k}) \Lambda e^{-\frac{c^2}{2T}} d\mathbf{C} \\ \phi^F(\mathbf{k}) &= \frac{1}{2\pi T^{5/2}} \int_{\mathbf{g}\cdot\mathbf{k}\geq 0} (\mathbf{g}\cdot\mathbf{k})(\mathbf{g}\cdot\mathbf{i} - v_r)^2 \Lambda e^{-\frac{c^2}{2T}} d\mathbf{C}. \end{aligned}$$

Following the same approach that we used to evaluate ψ^F and ϕ^F and using \bar{g}_0 to approximate g_0 , we find that up to an error on the order of ε

$$N^F = 0, \quad (2.79a)$$

$$S^F = \frac{1}{2}(1+e)\rho\chi T \frac{2}{\sqrt{\pi}} \frac{\mu}{\bar{\mu}_0} \frac{\bar{g}_0}{\sqrt{2T}}, \quad (2.79b)$$

$$D^F = \frac{1}{2}(1+e)\rho\chi T^{3/2} \sqrt{\frac{2}{\pi}} \frac{\mu}{\bar{\mu}_0} (1-\beta_0) \left(\theta \csc\theta + \frac{\bar{g}_0^2}{T} \right), \quad (2.80)$$

and

$$\begin{aligned} Q^F &= S^F \bar{g}_0 - D^F \\ &= \frac{1}{2}(1+e)\rho\chi T^{3/2} \sqrt{\frac{2}{\pi}} \frac{\mu}{\bar{\mu}_0} \left[(1+\beta_0) \frac{\bar{g}_0^2}{2T} - \frac{1}{2}(1-\beta_0)\theta \csc\theta \right], \end{aligned} \quad (2.81)$$

Hence, the total stress ratio and heat flux are

$$\frac{S}{N} = \frac{S^B + S^F}{N^B + N^F} = \frac{S^B}{N^B} + \frac{S^F}{N^B} \approx \frac{S^B}{N^B} + \frac{2}{\sqrt{\pi}} \frac{\mu}{\bar{\mu}_0} \frac{\bar{g}_0}{\sqrt{2T}}, \quad (2.82)$$

and

$$Q = Q^B + Q^F = Q^B + \frac{1}{2}(1+e)\rho\chi T^{3/2} \sqrt{\frac{2}{\pi}} \frac{\mu}{\bar{\mu}_0} \left[(1+\beta_0) \frac{\bar{g}_0^2}{2T} - \frac{1}{2}(1-\beta_0)\theta \csc\theta \right], \quad (2.83)$$

in which we have neglected $O(\varepsilon)$ terms containing $\mu\sin^2\theta$ and $\mu(\theta \csc\theta - 1)$. Comparing Eqs. (2.82) and (2.83) with the stress ratio and heat flux in Appendix B, we conclude that, in the ‘‘all-sticking’’ regime, the total stress ratio (or heat flux)

can also be obtained by superposing the contributions from a bumpy, frictionless boundary and a flat, frictional, elastic boundary with appropriate properties. This, together with our earlier result for the “all-sliding” case, suggests the following boundary conditions for plane granular flows interacting with a bumpy, frictional boundary,

$$\frac{S}{N} = \left(\frac{S}{N}\right)^B + \left(\frac{S}{N}\right)^F, \quad (2.84)$$

and

$$Q = Q^B + Q^F, \quad (2.85)$$

where $(S/N)^B$ and Q^B are found in section 2.1, and $(S/N)^F$ and Q^F are the boundary conditions derived in section 2.2. For example, if a Maxwellian velocity distribution is assumed for the velocity component normal to the wall, then Eqs. (2.48) and (2.49) are used. Figure 2.8 shows the corresponding stress ratios and heat fluxes in this case.

2.4 Three-Dimensional Flows of Spheres interacting with Bumpy, Frictional Walls

We consider the cylindrical bumps sketched in Fig 2.1. Jenkins [51] proposed that boundary conditions for a bumpy, frictional boundary be approximated by a superposition of the boundary conditions for a bumpy, frictionless boundary and those for a flat, frictional boundary. In that approach, Jenkins [51] used the boundary conditions derived by Richman & Chou [105] for a bumpy, frictionless boundary and he superimposed the wall stresses directly. In this work, we will use the more general boundary conditions derived in Section 2.1 for bumpy, frictionless walls. In addition, our direct two-dimensional calculations in section 2.3 suggest that

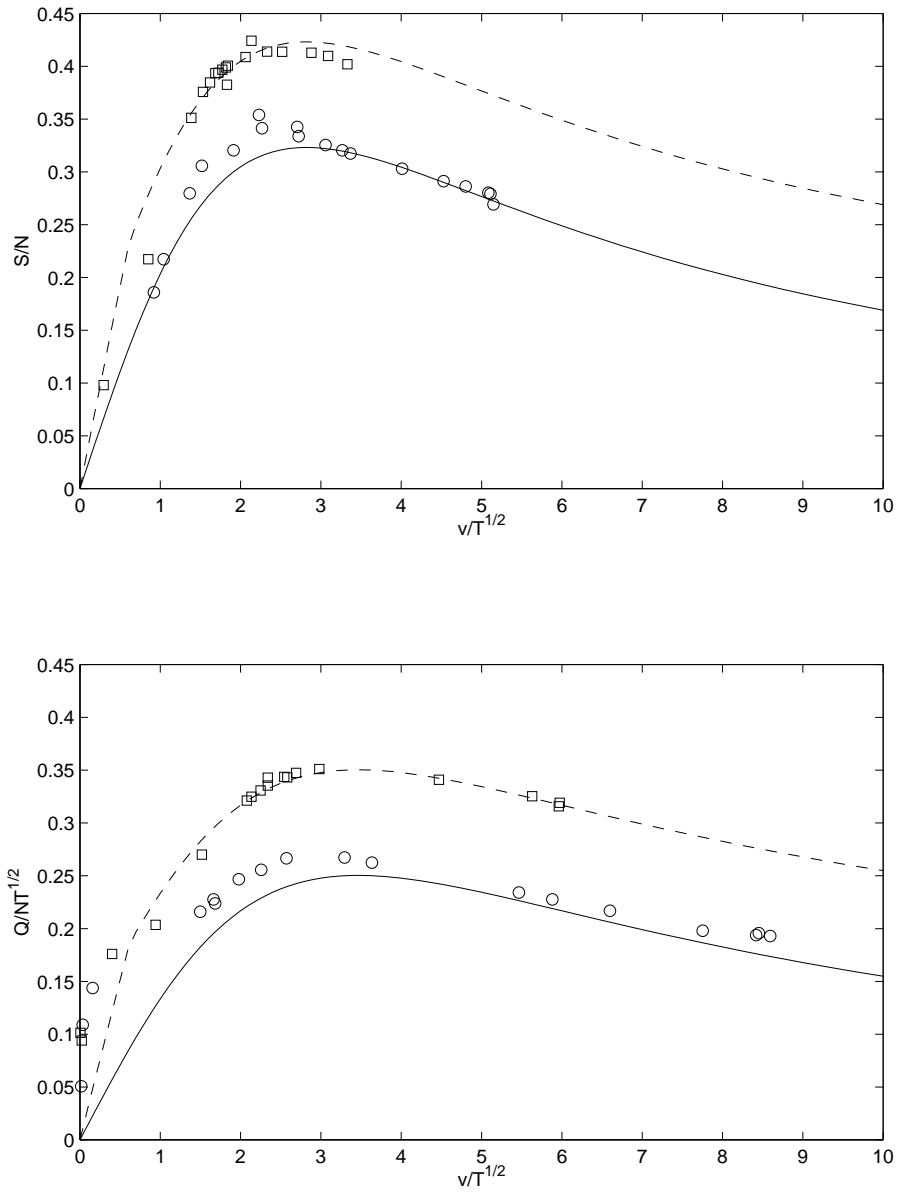


Figure 2.9: Stress ratio S/N for 3-D flows of spheres at a bumpy, frictional boundary. Top plot: $\sigma = 2$, $d = 3.2$, $s = 0$; bottom plot: $\sigma = d = 2$, $s = 0$. Lines are the superposition Eq. (2.86), symbols are simulation results. Solid lines and squares: $\mu_w = 0.1$; dashed lines and circles: $\mu_w = 0.0$.

our superposition of the stress ratios is appropriate for treating bumpy, frictional boundaries, rather than superimposing the stresses themselves.

$$\frac{S}{N} = \left(\frac{S}{N}\right)^B + \left(\frac{S}{N}\right)^F, \quad (2.86)$$

and the fluxes of fluctuation energy

$$Q = Q^B + Q^F. \quad (2.87)$$

In these Eqs., the superscripts B and F represent contributions from the bumps and from friction, respectively. The bumpy contributions to stress and flux of fluctuation energy are given by Eqs. (2.20) and (2.21), respectively. Because inelastic energy loss is included in Q^B (Eq. 2.21), Q^F is the heat flux due to friction alone.

In this work, we adopt the stress ratios obtained by Jenkins [50] for $(S/N)^F$ and the heat flux of Jenkins & Louge [56] for Q^F ,

$$\left(\frac{S}{N}\right)^F = \begin{cases} \sqrt{\frac{3}{2}} \frac{\mu}{\bar{\mu}_0} \frac{\bar{g}_0}{\sqrt{2T}} & \text{if } \frac{\bar{g}_0}{\sqrt{2T}} \leq \sqrt{\frac{2}{3}} \bar{\mu}_0 \\ \mu & \text{otherwise} \end{cases} \quad (2.88)$$

and

$$\frac{Q^F}{\frac{1}{2}\rho\chi T^{3/2}} = \begin{cases} \left(\frac{\pi}{2}\right)^{3/2} \mu \left(\frac{\bar{g}_0^2}{3T} - 1\right) & \text{if } \frac{\bar{g}_0^2}{3T} \leq 1 + \frac{28}{3\pi^2} \mu \\ \sqrt{\frac{2}{\pi}} \frac{7}{3} \mu^2 & \text{otherwise} \end{cases} \quad (2.89)$$

where $\bar{\mu}_0 \equiv \frac{7(1+\beta_0)}{2(1+\epsilon)} \mu$ for homogeneous spheres. To produce these expressions, we have replaced the relative velocity g_0 at the contact point that was invoked in the original works of Jenkins [50] and Jenkins & Louge [56] by its average over a bump,

$$\bar{g}_0 \equiv v - \frac{\sigma}{2} (\mathbf{n} \times \langle \boldsymbol{\omega} \rangle \cdot \mathbf{i}) \theta \csc \theta$$

Figure 2.9 shows stress ratios and heat fluxes for a typical boundary.

The frictional contributions $(S/N)^F$ and Q^F above are derived by assuming that all collisions are sliding if the slip velocity is large and all collisions are sticking

if it is small. As section 2.2 shows, the stress and heat flux obtained from these limiting case calculations are subject to errors, especially in the small-slip regime.

Chapter 3

Solutions of the Kinetic Theory for Bounded Collisional Granular Flows

In “rapid” granular flows, particles interact with one another through impulsive collisions rather than long-lasting contacts. These flows can be studied in three different ways: by conducting experiments; by deriving theories and solving the resulting set of equations; or by simulating the behavior of individual particles on a computer.

The challenge of experiments is to ensure that the particles do not experience long-lasting contacts, but rather interact briefly through impulsive, mostly binary collisions. From a practical standpoint, this implies that gravitational accelerations must be defeated by raising the particle agitation sufficiently [81].

Predictions for rapid granular flows are derived from kinetic theories that exploit analogies between the colliding particles and agitated molecules in a dense gas. The theories produce a set of partial differential equations and boundary conditions. Because analytical solutions are only possible in the simplest of cases, the differential equations are generally solved numerically by discretizing the flow domain and by employing numerical techniques that are robust enough to handle non-linearities in the system of equations. The success of theories in predicting practical flows is predicated upon an accurate experimental determination of the properties of individual impacts, see for example [33].

The principal difference between granular flows and dense gases is that kinetic energy is dissipated in collisions. In this paper, we consider cases in which the collisional energy dissipation is small. The corresponding theories were developed, for

example, by Lun *et al* [87], Jenkins and Richman [59], Goldshtein and Shapiro [37], Sela *et al* [111], Sela and Goldhirsch [110], and Montanero *et al* [92] for inelastic, smooth particles, and by Jenkins and Richman [60], Lun [86], and Luding *et al* [84] for inelastic, frictional particles. These theories have also been extended to flows of mixtures, in which grains of different properties are separated in a spatial gradient of fluctuation energy. Following the derivation by López de Haro and Cohen [73] and Kincaid *et al* [65, 64] of kinetic theories for molecular mixtures, Jenkins and Mancini [57] considered binary mixtures of inelastic, smooth disks. They later extended the theory to binary mixtures of inelastic, smooth spheres [58]. Their results were recently updated by Arnarson and Willits [6] in three dimensions, and Willits and Arnarson [133] and Alam *et al* [3] in two dimensions.

The impulsive nature of granular interactions makes it relatively straightforward to simulate flows of a large number of individual particles on the computer. Such numerical simulations have played an important role in testing and informing granular theories [16]. In “hard-sphere” simulations, see for example Campbell and Brennen [18], collisions are assumed to be instantaneous. The occurrence of an upcoming collision is determined by maintaining a list of future such events and the simulation marches accordingly from one collision to the next. The discrete element model (DEM) proposed by Cundall and Strack [27] inspired Walton and Braun [127, 126] to develop a “soft-sphere” simulation, in which particles are allowed to deform during collisions. The principal advantage of this technique is to let the simulation capture long-lasting, as well as impulsive, granular interactions. Here, detailed contact dynamics are resolved in small time steps typically much smaller than the time separating two successive collisions. Hopkins and Louge [44] used a “hard-sphere/overlap” simulation in which collisions are also assumed to

be instantaneous, but particles can overlap slightly with each other before detecting the occurrence of a contact. The simulation time increment is then adjusted to keep the mean overlap below a certain tolerance. This technique makes it redundant to maintain a collision list and facilitates simulations with complicated boundary geometry. Other simulation techniques include the “contact dynamics” simulation proposed by Moreau [95] and the Monte Carlo simulations of Hopkins and Shen [45] and Montanero and Santos [93, 94].

Although numerical simulations can in principle interrogate any flow variable of interest, they rely upon simplifying assumptions, such as the adoption of simple impact models. Thus it is important to validate them in physical experiments. Because multiple enduring contacts dominate all but the most agitated granular flows on earth, the most promising way to create collisional flows is to operate in microgravity. Louge *et al* [81] carried out such experiments with sheared flows of grains with known impact properties.

In this paper, we compare numerical solutions of the kinetic theory with “hard-sphere/overlap” simulations and with recent microgravity experiments. Details of the computer simulation and the experiments appear in papers by Hopkins and Louge [44] and Louge *et al* [81], respectively. Our results indicate that, at least in fully-developed, collisional, steady flows with relatively small collisional dissipation, the solutions of the kinetic theory, subject to the appropriate boundary conditions, agree well with both simulations and experimental data.

3.1 Flow of Identical Spheres

3.1.1 Conservation laws and constitutive relations

Jenkins and Richman [59] derived conservation laws of mass, momentum and fluctuation energy for a collisional granular flow of identical spheres of diameter σ ,

$$\frac{\partial \rho}{\partial t} + \nabla \cdot (\rho \mathbf{u}) = 0, \quad (3.1)$$

$$\rho \frac{\partial \mathbf{u}}{\partial t} + \rho \mathbf{u} \cdot \nabla \mathbf{u} = \nabla \cdot \mathbb{T} + \rho \mathbf{f}, \quad (3.2)$$

$$\frac{3}{2} \rho \frac{\partial T}{\partial t} + \frac{3}{2} \rho \mathbf{u} \cdot \nabla T = -\nabla \cdot \mathbf{q} + \mathbb{T} : \nabla \mathbf{u} - \gamma, \quad (3.3)$$

where $\rho = \rho_s \nu$ is the density of granular fluid, ρ_s is the material density of the spheres, $\nu = \frac{\pi}{6} n \sigma^3$ is the particle volume fraction, n is the number density of spheres, \mathbf{u} is the mean velocity, \mathbb{T} is the stress tensor, \mathbf{f} is the body force per unit mass, $T \equiv \frac{1}{3} \langle \mathbf{C} \cdot \mathbf{C} \rangle$ is the granular temperature, \mathbf{C} is the particle velocity relative to the mean flow, \mathbf{q} is the flux of fluctuation energy, and γ is the volumetric collisional dissipation rate of kinetic energy.

The stress tensor has the same form as in ordinary fluids:

$$\mathbb{T} = \left[-P + \left(\lambda - \frac{2}{3} \eta \right) \nabla \cdot \mathbf{u} \right] \mathbf{l} + \eta \left[(\nabla \mathbf{u}) + (\nabla \mathbf{u})^T \right], \quad (3.4)$$

where P is the pressure, \mathbf{l} is the identity tensor, λ and η are the bulk and the shear viscosity, respectively.

The flux of fluctuation energy satisfies Fourier's law:

$$\mathbf{q} = -\kappa \nabla T, \quad (3.5)$$

where κ is the conductivity of fluctuation energy.

For flows of smooth, slightly inelastic, identical spheres, Jenkins and Richman [59] derived constitutive relations for pressure, transport coefficients, and

energy dissipation rate. To the lowest order of $1 - e$, where e is the coefficient of restitution for collisions between two flow spheres, their results are

$$P = 4\rho FGT, \quad (3.6)$$

$$\lambda = \frac{8}{3\sqrt{\pi}}\rho\sigma GT^{1/2}, \quad (3.7)$$

$$\eta = \frac{8J}{5\sqrt{\pi}}\rho\sigma GT^{1/2}, \quad (3.8)$$

$$\kappa = \frac{4M}{\sqrt{\pi}}\rho\sigma GT^{1/2}, \quad (3.9)$$

and

$$\gamma = \frac{24}{\sqrt{\pi}}(1 - e)\rho\frac{T^{3/2}}{\sigma}G, \quad (3.10)$$

where $G = \nu g_0(\nu)$ and $g_0(\nu)$ is the radial distribution function at contact for identical spheres. A well known expression for $g_0(\nu)$ was given by Carnahan and Starling [22] as

$$g_{0,CS}(\nu) = \frac{2 - \nu}{2(1 - \nu)^3}. \quad (3.11)$$

It has been found that the Carnahan-Starling correlation is accurate up to $\nu \approx 0.5$. More seriously, this correlation allows particle volume fraction to approach 1, which is larger than the maximum possible volume fraction of identical spheres. Torquato [121] proposed that the Carnahan-Starling correlation can be used up to a “freezing” fraction $\nu_f = 0.49$. For higher volume fraction, the radial distribution is

$$g_0(\nu) = g_{0,CS}(\nu_f)\frac{\nu_c - \nu_f}{\nu_c - \nu}, \quad (3.12)$$

which diverges at the “random close-packing” fraction $\nu_c \approx 0.64$. In our work, we use the Carnahan-Starling correlation with Torquato correction for $g_0(\nu)$. The

functions F , J and M of ν are

$$F = 1 + \frac{1}{4G}, \quad (3.13)$$

$$J = 1 + \frac{\pi}{12} \left(1 + \frac{5}{8G}\right)^2, \quad (3.14)$$

and

$$M = 1 + \frac{9\pi}{32} \left(1 + \frac{5}{12G}\right)^2. \quad (3.15)$$

Recently, Jenkins and Zhang [54] showed that these constitutive relations can be extended to nearly elastic, slightly frictional spheres. The expressions for pressure, viscosities and conductivity remain unchanged to the lowest order, while the additional dissipation of kinetic energy due to friction is taken into account by using an effective coefficient of restitution e_{eff} that replaces e in Eq. (3.10). Following Walton's simple impact model [125] and the experimental verification of Foerster *et al* [33], Jenkins and Zhang [54] distinguished sticking (or rolling) collisions characterized by a coefficient of tangential velocity restitution β_0 , and sliding collisions featuring a Coulomb friction coefficient μ that represents the ratio of the tangential and normal impulses in gross slip. For small $1 - e$ and small μ , they derived the effective coefficient of restitution

$$e_{eff} \equiv e - \frac{1}{2}a_1 + \frac{1}{2}a_2 \frac{b_1}{b_2}, \quad (3.16)$$

where

$$a_1 = \frac{\mu}{\mu_0} \left[\pi \mu_0 \left(1 - \frac{2}{\pi} \arctan \mu_0\right) + \frac{2\mu_0^2}{1 + \mu_0^2} \left(1 - 2\frac{\mu}{\mu_0}\right) \right],$$

$$a_2 = \frac{5}{2} \frac{\mu}{\mu_0} \left[\frac{\pi}{2} \mu_0 \left(1 - \frac{2}{\pi} \arctan \mu_0\right) + \frac{\mu_0^2 - \mu_0^4}{(1 + \mu_0^2)^2} \right],$$

$$b_1 = \left(\frac{\mu}{\mu_0}\right)^2 \frac{\mu_0^2}{1 + \mu_0^2},$$

$$b_2 = \frac{1}{2} \frac{\mu}{\mu_0} \left[\frac{\pi}{2} \mu_0 \left(1 - \frac{2}{\pi} \arctan \mu_0\right) + \frac{\mu_0^2}{1 + \mu_0^2} \right],$$

and

$$\mu_0 \equiv \frac{7(1+e)}{2(1+\beta_0)}\mu. \quad (3.17)$$

3.1.2 Comparison with simulations and experiments

Two dimensional rectilinear flow

We first consider fully developed, steady flows in a rectilinear shear cell. As Figure 3.1 illustrates, spheres flow in a region bounded by two bumpy boundaries, which can move relative to each other, and two flat side walls. Their centers are located in the region $0 \leq y \leq H$ and $-W/2 \leq z \leq W/2$, where $H \equiv Y - \frac{1}{2}(d_1 + d_0) - \sigma$, $W \equiv Z - \sigma$, d_0 and d_1 are the diameters of the stationary and moving boundary bumps near $y = 0$ and $y = Y$, respectively, Y is the distance between the center of opposite boundary bumps and Z is the distance between the flat side walls. The relative velocity between the two bumpy boundaries is $U \equiv U_t - U_b$, where U_t and U_b are the velocity of the top and bottom boundary, respectively. Unless particularly specified, the examples we show in this chapter have the bottom boundary stationary, $U_b = 0$ and $U_t = U$. In this problem, we allow the existence of a small body force in the flow direction, which can be used, for example, to represent a uniform drag upon the solid spheres.

In a fully developed, steady, unidirectional flow, the mass conservation equation is automatically satisfied. The momentum balance in the flow direction becomes

$$\frac{\partial}{\partial y} \left(\eta \frac{\partial u}{\partial y} \right) + \frac{\partial}{\partial z} \left(\eta \frac{\partial u}{\partial z} \right) + \rho f = 0, \quad (3.18)$$

where u and f are the x -components of mean velocity and body force, respectively.

The momentum balances in the y - and z -directions reduce to

$$P = \text{const.} \quad (3.19)$$

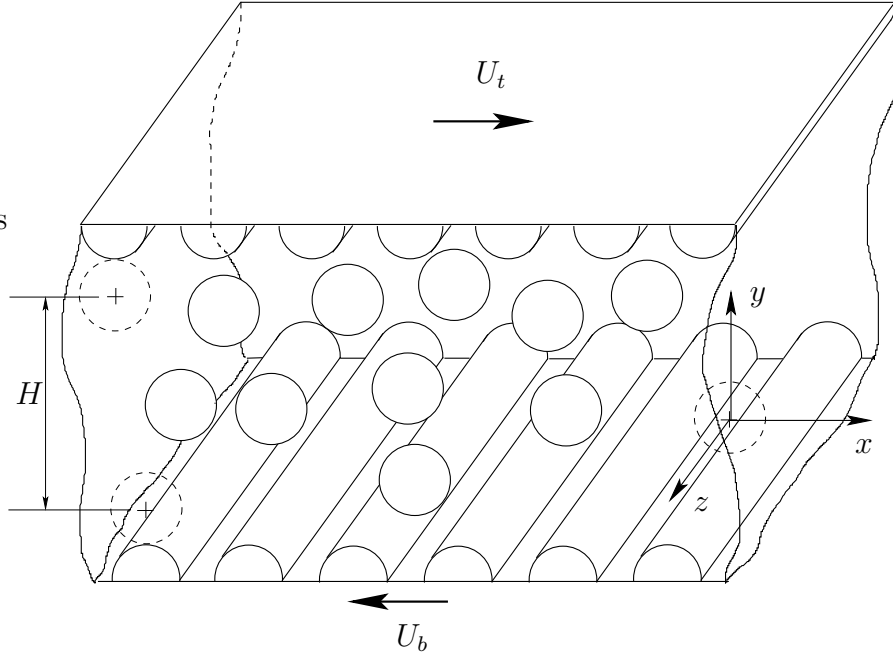


Figure 3.1: Fully developed, steady flows in a rectilinear cell.

The energy conservation requires

$$\frac{\partial}{\partial y} \left(\kappa \frac{\partial T}{\partial y} \right) + \frac{\partial}{\partial z} \left(\kappa \frac{\partial T}{\partial z} \right) + \eta \left(\frac{\partial u}{\partial y} \right)^2 + \eta \left(\frac{\partial u}{\partial z} \right)^2 - \gamma = 0. \quad (3.20)$$

For convenience, we define the fluctuation velocity $w \equiv T^{1/2}$ and transform the energy conservation (3.20) to

$$\frac{\partial}{\partial y} \left(\frac{M}{F} \frac{\partial w}{\partial y} \right) + \frac{\partial}{\partial z} \left(\frac{M}{F} \frac{\partial w}{\partial z} \right) + \frac{J}{5Fw} \left[\left(\frac{\partial u}{\partial y} \right)^2 + \left(\frac{\partial u}{\partial z} \right)^2 \right] - \frac{3}{F\sigma^2} (1 - e_{eff}) w = 0. \quad (3.21)$$

To obtain boundary conditions for u and w , we assume that the constitutive relations in the bulk can be extended to the boundary. For example, at the bottom wall, we write

$$\frac{\tau_{xy}}{P} = \frac{2J}{5\sqrt{\pi}F} \frac{\sigma}{W} \frac{\partial u}{\partial y} \Big|_{y=0} = \frac{S}{N} \Rightarrow \frac{\partial u}{\partial y} \Big|_{y=0} = \frac{5\sqrt{\pi}F}{2J} \frac{W}{\sigma} \frac{S}{N} \quad (3.22)$$

and

$$\frac{q_y}{PT^{1/2}} = -\frac{2M}{\sqrt{\pi}F} \frac{\sigma}{W} \frac{\partial w}{\partial y} \Big|_{y=0} = \frac{Q}{NT^{1/2}} \Rightarrow \frac{\partial w}{\partial y} \Big|_{y=0} = -\frac{\sqrt{\pi}FW}{2M} \frac{Q}{NT^{1/2}}, \quad (3.23)$$

where S/N and $Q/NT^{1/2}$ are given by the superposition Eq. (2.86) and Eq. (2.87) that we proposed in Chapter 2, respectively.

Equations (3.18) and (3.21) are solved subject to boundary conditions (3.22) and (3.23). Because these equations are elliptic, we use the ADI method [103], which has been widely tested in numerical heat conduction problems. Equation (3.19) then determines the particle volume fraction. In that Eq., the constant is set by imposing the number of particles in the system or, equivalently,

$$\frac{1}{WH} \int_{-W/2}^{W/2} \int_0^H \nu(y, z) dy dz = \bar{\nu},$$

where $\bar{\nu}$ is the average solid volume fraction. Details of the numerical scheme are included in Appendix C.1.

Figure 3.2 compares the theoretical predictions for mean and fluctuation velocity through the channel cross-section with results from the numerical simulations. The conditions are $Y = 18.81$, $Z = 39.84$, $\sigma = d_0 = 2$, $d_1 = 3.175$, $s_1 = s_0 = 0$, $\bar{\nu} = 0.311$. The impact parameters are those of acrylic spheres flowing in a microgravity shear cell [81]. For binary impacts, $e = 0.93$, $\mu = 0.12$, $\beta_0 = 0.35$; for impacts between a sphere and a bumpy boundary: $e_w = 0.965$, $\mu_w = 0.219$, $\beta_{0w} = 0.28$; between a sphere and the front side wall at $z = Z/2$: $e_{sf} = 0.94$, $\mu_{sf} = 0.14$, $\beta_{0,sf} = 0.51$; and between a sphere and the rear side wall at $z = -Z/2$: $e_{sr} = 0.83$, $\mu_{sr} = 0.12$, $\beta_{0,sr} = 0.34$. In the computer simulation, we did not observe any noticeable changes in the mean and fluctuation velocities with time, which indicates that the flow is stable. All other simulation results shown in this chapter have also been verified to be stable.

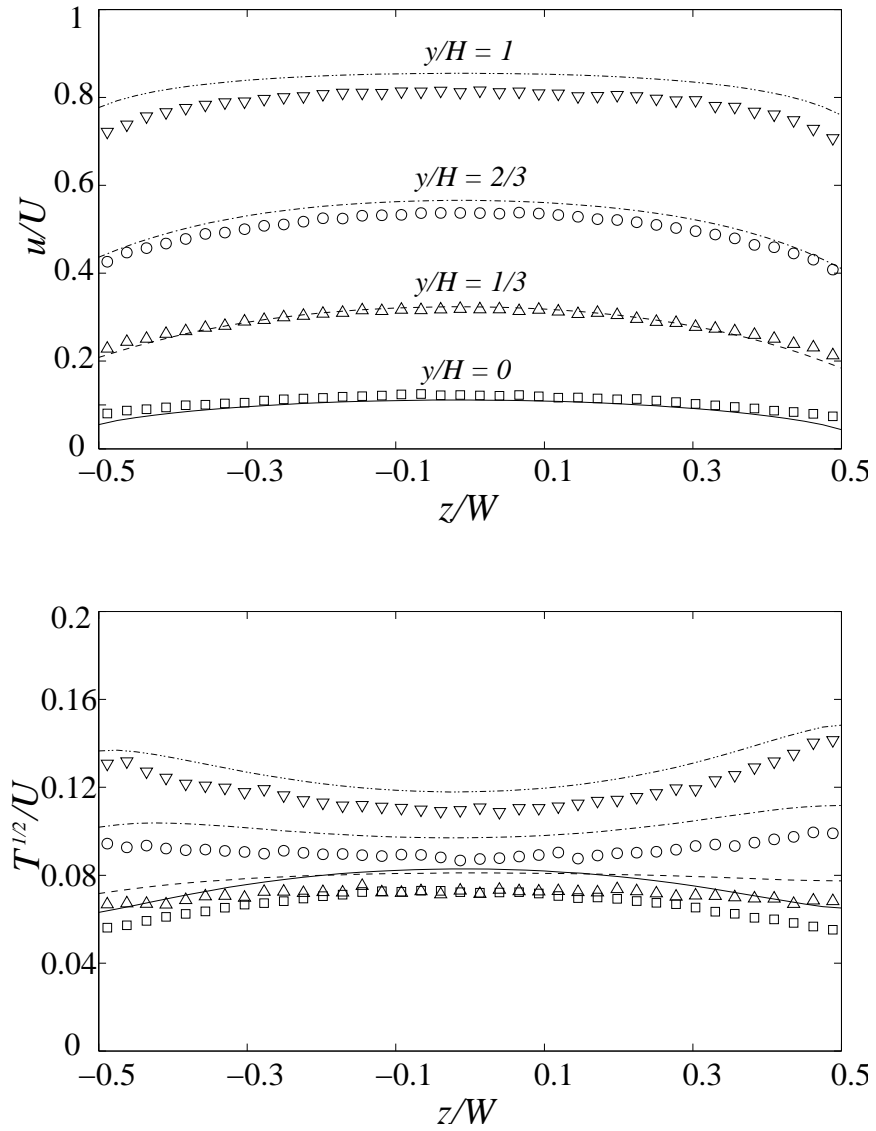


Figure 3.2: Mean and fluctuation velocities in the cross-section of a rectilinear cell. Top: mean velocity in x -direction made dimensionless with the velocity U of the top boundary. Bottom: fluctuation velocity made dimensionless with U . The symbols and lines represent, respectively, the results of the simulations and the predictions of the theory. Solid lines and squares are $y/H = 0$; dashed lines and upward triangles, $y/H = 1/3$; dash-dotted lines and circles, $y/H = 2/3$; dotted lines and downward triangles, $y/H = 1$.

Friction reduces the mean velocity in the vicinity of the flat side walls. Because the mean flow velocity varies in the y -direction, the resulting side wall drag influences the velocity gradient differently at different values of y . Near the moving boundary, friction increases the velocity gradient in the y -direction, thus raising the production rate of fluctuation energy. Therefore, in this case, the granular temperature is higher near the flat side walls than in the interior. On the other hand, near the stationary bumpy boundary, the velocity gradient in the y -direction is reduced by the wall friction. Therefore, both the energy production rate and the granular temperature are lower near the side walls. As Fig. 3.2 shows, the theory captures these features well.

Integral equations

In physical experiments [81], high speed photography can only observe granular flows through the flat side walls. Fortunately, because changes in the mean and fluctuation velocities are relatively small in the z -direction (Fig. 3.2), it is possible to infer the state of flow in the interior from such observations. In this context, our interest resides chiefly in the variations of u and T in the y -direction. Thus, it is convenient to integrate the momentum and energy balances (3.18), (3.19) and (3.21) in the z -direction. To that end, we follow Jenkins and Arnarson [52] in assuming that $u = u(y)$, $T = T(y)$ and $\nu = \nu(y)$, and that the shear stress τ_{xz} varies linearly in the z -direction. The results of the integration along z are

$$P = P(y) = \text{const}, \quad (3.24)$$

$$\frac{d}{dy} \left(\eta \frac{du}{dy} \right) + \frac{1}{W} \left(\tau_{xz}^+ - \tau_{xz}^- \right) + \rho f = 0, \quad (3.25)$$

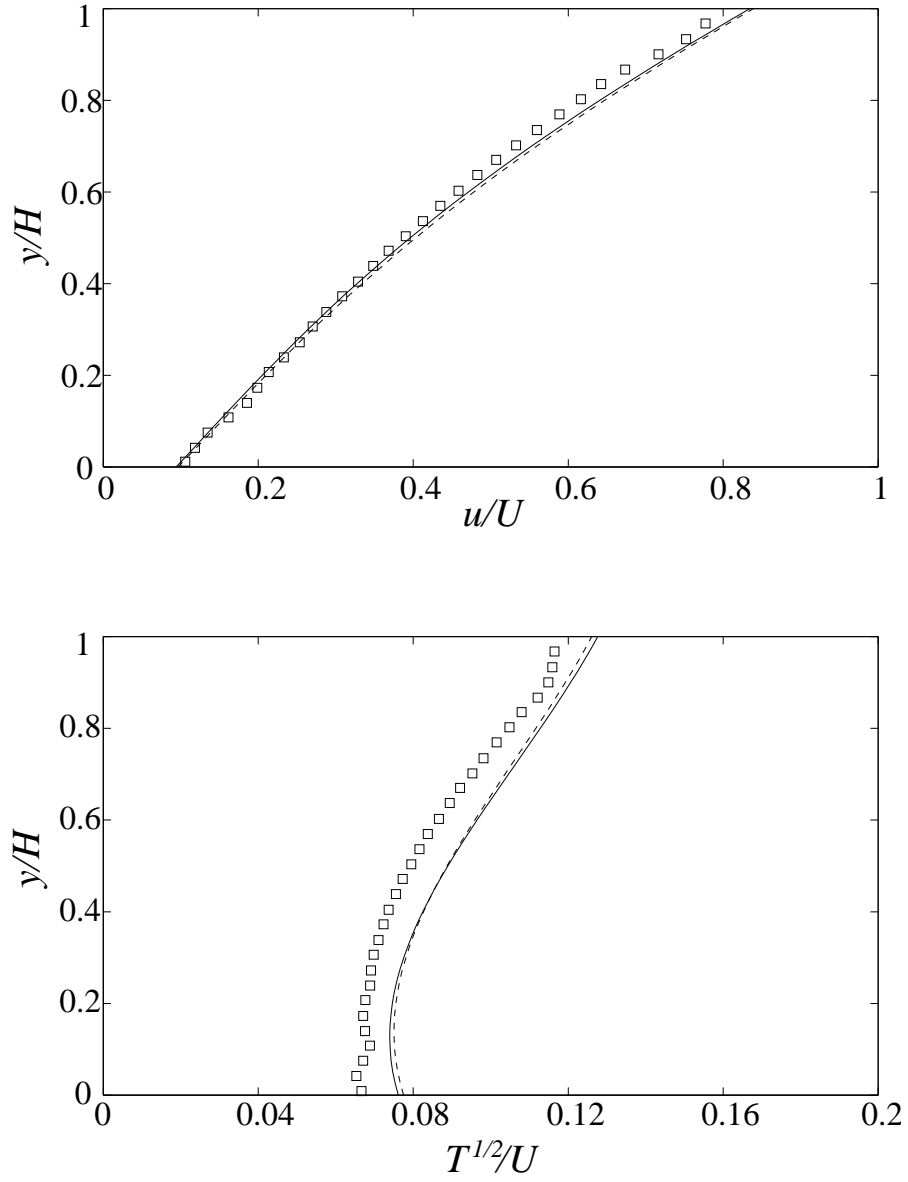


Figure 3.3: Transverse profiles of depth-averaged mean and fluctuation velocities made dimensionless with U for the conditions of Fig. 3.2. Symbols are simulation data averaged from side wall to side wall. Solid lines are the two-dimensional solutions of Fig. 3.2 averaged in the z -direction. Dashed lines are solutions from the depth-averaged Eqs. (3.25) and (3.26).

and

$$\begin{aligned} \frac{d}{dy} \left(\frac{M}{F} \frac{dw}{dy} \right) + \frac{\sqrt{\pi}}{2W\sigma} \left(\frac{q_z^+ + q_z^-}{Pw} \right) w + \frac{J}{5Fw} \left(\frac{du}{dy} \right)^2 \\ + \frac{5\pi Fw}{12J\sigma^2} \left[\left(\frac{\tau_{xz}^+ - \tau_{xz}^-}{2P} \right)^2 + 3 \left(\frac{\tau_{xz}^+ + \tau_{xz}^-}{2P} \right)^2 \right] - \frac{3}{F\sigma^2} (1 - e_{eff}) w = 0, \end{aligned} \quad (3.26)$$

where $\tau_{xz}^+ = \tau_{xz}|_{z=W/2}$ and $\tau_{xz}^- = \tau_{xz}|_{z=-W/2}$ are shear stresses on the front and rear side walls, respectively. The quantities q_z^+ and q_z^- are the corresponding fluctuation energy fluxes into the flow. Wall stresses (τ_{xz}^+ , τ_{xz}^-) and fluxes (q_{xz}^+ , q_{xz}^-) are evaluated using the boundary conditions (2.88) and (2.89). For example, on the flat wall at $z = -W/2$,

$$\tau_{xz}^- = \text{sign}(u) \min \left(\frac{\sqrt{3}}{14} (1 + \beta_{0,sr}) \frac{u}{w} P, \mu_{sr} P \right) \quad (3.27)$$

and

$$q_{xz}^- = \min \left(\begin{aligned} & Pw \sqrt{\frac{\pi}{2}} \left[7\mu_{sr}^2 - \frac{\pi}{2} \mu_{sr} \left(1 - \frac{u^2}{3w^2} \right) - \frac{2}{\pi} (1 - e_{sr}) \right] \\ & Pw \sqrt{\frac{2}{\pi}} \left[\frac{7}{3} \mu_{sr}^2 - (1 - e_{sr}) \right] \end{aligned} \right) \quad (3.28)$$

where e_{sr} , μ_{sr} , and $\beta_{0,sr}$ are the impact parameters for collisions between flow particles and the flat wall. In these expressions, the granular pressure P , the mean velocity u and the fluctuation w are evaluated at the relevant y . When writing Eqs. (3.27) and (3.28), we use the boundary conditions (2.88) and (2.89) for flat walls, but ignore the particle spin around the y -axis.

To determine the particle volume fraction $\nu(y)$ while enforcing the known mean volume fraction $\bar{\nu}$, we define the ‘‘volume fraction integral’’

$$I(y) \equiv \frac{1}{H} \int_0^y \nu(y) dy. \quad (3.29)$$

We then differentiate the equation of state (3.6) to obtain the governing equation for I ,

$$\frac{d^2 I}{dy^2} = \frac{1}{H} \frac{d\nu}{dy} = -\frac{\nu}{HFGT} \frac{d(FGT)}{dy} + \frac{1}{4\rho_s FGTH} \frac{dP}{dy}, \quad (3.30)$$

which is subject to the boundary conditions $I(0) = 0$ and $I(H) = \bar{v}$.

The averaged Eqs. (3.25), (3.26) and (3.30) are solved simultaneously by iteration. The boundary conditions for u and w at the two bumpy boundaries are derived from (2.86) and (2.87) in a manner similar to that leading to Eqs. (3.22) and (3.23). At each iteration step, we use an efficient algorithm for tri-diagonal matrix inversion [112]. Appendix C.1 contains details of the solution procedure.

As Fig. 3.3 shows, Eqs. (3.25) and (3.26) yield solutions that are nearly identical to the depth-averaged two-dimensional solutions shown in Fig. 3.2. Thus, in the rest of this paper, we will only compare solutions of the averaged Eqs. (3.25) and (3.26) with simulations and experiments.

Effect of a streamwise body force

It is instructive to consider the effects of a streamwise body force on granular flows. Like ordinary fluids, the presence of such a force creates a Poiseuille flow, which is superimposed on the shearing created by the moving boundary (Fig. 3.4). Because Poiseuille's flow has a parabolic-like velocity profile, it affects the fluctuation energy balance in two ways. First, by changing the local velocity gradient, it reduces the shear production of granular agitation near the moving wall, while increasing it near the stationary bumpy boundary. Second, the body force raises the slip velocity at the stationary boundary to a value much larger than its counterpart at the moving boundary. In turn, this induces a larger fluctuation energy flux into the flow through the stationary boundary. These two effects contribute to a much higher granular temperature near the stationary boundary and, because the pressure must remain constant, the solid volume fraction becomes higher near the moving boundary and lower near the stationary boundary.

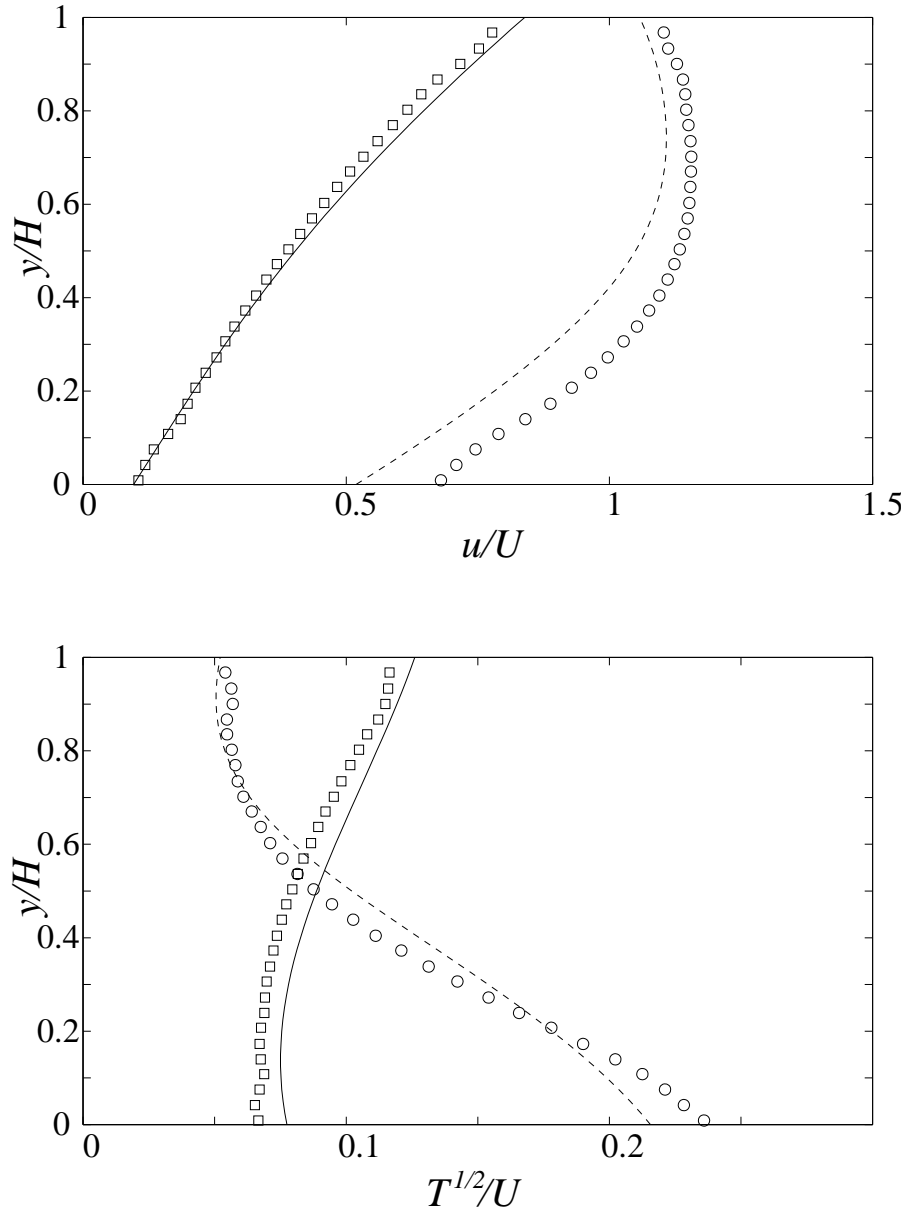


Figure 3.4: Effects of a streamwise body force on the mean and fluctuation velocities made dimensionless with U . Symbols are simulation data. Lines are solutions of Eqs. (3.25) and (3.26). Squares and solid lines denote $Fr = 0$, where $Fr \equiv g\sigma/U^2$ is a Froude number representing the relative magnitude of the body force g . Circles and dashed lines are $Fr = 0.005$. Conditions are otherwise those of Fig. 3.2.

Because a body force can induce large slip velocities, it is important to use boundary conditions (2.20)- (2.21), which include non-linear terms derived for this purpose. As Fig. 3.4 illustrates, the theory captures well the mean and fluctuation velocity profiles in the absence of gravity. We note a modest discrepancy when gravity is applied ($Fr = 0.005$). We attribute the discrepancy to the relatively crude superposition leading to the boundary conditions (2.86) and (2.87). We expect that the agreement will improve when a more comprehensive derivation of these boundary conditions is produced.

Axisymmetric flow

Confined physical experiments in a shearing apparatus require the recirculation of the granular material [80, 81], and thus they involve centripetal accelerations in the bulk. To illustrate the corresponding analyses, we now focus on sheared granular flows in an axisymmetric shear cell, whose rotating inner and outer bumpy boundaries are composed of half-cylindrical bumps parallel to the axis of rotation, and whose flat side walls remain at rest. Here, it is natural to adopt a cylindrical coordinate system with origin at the center of the cell. At steady state, the averaged one-dimensional Eqs.(3.25) and (3.26) become

$$\frac{dP}{dr} = \rho \frac{u^2}{r}, \quad (3.31)$$

$$\frac{1}{r^2} \frac{d}{dr} \left[\eta r^3 \frac{d}{dr} \left(\frac{u}{r} \right) \right] + \frac{1}{W} (\tau_{\theta z}^+ - \tau_{\theta z}^-) = 0, \quad (3.32)$$

and

$$\begin{aligned} \frac{1}{r} \frac{d}{dr} \left(2r\kappa w \frac{dw}{dr} \right) + \frac{1}{W} (q_z^+ + q_z^-) + \eta \left[r \frac{d}{dr} \left(\frac{u}{r} \right) \right]^2 \\ + \frac{1}{12\eta} (\tau_{\theta z}^+ - \tau_{\theta z}^-)^2 + \frac{1}{4\eta} (\tau_{\theta z}^+ + \tau_{\theta z}^-)^2 - \gamma = 0, \end{aligned} \quad (3.33)$$

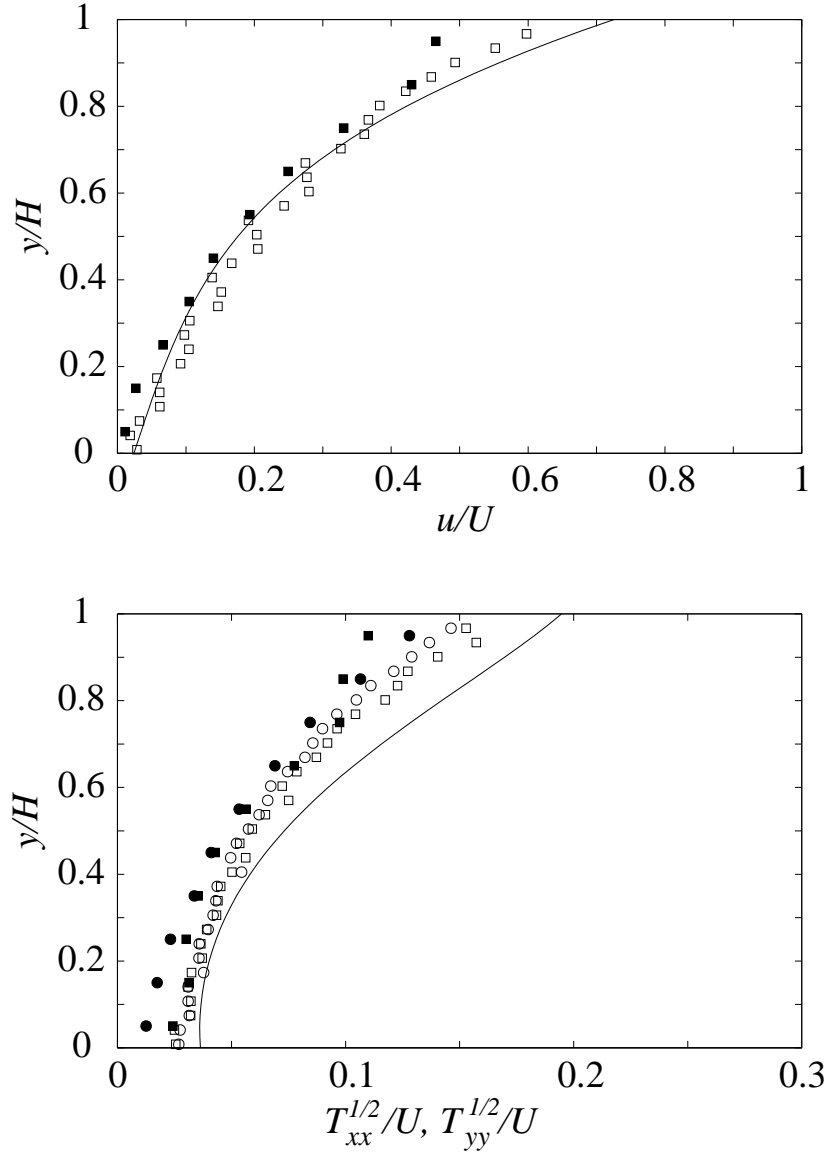


Figure 3.5: Granular flows in the round section of a shear cell shaped as a race track. Actual dimensions of the shear cell are given in [80, 81]. Solid symbols are experimental data, open symbols are numerical simulations and solid lines are theoretical predictions. Top: dimensionless mean velocity profile $u(r)/U$. Bottom: dimensionless fluctuation velocities $w(r)/U$. Squares represent the component $T_{xx}^{1/2}/U$ along the x -direction, and circles are $T_{yy}^{1/2}/U$. Here, $y = 0$ at the stationary outer boundary and $y = H$ at the moving inner boundary.

where $u = u(r)$ is the mean velocity in azimuthal direction; $\tau_{\theta z}^+ = \tau_{\theta z}|_{z=W/2}$ and $\tau_{\theta z}^- = \tau_{\theta z}|_{z=-W/2}$ are shear stresses at the front and rear side walls, respectively; and q_z^+ and q_z^- are fluxes of fluctuation energy into the flow through the front and rear flat side walls. The shear stresses and energy fluxes at flat side walls are determined by equations that resemble Eqs. (3.27) and (3.28).

Boundary conditions for u and w are the same as in Sec. 3.1.2. The solution must also uphold the known average volume fraction

$$\bar{\nu} \equiv \frac{1}{\bar{R}H} \int_{R_i}^{R_o} r\nu(r)dr, \quad (3.34)$$

where R_i and R_o are the inner and outer radius, respectively; $\bar{R} = (R_i + R_o)/2$ is the mean radius of the flow channel and $H = R_o - R_i$ is the depth of the channel.

As in Sec 3.1.2, we define the volume fraction integral

$$I(r) \equiv \frac{1}{\bar{R}H} \int_{R_i}^r r\nu(r)dr,$$

and obtain the following differential equation

$$\frac{d^2 I}{dr^2} = \frac{\nu}{\bar{R}H} - \frac{r\nu}{\bar{R}HFGT} \frac{d(FGT)}{dr} + \frac{r\nu}{4FGT\bar{R}H} \frac{u^2}{r}, \quad (3.35)$$

in which we have used Eq. (3.31) to simplify the expression. The boundary conditions for $I(r)$ are $I(R_i) = 0$ and $I(R_o) = \bar{\nu}$. We solve Eqs. (3.32), (3.33) and (3.35) to find the mean and fluctuation velocities and the volume fraction.

The iterative procedure is the same as in Sec. 3.1.2.

Figure 3.5 compares the numerical solutions with simulation and experimental measurements of the mean and fluctuation velocity profiles. Experiments were conducted in the microgravity “race track” shear cell of Louge *et al* [80, 81]. The axes of cylindrical bumps on the inner and outer boundaries are located at the radial positions $R_i = 61.97$ and $R_o = 80.78$, respectively. The distance between

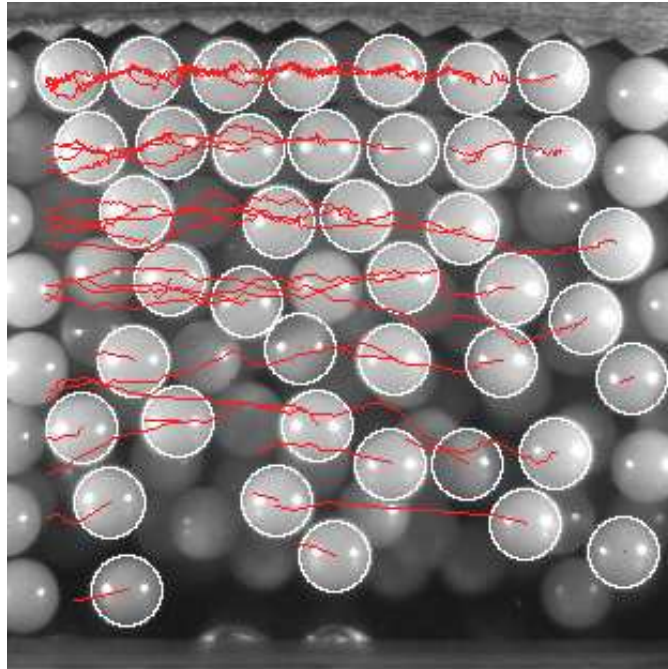


Figure 3.6: A typical digital image of the curved region in the race-track Couette cell of Louge *et al* [81]. The top boundary is fixed while the bottom boundary moves from right to left. Persistent scratches on the window hide the moving boundary. Circles and lines are superimposed to indicate the location and trajectory of detected spheres.

flat side walls is $Z = 39.84$. The outer boundary bumps have a diameter $d_o = \sigma = 2$, and the inner bumps have $d_i = 3.175$. The bumps are closely spaced with $s_i = s_o = 0$. Images of the flow were obtained with a Kodak Ektapro digital video camera operating at 1000 Hz. A typical image taken by the camera is shown in Figure 3.6. The camera was trained half-way between the entrance and exit of the curved region of the cell, where our numerical simulations indicate that the axisymmetric flow is fully-developed.

In general, we observed that high solid concentration caused particles to form layers parallel to the stationary boundary. Because our experimental data were obtained from images taken through the front side wall, we could only measure two components of the granular temperature. However, for these spheres with relatively modest collisional energy dissipation, the anisotropy was not significant. Thus, in this case, the isotropic theory agreed well with simulations and experiments. The deviation of experimental data from simulation and theory near the moving inner boundary was likely due to an insufficient camera frequency, which produced experimental errors that we discuss in detail in Chapter 6.

Flow at Knudsen number of $O(1)$

Our last example of bounded granular flows with a single constituent concerns flows at a relatively large Knudsen number, $Kn \equiv \lambda/L$. In this expression, λ is the mean free path of the flowing spheres and L is a characteristic length scale of the flow, such as the distance between bumpy boundaries. At low volume fractions, the mean free path is well represented by the classical expression $\lambda = d/6\sqrt{\pi}\nu H$. In general, one would expect the kinetic theory to be valid only for flows with $Kn \ll 1$. Surprisingly, Fig. 3.7 shows that it remains valid even at

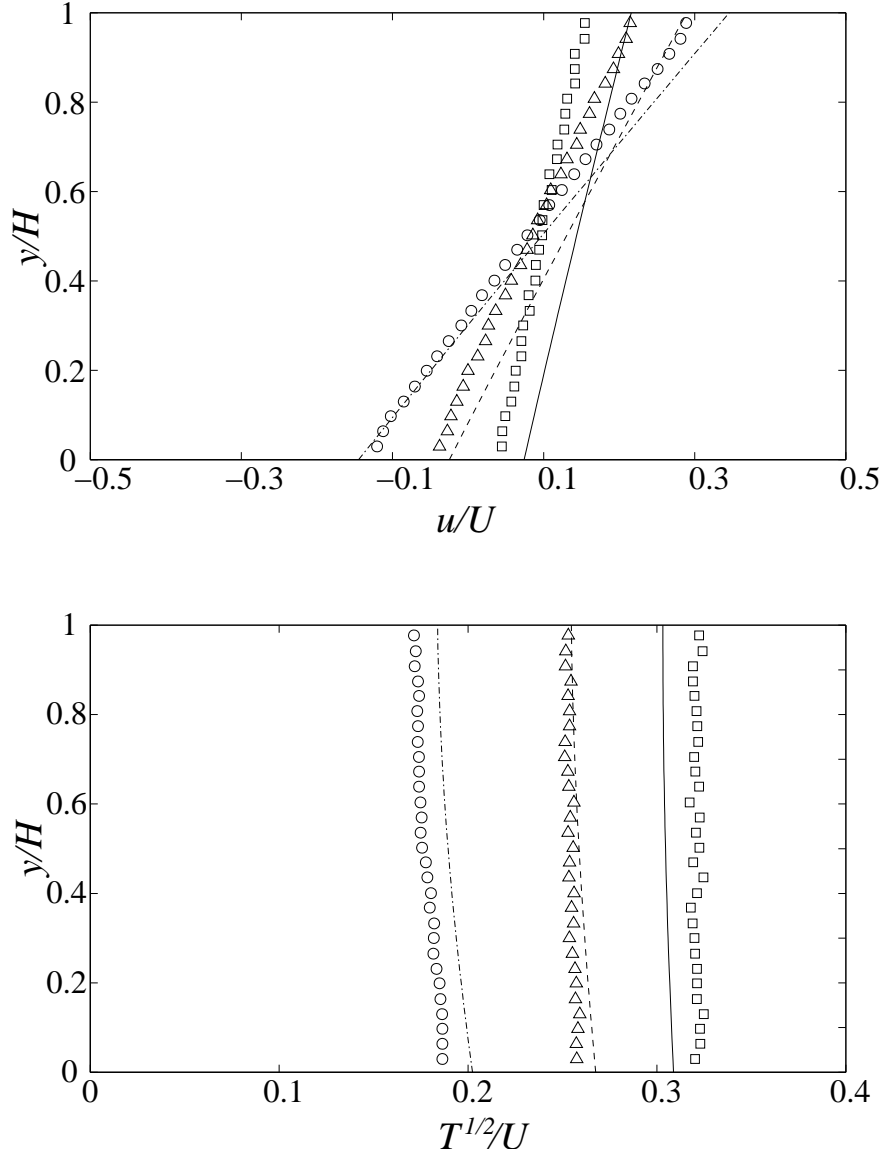


Figure 3.7: Granular flows with $O(1)$ Knudsen number. The top and bottom graphs show dimensionless mean and fluctuation velocities, respectively. The simulations (symbols) are periodic in the z -direction and do not possess side walls. The lines are theoretical solutions. For squares and solid lines, $Kn = 0.75$; for triangles and dashed lines, $Kn = 0.30$; for circles and dash-dotted lines: $Kn = 0.15$. Conditions are $Y = 17.24$, $\sigma = d_0 = 2$, $d_1 = 3$, $s_0 = s_1 = 0$, $e = 0.95$, $\mu = 0.1$, $\beta_0 = 0.4$, $e_w = 0.85$, $\mu_w = 0.1$ and $\beta_{0w} = 0.4$.

low volume fractions, for which Knudsen numbers lie between 0.15 and 0.75. A possible reason for the agreement is that our boundary conditions take proper account of the geometry of the boundary and of its collisional interactions with the flowing grains. Thus, they remain valid even when the collision frequency between the spheres and the boundary becomes comparable to that in the flow. In addition, the bumpy character of the boundary may keep the particle velocity distribution nearly Maxwellian, an assumption which underlies the derivation of both the kinetic theory and the boundary conditions.

3.2 Flow of Binary Mixtures

Jenkins and Mancini [58] derived balance laws and constitutive relations for unbounded flows of binary mixtures of smooth, inelastic spheres assuming an equipartition of fluctuation energy between the two species. Arnarson and Willits [6] recently published a correction to some of those calculations. Louge *et al* [81] reported segregation experiments carried out in microgravity with binary mixtures and compared experiment data, numerical simulation and theory. After summarizing the prediction of Jenkins and Mancini [58], we develop numerical solutions for such flows in bounded geometries that are suitable for experimental verification of the theory.

3.2.1 Exact theory

We consider a granular flow between two moving bumpy boundaries that is similar to that shown in Figure 3.1. The flowing spheres are a mixture of species A and B with radii r_i , masses m_i , and number density n_i , where i represents A or B . The temperature of species i is defined as $T_i \equiv \frac{1}{3}m_i \langle \mathbf{C}_i \cdot \mathbf{C}_i \rangle$, where

\mathbf{C}_i is the fluctuation velocity of species i spheres relative to their mean velocity. The mixture temperature is $T \equiv (n_A T_A + n_B T_B)/n$, where $n \equiv n_A + n_B$ is the number density of the mixture. In the limit of small dissipation of fluctuation energy, the latter is equally distributed between two species, $T = T_A = T_B$, and the fluctuation velocity of species i is $w_i = (T/m_i)^{1/2}$. In contrast, Garzó and Dufty [35], Montanero and Garzó [91], and Alam and Luding [1] showed examples in which equipartition of energy does not hold. For convenience, we also define the parameters $m_{ij} = m_i + m_j$, $r_{ij} = r_i + r_j$ and $M_{ij} = m_i/m_{ij}$, where $i, j = A$ or B . We first consider a geometry without flat side walls, which is simulated with periodic boundary conditions in the z -direction, and on which the only possible external force on the spheres is the downward gravity \mathbf{g} . At fully-developed, steady state, the only non-zero velocity component is parallel to the boundary velocity and the mass conservation equation is satisfied automatically. The momentum balances in the x - and y -directions thus become

$$\frac{dS}{dy} = 0, \quad (3.36)$$

$$\frac{dP}{dy} = -\rho g, \quad (3.37)$$

and the conservation of fluctuation energy requires

$$-\frac{dq}{dy} + S \frac{du}{dy} - \gamma = 0, \quad (3.38)$$

where S is the shear stress of the mixture, P is the mixture pressure, g is the gravitational acceleration, q is the flux of fluctuation energy in the y -direction, γ is the volumetric energy dissipation rate, $\rho \equiv \rho_A + \rho_B$ and $u \equiv (\rho_A u_A + \rho_B u_B)/\rho$ are the mixture density and mean velocity, respectively, and $\rho_i \equiv n_i m_i$ and u_i are the density and mean velocity of species i with $i = A$ or B .

The mixture pressure P is given by

$$P = \left(n + K_{AA} + K_{BB} + 2K_{AB} \right) T, \quad (3.39)$$

where the factor

$$K_{ij} = \frac{2}{3} \pi n_i n_j g_{ij} r_{ij}^3$$

accounts for the effects of finite particle size on pressure at high volume fraction.

The radial distribution function at contact is

$$g_{ij} = \frac{1}{1 - \nu} + \frac{3r_i r_j}{r_i + r_j} \frac{\xi_2}{(1 - \nu)^2} + 2 \left(\frac{r_i r_j}{r_i + r_j} \right)^2 \frac{\xi_2^2}{(1 - \nu)^3}, \quad (3.40)$$

where $\xi_\alpha \equiv \frac{4}{3} \pi (n_A r_A^\alpha + n_B r_B^\alpha)$, $\alpha = 1, 2$, or 3 , and $\nu = \xi_3$ is the total volume fraction.

The shear stress S is related to the strain rate through

$$S = \eta \frac{du}{dy}, \quad (3.41)$$

where the mixture viscosity is

$$\eta = \frac{1}{2} \sum_{i=A,B} b_{i0} T^{\frac{1}{2}} n_i K'_i + \frac{2}{5} \sum_{i,j=A,B} \left(\frac{2\Gamma m_i m_j}{\pi m_{ij}} \right)^{1/2} K_{ij} r_{ij}, \quad (3.42)$$

with

$$K'_i = 1 + \frac{2}{5} \frac{K_{ii}}{n_i} + \frac{4}{5} M_{ki} \frac{K_{ik}}{n_i}, \quad (k \neq i)$$

$$b_{i0} = \frac{15\sqrt{2} m_i^{1/2}}{8\sqrt{\pi} g_{ik} n_i n_k r_{ik}^2 M_{ki}^{1/2}} \left(\frac{\beta_i n_i K'_i + 4n_k K'_k M_{ki}}{\beta_i \beta_k - 16M_{ik} M_{ki}} \right), \quad (k \neq i)$$

and

$$\beta_i = 10M_{ki} + 6M_{ik} + 3\sqrt{2} \frac{n_k}{n_i} \frac{g_{kk}}{g_{ik}} \frac{r_{kk}^2}{r_{ik}^2} M_{ik}^{-1/2}, \quad (k \neq i).$$

The flux of fluctuation energy is given by Fourier's law

$$q = -\kappa \frac{dT}{dy}, \quad (3.43)$$

where κ is the conductivity of the mixture

$$\kappa = -\frac{5}{4} \sum_{i=A,B} n_i K_i \left(\frac{2T}{m_i} \right)^{1/2} a_{i1} + 2 \sum_{i,j=A,B} K_{ij} r_{ij} \left(\frac{2T m_i m_j}{\pi m_{ij}^3} \right)^{1/2}, \quad (3.44)$$

with

$$K_i = 1 + \frac{2}{5} \pi n_i g_{ii} r_{ii}^3 + \frac{8}{5} \pi M_{ik} M_{ki} n_k g_{ik} r_{ik}^3, \quad (k \neq i)$$

$$a_{i1} = \frac{15}{8\sqrt{\pi} n_i n_k g_{ik} r_{ik}^2 M_{ki}^{1/2}} \left(\frac{\alpha_i n_i K_i + 13 M_{ik} M_{ki} n_k K_k}{169 M_{ik}^2 M_{ki}^2 - \alpha_i \alpha_k} \right), \quad (k \neq i)$$

and

$$\alpha_i = 15 M_{ki}^2 + 8 M_{ik} M_{ki} + 6 M_{ik}^2 + 2\sqrt{2} \frac{n_k g_{kk} r_{kk}^2}{n_i g_{ik} r_{ik}^2} \frac{1}{M_{ik}^{1/2}}, \quad (k \neq i).$$

The energy dissipation rate per unit volume of the mixture is

$$\gamma = \sum_{i,j=A,B} 4g_{ij} r_{ij}^2 n_i n_j M_{ji} (1 - e_{ij}) \left(\frac{2\pi m_{ij} T^3}{m_i m_j} \right)^{1/2}, \quad (3.45)$$

where e_{ij} is the coefficient of restitution for collisions between a sphere of species i and a sphere of species j . For frictional spheres, we substitute effective coefficients of restitution $e_{ij,eff}$ wherever e_{ij} appears as we did in Section 3.1.

Jenkins and Mancini [58] showed that the diffusion velocity between the two species vanishes at steady-state, which results in the following balance between the gradient of species concentration and the gradient of mixture temperature,

$$-\frac{\rho_A}{n\rho T} \frac{dP}{dy} + \left[\frac{1}{n} \left(n_A + 2M_{AB} K_{AB} + K_{AA} \right) + K_T^{(A)} \right] \frac{1}{T} \frac{dT}{dy} + \frac{n_A}{nT} \left(\frac{\partial \mu_A}{\partial n_A} \frac{dn_A}{dy} + \frac{\partial \mu_A}{\partial n_B} \frac{dn_B}{dy} \right) = 0, \quad (3.46)$$

where $K_T^{(A)}$ is the thermal diffusion coefficient,

$$K_T^{(A)} = \frac{a_{A0}}{n t_{A0}}, \quad (3.47)$$

with

$$\begin{aligned}
a_{A0} &= \frac{1}{2\rho} \left(m_{AB} m_B \right)^{1/2} n_B \left(M_{BA}^{3/2} a_{A1} - M_{AB}^{3/2} a_{B1} \right), \\
t_{A0} &= \frac{3m_B}{8\sqrt{\pi}\rho n_A g_{AB} r_{AB}^2 M_{BA}^{1/2}} + \frac{1}{2\rho} \left(m_{AB} m_B \right)^{1/2} n_B \left(M_{BA}^{3/2} t_{A1} + M_{AB}^{3/2} t_{B1} \right), \\
t_{i1} &= \frac{3M_{ki}^{1/2}}{8\sqrt{\pi}n_i n_k g_{ik} r_{ik}^2} \left(\frac{\alpha_i - 13M_{ik}^2}{\alpha_i \alpha_k - 169M_{ik}^2 M_{ki}^2} \right), \quad (k \neq i)
\end{aligned} \tag{3.48}$$

and μ_A is the chemical potential of species A,

$$\begin{aligned}
\frac{\mu_A}{T} &= \ln n_A - \ln(1 - \nu) + \frac{4}{3}\pi r_A^3 \frac{P}{T} + \frac{3\xi_2 r_A}{1 - \nu} + \frac{3\xi_1 r_A^2}{1 - \nu} + \frac{9\xi_2^2 r_A^2}{2(1 - \nu)^2} \\
&\quad + 3 \left(\frac{\xi_2 r_A}{\nu} \right)^2 \left[\ln(1 - \nu) + \frac{\nu}{1 - \nu} - \frac{\nu^2}{2(1 - \nu)^2} \right] \\
&\quad - \left(\frac{\xi_2 r_A}{\nu} \right)^3 \left[2 \ln(1 - \nu) + \frac{\nu(2 - \nu)}{1 - \nu} \right].
\end{aligned} \tag{3.49}$$

Another balance equation for the concentration and temperature gradients is obtained by substituting the pressure equation (3.39) into the momentum balance Eq. (3.37),

$$\frac{\partial P}{\partial n_A} \frac{dn_A}{dy} + \frac{\partial P}{\partial n_B} \frac{dn_B}{dy} + \frac{\partial P}{\partial T} \frac{dT}{dy} = -\rho g. \tag{3.50}$$

This equation, together with Eq. (3.46), determines the concentration gradients for each species

$$\begin{aligned}
\frac{dn_A}{dy} &= -\frac{n}{DT} \frac{dT}{dy} \left\{ \frac{n}{n_A} \left(\frac{1}{T} \frac{\partial P}{\partial n_B} \right) \left[\frac{\rho_A g}{n \frac{dT}{dy}} + \frac{1}{n} \left(n_A + K_{AA} + 2M_{AB} K_{AB} \right) + K_T^{(A)} \right] \right. \\
&\quad \left. - \left(\frac{n}{T} \frac{\partial \mu_A}{\partial n_B} \right) \left(\frac{\rho g}{n \frac{dT}{dy}} + \frac{P}{nT} \right) \right\}
\end{aligned} \tag{3.51}$$

and

$$\begin{aligned}
\frac{dn_B}{dy} &= \frac{n}{DT} \frac{dT}{dy} \left\{ \frac{n}{n_A} \left(\frac{1}{T} \frac{\partial P}{\partial n_A} \right) \left[\frac{\rho_A g}{n \frac{dT}{dy}} + \frac{1}{n} \left(n_A + K_{AA} + 2M_{AB} K_{AB} \right) + K_T^{(A)} \right] \right. \\
&\quad \left. - \left(\frac{n}{T} \frac{\partial \mu_A}{\partial n_A} \right) \left(\frac{\rho g}{n \frac{dT}{dy}} + \frac{P}{nT} \right) \right\},
\end{aligned} \tag{3.52}$$

where

$$D \equiv \det \begin{bmatrix} \frac{n}{T} \frac{\partial \mu_A}{\partial n_A} & \frac{n}{T} \frac{\partial \mu_A}{\partial n_B} \\ \frac{1}{T} \frac{\partial P}{\partial n_A} & \frac{1}{T} \frac{\partial P}{\partial n_B} \end{bmatrix}.$$

The expressions of $\frac{1}{T} \frac{\partial P}{\partial n_A}$, $\frac{1}{T} \frac{\partial P}{\partial n_B}$, $\frac{n}{T} \frac{\partial \mu_A}{\partial n_A}$, and $\frac{n}{T} \frac{\partial \mu_A}{\partial n_B}$ are listed in Appendix D.

Equations (3.36), (3.38), (3.51), and (3.52) can be solved for $u(y)$, $T(y)$, $n_A(y)$, and $n_B(y)$, respectively. For simplicity, we adopt boundary conditions for the mixture velocity and temperature that are derived from their counterparts for single constituent flows by merely substituting $(\sigma_A + \sigma_B)/2$ for the sphere diameter when defining the boundaries of the flow field with $H \equiv Y - \frac{1}{2}(d_1 + d_0) - \sigma$.

The ratio of mixture shear stress to the normal stress at a bumpy boundary is

$$\frac{S}{P} = \frac{S_A + S_B}{P} = \frac{P_A}{P} \frac{S_A}{P_A} + \frac{P_B}{P} \frac{S_B}{P_B}, \quad (3.53)$$

where $P_i = (n_i + K_{ii} + K_{ik})T$, ($k \neq i$), is the partial pressure of species i , and the ratio S_i/P_i of wall shear stress to normal stress of species i is calculated from Eq. (2.84) for a single constituent flow, in which we substitute $\theta_i \equiv \arcsin((d + s)/(d + 2r_i))$ for θ and w_i^2 for T .

Similarly, the flux of fluctuation energy into the mixture is

$$Q = Q_A + Q_B, \quad (3.54)$$

where the fluctuation energy flux Q_i from the bumpy boundary into species i is calculated from Eq. (2.85).

The known overall number density of species i imposes an integral constraint on the solution,

$$\frac{1}{H} \int_0^H n_i(y) dy = \bar{n}_i,$$

which we change into a boundary value problem by defining the new variable

$$I_i = \frac{1}{H} \int_0^y n_i(y) dy, \quad i = A \text{ or } B.$$

We then write the governing equation for I_i as

$$\frac{d^2 I_i}{dy^2} = \frac{1}{H} \frac{dn_i}{dy}, \quad (3.55)$$

with the boundary conditions $I_i(0) = 0$ and $I_i(H) = \bar{n}_i$.

We solve the four coupled boundary value problems for $u(y)$, $T(y)$, $I_A(y)$, and $I_B(y)$ by iterations using an efficient tri-diagonal matrix algorithm at each step [112].

3.2.2 Simplified theory

Conscious that the complicated expressions summarized above could obscure the physics of particle segregation and mixing, Arnarson and Jenkins [4] derived simpler relations in the limit where the two species have nearly the same size and mass. They did so by taking a perturbation of the exact theory of Jenkins and Mancini [58], properly corrected by Arnarson and Willits [6].

They showed that, to first order in the size difference $\delta r \equiv r_A/r_B - 1$ and mass difference $\delta m \equiv (m_A - m_B)/m_{AB}$, a binary mixture can be treated as a single constituent with size r_{AB} and mass $\frac{1}{2}m_{AB}$ but with modified transport coefficients.

In this simpler formulation, the mixture pressure is approximately

$$P = \frac{6\nu}{\pi r_{AB}^3} (1 - 3\bar{x}\delta r) T (1 + 4G), \quad (3.56)$$

where

$$x \equiv \frac{1}{2} \left(\frac{n_A}{n} - \frac{n_B}{n} \right)$$

is a parameter characterizing the segregation and the overbar denotes the average over the entire flow field.

The effective viscosity and conductivity of the equivalent single constituent flow are

$$\eta = \frac{4}{5} \sqrt{\frac{2}{\pi}} GJ \left[1 + \bar{x}(\delta r + \delta m) \right] n r_{AB} m_{AB}^{1/2} T^{1/2}, \quad (3.57)$$

$$\kappa = 4 \sqrt{\frac{2}{\pi}} GM \left[1 + \bar{x}(\delta r - \delta m) \right] n r_{AB} \left(\frac{T}{m_{AB}} \right)^{1/2}. \quad (3.58)$$

If $e_{AA} = e_{BB} = e_{AB} = e$, the perturbed energy dissipation rate is

$$\gamma = 24 \sqrt{\frac{2}{\pi}} G(1 - e) \left[1 - \bar{x}(\delta r + \delta m) \right] \frac{n T^{3/2}}{r_{AB} m_{AB}^{1/2}}. \quad (3.59)$$

If the coefficients of restitution between two species are not the same, we use an averaged e in Eq. (3.59) such that the simplified dissipation rate Eq. (3.59) gives the same result as its exact counterpart Eq. (3.45). As before, we substitute an effective coefficient of restitution if the spheres are frictional.

With these constitutive relations, we can solve the mixture flows as we did in Section 3.1 for a single species to obtain the profiles of mean velocity and fluctuation velocities. In the boundary conditions, we use r_{AB} as the equivalent single species diameter.

We then combine Eqs. (3.51) and (3.52) to write a governing equation for the segregation parameter x ,

$$\frac{dx}{dy} = - \left(\frac{1 - 4x^2}{2} \right) \left\{ \frac{1}{w} \frac{dw}{dy} \left[R(\nu) \delta r + \frac{105}{116} \delta m \right] + \frac{179}{29} G \frac{g}{w^2} \delta m \right\}, \quad (3.60)$$

where

$$w \equiv \sqrt{\frac{2T}{m_{AB}}}$$

is the fluctuation velocity of the equivalent single constituent,

$$R(\nu) = \frac{5}{58} \left[2 + \frac{\nu(3 - \nu)}{2 - \nu} - \frac{12}{5} G \right] + 2G \left[3 + \frac{\nu(3 - \nu)}{2 - \nu} \right] - \frac{12\nu H(\nu)(1 + 4G)}{1 + 4G + 4\nu H(\nu)},$$

and

$$H(\nu) \equiv \frac{dG}{d\nu} = \frac{2 + 2\nu - \nu^2}{2(1 - \nu)^4}.$$

The solution of Eq. (3.60) requires one boundary condition. To that end, Arnarson *et al* [5] specified the average value of x in the flow field, $\bar{x} = \frac{1}{2}\overline{(n_A - n_B)}/\bar{n}$, and suggested that this quantity is approximately $\frac{1}{2}(\bar{n}_A - \bar{n}_B)/\bar{n}$. Unfortunately, that solution could yield a value of \bar{n}_i that is different from the assumed value. To remedy this shortcoming, we introduce the new parameter

$$\zeta \equiv \frac{1}{2} \left(\frac{n_A}{\bar{n}} - \frac{n_B}{\bar{n}} \right), \quad (3.61)$$

which is related to x using

$$x = \frac{(\tilde{\nu}_A + \tilde{\nu}_B)\zeta}{2[\nu - (\tilde{\nu}_A - \tilde{\nu}_B)\zeta]}, \quad (3.62)$$

where $\tilde{\nu}_A \equiv \bar{\nu}\bar{n}/\bar{n}_A$ and $\tilde{\nu}_B \equiv \bar{\nu}\bar{n}/\bar{n}_B$ are constants. The governing equation for ζ derives from Eqs. (3.51) and (3.52),

$$\begin{aligned} \frac{d\zeta}{dy} = -\frac{1}{w} \frac{dw}{dy} & \left[2 \frac{1 + 4G + \beta_g + \beta_m \delta m}{1 + 4G + 4\nu H} \zeta \right. \\ & \left. + \frac{(\nu - 2\tilde{\nu}_A \zeta)(\nu + 2\tilde{\nu}_B \zeta)}{[\nu - (\tilde{\nu}_A - \tilde{\nu}_B)\zeta](\tilde{\nu}_A + \tilde{\nu}_B)} \left(R\delta r + \frac{105}{116} \delta m + \frac{358}{29} G\beta_m \delta m \right) \right], \quad (3.63) \end{aligned}$$

where

$$\beta_g \equiv \frac{g}{2w dw/dy}$$

and

$$\beta_m \equiv \frac{(\tilde{\nu}_A + \tilde{\nu}_B)\zeta}{\nu - (\tilde{\nu}_A - \tilde{\nu}_B)\zeta} \beta_g$$

are two parameters that vanish in the absence of a body force.

To solve Eq. (3.63), we transform it to a boundary value problem as in Section 3.2.1. We define

$$I_\zeta(y) \equiv \frac{1}{H} \int_0^y \zeta(y) dy,$$

and obtain

$$\frac{d^2 I_\zeta}{dy^2} = \frac{1}{H} \frac{d\zeta}{dy},$$

with boundary conditions $I_\zeta(0) = 0$ and $I_\zeta(H) = \bar{\zeta} = \frac{1}{2}(\bar{n}_A - \bar{n}_B)/\bar{n}$.

The number fraction of each species can then be calculated from $\zeta(y)$,

$$\frac{n_A}{n} = \frac{1}{2} + x = \frac{\nu + 2\tilde{\nu}_B\zeta}{2[\nu - (\tilde{\nu}_A - \tilde{\nu}_B)\zeta]} \quad (3.64)$$

and

$$\frac{n_B}{n} = 1 - \frac{n_A}{n} = \frac{\nu - 2\tilde{\nu}_A\zeta}{2[\nu - (\tilde{\nu}_A - \tilde{\nu}_B)\zeta]}. \quad (3.65)$$

3.2.3 Comparison of theory, simulations and experiments

We first compare results of our numerical simulations with theoretical solutions from both the exact and the simplified theories.

Segregation in a bounded flow

Because rigid boundaries tend to order spheres in their neighborhood, transverse profiles of solid volume fraction near a wall exhibit spatial oscillations on the order of a sphere diameter. Because the theory ignores these fluctuations, their presence can complicate comparisons with experiments or simulations. In grain mixtures, we alleviate this difficulty by defining a relative number fraction that quantifies segregation,

$$\phi_i \equiv \frac{n_i/n}{\bar{n}_i/\bar{n}}, \quad i = A, B.$$

As long as the radii of the two species are not greatly different, the relative number fractions contain ratios of volume fractions that nearly oscillate in phase and, consequently, their own spatial fluctuations are considerably reduced [81]. In this

definition, a region where $\phi_i < 1$ has a species i number fraction less than the average and vice versa. Segregation is stronger the farther ϕ_i deviates from 1.

Figure 3.8 shows typical results for a mixture with same size but different material densities sheared between two bumpy walls moving in opposite directions, $U_t = U/2$ and $U_b = -U/2$. Parameters used in simulation are: $\rho_A/\rho_B = 0.5842$, $r_A = r_B = 1$, $Y = 17.24$, $d_0 = d_1 = 2$, $s_0 = 0$, $s_1 = 1$, $\bar{\nu} = 0.338$, $\bar{n}_A/\bar{n} = 0.5$, and impact parameters: $e_{AA} = e_{BB} = 0.9$, $e_{AB} = 0.85$, $\mu_{ij} = \beta_{0,ij} = 0$, where $i, j = A, B$; between particles and bumpy boundaries: $e_w = 0.8$, $\mu_w = \beta_{0w} = 0$. Although the exact and the simplified theories both predict segregation qualitatively, they overestimate the effect. Here, the exact theory is marginally closer to the simulation profiles.

In Figure 3.9, the two species share the same material, but exhibit different sizes, $r_A/r_B = 1.25$. Once again, predictions from both theories agree reasonably well with simulations. However, the simplified theory yields a slightly better agreement than the exact theory.

The simplified theory also reveals interesting conditions whereby two different species mix uniformly rather than segregate in a gradient of fluctuation energy. In the absence of body forces, Eq. (3.60) reveals that if

$$R(\nu)\delta r + \frac{105}{116}\delta m = 0 \quad (3.66)$$

at a point, then $dx/dy = 0$ there. If we can maintain condition (3.66) everywhere in the flow field, then, according to the simplified theory, the two species will not segregate even if they differ in size or mass. Coincidentally, we find that the quantity $-116R(\nu)/105$ is approximately equal to 0.38 when $\nu > 0.2$. Therefore, if two species are such that $\delta m = 0.38\delta r$, then they should not segregate in a temperature gradient alone. Figure 3.10 confirms the existence of this state of

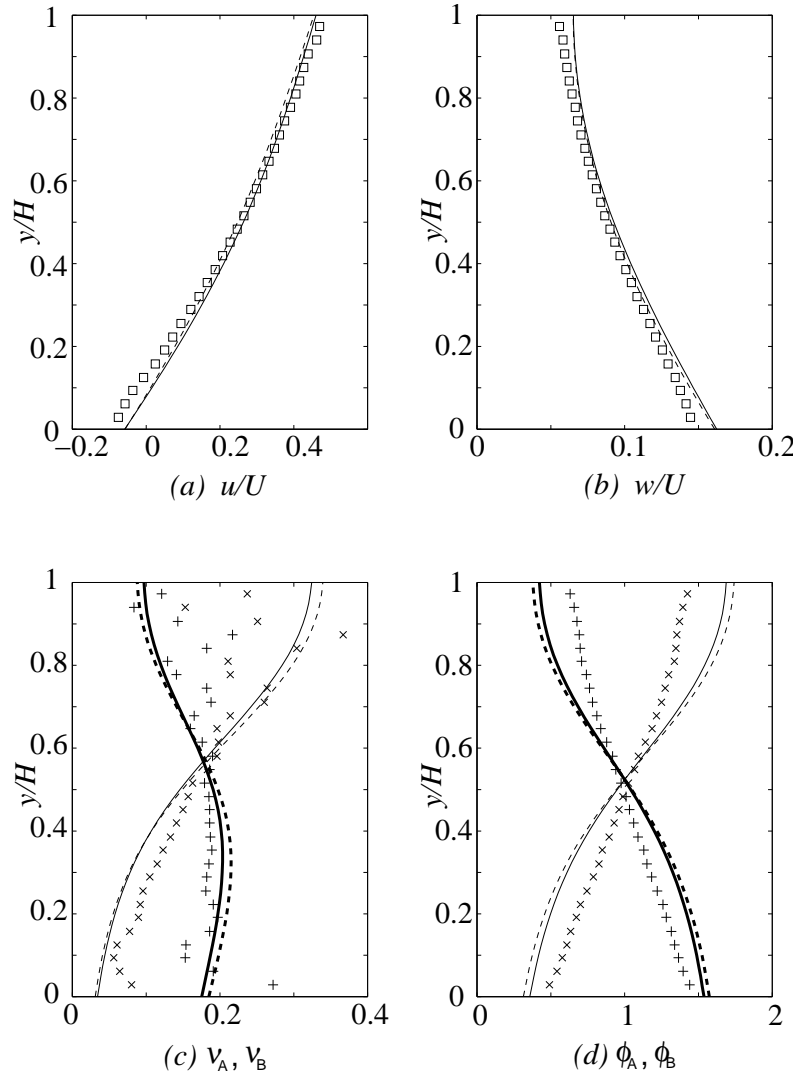


Figure 3.8: Flow of a binary mixture of grains with the same size, but different material densities in a Couette cell without flat side wall and with bumpy boundaries moving in opposite directions. (a) Mixture velocity u/U , (b) mixture fluctuation velocity w/U , (c) volume fraction of each species, (d) relative number fraction of each species. Symbols are simulation results. Solid and dashed lines are solutions of the exact and simplified theory, respectively. In (c) and (d), pluses and thick lines are for species A , while crosses and thin lines are for species B .

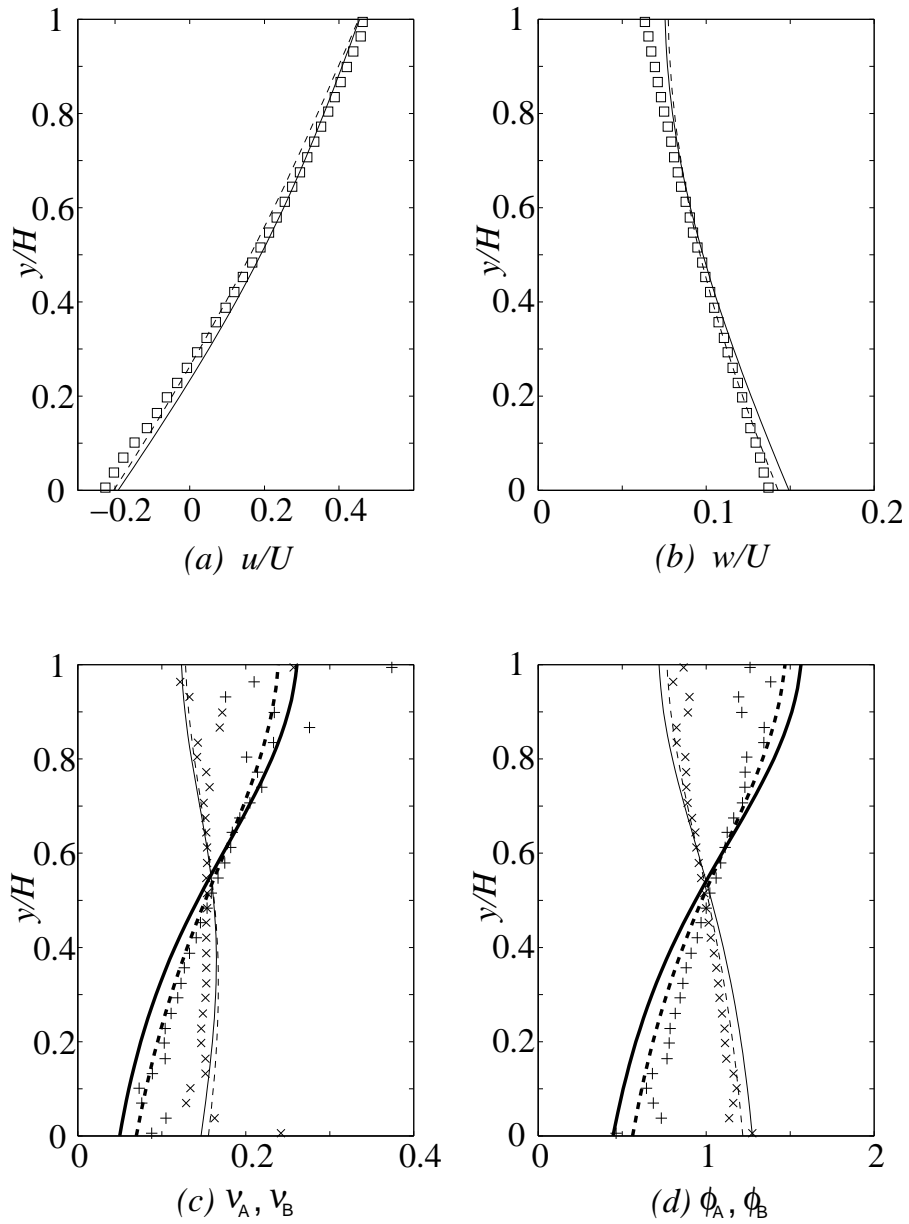


Figure 3.9: Flow of a binary granular mixture with the same material density, but different sizes. See Figure 3.8 for cell geometry and impact properties. Parameters: $\rho_A = \rho_B$, $r_A = 1$, $r_B = 0.8$, $\bar{v} = 0.308$, $\bar{n}_A/\bar{n} = 0.339$.

“no-segregation” with theoretical predictions and numerical simulations.

In the three examples above, the simplified theory predicted well the mixture mean and fluctuation velocities and the extent to which the two species segregate. Surprisingly, although the simplified theory is a first order perturbation of the exact theory, it performed better than its exact counterpart in some cases. This paradox is probably due to the crude treatment of the mixture boundary conditions that we introduced in the exact theory. In fact, the assumptions that permit us to evaluate S^A/P^A , S^B/P^B , P^A/P and P^B/P in Eq. (3.53) might fail for two reasons. First, the contribution of each species to Eq. (2.84) may be affected by the presence of another species. Second, because spheres near a solid boundary arrange in layers with a wavelength on the order of their individual diameter, their pair distribution function at contact may not be captured by Eq. (3.40), and thus the differences in the mixture pressure and the species partial pressures between the boundary and the interior may be affected. Therefore, inaccuracies in the boundary conditions of the exact theory may lead to errors in the predicted velocity and temperature profiles, which in turn induce errors in species concentration. Conversely, our use of boundary conditions for a single constituent in the simplified theory is consistent with our approximation of an equivalent single species. This consistency may help the simplified theory yield better predictions for velocity and temperature.

Segregation with distant boundaries

When a granular material consists of two different species, it is *de facto* impossible to create a uniform simple shear flow in which particle segregation exists. Thus, segregation is inextricably tied to the presence of solid boundaries. In this case, the accuracy of theoretical predictions for the segregation depends upon the accuracy

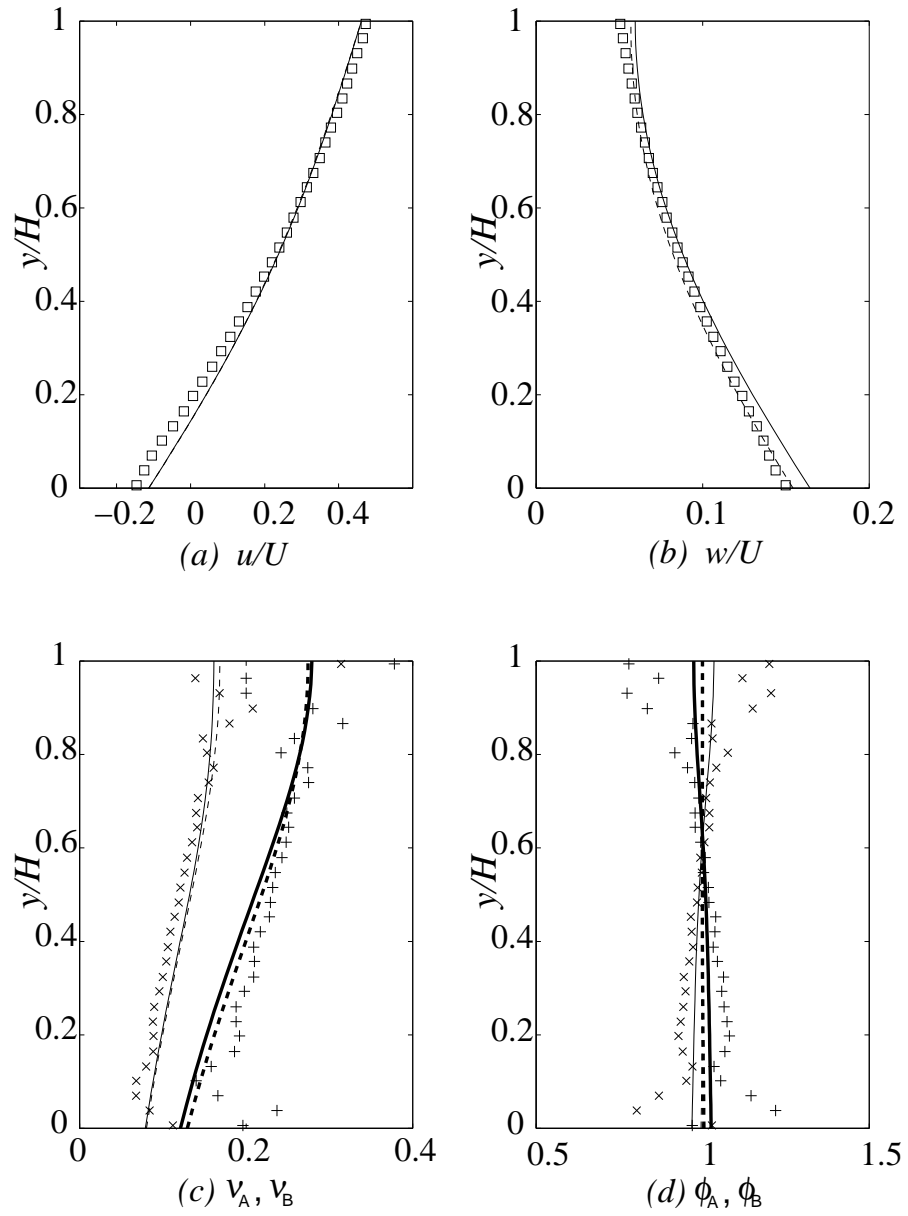


Figure 3.10: Flow of a binary granular mixture exhibiting no segregation. See Figure 3.8 for cell geometry and impact properties. Parameters: $\rho_A/\rho_B = 0.5842$, $r_A = 1.02$, $r_B = 0.8$, $\bar{\nu} = 0.344$, $\bar{n}_A/\bar{n} = 0.442$.

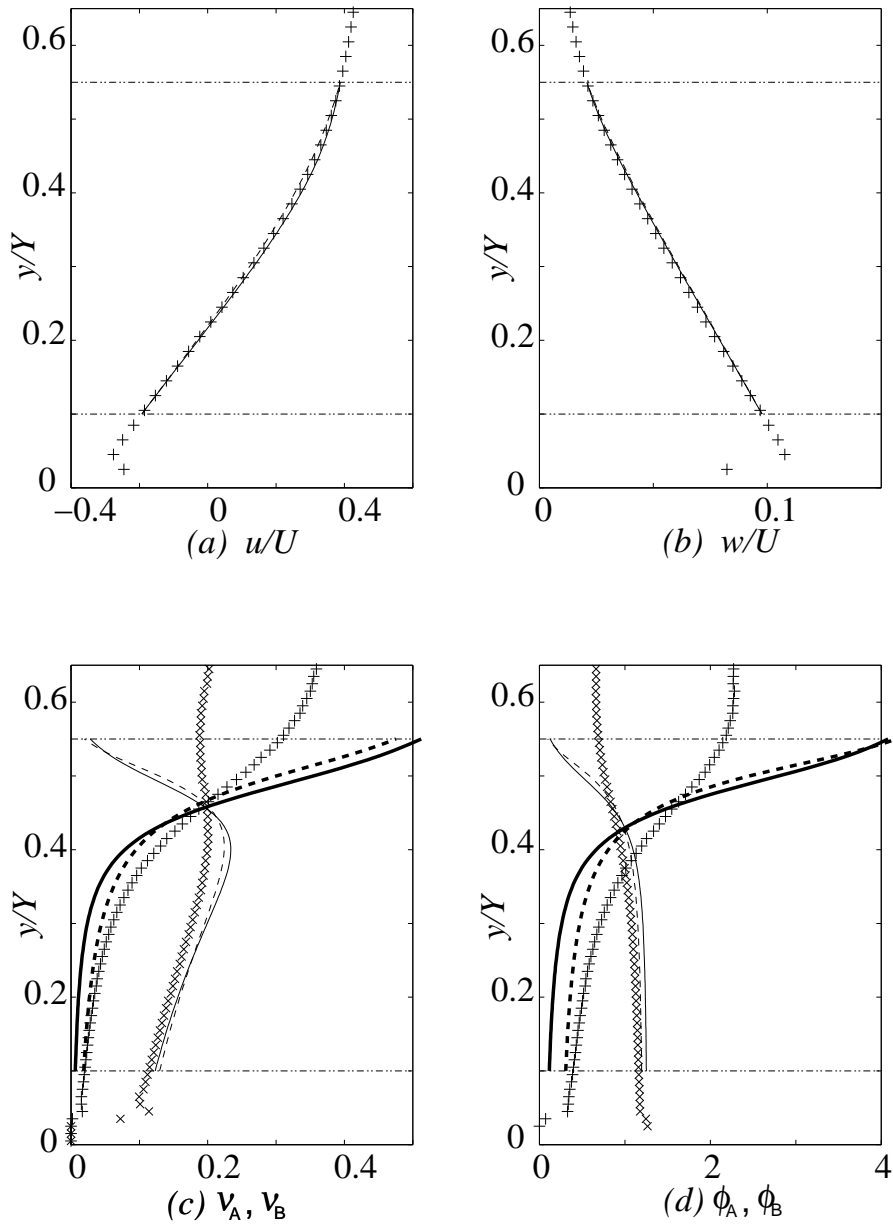


Figure 3.11: Flow of a granular mixture in a wide cell with $Y/r_{AB} = 25$. See Figure 3.8 for other dimensions and impact properties. The interior region in the range $0.1 \leq y/Y \leq 0.55$ has $\bar{\nu} = 0.28$ and $\bar{\nu}_A = 0.11$.

of the boundary conditions. Thus, in the relatively narrow cell used in Figs. 3.8 and 3.9, it is difficult to distinguish the role of the boundary conditions and that of the segregation theory in producing good agreement with the data.

To gauge the accuracy of the theory without undue influence from boundary conditions, we then resorted to considering the granular flow in a wide cell of $Y/r_{AB} = 25$ and without side walls. We employed the same granular mixture as in Figure 3.9. At steady state, we focused upon an interior region with $0.1 \leq y/Y \leq 0.55$, where we compared simulations and theory. Rather than enforcing boundary conditions at the moving bumpy walls, we set the values of u and T measured in the simulations at $y/Y = 0.1$ and 0.55 . As Figure 3.11 shows, the mean and fluctuation velocities from the exact and simplified theories agree almost perfectly with simulation data, but the particle number fractions do not. Although the simplified theory gives a slightly better solution than its exact counterpart, both theories overestimate segregation effects, particularly in the dense region. There, it is possible that the segregation is frustrated by a steric hindrance, in which individual spheres are compelled to remain locked in a cage formed by their nearest neighbors [24].

Segregation in an axisymmetric Couette cell

Our last example is a prelude to physical experiments. Here, we consider the flow of a binary mixture in a Couette cell with flat side walls. We account for the shear stress on the latter by integrating the governing equations. in the same way as we did for flows of a single constituent in Section 3.1. Because the presence of a centripetal acceleration ensures that the pressure is not a constant in the radial direction, we replace the gravitational acceleration g in Eqs. (3.37) and (3.63) by

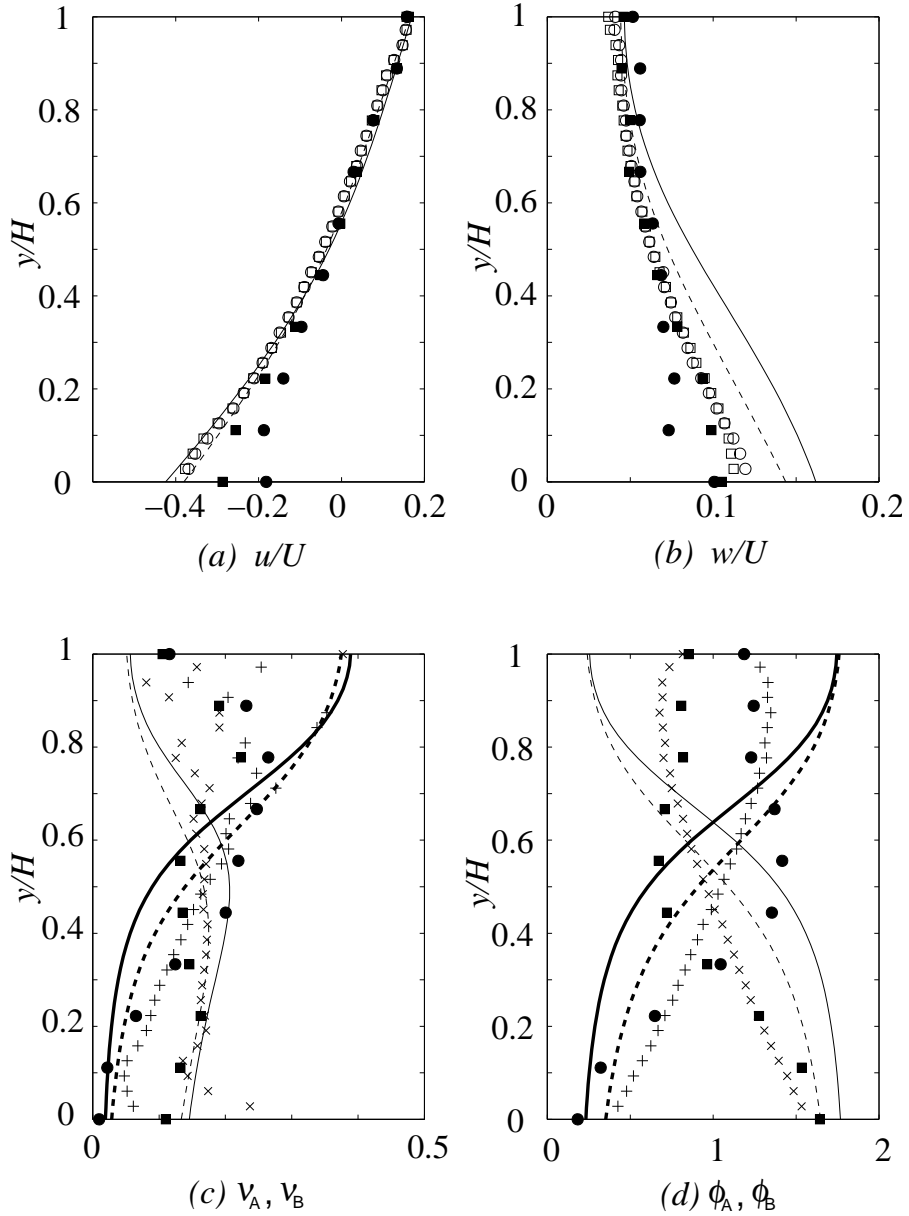


Figure 3.12: Flow of a binary granular mixture in an axisymmetric Couette cell. The inner and the outer bumpy boundaries are moving at $0.2U$ and $-0.8U$, respectively, and the two flat side walls are stationary. Solid symbols are experimental data. In (a) and (b), open symbols are simulation results; squares and circles represent species A and B , respectively. For pluses, crosses and lines, see Figure 3.8.

the centripetal acceleration u^2/r . Figure 3.12 compares theoretical solutions with simulation and experimental data. Species A is ceramic spheres. Species B is nitinol spheres. Parameters are: $R_i = 209mm$, $R_o = 226.2mm$, $Z = 19.39mm$, $\rho_A = 3.92g/cm^3$, $\rho_B = 6.71g/cm^3$, $\rho_A/\rho_B = 0.5842$, $r_A = r_B = 1mm$, $d_0 = d_1 = 2mm$, $s_0 = 0$, $s_1 = 1mm$, $\bar{v} = 0.30$, $\bar{n}_A/\bar{n} = 0.5$. Impact parameters of flowing spheres: $e_{AA} = 0.98$, $e_{AB} = 0.88$, $e_{BB} = 0.92$, $\mu_{AA} = 0.1$, $\mu_{AB} = 0.16$, $\mu_{BB} = 0.22$, $\beta_{0,AA} = 0.42$, $\beta_{0,AB} = 0.25$, $\beta_{0,BB} = 0.25$; between spheres and bumpy boundaries and between spheres and the rear side wall: $e_{wA} = 0.684$, $\mu_{wA} = 0.175$, $\beta_{0w,A} = 0.2$, $e_{wB} = 0.86$, $\mu_{wB} = 0.15$, $\beta_{0w,B} = 0.68$; and between spheres and the front side wall: $e_{sA} = 0.96$, $\mu_{sA} = 0.09$, $\beta_{0s,A} = 0.15$, $e_{sB} = 0.995$, $\mu_{sB} = 0.109$, $\beta_{0s,B} = 0.85$. The reasonable agreement of theory and simulation suggests that collisional flows of binary mixtures are captured by theory as long as the interactions among particles are collisional.

3.3 Conclusion

In this chapter, we provided numerical solutions of the kinetic theory for collisional flows of a single species or binary mixtures of spheres that exhibit relatively small collisional energy dissipation. We summarized the form of the boundary conditions, which others derived by considering the momentum and energy exchanged in collisions between flowing particles and the boundary. We compared the numerical solutions with molecular dynamic simulations and physical experiments in microgravity.

For flows of a single species, we found that the kinetic theory agrees well with both simulation and experiments. For flows of binary mixtures, solutions for the mean and fluctuation velocities were also consistent with simulation results and

experimental data, but the kinetic theory overestimated the segregation, especially at high particle volume fraction. In dense flows, the theory should thus be improved by accounting for velocity correlations in successive collisions and by considering the role of particle “cages” in frustrating diffusive transport.

Our calculations emphasized the importance of boundary conditions in ensuring the success of the kinetic theory for bounded collisional granular flows. Because boundary conditions for a single species have contributed to the accuracy of the theoretical predictions, we recommend that similar conditions be derived for binary mixtures to avoid using expressions meant for a single species in flows of several constituents.

Finally, we focused on flows of nearly elastic, nearly frictionless grains. Although theories have been proposed for more dissipative particles, they have not yet been tested in sheared, bounded geometries. With greater inelasticity or friction, the fluctuation energy becomes strongly anisotropic, and it is not distributed equally among different granular species. In practical flows, collisional dissipation also creates regions where the grains condense into amorphous assemblies or clusters. In these regions, the stresses develop a component that is not rate-dependent [17]. A challenge for future research is to produce a theory that can successfully reconcile the collisional flows considered in this paper and flows where rate-dependent and rate-independent stresses coexist.

Chapter 4

Flow of Collisional Grains in a Viscous Gas

In this chapter, we consider the effects of a viscous gas on flows of colliding grains. The presence of an interstitial fluid is inevitable in most realistic situations. Moreover, the ability to transport particulate materials predictably and efficiently using a flowing gas is playing an important role in a number of applications from the chemical, mining, power and oil industries.

The role of collisional interactions in gas-solid flows has received wide attention, whether the suspensions are laminar [113] or turbulent [82, 28, 11, 116]. In these flows, collisions can transfer a significant amount of momentum, which helps maintain homogeneity and may prevent the formation of clusters.

To understand the interaction between collisional grains and an interstitial viscous gas, we focus attention on flows in which the particle velocity distribution is determined by granular collisions, so we can use the kinetic theory to describe the momentum and energy transfer in the particle phase. In this case, the viscous gas contributes a drag force to the mean granular flow and a viscous dissipation to the particle fluctuation energy, but it hardly affects the character of the particle velocity distribution function.

“Rapid granular flows” can be regarded as an extreme limit of this regime. In rapid flows, particles only experience collisional interactions, their inertia overwhelms the momentum transfer in the granular phase, and the presence of the gas does not affect their motion. In this case, the approach described in previous chapters is suitable. However, as the particle inertia decreases, hydrodynamic

interactions between particles and gas progressively cause the particle velocity distribution to deviate from the expressions derived for colliding particles alone. Therefore at some point, the kinetic theory itself must take into account gas-particle interactions.

Several researchers have studied sheared gas-particle suspensions in which the viscous dissipation plays a role in the balance of granular fluctuation energy [107, 67, 135]. They all considered homogeneous, unbounded flows. However, physical experiments cannot be carried out in a boundless domain. Moreover, to remain suitably agitated, solids must be relatively close to boundaries. Our experience further indicates that boundary interactions are crucial to the balance of momentum and particle fluctuation energy of rapid granular flows. Therefore, a successful description of particulate flows must incorporate proper boundary conditions.

We begin this chapter with an outline of the governing equations for both the gas and solid phases. We then consider shear flows of gas-particle suspensions bounded by solid walls. Our theory reduces to the kinetic theory for collisional granular flows in the limit of large particle inertia. We show that its predictions agree with the recent Lattice-Boltzmann simulations of Verberg and Koch [123] in an intermediate regime where the gas begins to affect granular motion. The simulations also reveal at which point the forces exerted by the gas are too important for the kinetic theory to succeed without taking proper account of the gas in the velocity distribution of the grains.

4.1 Governing Equations

If the particle velocity distribution is determined by collisions alone, the constitutive relations of the granular phase are given by the kinetic theory. In this case,

the conservation laws for the mass, momentum and particle fluctuation energy of the solid phase are similar to Eqs. (3.1)-(3.3),

$$\frac{\partial \rho}{\partial t} + \nabla \cdot (\rho \mathbf{u}_s) = 0, \quad (4.1)$$

$$\rho \frac{\partial \mathbf{u}_s}{\partial t} + \rho \mathbf{u}_s \cdot \nabla \mathbf{u}_s = \nabla \cdot \mathbb{T}_s + \rho \mathbf{f}_s - \nu \nabla P_g + \beta (\mathbf{u}_g - \mathbf{u}_s), \quad (4.2)$$

$$\frac{3}{2} \rho \frac{\partial T}{\partial t} + \frac{3}{2} \rho \mathbf{u}_s \cdot \nabla T = -\nabla \cdot \mathbf{q} + \mathbb{T}_s : \nabla \mathbf{u}_s - \gamma_{inelas} - \gamma_{vis} + \gamma_{rel}, \quad (4.3)$$

where ν is particle volume fraction, $\rho = \nu \rho_s$ is the bulk density of the solid phase, \mathbf{u}_s is the mean particle velocity, \mathbf{f}_s is the body force on the solid phase, and T is the granular temperature defined in previous chapters. In Eqs. (4.2) and (4.3), \mathbb{T}_s is the solid phase stress tensor, P_g is the gas phase pressure, \mathbf{u}_g is the mean gas velocity, $\beta \equiv 18\mu_g\nu(1-\nu)^2 R_{drag}(\nu)/\sigma^2$ is the drag coefficient, $R_{drag}(\nu)$ is a function of ν that we will discuss later, σ is the grain diameter, \mathbf{q} is the flux of particle fluctuation energy, and γ_{inelas} is the collisional dissipation rate of particle fluctuation energy; γ_{vis} is the additional dissipation of particle fluctuation energy due to the viscous gas, and γ_{rel} is the production of particle fluctuation energy due to the mean relative motion between the gas phase and particle phases.

In this work, we consider flows of colliding grains with large particle inertia so that the particle velocity distribution is determined by collisions. In this case, the flux of particle fluctuation energy \mathbf{q} and the collisional dissipation rate γ_{inelas} are those derived using the kinetic theory; the expressions are given in (3.5) and (3.10), respectively.

Sangani *et al* [107] determined the viscous dissipation of particle fluctuation energy in random flights of particles between collisions. They considered simple shear flows in which the particle Reynolds number is vanishingly small but the particle Stokes number is large enough to maintain a Maxwellian velocity distri-

bution. They define the particle Reynolds number as $\rho_g \Gamma \sigma^2 / 4\mu_g$ and the Stokes number as $\Gamma \tau_v$, where ρ_g is the gas density, Γ is the shear rate, and $\tau_v = \rho_s \sigma^2 / 18\mu_g$ is the viscous relaxation time of the particle velocity. They showed that the viscous dissipation can be expressed as

$$\gamma_{vis} = 54\mu_g T \frac{\nu}{\sigma^2} R_{diss},$$

in which R_{diss} is a dimensionless coefficient that depends on the particle volume fraction ν and a dimensionless lubrication cut-off parameter ε_m , which takes into account the non-continuum breakdown of the lubrication force in the Stokes equation when the gap between two particles is comparable to the mean free path of gas molecules. Sundararajakumar and Koch [118] studied the non-continuum flow of the gas in the gap between two spheres approaching one another. By comparing the total energy dissipated during the approaching, they showed that the lubrication cut-off ε_m is related to the molecular mean free path of the gas as

$$\varepsilon_m = 9.76 \frac{\lambda_g}{\sigma}, \quad (4.4)$$

where λ_g is the mean free path of gas molecules. Hence $\varepsilon_m \sigma = 9.76 \lambda_g$ can be regarded as a length scale to characterize the non-continuum effects on lubrication flow.

The gas compressibility can also affect R_{diss} when the gap separating two spheres is less than

$$h_c \equiv \sqrt{\mu_g \sigma \sqrt{T} / P_g}, \quad (4.5)$$

where P_g is the absolute pressure of the gas and \sqrt{T} represents an estimate of the relative velocity between spheres about to collide [39]. Because R_{diss} is dominated by contributions from gaps exceeding $\varepsilon_m \sigma$, this suggests that, as far as viscous dissipation is concerned, compressibility is negligible when $h_c < \varepsilon_m \sigma$. Because this

condition is satisfied in our projected microgravity experiments, we neglect the contributions of gas compressibility to R_{diss} . In the simulations of Verberg and Koch [123] that we discuss later in this chapter, gas compressibility is *de facto* ignored by the Lattice-Boltzmann method.

Grain elasticity can also affect R_{diss} when lubrication forces induce deformations in the solid. Davis, Serayssol & Hinch [30] and Davis [29] showed that the effect is significant when the gap is less than

$$h_d \sim \left(\frac{\sqrt{2}\mu_g\sigma^{3/2}\sqrt{T}}{\pi E^*} \right)^{2/5}, \quad (4.6)$$

where $E^* \equiv E/2(1-\nu_p^2)$ combines Poisson's ratio ν_p and Young's modulus E . Once again, this effect is negligible in our projected microgravity experiments. Because the simulations of Verberg and Koch [123] involve rigid elastic spheres, we also ignore solid elasticity in this chapter.

Sangani *et al* [107] used multipole simulation to determine $R_{diss}(\nu; Re = 0)$. They assumed that the force remains constant when the gap is less than $\varepsilon_m\sigma$. Wylie, Koch & Ladd [135] showed that R_{diss} also depends on fluid inertia and increases with Reynolds number based on the particle fluctuation velocity. Recently, using Lattice-Boltzmann simulations, Verberg & Koch [123] studied viscous dissipation of particle fluctuation energy in simple shear flows with finite Reynolds numbers. They found that the viscous dissipation increases linearly with Reynolds number. Their results can be fitted as

$$R_{diss} = R_{diss,0} + K(\nu)Re_T, \quad (0 \leq Re_T \leq 40, 0.1 \leq \nu \leq 0.4) \quad (4.7)$$

where the Reynolds number is defined as

$$Re_T \equiv \frac{\rho_g\sigma T^{1/2}}{\mu_g},$$

if $Re_T \leq Re_{T,0}$,

$$R_{diss,0} = R_{diss,s} = 1 + \frac{3}{\sqrt{2}}\nu^{1/2} + \frac{135}{64}\nu \ln \nu + 7.4221\nu + G(\nu) \ln(1/\varepsilon_m),$$

$$K(\nu) = K_s(\nu) = \nu(3.1490 - 8.5426\nu + 24.9271\nu^2),$$

and if $Re_T > Re_{T,0}$,

$$R_{diss,0} = R_{diss,l} = 1 + \frac{3}{\sqrt{2}}\nu^{1/2} + \frac{135}{64}\nu \ln \nu + 14.7569\nu + G(\nu) \ln(1/\varepsilon_m),$$

$$K(\nu) = K_l(\nu) = \nu(2.2423 - 7.1515\nu + 19.9250\nu^2),$$

in which $Re_{T,0}$ represents a transition from an initially rapid increase of R_{diss} with Re_T to a slower increase. $Re_{T,0}$ depends on volume fraction ν and is given by

$$Re_{T,0} = \frac{R_{diss,l} - R_{diss,s}}{K_s - K_l},$$

and the function $G(\nu)$ is defined in Chapter 3. In the expressions above, the term $G(\nu) \ln(1/\varepsilon_m)$ comes from the dissipation due to lubrication forces in particle-particle collisions. $G(\nu)$ is proportional to the collision frequency and $\ln(1/\varepsilon_m)$ characterizes the dissipation of particle kinetic energy due to the non-continuum lubrication force during each collision. The dependence of R_{diss} on Re_T is analogous to the increase of drag with Reynolds number in a fixed bed, as captured in the Ergun equation [32]. As Figure 4.1 shows, Eq. (4.7) lies within $\pm 6\%$ of the Lattice-Boltzmann simulation data by Verberg & Koch [123] over the range of $0 \leq Re_T \leq 40$ and the error is less than 5% for most of the data.

Koch & Sangani [67] also considered flows where there is a relative mean velocity between the gas and solids. In this case, the relative velocity produces additional particle agitation. The production rate can be expressed as

$$\gamma_{rel} = \frac{162\mu_g^2\nu(1-\nu)^2}{\rho_s\sigma^3\sqrt{T}} S^*(\nu)(\mathbf{u}_g - \mathbf{u}_s) \cdot (\mathbf{u}_g - \mathbf{u}_s), \quad (4.8)$$

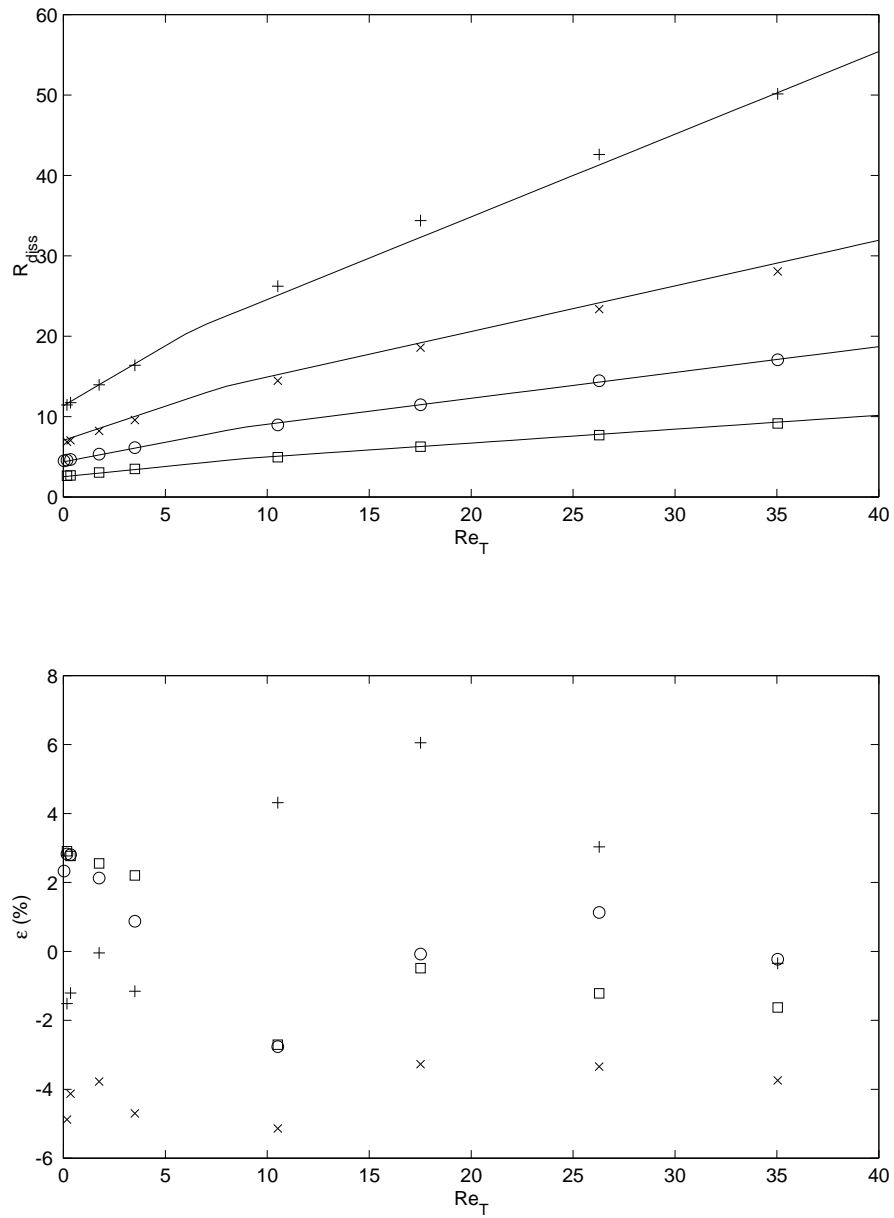


Figure 4.1: Change of R_{diss} with Re_T . The symbols are Lattice-Boltzmann data by Verberg & Koch [123]. Squares: $\nu = 0.1$, circles: $\nu = 0.2$, crosses: $\nu = 0.3$, pluses: $\nu = 0.4$. Lines are curve fits of Eq. (4.7).

where

$$S^*(\nu) = \frac{\nu}{2\sqrt{\pi}G(\nu)(1 + 3.5\nu^{1/2} + 5.9\nu)} R_{drag}^2, \quad (4.9)$$

and R_{drag} is a function of ν measured in the numerical simulations. According to Koch & Sangani [67], the following expression agrees well with numerical simulations for $0 < \nu < 0.4$,

$$R_{drag} = \frac{1 + 3(\nu/2)^{1/2} + \frac{135}{64}\nu \ln \nu + 17.14\nu}{1 + 0.681\nu - 8.48\nu^2 + 8.16\nu^3}. \quad (4.10)$$

For $\nu \geq 0.4$, they suggest the empirical correlation of Carman [21]

$$R_{drag} = \frac{10\nu}{(1 - \nu)^3} + 0.7, \quad (4.11)$$

where the constant 0.7 is added to match the two equations (4.10) and (4.11) for R_{drag} at $\nu = 0.4$.

Conservation of mass and momentum for the gas phase requires

$$\frac{\partial(1 - \nu)\rho_g}{\partial t} + \nabla \cdot ((1 - \nu)\rho_g \mathbf{u}_g) = 0, \quad (4.12)$$

$$(1 - \nu)\rho_g \left(\frac{\partial \mathbf{u}_g}{\partial t} + \mathbf{u}_g \cdot \nabla \mathbf{u}_g \right) = \nabla \cdot \mathbb{T}_g - (1 - \nu)\nabla P_g + (1 - \nu)\rho_g \mathbf{f}_g - \beta(\mathbf{u}_g - \mathbf{u}_s), \quad (4.13)$$

where \mathbf{f}_g represents the body force on gas phase, and \mathbb{T}_g is the gas phase shear stress tensor.

To close the set of governing equations, we must determine the particle phase stress tensor \mathbb{T}_s and its counterpart \mathbb{T}_g in the gas phase. The particle phase stress includes contributions from particle streaming, particle collisions, and interactions among grains that are exerted through the gas. The first two arise in collisional granular flows without an interstitial fluid. They constitute the usual granular stress \mathbb{T} in Eq. (3.4). For simplicity, we add the contribution of the gas as

$$\mathbb{T}_s = \mathbb{T} + \mathbb{T}_{gs}. \quad (4.14)$$

In principle, the stress tensors \mathbb{T}_{gs} and \mathbb{T}_g should be derived from detailed considerations of gas-particle interactions. Unfortunately, despite the publication of several theories and experiments on the mixture viscosity of particle-fluid systems, the exact form of the stress on each phase is not well understood. Because, in the case of large particle inertia, these stresses will be dominated by the particle phase stress, we merely postulate their form, while ensuring that the latter agrees with existing mixture theories and in the two limits where no gas or no solids are present.

In particular, we assume that the stress on each phase is proportional to its volume fraction,

$$\mathbb{T}_{gs}/\nu = \mathbb{T}_g/(1 - \nu), \quad (4.15)$$

and we adopt the mixture theory of Happel and Brenner [42], even though it was derived for flows at low Reynolds and Stokes numbers,

$$\mathbb{T}_{gs} + \mathbb{T}_g = R_\mu(\nu)\mu_g \left[(\nabla \mathbf{u}_g) + (\nabla \mathbf{u}_g)^T - \frac{2}{3}(\nabla \cdot \mathbf{u}_g)\mathbf{I} \right], \quad (4.16)$$

where μ_g is the molecular viscosity of the gas, \mathbf{u}_g is the mean gas velocity, and $R_\mu(\nu)$ is the ratio of the suspension viscosity to μ_g . According to Happel & Brenner [42], the expression

$$R_\mu(\nu) = \exp(4.58\nu) \quad (4.17)$$

fits experimental data well in the moderate range of particle volume fraction $\nu \lesssim 0.4$ that is of interest here.

Our choices of \mathbb{T}_g and \mathbb{T}_{gs} are arbitrary. However, their role is small in the gas-particle systems under consideration. In fact, as Verberg's simulations will reveal [123], the particle phase stress is always much larger than either \mathbb{T}_g or \mathbb{T}_{gs} . In order to test the expressions of \mathbb{T}_{gs} and \mathbb{T}_g that we have proposed, one should

attempt to create different shear rates in the gas and particle phase over a distance larger than a particle diameter.

As Hwang & Shen [48] showed, there remains a disagreement as to the form of the constitutive equations for two-phase flows, particularly whether the volume fraction should lie inside the differentiation of the stress term for the gas phase, and how the volume fraction should appear in the pressure gradient term. For our part, we adopt Eqs. (4.1) – eqrefeq:granphaseEnergy and Eqs. (4.12) – (4.13). In these equations, we neglect the added mass effect, the history force, and other forces that are proportional to the gas inertia.

In Eq. (4.2), note that, unlike their counterpart in the solid phase, the stress tensors \mathbb{T}_g and \mathbb{T}_{gs} in the gas are written in deviatoric form. This is consistent with the common practice that the thermodynamic pressure gradient appears as a separate term in the Navier-Stokes equations. However, in the granular phase, such convention is not always adopted (see, for example, our chapter 3), so the gradient of the particle normal stress does not appear alone in the momentum equation.

Finally, note that, as $\nu \rightarrow 0$, the momentum of the solid phase, Eq. (4.2) appropriately tends to zero, while its gas counterpart Eq. (4.13) reduces to the Navier-Stokes equations. Similarly, if the flow is fully-developed, or the flow Reynolds number is low, or the gas and solid velocities are equal, the sum of the two momentum balances in the gas and solid phases produces a mixture equation in which the stress tensors feature a bulk viscosity consistent with the mixture expression of Happel & Brenner [42].

4.2 Bounded Shear Flows

4.2.1 One-Dimensional Rectilinear Flow

We first consider fully developed flows of collisional grains in a viscous gas sheared between two parallel bumpy boundaries. The flow is unbounded in the vorticity direction and its variables only change along the direction perpendicular to the boundaries.

In this case, the mass conservation of both phases is satisfied automatically, and the solid momentum balance in the flow direction reduces to

$$\frac{d}{dy} \left(\eta \frac{du_s}{dy} + \nu R_\mu \mu_g \frac{du_g}{dy} \right) + \beta(u_g - u_s) - \nu \frac{dP_g}{dx} = 0, \quad (4.18)$$

where η is the shear viscosity of the solid phase and u_s and u_g are, respectively, the mean solid and gas velocity in the x -direction along the flow. The solid momentum balance in the z -direction vanishes and the y -direction momentum balance requires $P_s = \text{const.}$

For the gas phase, we have

$$\frac{d}{dy} \left((1 - \nu) R_\mu \mu_g \frac{du_g}{dy} \right) - \beta(u_g - u_s) - (1 - \nu) \frac{dP_g}{dx} = 0. \quad (4.19)$$

The particle fluctuation energy balance simplifies to

$$\frac{d}{dy} \left(\kappa \frac{dT}{dy} \right) + \eta \left(\frac{du_s}{dy} \right)^2 + \nu R_\mu \mu_g \frac{du_g}{dy} \frac{du_s}{dy} - \gamma_{inelas} - \gamma_{vis} + \gamma_{rel} = 0, \quad (4.20)$$

where κ is the thermal conductivity of the granular phase.

Boundary conditions for the mean velocity and for the fluctuation energy of the grains were derived in Chapter 2. In the kinetic theory, the particle phase boundary conditions are applied at a particle radius away from the crests of wall spheres. For simplicity, we solve the gas phase in the same domain as the particle

phase, and thus apply the usual “no-slip” boundary condition for the gas at a particle radius away from the wall spheres. Because our flows have relatively large volume fraction and Stokes number, the actual location where the gas boundary condition is imposed barely affects our flows.

To evaluate the relative importance of each term in the governing equations, we write the latter in dimensionless form. We adopt the following dimensionless variables: $y^* \equiv y/H$, $u_s^* \equiv u_s/U$, $u_g^* \equiv u_g/U$, and $T^* \equiv T/U^2$, where $U \equiv U_t - U_b$ is the relative velocity between the top and bottom bumpy boundaries separated by a distance H . We then define the particle fluctuation velocity as $w^* \equiv \sqrt{T^*}$.

The dimensionless particle phase momentum equation in the flow direction is

$$\begin{aligned} \frac{d^2 u_s^*}{dy^{*2}} + \left(\frac{1}{P_s^*} \frac{dP_s^*}{dy^*} + \frac{1}{J} \frac{dJ}{dy^*} - \frac{1}{F} \frac{dF}{dy^*} - \frac{1}{w^*} \frac{dw^*}{dy^*} \right) \frac{du_s^*}{dy^*} \\ + \frac{5\sqrt{\pi}}{8} \frac{1}{JGw^*} \left[\frac{1}{18(H/\sigma)St} \frac{d}{dy^*} \left(\nu R_\mu \frac{du_g^*}{dy^*} \right) \right. \\ \left. + (1-\nu)^2 \frac{H}{\sigma} \frac{R_{drag}}{St} (u_g^* - u_s^*) + R_\tau \right] = 0, \end{aligned} \quad (4.21)$$

where the Stokes number based on the nominal shear rate U/H

$$St \equiv \frac{\rho_s \sigma^2 U}{18\mu_g H}$$

is a measure of particle inertia relative to visous forces in the fluid and

$$R_\tau \equiv \frac{-\frac{dP_g}{dx}}{\rho_s \sigma \left(\frac{U}{H}\right)^2},$$

is the dimensionless gas pressure gradient.

The gas momentum equation is

$$\begin{aligned} \frac{d^2 u_g^*}{dy^{*2}} + \frac{1}{(1-\nu)R_\mu} \frac{d(1-\nu)R_\mu}{dy^*} \frac{du_g^*}{dy^*} \\ + 18 \frac{H}{\sigma} \frac{1}{R_\mu} \left[\frac{H}{\sigma} \nu (1-\nu) R_{drag} (u_s^* - u_g^*) + R_\tau St \right] = 0. \end{aligned} \quad (4.22)$$

Finally, the solid fluctuation energy balance is

$$\begin{aligned}
& \frac{d^2 w^*}{dy^{*2}} + \left(\frac{1}{P_s^*} \frac{dP_s^*}{dy^*} + \frac{1}{M} \frac{dM}{dy^*} - \frac{1}{F} \frac{dF}{dy^*} \right) \frac{dw^*}{dy^*} \\
& + \frac{\sqrt{\pi}}{16} \frac{1}{MG} \left[\frac{1}{9(H/\sigma)St} \frac{R_\mu}{w^{*2}} \frac{du_g^*}{dy^*} \frac{du_s^*}{dy^*} - 6 \frac{H}{\sigma} \frac{R_{diss}}{St} - (1-\nu)^2 \frac{S^*(u_g^* - u_s^*)^2}{St^2 w^{*3}} \right] \\
& + \frac{1}{M} \left[\frac{J}{5} \left(\frac{1}{w^*} \frac{du_s^*}{dy^*} \right)^2 - 3(1 - e_{eff}) \left(\frac{H}{\sigma} \right)^2 \right] w^* = 0. \tag{4.23}
\end{aligned}$$

In the limit where the particle inertia overwhelms viscous forces in the gas (either by increasing the shear rate or by using more massive particles), the dimensionless numbers tend to values, $St \rightarrow \infty$, $R_{drag}/St \rightarrow 0$, $R_{diss}/St \rightarrow 0$, and $R_\tau \rightarrow 0$, which reduce the governing equations for the granular phase to the form derived in the absence of a gas in chapter 3.

4.2.2 Comparison with Lattice-Boltzmann Simulation

Verberg & Koch [123] recently simulated sheared gas-particle flows between two parallel bumpy boundaries using the Lattice-Boltzmann method [69, 70]. They made the boundaries bumpy by attaching spheres of the same size as in the suspension, as shown in Figure 4.2. They used periodic boundary conditions in both the x - and the z -directions, so that flow variables only change in the y -direction perpendicular to the bumpy boundaries.

In Chapter 2, we derived boundary condition for bumpy boundaries with randomly attached spheres. For the arrangement of spheres shown in Figure 4.2, we can in principle derive the boundary condition by considering the transfer of momentum and energy at the boundary by collisional interactions between wall spheres and flow spheres. However, variations of the maximum penetration angle θ in the azimuthal direction prevent us from finding analytical expressions for the momentum and energy transfer rates at the boundary. In this geometry, the

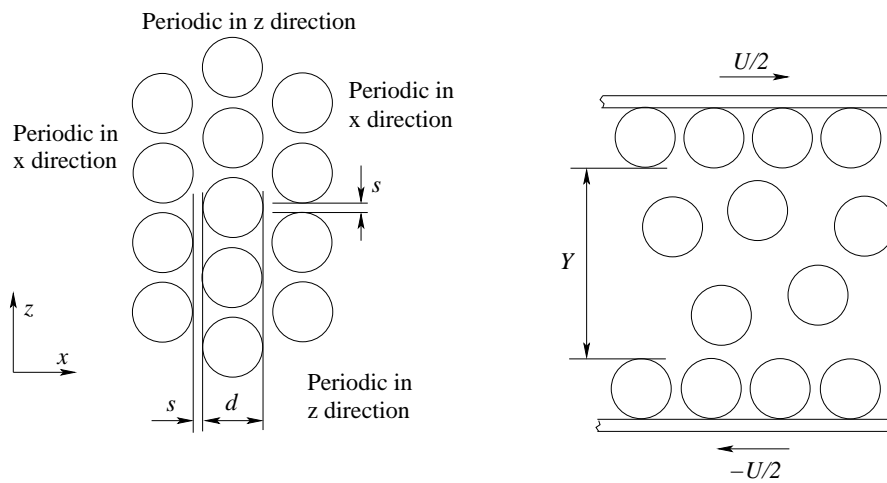


Figure 4.2: Bumpy boundary used in the Lattice-Boltzmann simulation of Verberg & Koch [123]. Boundaries normal to the x - and the z - directions are periodic. In the Lattice-Boltzmann simulations, the boundary spheres have a diameter $d = 5.84$ and the gap separating them is $s = 0.16$, so as to obtain a periodic array with $d + s = 6$ “lattice units”. The flow spheres are of the same size as the boundary particles.

maximum and minimum values of bumpiness are $\sin \theta_{\max} = 5(d + s)/[4(d + \sigma)]$ and $\sin \theta_{\min} = (d + s)/(d + \sigma)$, respectively. Thus, for simplicity, we adopt the arithmetic average $\sin \theta \equiv (\sin \theta_{\max} + \sin \theta_{\min})/2$ to capture the bumpiness of the boundary shown in Figure 4.2. Jenkins [51] instead calculated the average penetration $\bar{\theta}$ by integrating in the circumferential direction. For a tight hexagonal packing of equal sized spheres, which is similar to the boundary that Verberg & Koch [123] implemented in their simulation, Jenkins found $\sin \bar{\theta} = 0.5216$, while the arithmetic average yields 0.5387. To establish whether such uncertainty in the bumpiness might affect the profiles of mean velocities and granular temperature, we solved the governing equations with the two extreme values $\sin \theta_{\min}$ and $\sin \theta_{\max}$. We found negligible sensitivity of the profiles to $\sin \theta$.

In their recent Lattice-Boltzmann simulations, Verberg & Koch [123] defined the Reynolds number as

$$Re' \equiv \frac{\rho_g \sigma^2 U}{4\mu_g Y'}, \quad (4.24)$$

where Y' is the distance between the crest of boundary spheres, and the Stokes number as

$$St' \equiv \frac{\rho_s \sigma^2 U}{18\mu_g Y'}. \quad (4.25)$$

Therefore, for the same system, the Stokes number defined in Eq. (4.25) is slightly smaller than what we defined in the dimensionless equations.

To isolate the effects of the viscous gas on the suspension flow, Verberg & Koch [123] set the coefficient of restitution of spheres to one. Thus, the particle fluctuation energy is only dissipated by viscous forces.

4.2.3 Effects of Stokes number

Figure 4.3 shows profiles of the dimensionless fluctuation velocity $2T^{1/2}/\Gamma\sigma$, where $\Gamma \equiv U/Y'$ is the overall simulation shear rate, for flows at different Stokes numbers St' . Consistent with the predictions of Sangani *et al* [107] for simple shear flows, the granular temperature decreases with St' . However, as the temperature decreases, the solid boundary plays an increasingly important role in providing fluctuation energy to the flow. As a result, the temperature profile gradually exhibits a concave shape that betrays a transfer of fluctuation energy from the boundary to the flow. This effect, which is not present in simple shear flow, is captured by our two-phase flow theory.

The mean velocity profile and the slip velocity at the bumpy boundary are also affected by variations in the Stokes number. The slip velocity is defined as the difference between the velocity of the solid boundary and the mean velocity of flow spheres touching the crest of wall spheres. As Fig. 4.4 shows, the theory predicts a slip velocity greater than that observed in the simulations at high Stokes numbers.

At first sight, this failure may be surprising. Because the LB simulations assumed elastic spheres, $e = 1$, the only dissipation mechanism in the solid phase derives from interactions with the gas. One would expect that as the Stokes number increases, the effects of the gas should become negligible, and thus the gas-particle system would begin to resemble dry collisional granular flows, for which the particle phase boundary conditions were derived. Because the boundary conditions were otherwise successful in dry granular flows, their failure to lead to the proper slip is unexpected.

However, there are two reasons why the slip velocity measured in the LB simulations may not agree with the current theory or with our intuition.

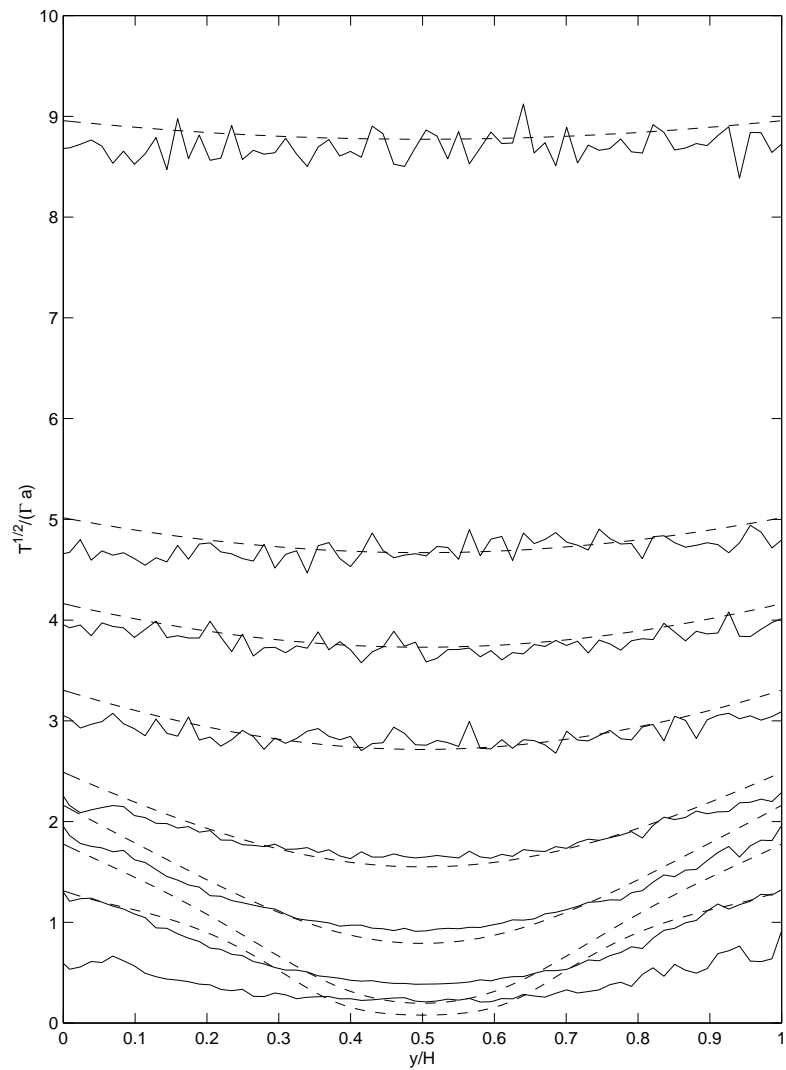


Figure 4.3: Variations of the granular temperature with Stokes number. Solid lines are results from Lattice-Boltzmann simulation [123]. Dashed lines are solutions of the continuum theory. Simulation parameters: $Y'/\sigma = 12$, $Re' = 0.1$, and overall particle volume fraction $\bar{\nu} = 0.3$. From top to bottom: $St' = 100, 50, 40, 30, 20, 15, 10$, and 5 .

First, because the LB simulations increase the Stokes number while maintaining $Re' = 0.1$, they possess a peculiar mechanism for fluctuation energy dissipation, which is not equivalent to that in a granular flows without a gas. In this case, the granular temperature in a simple shear flow is given by

$$\frac{T^{1/2}}{\Gamma\sigma} = \frac{-R_{diss,0} + \sqrt{R_{diss,0}^2 + \frac{128}{15\sqrt{\pi}}GJStKRe}}{8KRe}, \quad (4.26)$$

where $R_{diss,0}$ and K are functions of particle volume fraction defined in Eq. (4.7). Eq. (4.26) indicates that $T^{1/2}/\Gamma\sigma$ increases with $St^{1/2}$ at large St . If this was a dry granular flow, this dissipation mechanism would be associated with a coefficient of restitution such that $1 - e$ decreases with $\Gamma^{-1/2}$. Such dry granular flow might behave differently from one with constant e . We intend to run molecular dynamic simulations to check whether dry granular flows with small dissipation maintain a constant slip as $e \rightarrow 1$.

Note that if, on the other hand, the LB simulations had increased St while keeping the gas-solid density ratio ρ_g/ρ_s constant, then because $Re/St = (9/2)\rho_g/\rho_s$, the granular temperature of the corresponding simple shear flow would scale as

$$\frac{T^{1/2}}{\Gamma\sigma} = \frac{-R_{diss,0}/St + \sqrt{(R_{diss,0}/St)^2 + \frac{192}{5\sqrt{\pi}}GJK(\rho_g/\rho_s)}}{36K(\rho_g/\rho_s)}. \quad (4.27)$$

Then, in this case, the granular temperature would approach a constant as $St \rightarrow \infty$,

$$\frac{T^{1/2}}{\Gamma\sigma} = \sqrt{\frac{16}{135\sqrt{\pi}} \frac{GJ}{K} \frac{\rho_s}{\rho_g}}. \quad (4.28)$$

The dissipation mechanism from the gas would then scale as its counterpart in an inelastic granular system, thus producing an asymptotic slip at high St that resembles the behavior of such system. One could then define an effective coefficient

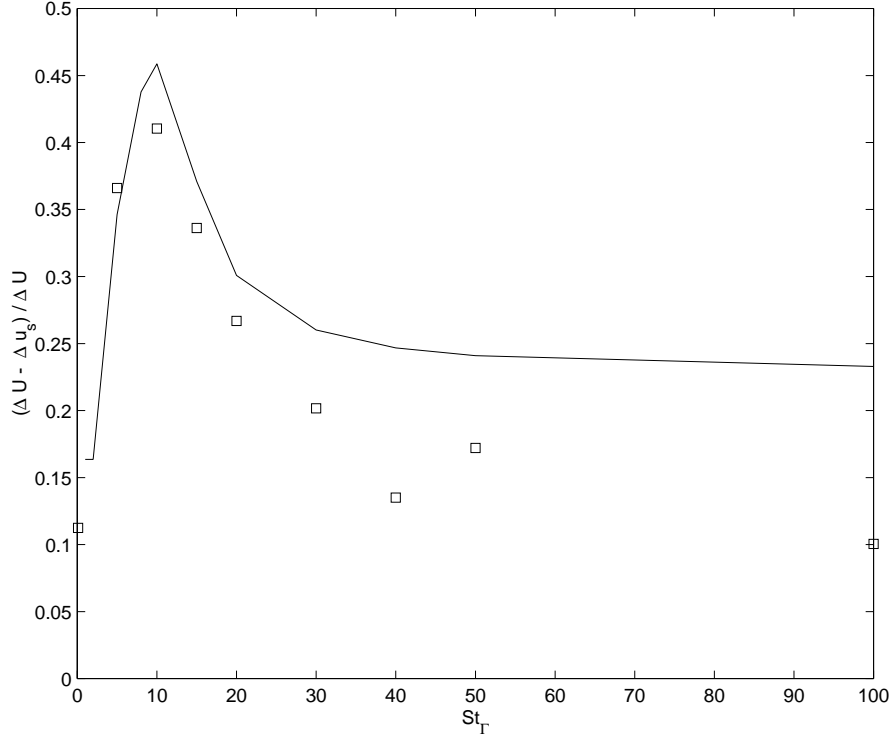


Figure 4.4: Changes in the slip velocity at the solid boundary with Stokes number. Symbols are data from Lattice-Boltzmann simulations [123]. The line is the prediction of the theory.

of restitution $e_{eff,vis}$ to account for the viscous dissipation,

$$e_{eff,vis} = 1 - \frac{9\sqrt{\pi}}{4} \frac{K}{G} \frac{\rho_g}{\rho_s}. \quad (4.29)$$

The second reason why the measured slip at high St may not agree with the theory is that the latter, by adopting $e = 1$, ignores the energy dissipation due to the gas at the boundary. To verify whether the failure of the theory at large St is related to its improper description of energy dissipation at the boundary, we will attempt to capture the gas dissipation with an effective inelastic restitution at the boundary and examine the corresponding variations of the slip with St .

By analyzing simple shear flows of a particle-gas suspension, Sangani *et al* [107] showed that anisotropies in the particle phase pressure become significant when $St/R_{diss} \lesssim 5$, so that an isotropic theory could no longer be used. However, Figure 4.3 indicates that the theory starts to deviate from the simulations at $St' \approx 15$, which corresponds to $St/R_{diss} \approx 2$. As Figure 4.5 shows, the theory gives good predictions of the transverse profiles of mean particle velocity u_s^* , the fluctuation velocity w^* , and the particle volume fraction for St' as low as 20.

Figure 4.6 compares the xy shear stress due to particles, i.e., $\eta du_s/dy$ and the shear stress due to the viscous gas, $R_\mu(\nu)\mu_g du_g/dy$ for $St' = 20$ and $St' = 100$. In the LB simulation, the stress tensors are calculated using the expressions given by Strating [115]. In particular, the particle phase stress is obtained by adding the contributions of particle streaming and particle-particle collisions, which we compare with $\eta du_s/dy$ predicted by the theory. The gas phase stress is found by adding the “viscous” stress arising from momentum transfer due to random molecular motion, and the “particle-fluid” stress acting on particle surfaces that is due to interactions of the particles and the gas. We compare the total gas phase stress thus measured with $R_\mu(\nu)\mu_g du_g/dy$. As expected, the particle phase stress dominates the suspension stress at high Stokes number, and the effect of gas on momentum transfer is negligible. At lower Stokes number, the contribution of the viscous gas to the total shear stress increases, especially in the region near the solid boundary, but it is still small compared to the particle phase shear stress. This relative diminution of the role of the solids might explain why the isotropic Maxwellian theory for the grains still yields a satisfactory prediction despite the low magnitude of the Stokes number.

In Fig. 4.6, the discrepancy near the solid boundary is due to the approximate

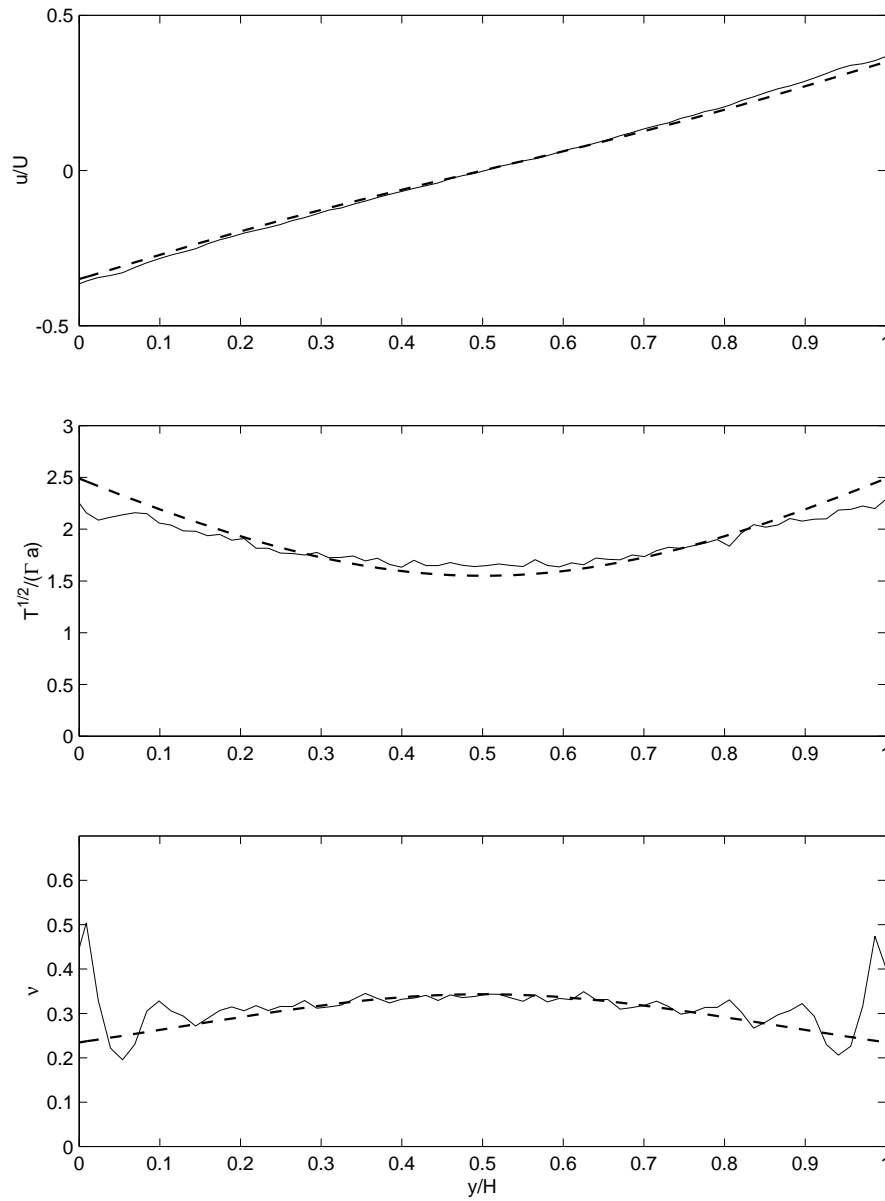


Figure 4.5: Transverse profiles at $St' = 20$ and $Re' = 0.1$. Solid lines are simulation results [123] and dashed lines are predictions of the theory. Top plot: mean particle velocity u_s^* ; middle plot: granular fluctuation velocity, made dimensionless with $\Gamma\sigma/2$; bottom plot: particle volume fraction. For other simulation parameters, see Figure 4.3.

treatment of the “no-slip” boundary condition in gas phase equation. In our current numerical implementation of the theory, we set the “no-slip” boundary condition for the gas at a particle radius away from the crest of the wall spheres, which is where we also enforce boundary conditions for the granular phase. We may obtain better agreement if we implemented a more realistic model for the gas flow in the excluded volume near the solid wall. However, because our flows exhibit relatively high solid volume fraction and Stokes number, the exact location of the boundary for the gas has relatively little effect on the flow profiles.

Effects of Reynolds number

Sangani *et al* [107] considered a simple shear flow in which the fluid inertia is so small that viscous forces and granular elasticity alone determine the granular temperature. In that case, the temperature is a function of the Stokes number and the normal restitution coefficient. However, the Lattice-Boltzmann simulations of Verberg and Koch [123] clearly show that viscous dissipation increases with fluid inertia, and therefore the Reynolds number must also play a role in determining the granular temperature.

Figure 4.7 shows the effects of Reynolds number on granular temperature when the Stokes number is fixed at $St' = 100$ and the spheres are elastic. As Re' increases from 0.1 to 10, the granular temperature decreases to about 1/16 of its original value. The corresponding increase in the wall flux of fluctuation energy causes the suspension to become inhomogeneous.

A comparison of Figures 4.7 and 4.3 indicates that an increase in Re' is nearly equivalent to a decrease in St' . In fact, as Sangani *et al* [107] showed for a simple shear flow of elastic particles in a viscous gas, $T^{1/2}$ is proportional to St/R_{diss} . In

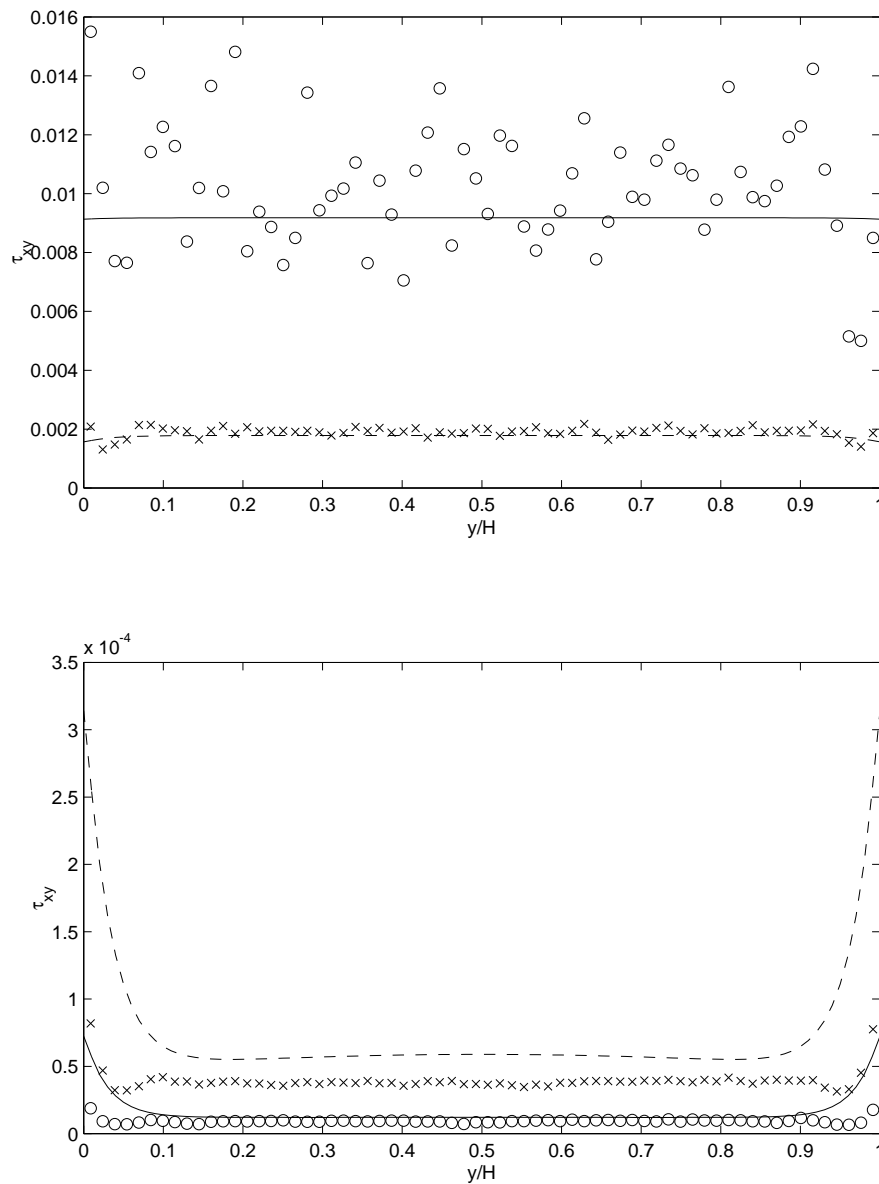


Figure 4.6: Shear stresses at $St' = 20$ and $St' = 100$. Symbols are results of the Lattice-Boltzmann simulations [123] and lines are predictions of the theory. Circles and solid lines: $St' = 100$; crosses and dashed lines: $St' = 20$. Top plot: shear stress in the particle phase, $\eta du_s/dy$; bottom plot: shear stress due to the viscous gas, $R_\mu \mu_g du_g/dy$. All stresses are made dimensionless with $\rho_s U^2$. For other simulation parameters, see Figure 4.3.

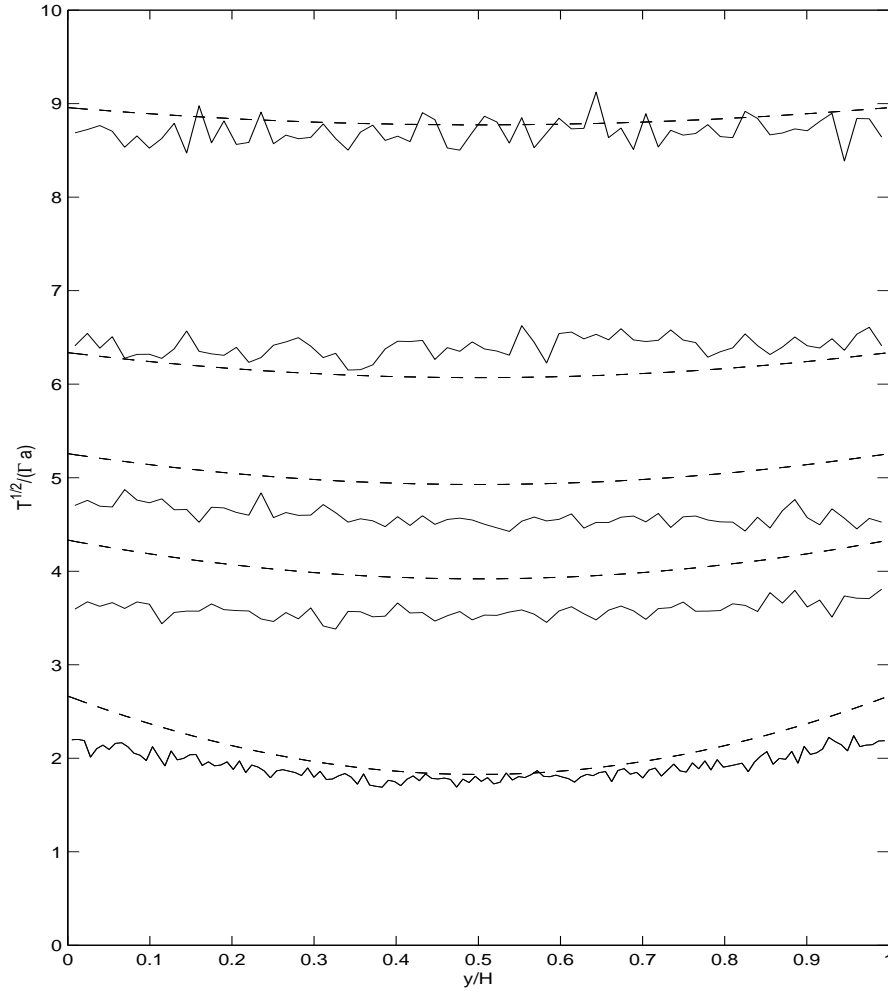


Figure 4.7: Effects of Reynolds number on the granular temperature at a fixed $St' = 100$. Solid lines are simulation results [123], and dashed lines are prediction of the theory. From top to bottom: $Re' = 0.1, 0.5, 1, 2,$ and 10 . The simulation parameters are: $Y'/\sigma = 12$ and $\sigma = 5.84$ lattice units for $Re' = 0.1, 0.5, 1$ and 2 ; $Y'/\sigma = 12$ and $\sigma = 11.68$ lattice units for $Re' = 10$. In general, the simulation accuracy increases with the resolution, i.e., the sphere size in lattice units. The discrepancy between theory and simulation at $Re' = 1$ and $Re' = 2$ may be due to a low resolution in the simulation.

bounded shear flows, the energy balance (4.23) indicates that the dimensionless viscous dissipation term is proportional to R_{diss}/St . Because R_{diss} increases linearly with $Re_T \propto Re'$, a decrease in $St' \propto St$ or an increase in Re' both result in lower values of St/R_{diss} . In turn, this produces an increase of viscous dissipation and a reduction in the granular temperature.

If we assume a simple shear flow, we find that conditions of $St = 20$ and $Re = 0.1$ yield the same granular temperature as $St = 100$ and $Re = 6.3$. This simple equivalence is slightly different in the case of a bounded flow. The principal reason is that there is no longer a simple balance between production and dissipation of granular fluctuation energy. In particular, the boundaries promote inhomogeneities in the flow, and they create a relative velocity between gas and solids in their vicinity. For example, in Figure 4.8, the transverse profiles with $St' = 100$ and $Re' = 10$ are nearly identical to those with $St' = 20$ and $Re' = 0.1$. However, they differ slightly in their overall value of St/R_{diss} , which we calculate using the average particle fluctuation velocity across the flow domain in the LB simulations. They respectively have $St/R_{diss} \approx 3.23$ and 2.72 .

Figure 4.9 compares measured shear stresses for $Re' = 0.1$ and $Re' = 10$ at $St' = 100$ with predictions of the theory for elastic spheres. As Re' increases, the granular temperature decreases and the particle phase shear stress decreases. In the range of Re' under consideration, the particle stress dominates its viscous counterpart. Although the simulation shows that the gas shear stress increases with Reynolds number, the model predicts that it is almost independent of Reynolds number. This discrepancy may reflect our choice of a correlation for $R_\mu(\nu)$ that was derived for low Reynolds numbers.

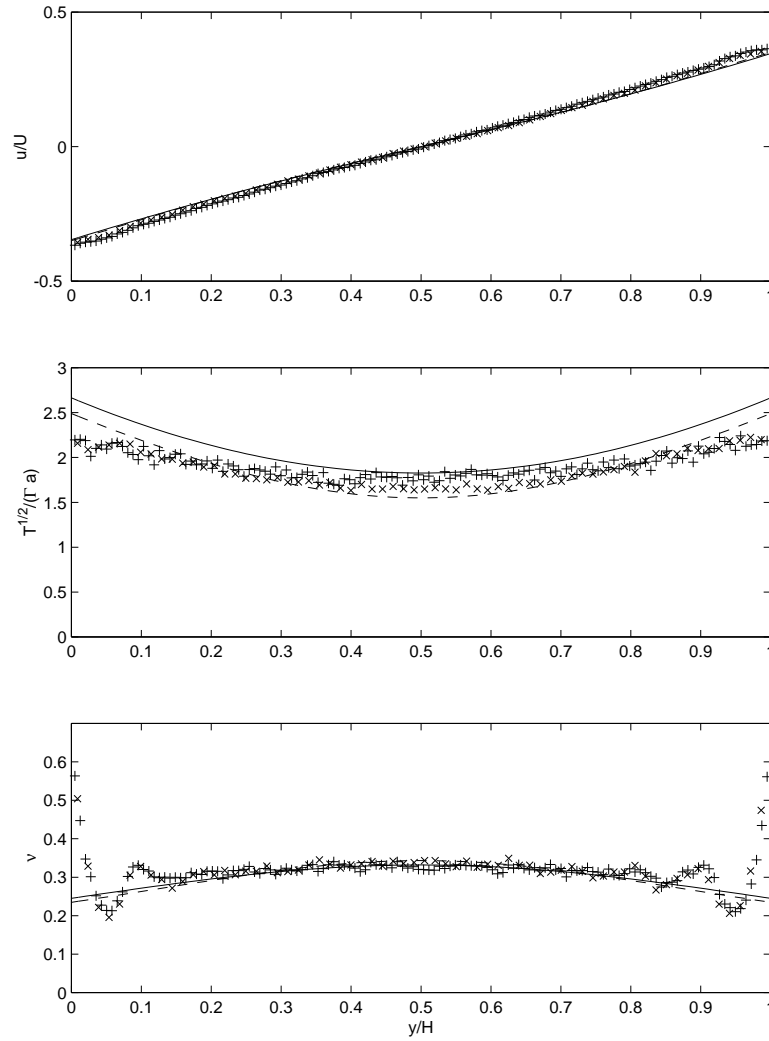


Figure 4.8: Comparison of transverse profiles with $St' = 100$ and $Re' = 10$, and with $St' = 20$ and $Re' = 0.1$. Symbols are LB simulation result [123] and lines are predictions of the theory. Pluses and solid lines: results for $St' = 100$ and $Re' = 10$, crosses and dashed lines: results for $St' = 20$ and $Re' = 0.1$. Top plot: mean particle velocity u_s^* ; middle plot: granular fluctuation velocity w^* ; bottom plot: particle volume fraction. Other simulation parameters: $Y'/\sigma = 12$ and $\bar{v} = 0.3$.

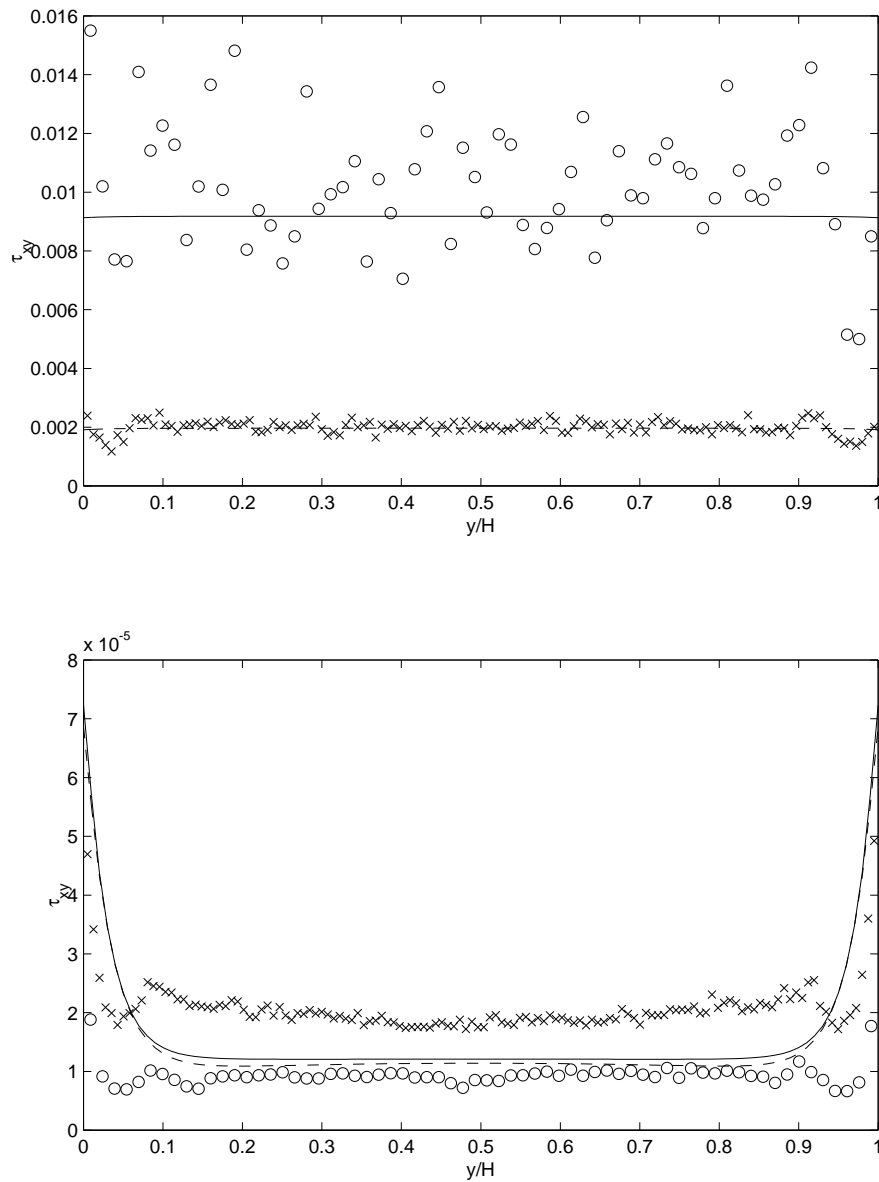


Figure 4.9: Shear stresses at $Re' = 0.1$ and $Re' = 10$ for a fixed $St' = 100$. Symbols are results from the Lattice-Boltzmann simulations [123] and lines are predictions of the theory. Circles and solid lines: $Re' = 0.1$; crosses and dashed lines: $Re' = 10$. Top plot: particle phase shear stress $\eta du_s/dy$; bottom plot: viscous gas shear stress $R_\mu \mu_g du_g/dy$. All stresses are made dimensionless with $\rho_s U^2$. For other simulation parameters, see Figure 4.7.

Effects of particle volume fraction

Figure 4.10 shows the effects of the overall particle volume fraction on granular temperature. Because R_{diss} increases with ν , the granular temperature decreases as the particle volume fraction increases at fixed St' and Re' . However, because the granular shear viscosity increases with ν , the collisional transfer of momentum is more effective as the particle volume fraction increases, and thus the granular temperature remains high. These two mechanisms seem to balance each other when $\nu \gtrsim 0.3$ and further increases of ν have only a minor effect on the granular temperature. The larger discrepancy in granular temperature at $\nu = 0.1$ is probably due to the error in Eq. (4.7), the curve-fit of R_{diss} . Note that in Figure 4.10, the channel widths are not exactly the same for all cases. The small differences in Y'/σ are for the convenience of simulation and have only minor effects on either granular temperature or particle volume fraction profiles.

Effects of channel width

One important feature of the current theory is that it captures the role of solid boundaries on the gas-particle flow. As Figure 4.11 shows at a mean volume fraction $\bar{\nu} = 0.3$, the cross-sectional average granular temperature made dimensionless with $\Gamma^2\sigma^2$ remains roughly constant as the channel narrows. However, through the agitation provided by the bumpy boundary, a narrower channel also helps maintain a more homogeneous flow, so the particle volume fraction becomes more uniform. In Figure 4.11, the data are obtained by boxcar-averaging the raw simulation results of center-average solid volume fraction, which, by exhibiting wide natural oscillations with wavelength on the order of a sphere diameter, make it difficult to compare with the corresponding theoretical profiles Louge [76].

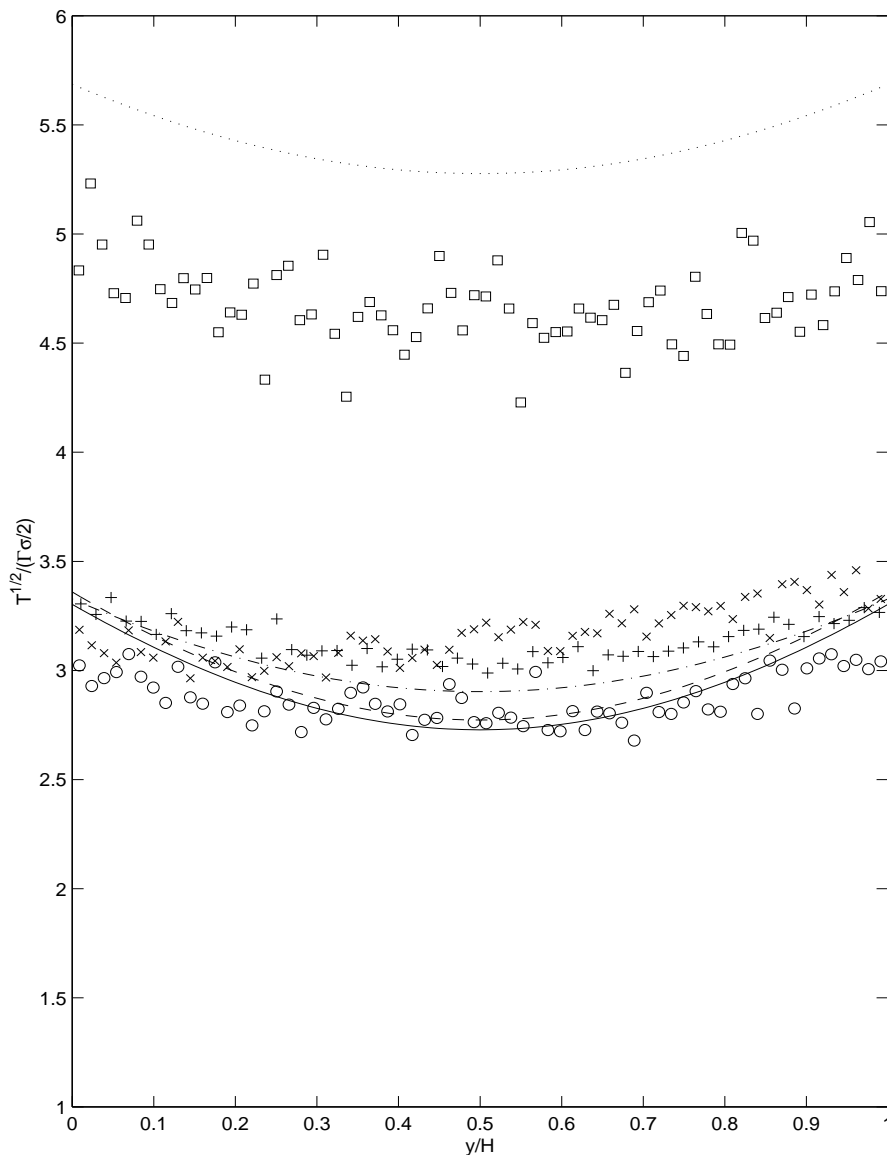


Figure 4.10: Effects of overall particle volume fraction on granular temperature (top) and volume fraction profiles (bottom) at fixed $St' = 30$ and $Re' = 0.1$, Symbols are simulation results [123] and lines are prediction of the theory. Dotted line and squares: $\nu = 0.1$, $Y'/\sigma = 12.7$; dash-dotted line and pluses: $\nu = 0.2$, $Y'/\sigma = 10$; solid line and circles: $\nu = 0.3$, $Y'/\sigma = 12$; dashed line and crosses: $\nu = 0.4$, $Y'/\sigma = 12$. All simulations are with $\sigma = 5.84$ lattice units.

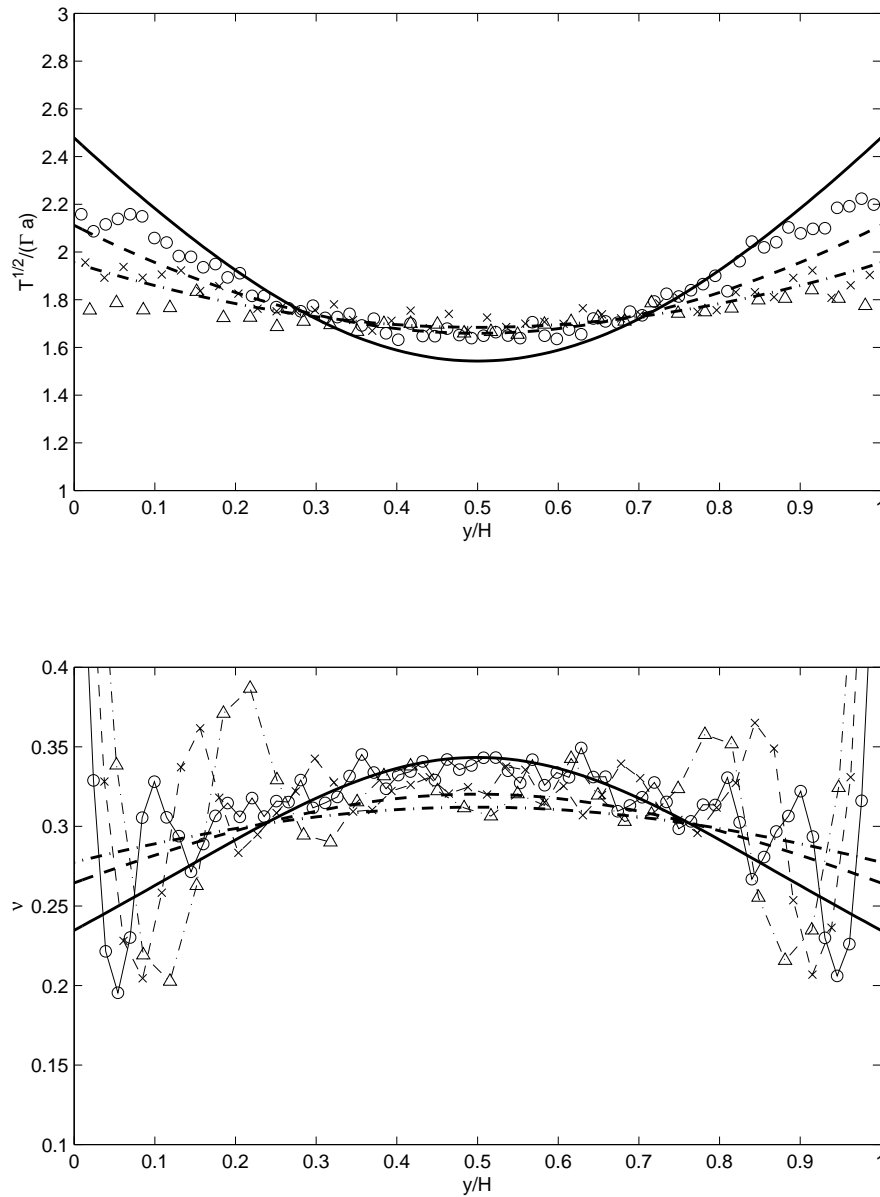


Figure 4.11: Effects of channel width Y on granular temperature (top) and particle volume fraction (bottom) at fixed $St' = 20$, $Re' = 0.1$, and $\bar{v} = 0.3$. Symbols are simulation results [123], thick lines are prediction of the theory. Solid line and circles: $Y'/\sigma = 12$; dashed line and crosses: $Y'/\sigma = 8$; dash-dotted line and triangles: $Y'/\sigma = 6$. Parameters in simulation: $\sigma = 5.84$ lattice units.

In this section, we assumed that the solid spheres are perfectly elastic so that there is no collisional dissipation of granular fluctuation energy. In real gas-particle flows, the inelastic dissipation may dominate the viscous dissipation, especially at high Stokes numbers. Since the inelastic dissipation is proportional to $T^{3/2}$, but the viscous dissipation is proportional to T , the relative importance of inelastic dissipation decreases as the Stokes number decreases. On the other hand, the presence of inelastic dissipation may cause the viscous theory to fail at higher Stokes number. Simulations with inelastic particles in a gas should be carried out to resolve these questions.

4.2.4 Two-Dimensional Rectilinear Flow

We now consider fully developed flows between two bumpy boundaries and two flat side walls, with possible body forces acting on the solid phase along the flow direction, as shown in Figure 3.1. In this case, like the one-dimensional flow considered in Chapter 3, the conservations of mass in the solid and gas phases are satisfied automatically. The solid momentum balance in the flow direction becomes

$$\begin{aligned} \frac{\partial}{\partial y} \left(\eta \frac{\partial u_s}{\partial y} + \nu R_\mu \mu_g \frac{\partial u_g}{\partial y} \right) + \frac{\partial}{\partial z} \left(\eta \frac{\partial u_s}{\partial z} + \nu R_\mu \mu_g \frac{\partial u_g}{\partial z} \right) \\ + \beta(u_g - u_s) - \nu \frac{dP_g}{dx} + \rho f_x = 0, \end{aligned} \quad (4.30)$$

where u_g and u_s are, respectively, the mean gas and solid velocities in the flow direction along x .

The solid momentum balances in the y - and z -directions reduce to

$$\frac{\partial P_s}{\partial y} = \frac{\partial P_s}{\partial z} = 0, \quad (4.31)$$

which, taken together with the fully-developed flow assumption, indicate that the solid phase pressure P_s is constant.

Similarly, for the gas phase, we have

$$\frac{\partial}{\partial y} \left((1-\nu) R_\mu \mu_g \frac{\partial u_g}{\partial y} \right) + \frac{\partial}{\partial z} \left((1-\nu) R_\mu \mu_g \frac{\partial u_g}{\partial z} \right) - \beta(u_g - u_s) - (1-\nu) \frac{dP_g}{dx} = 0, \quad (4.32)$$

where the pressure gradient dP_g/dx is a constant.

The particle fluctuation energy balance becomes

$$\begin{aligned} \frac{\partial}{\partial y} \left(\kappa \frac{\partial T}{\partial y} \right) + \frac{\partial}{\partial z} \left(\kappa \frac{\partial T}{\partial z} \right) + \eta \left[\left(\frac{\partial u_s}{\partial y} \right)^2 + \left(\frac{\partial u_s}{\partial z} \right)^2 \right] \\ + \nu R_\mu \mu_g \left(\frac{\partial u_g}{\partial y} \frac{\partial u_s}{\partial y} + \frac{\partial u_g}{\partial z} \frac{\partial u_s}{\partial z} \right) - \gamma_{inelas} - \gamma_{vis} + \gamma_{rel} = 0. \end{aligned} \quad (4.33)$$

We assume that the boundary conditions for the solid phase in Chapter 3 are unaffected by the gas. For simplicity, we apply the “no-slip” boundary condition for the gas phase at a flow sphere radius away from the crest of the boundary spheres or away from the flat side walls. This permits us to solve the differential equations of the solid and gas phase in the same flow domain.

We calculate the mean solid and gas velocities, the solid volume fraction and the solid fluctuation velocity in the cross section $0 \leq y \leq H$ and $-W/2 \leq z \leq W/2$, where the height H and the width W of the flow channel are defined in Chapter 3. We first write the governing equations in dimensionless form using the same dimensionless variables as in the one dimensional flow problem, and we define a new variable $z^* \equiv Z/H$.

Then, the dimensionless solid phase momentum equation in the flow direction

is

$$\begin{aligned}
& \frac{\partial^2 u_s^*}{\partial y^{*2}} + \frac{\partial^2 u_s^*}{\partial z^{*2}} + \left(\frac{1}{P_s^*} \frac{\partial P_s^*}{\partial y^*} + \frac{1}{J} \frac{\partial J}{\partial y^*} - \frac{1}{F} \frac{\partial F}{\partial y^*} - \frac{1}{w^*} \frac{\partial w^*}{\partial y^*} \right) \frac{\partial u_s^*}{\partial y^*} \\
& + \left(\frac{1}{P_s^*} \frac{\partial P_s^*}{\partial z^*} + \frac{1}{J} \frac{\partial J}{\partial z^*} - \frac{1}{F} \frac{\partial F}{\partial z^*} - \frac{1}{w^*} \frac{\partial w^*}{\partial z^*} \right) \frac{\partial u_s^*}{\partial z^*} \\
& + \frac{5\sqrt{\pi}}{8} \frac{1}{18(H/\sigma)St} \frac{1}{JGw^*} \left[\frac{\partial}{\partial y^*} \left(\nu R_\mu \frac{\partial u_g^*}{\partial y^*} \right) + \frac{\partial}{\partial z^*} \left(\nu R_\mu \frac{\partial u_g^*}{\partial z^*} \right) \right] \\
& + \frac{5\sqrt{\pi}}{8} \frac{1}{JGw^*} \left[(1-\nu)^2 \frac{H}{\sigma} \frac{R_{drag}}{St} (u_g^* - u_s^*) + R_\tau \right] = 0, \tag{4.34}
\end{aligned}$$

where St and R_τ are defined in the same way as before.

The dimensionless solid phase momentum equation in other directions is

$$P_s^* = constant, \tag{4.35}$$

where $P_s^* \equiv P_s/\rho_s U^2$ is the dimensionless granular pressure.

The gas momentum balance in the flow direction is

$$\begin{aligned}
& \frac{\partial^2 u_g^*}{\partial y^{*2}} + \frac{\partial^2 u_g^*}{\partial z^{*2}} + \frac{1}{(1-\nu)R_\mu} \frac{\partial(1-\nu)R_\mu}{\partial y^*} \frac{\partial u_g^*}{\partial y^*} + \frac{1}{(1-\nu)R_\mu} \frac{\partial(1-\nu)R_\mu}{\partial z^*} \frac{\partial u_g^*}{\partial z^*} \\
& + 18 \frac{H}{\sigma} \frac{1}{R_\mu} \left[\nu(1-\nu) \frac{H}{\sigma} R_{drag} (u_s^* - u_g^*) + R_\tau St \right] = 0. \tag{4.36}
\end{aligned}$$

Finally, we write the dimensionless particle fluctuation energy equation in terms of w^* as

$$\begin{aligned}
& \frac{\partial^2 w^*}{\partial y^{*2}} + \frac{\partial^2 w^*}{\partial z^{*2}} + \left(\frac{1}{M} \frac{\partial M}{\partial y^*} - \frac{1}{F} \frac{\partial F}{\partial y^*} + \frac{1}{P_s^*} \frac{\partial P_s^*}{\partial y^*} \right) \frac{\partial w^*}{\partial y^*} \\
& + \left(\frac{1}{M} \frac{\partial M}{\partial z^*} - \frac{1}{F} \frac{\partial F}{\partial z^*} + \frac{1}{P_s^*} \frac{\partial P_s^*}{\partial z^*} \right) \frac{\partial w^*}{\partial z^*} \\
& + \frac{1}{M} \left\{ \frac{J}{5} \left[\left(\frac{1}{w^*} \frac{\partial u_s^*}{\partial y^*} \right)^2 + \left(\frac{1}{w^*} \frac{\partial u_s^*}{\partial z^*} \right)^2 \right] - 3(1 - e_{eff}) \left(\frac{H}{\sigma} \right)^2 \right\} w^* \\
& + \frac{\sqrt{\pi}}{8} \frac{1}{18(H/\sigma)St} \frac{R_\mu}{MGw^{*2}} \left(\frac{\partial u_g^*}{\partial y^*} \cdot \frac{\partial u_s^*}{\partial y^*} + \frac{\partial u_g^*}{\partial z^*} \cdot \frac{\partial u_s^*}{\partial z^*} \right) \\
& + \frac{\sqrt{\pi}}{16} \frac{1}{MG} \left[6 \left(\frac{H}{\sigma} \right) \frac{R_{diss}}{St} + (1-\nu)^2 \frac{S^* (u_g^* - u_s^*)^2}{St^2 w^{*3}} \right] = 0. \tag{4.37}
\end{aligned}$$

We solve Eqs. (4.34) - (4.37) for u_s^* , u_g^* and w_s^* subject to boundary conditions in the rectangular flow domain using the method described in Chapter 3. The solid phase pressure is determined by iteration for the imposed overall particle volume fraction.

Figure 4.12 shows the solution of Eqs. (4.34) - (4.37) in the cross section of a rectilinear flow. In this example, there is no gas pressure imposed and the gas is entrained by the particles. The solid velocity profiles from side walls to side walls are not flat. The particles are dragged near the flat side walls by both the frictional collisions with the wall and the slower gas near the wall, which obeys the no-slip boundary condition at the side walls. The gas and solid velocities are nearly the same everywhere in the flow field except in the near vicinity of the solid boundaries. The granular temperature from side wall to side wall is not uniform either, mainly due to the variation of local shear rate.

Integral equations

Figure 4.12 shows that in general the gradients of mean particle velocity, fluctuation velocity and gas velocity in the z -direction perpendicular to the flat side walls are smaller than the corresponding gradients in the y -direction normal to the bumpy boundaries. Thus, we integrate the governing equations in the z -direction to find transverse profiles of the averaged u_s , u_g and T , as we did for granular flows in Chapter 3. The results closely resemble the governing equations for one dimensional flow, except for terms that involve stresses and flux of particle fluctuation energy at the flat walls.

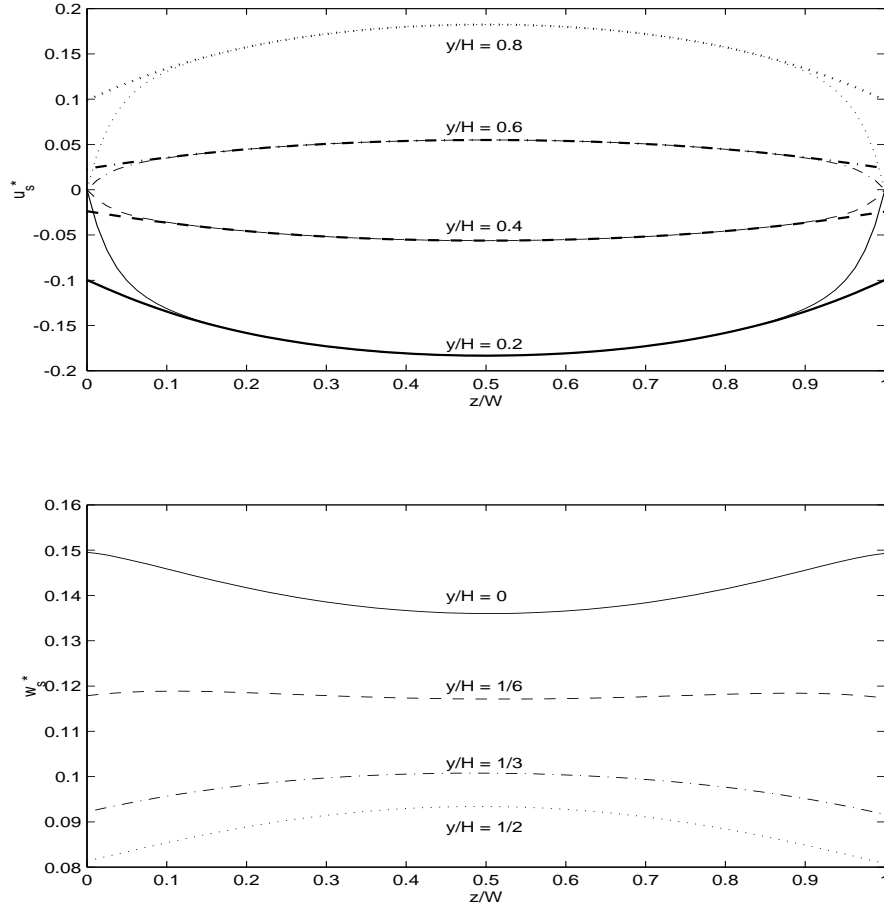


Figure 4.12: Theoretical solutions of mean solid velocity, gas velocity, and granular temperature in the cross-section. Parameters: $H/\sigma = W/\sigma = 11$, $St' = 30$, $Re' = 0.1$, lubrication cut-off $\varepsilon_m = 0.01$, and overall particle volume fraction is 0.3. Top and bottom boundary velocities are $U_t = 0.5U$ and $U_b = -0.5U$. The flat side walls are stationary. Impact parameters are $e = 1$, $\mu = 0$, and $\beta_0 = 0$ except for the flat side walls which have $\mu = 0.1$ and $\beta_0 = 0.4$. Top plot: profiles of mean solid velocity u_s^* and gas velocity u_g^* from side wall to side wall at different y/H . Thick lines: u_s^* , thin lines: u_g^* . Bottom plot: profiles of granular fluctuation velocity w^* at different y/H . Only granular temperature in $y/H \leq 1/2$ is shown because it is symmetrical about $y/H = 1/2$.

The governing equation for the averaged mean particle velocity is

$$\begin{aligned}
& \frac{d^2 u_s^*}{dy^{*2}} + \left(\frac{1}{P_s^*} \frac{dP_s^*}{dy^*} + \frac{1}{J} \frac{dJ}{dy^*} - \frac{1}{F} \frac{dF}{dy^*} - \frac{1}{w^*} \frac{dw^*}{dy^*} \right) \frac{du_s^*}{dy^*} \\
& + \frac{H}{W} \frac{H}{\sigma} \frac{5\sqrt{\pi}F}{2J} w^* \left(\frac{\tau_{xz+}^s}{P_s} - \frac{\tau_{xz-}^s}{P_s} + \frac{\tau_{xz+}^{gs}}{P_s} - \frac{\tau_{xz-}^{gs}}{P_s} \right) \\
& + \frac{5\sqrt{\pi}}{8} \frac{1}{JGw^*} \left[\frac{1}{18(H/\sigma)St} \frac{d}{dy^*} \left(\nu R_\mu \frac{du_g^*}{dy^*} \right) \right. \\
& \left. + (1-\nu)^2 \frac{H}{\sigma} \frac{R_{drag}}{St} (u_g^* - u_s^*) + R_\tau \right] = 0, \tag{4.38}
\end{aligned}$$

where τ_{xz+}^s and τ_{xz-}^s are granular shear stresses at $z = +W/2$ and $z = -W/2$, respectively; and τ_{xz+}^{gs} and τ_{xz-}^{gs} are shear stresses at $z = +W/2$ and $z = -W/2$ on the grains due to the viscous gas. The granular shear stresses τ_{xz+}^s and τ_{xz-}^s are evaluated using boundary conditions for a granular flow at a flat frictional wall in terms of the granular mean velocity and temperature in the flow, assuming negligible spin of the grains around the y -axis [50, 56]. The shear stress due to the viscous gas is

$$\tau_{xz+}^{gs} = \nu R_\mu \mu_g \left. \frac{\partial u_g}{\partial z} \right|_{z=W/2}, \tag{4.39}$$

in which the gas velocity gradient at the wall will be determined later.

The integral equation for the granular fluctuation velocity is

$$\begin{aligned}
& \frac{d^2 w^*}{dy^{*2}} + \left(\frac{1}{P_s^*} \frac{dP_s^*}{dy^*} + \frac{1}{M} \frac{dM}{dy^*} - \frac{1}{F} \frac{dF}{dy^*} \right) \frac{dw^*}{dy^*} \\
& + \frac{1}{M} \left[\frac{J}{5} \left(\frac{1}{w^*} \frac{du_s^*}{dy^*} \right)^2 - 3(1-e_{eff}) \left(\frac{H}{\sigma} \right)^2 \right] w^* + \frac{\sqrt{\pi}}{2} \frac{H^2}{W\sigma} \frac{F}{M} \left(\frac{q_{z+}}{P_s w} + \frac{q_{z-}}{P_s w} \right) w^* \\
& + \frac{\sqrt{\pi}}{16} \frac{1}{MG} \left[\frac{1}{9(H/\sigma)St} \frac{R_\mu}{w^{*2}} \frac{du_g^*}{dy^*} \frac{du_s^*}{dy^*} - 6 \frac{H}{\sigma} \frac{R_{diss}}{St} - (1-\nu)^2 \frac{S^* (u_g^* - u_s^*)^2}{St^2 w^{*3}} \right] \\
& + \frac{5\pi}{48} \frac{H^2}{\sigma^2} \frac{F^2}{MJ} \left[\left(\frac{\tau_{xz+}^s}{P_s} - \frac{\tau_{xz-}^s}{P_s} + \frac{\tau_{xz+}^{gs}}{P_s} - \frac{\tau_{xz-}^{gs}}{P_s} \right)^2 \right. \\
& \left. + 3 \left(\frac{\tau_{xz+}^s}{P_s} + \frac{\tau_{xz-}^s}{P_s} + \frac{\tau_{xz+}^{gs}}{P_s} + \frac{\tau_{xz-}^{gs}}{P_s} \right)^2 \right] w^* = 0, \tag{4.40}
\end{aligned}$$

where q_{z+} and q_{z-} are fluxes of particle fluctuation energy through the flat walls at $z = W/2$ and $z = -W/2$, respectively. Once again, they are evaluated using

boundary conditions for a granular flow at a flat frictional wall in terms of the granular mean velocity and temperature in the flow, assuming negligible spin of the grains around the y -axis [50, 56].

The averaged equation for mean gas velocity is

$$\begin{aligned} \frac{d^2 u_g^*}{dy^{*2}} + \frac{1}{(1-\nu)R_\mu} \frac{d(1-\nu)R_\mu}{dy^*} \frac{du_g^*}{dy^*} + \frac{H}{W} \frac{\tau_{xz+}^g - \tau_{xz-}^g}{(1-\nu)R_\mu \mu_g U/H} \\ + 18 \frac{H}{\sigma} \frac{1}{R_\mu} \left[\frac{H}{\sigma} \nu(1-\nu) R_{drag} (u_s^* - u_g^*) + R_\tau St \right] = 0, \end{aligned} \quad (4.41)$$

where τ_{xz+}^g and τ_{xz-}^g are gas phase shear stresses at $z = +W/2$ and at $z = -W/2$, respectively; for example,

$$\tau_{xz+}^g = (1-\nu)R_\mu \mu_g \left. \frac{\partial u_g}{\partial z} \right|_{z=W/2}. \quad (4.42)$$

To model the gas velocity gradient at the wall, we consider the idealized case of a simple shear flow of gas and particles confined between two flat plates. The flat plates are parallel to the flow and are perpendicular to the vorticity axis. We ignore the effect of the flat plates on particles and assume that the particle phase is homogeneous with a mean velocity profile $u_s = \Gamma y$, where Γ is the constant shear rate of a simple shear flow. However, the gas must satisfy the “no-slip” boundary condition at the flat plates. The analytical solution to the gas momentum balance (4.36) is

$$u_g = \left(\Gamma y - \frac{(1-\nu)}{\beta} \frac{dP_g}{dx} \right) \left[1 - \frac{\cosh(2kz/W)}{\cosh(k/2)} \right], \quad (4.43)$$

where

$$k \equiv \frac{W}{\sigma} \sqrt{18\nu(1-\nu) \frac{R_{drag}}{R_\mu}} \quad (4.44)$$

is a dimensionless variable. The velocity gradient at the wall is

$$\left. \frac{\partial u_g}{\partial z} \right|_{z=W/2} = - \left(\Gamma y - \frac{(1-\nu)}{\beta} \frac{dP_g}{dx} \right) \frac{k}{W} \tanh(k/2). \quad (4.45)$$

In cases of our interest, $W/\sigma \gg 1$ and $k \gg 1$. For example, when $W/\sigma = 10$, $\tanh(k/2)$ is nearly unity except for very dilute flow with $\nu \lesssim 0.02$. Another consequence of $k \gg 1$ is that the average gas velocity is nearly identical to its maximum, i.e.,

$$\begin{aligned} \frac{1}{W} \int_{-W/2}^{W/2} u_g dz &\approx \left(\Gamma y - \frac{(1-\nu)}{\beta} \frac{dP_g}{dx} \right) \left(1 - \frac{1}{\cosh(k/2)} \right) \\ &\approx \Gamma y - \frac{(1-\nu)}{\beta} \frac{dP_g}{dx}. \end{aligned} \quad (4.46)$$

Therefore, the gas velocity gradient normal to the wall is, approximately,

$$\left. \frac{\partial u_g}{\partial z} \right|_{z=W/2} \approx -\frac{k}{W} u_g, \quad (4.47)$$

where u_g indicates the gas velocity averaged from side wall to side wall.

We extend this simplified analysis to the bounded inhomogeneous gas-particle flow and obtain, for example,

$$\tau_{xz+}^g = (1-\nu) R_\mu \mu_g \left. \frac{\partial u_g}{\partial z} \right|_{z=W/2} \approx -(1-\nu) R_\mu \mu_g \frac{k}{W} u_g. \quad (4.48)$$

Therefore, the terms in Eqs. (4.38) - (4.41) involving gas velocity gradient normal to the wall can be approximated as

$$\frac{\tau_{xz+}^{gs}}{P_s} \approx -\frac{k R_\mu}{4FG} \frac{\sigma^2}{HW} \frac{u_g^*}{18Stw^{*2}}, \quad (4.49)$$

and

$$\frac{H}{W} \frac{\tau_{xz+}^g - \tau_{xz-}^g}{(1-\nu) R_\mu \mu_g U/H} \approx -2 \frac{H^2}{W^2} k u_g^*. \quad (4.50)$$

With this approximate gas velocity gradient normal to the flat side walls, we then solve Eqs (4.38) - (4.41) for the average mean gas and particle velocities and for the particle fluctuation velocity. Figure 4.13 compares the transverse profiles of cross-sectional average mean and fluctuation velocities from the two-dimensional

solution of Eqs. (4.34) – (4.37) and from the one-dimensional integral Eqs. (4.38), (4.40), and (4.41). The results for solid mean and fluctuation velocities and the solid volume fraction from the two approaches are almost identical. The results for gas velocity are only slightly different at this relatively large pressure gradient. Therefore, we can use the simpler integral Eqs. (4.38), (4.40) and (4.41) to obtain the profiles of averaged flow variables and to significantly save computation time.

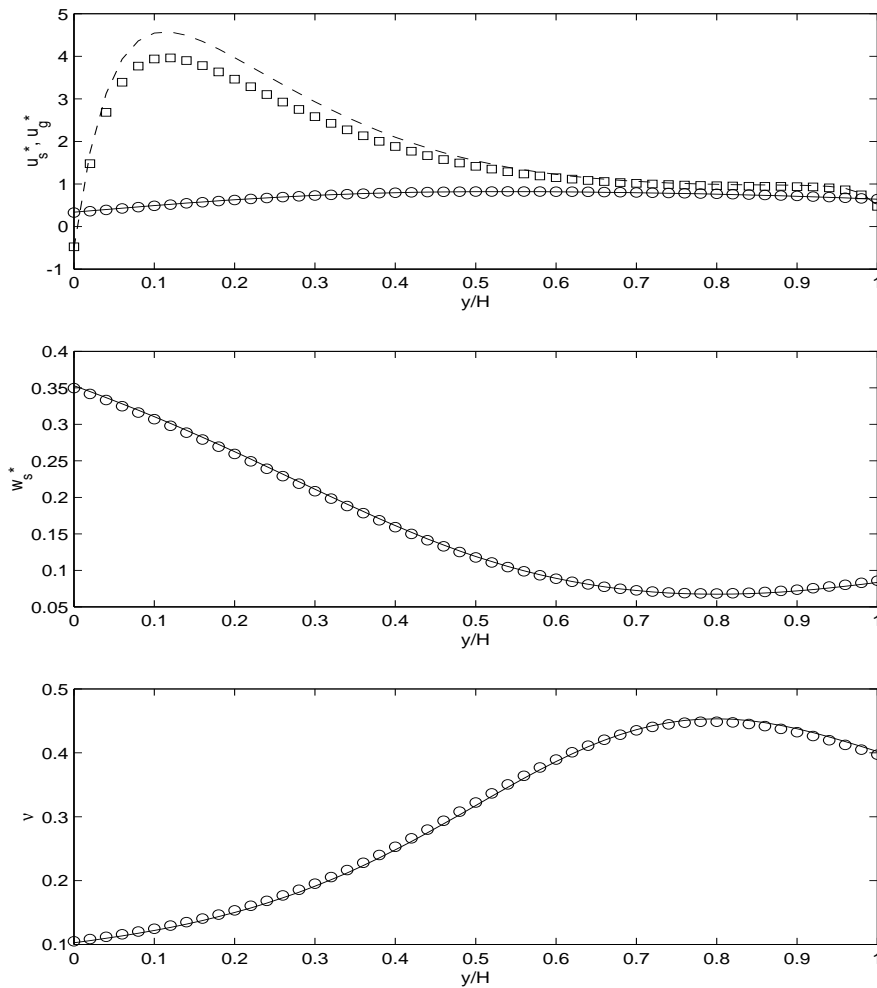


Figure 4.13: Comparison of two-dimensional solution with one-dimensional integral solution. Parameters: $St' = 100$ and $R_\tau = 0.2$. All others are the same as in Figure 4.12. Impact parameters: for collisions between flow spheres and between a flow sphere and the boundary spheres: $e = 0.9$, $\mu = 0$, and $\beta_0 = 0$, for collisions between a flow sphere and the side walls: $e = 1$, $\mu = 0.1$, and $\beta_0 = 0.4$. Symbols are results from 2-D solution averaged from side wall to side wall, lines are results of the 1-D integral theory. Top plot: u_s^* (solid line and circles) and u_g^* (dashed line and squares). Middle plot: w_s^* . Bottom plot: ν .

Chapter 5

Flow Development of Bounded

Collisional Granular Flows

In previous chapters, we studied steady collisional granular flows with or without gas in which all flow parameters, except the longitudinal pressure gradient, are independent of position along the flow. It is straightforward to achieve such “fully developed” conditions in computer simulations by making virtual boundaries perpendicular to the flow periodic. However, in most physical experiments and practical applications, granular flows require a significant length before developing fully. An attempt to reach such a state is the experiments of Louge *et al* [80, 81], who studied the segregation of granular material by transverse gradients of granular temperature in a shear cell shaped as a race track. In that apparatus, collisional granular flows accelerated at the entrance of the straight sections and decelerated at their exit. Understanding flow development is crucial for the design of an experiment and for locating video cameras to observe the flow. In the industrial pneumatic transport of particles, flows also experience change at entrances, exits, bends, or near pumping stations. In these locations, the flow takes some distance to adjust to a new fully developed state.

In this chapter, we study the development of collisional granular flows in two kinds of shear cells. The first is the race track apparatus of Louge *et al* [80, 81], in which the flow develops around a change in the geometry of its channel. The second is an axisymmetric shear cell in which the flow develops because of a streamwise body force or a gradient of gas pressure. Our main purpose is to locate fully developed regions in these experiments.

To that end, we focus on the variations of cross-sectional averages of particle volume fraction, mean particle velocity, granular temperature, and if applicable, mean gas velocity. Using a method similar to the integral treatment of a laminar boundary layer, we derive a theory to describe flow development and we compare its predictions with event-driven molecular dynamic simulations. We then look at the effects of specific design parameters, such as the impact properties of the side walls, the distance between these, the length of the straight section, etc., on flow development.

We begin this chapter by considering the granular flow in the straight section of the race track shear cell. We derive equations for the evolution of the cross-sectional average particle volume fraction and granular temperature along the channel. Comparisons with computer simulations show that the theory captures the effects of side walls and channel length. We then consider the axisymmetric shear cell, in which centripetal accelerations play a role. In the case where a streamwise body force is acting on the grains, we check the theory against computer simulations. By combining the theory for straight sections and that for axisymmetric cells, we predict the flow development in the entire channel of the race track shear cell. Finally, in anticipation of an upcoming microgravity experiment, we derive the evolution of gas-particle flows in an axisymmetric cell and show examples of our theoretical predictions.

5.1 Granular Flow in a Rectilinear Channel

In an experimental study of particle segregation driven by transverse gradients of granular temperature, Louge *et al* [80, 81] used the race track shear cell sketched in Figure 5.1. These authors used binary mixtures consisting of two kinds of spheres.

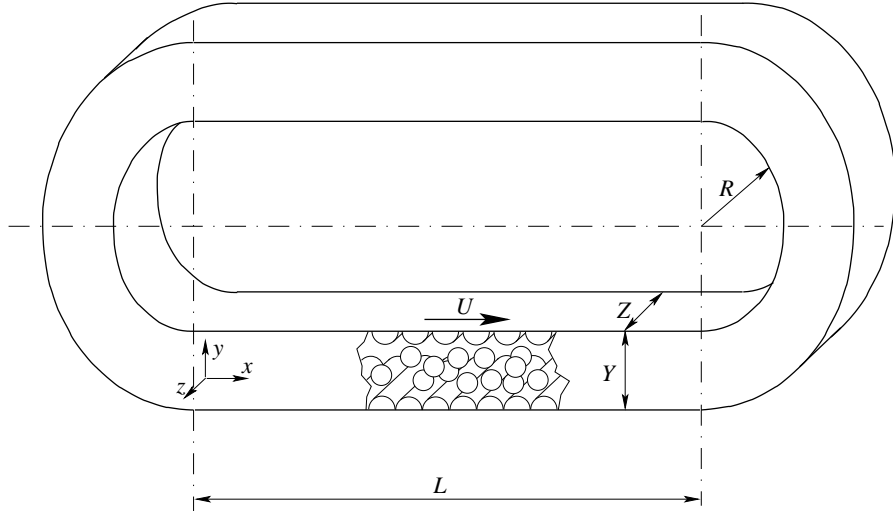


Figure 5.1: A sketch of the microgravity “race track” shear cell used by Louge *et al* [80].

In this chapter, for simplicity, we ignore the binary character of their granular material and consider instead identical spheres of diameter σ that are driven by the inner boundary moving at a velocity U . To agitate the flow spheres, the inner and outer boundaries are made bumpy by attaching half cylinders of respective diameters d_i and d_o orientated in the direction perpendicular to the flow. The gaps separating the half cylinders on the inner and outer boundaries are s_i and s_o , respectively (Fig. 2.1). The distance between the centers of the inner and outer boundary cylinders is Y , and the distance between the two flat side walls is Z . The centers of flow particles are confined to a flow channel with height $H \equiv Y - \sigma - (d_i + d_o)/2$ and width $W \equiv Z - \sigma$.

In the race track design, curved regions are meant to recirculate particles. However, they disturb the flow, so that it takes a finite distance to reach a fully developed state in the straight sections of the cell. To understand the effects of various design parameters on flow development, we first analyze the flow in the

straight sections. We adopt a Cartesian coordinate system with x pointing from the entrance of the straight region toward its exit. The origin of the coordinate system is on the entrance plane at a distance $\sigma/2$ above the crests of the half cylinders on the outer boundary and is located midway between the flat side walls (Fig. 3.1). In short, the flow domain is $0 \leq x \leq L$, $0 \leq y \leq H$, and $-W/2 \leq z \leq W/2$.

The conservation equations (3.1) – (3.3) are given in chapter 3. In the straight sections, we assume that the mean particle velocity in the z direction vanishes, and we call its components in the x - and the y -directions u and v , respectively. At steady state, the conservation equations reduce to

$$\frac{\partial \rho u}{\partial x} + \frac{\partial \rho v}{\partial y} = 0, \quad (5.1)$$

$$\frac{\partial}{\partial x}(\rho u u) + \frac{\partial}{\partial y}(\rho u v) = -\frac{\partial P}{\partial x} + \frac{\partial \tau_{xx}}{\partial x} + \frac{\partial \tau_{xy}}{\partial y} + \frac{\partial \tau_{xz}}{\partial z} + \rho f_x, \quad (5.2)$$

$$\begin{aligned} \frac{3}{2} \left[\frac{\partial}{\partial x}(\rho u T) + \frac{\partial}{\partial y}(\rho v T) \right] = & -\frac{\partial q_x}{\partial x} - \frac{\partial q_y}{\partial y} - \frac{\partial q_z}{\partial z} - P \left(\frac{\partial u}{\partial x} + \frac{\partial v}{\partial y} \right) \\ & + P_{prod} - \gamma_{inelas}, \end{aligned} \quad (5.3)$$

in which $\rho = \nu \rho_s$ is the density of the flow, ν is the particle volume fraction, f_x is the body force in the x direction, P is the granular pressure, τ_{ij} and q_i ($i, j = x, y, z$) are viscous stress and flux of fluctuation energy, respectively, γ_{inelas} is the volumetric dissipation rate of fluctuation energy due to inelastic collisions, and

$$P_{prod} = \sum_{i,j=x,y,z} \tau_{ij} \frac{1}{2} \left(\frac{\partial u_i}{\partial x_j} + \frac{\partial u_j}{\partial x_i} \right)$$

is the production of fluctuation energy due to the working of viscous granular stresses.

Because $L \gg H$ in the straight section, we generally have $u \gg v$ and $\frac{\partial}{\partial y} \gg \frac{\partial}{\partial x}$,

which simplifies the expressions for stresses and the production term. For example,

$$\tau_{xy} = \eta \left(\frac{\partial u}{\partial y} + \frac{\partial v}{\partial x} \right) \approx \eta \frac{\partial u}{\partial y}, \quad (5.4)$$

$$\tau_{yz} = \eta \frac{\partial v}{\partial z} \approx 0, \quad (5.5)$$

and

$$P_{prod} \approx \eta \left(\frac{\partial u}{\partial y} \right)^2 + \frac{\tau_{xz}^2}{\eta} + \left(\lambda + \frac{4}{3}\eta \right) \left[\left(\frac{\partial u}{\partial x} \right)^2 + \left(\frac{\partial v}{\partial y} \right)^2 \right] + 2 \left(\lambda - \frac{2}{3}\eta \right) \frac{\partial u}{\partial x} \frac{\partial v}{\partial y}, \quad (5.6)$$

where λ and η are the bulk and shear viscosities, respectively. Equation (5.5) indicates that $\tau_{yz} \ll \tau_{xy}$ and $\tau_{yz} \ll \tau_{xz}$.

To focus our analysis on streamwise variations of particle volume fraction, mean velocity and granular temperature, we average these in the channel cross-section. To that end, we integrate the conservation equations (5.1)-(5.3) in the y - and z -directions and find the evolution equations for average volume fraction, mean velocity and granular temperature along x .

The average of any flow quantity ψ is defined as

$$\bar{\psi}(x) \equiv \frac{1}{HW} \int_0^H \int_{-W/2}^{W/2} \psi(x, y, z) dz dy. \quad (5.7)$$

To make the integration tractable, we invoke the following assumptions:

1. The particle volume fraction and granular temperature are uniform in any cross section, i.e., $\nu = \nu(x)$ and $T = T(x)$.
2. The shear stress τ_{xz} varies linearly with depth as in Chapter 3, i.e.,

$$\tau_{xz} = \frac{2z}{W} \tau_{xz} \Big|_{z=W/2}. \quad (5.8)$$

In writing Eq. (5.8), we assume implicitly that τ_{xz} is anti-symmetric about $z = 0$. This might not be the case if the flat walls had different impact

properties. If the event, we still use Eq. (5.8) but we evaluate the wall shear stress using the impact properties averaged between the two side walls.

3. The streamwise mean particle velocity is given by

$$u = u(x, y) = \bar{u}(x) - \bar{u}_{FD} + u_{FD}(y), \quad (5.9)$$

in which $u_{FD}(y)$ is the fully developed profile of mean velocity averaged from side wall to side wall (Eq. (3.25)), and \bar{u}_{FD} is the average of $u_{FD}(y)$ in $0 \leq y \leq H$.

This assumption means that the transverse profile of u at an arbitrary cross-section is parallel to its fully developed counterpart. The slip velocities at the inner and outer bumpy boundaries thus change with the mean velocity $\bar{u}(x)$.

Although we assume $\partial u / \partial z = 0$, we capture the role of the flat side walls by keeping their shear stresses in the integral momentum equation. Similarly, we retain the fluxes of fluctuation energy q_z through these walls despite $T = T(x)$. Because the grains acquire a relatively large velocity in the channel, we invoke the boundary conditions on the flat stationary walls that Jenkins [50] and Jenkins & Louge [56] calculated in the limit of large slip. In particular, the stress on these walls is, for example

$$\tau_{xz} \Big|_{z=W/2} = \mu_{sw} P, \quad (5.10)$$

where μ_{sw} is the friction coefficient of grains sliding on the flat walls. Note that this formulation is strictly valid only when one bumpy boundary is moving. This ensures that the frictional shear stress on the flat side walls is everywhere pointing in the same direction. Later, in section 5.2, we will show how to update the

boundary condition in Eq. (5.10) to account for the reversal of the sliding shear stress in different regions of the side walls.

In a fully developed flow with constant ν and T , the mean velocity profile is governed by

$$\frac{d^2 u_{FD}}{dy^2} = \frac{1}{\eta} \left(\frac{2}{W} \mu_{sw} P - \rho f_x \right), \quad (5.11)$$

which yields a parabolic velocity profile

$$u_{FD}(y) = \bar{u}_{FD} - \frac{1}{2}(u_{i,FD} - u_{o,FD}) + \frac{A}{12} + \left(u_{i,FD} - u_{o,FD} - \frac{A}{2} \right) \frac{y}{H} + \frac{A}{2} \left(\frac{y}{H} \right)^2, \quad (5.12)$$

where

$$\bar{u}_{FD} = \frac{1}{H} \int_0^H u_{FD}(y) dy = \frac{1}{2}(u_{i,FD} + u_{o,FD}) - \frac{A}{12}$$

is the average fully developed velocity, $u_{i,FD}$ and $u_{o,FD}$ are the mean velocity at the inner and outer boundary, respectively,

$$A = U \frac{5\sqrt{\pi} F}{2J} \frac{H}{\sigma} T_{FD}^{*1/2} \left(\frac{2H}{W} \mu_{sw} - \frac{Fr_x \frac{H}{\sigma}}{4FGT_{FD}^{*1/2}} \right), \quad (5.13)$$

$$Fr_x \equiv \frac{f_x \sigma}{U^2}$$

is a Froude number representing the relative magnitude of the body force, and

$$T_{FD}^* \equiv \frac{T_{FD}}{U^2}$$

is the average dimensionless fully developed granular temperature. For convenience, we define the constant difference $u_{sh} \equiv u_{i,FD} - u_{o,FD}$.

We integrate the conservation equations with the velocity profile given by Eqs. (5.9) and (5.12). In dimensionless form, the mass conservation becomes

$$\nu \bar{u}^* = Q^* = const, \quad (5.14)$$

where $\bar{u}^* \equiv \bar{u}/U$ is the dimensionless average velocity. The momentum conservation can then be written as an equation in ν ,

$$\begin{aligned} \frac{d^2\nu}{dx^{*2}} + \frac{1}{K^*} \left\{ \frac{dK^*}{dx^*} - \frac{L}{H} \left[\left(\frac{Q^*}{\nu} \right)^2 - \left(\frac{u_{sh}^{*2}}{12} + \frac{A^{*2}}{720} \right) \right] \right\} \frac{d\nu}{dx^*} \\ - \nu \frac{Fr_x}{K^*} \frac{L^2}{H\sigma} + \frac{L}{H} \frac{1}{K^*} \frac{dP^*}{dx^*} - \frac{L^2}{H^2} \frac{P^*}{K^*} \left[\left(\frac{S}{N} \right)_i - \left(\frac{S}{N} \right)_o - \frac{2H}{W} \mu_{sw} \right] = 0, \end{aligned} \quad (5.15)$$

where $x^* \equiv x/L$, $u_{sh}^* \equiv u_{sh}/U$, $A^* \equiv A/U$,

$$\begin{aligned} P^* &\equiv \frac{P}{\rho_s U^2} = \nu(1 + 4G)T^*, \\ K^* &\equiv \left(\frac{\lambda + \frac{4}{3}\eta}{\rho_s U H} \right) \frac{Q^*}{\nu^2} = \frac{8}{3\sqrt{\pi}} \frac{\sigma}{H} \left(1 + \frac{4J}{5} \right) G \frac{Q^*}{\nu} \sqrt{T^*} \end{aligned}$$

and $T^* \equiv T/U^2$ is the dimensionless granular temperature. The ratios of shear to normal stress at the inner and outer boundaries, $(S/N)_i$ and $(S/N)_o$, are evaluated using the boundary conditions derived in Chapter 2.

The integrated energy conservation equation is

$$\begin{aligned} \frac{d^2T^*}{dx^{*2}} + \frac{1}{\kappa^*} \left(\frac{d\kappa^*}{dx^*} - \frac{3L}{2H} Q^* \right) \frac{dT^*}{dx^*} + \frac{L^2}{\sigma^2} \frac{1}{M} \left[\frac{5\pi F^2}{6J} \mu_{sw}^2 - 6(1 - e_{eff}) \right] T^* \\ + \frac{L^2}{H^2} \left(\frac{u_{sh}^{*2}}{12} + \frac{A^*}{12} \right) \frac{\eta^*}{\kappa^*} + \frac{L^2}{H^2} \frac{P^* \sqrt{T^*}}{\kappa^*} \left(\frac{2H}{W} q_z^* + q_{y,i}^* + q_{y,o}^* \right) \\ - \frac{L}{H} \frac{P^*}{\kappa^*} \frac{d\bar{u}^*}{dx^*} + \frac{2}{3M} \left(1 + \frac{4J}{5} \right) \left(1 + \frac{u_{sh}^{*2}}{12\bar{u}^{*2}} + \frac{A^{*2}}{720\bar{u}^{*2}} \right) \left(\frac{d\bar{u}^*}{dx^*} \right)^2 = 0, \end{aligned} \quad (5.16)$$

where

$$\begin{aligned} \eta^* &\equiv \frac{\eta}{\rho_s U H} = \frac{8J}{5\sqrt{\pi}} \frac{\sigma}{H} \nu G \sqrt{T^*}, \\ \kappa^* &\equiv \frac{\kappa}{\rho_s U H} = \frac{4M}{\sqrt{\pi}} \frac{\sigma}{H} \nu G \sqrt{T^*}, \end{aligned}$$

and κ is the heat conductivity. The dimensionless quantities q_z^* , $q_{y,i}^*$, and $q_{y,o}^*$ are the fluxes of fluctuation energy through the flat side wall, and through the inner

and outer bumpy boundaries, respectively. They are evaluated using the boundary conditions derived in Chapter 2 and they are made dimensionless with $P\sqrt{T}$.

To obtain Eqs. (5.14)-(5.16), we used the fact that $v = 0$ at both $y = 0$ and $y = H$. Thus, the following integral vanishes:

$$\int_0^H \frac{\partial v}{\partial y} dy = v(y = H) - v(y = 0) = 0.$$

However, $(\partial v / \partial y)^2$ or $\partial v / \partial y$ do not. They can be evaluated using the continuity equation,

$$\begin{aligned} \frac{\partial v}{\partial y} &= -\frac{1}{\nu} \frac{\partial \nu u}{\partial x} \\ &= -\frac{1}{\nu} \frac{d\nu}{dx} \left[\frac{A}{12} - \frac{u_{sh}}{2} + \left(u_{sh} - \frac{A}{2} \right) \frac{y}{H} + \frac{A}{2} \left(\frac{y}{H} \right)^2 \right], \end{aligned}$$

and therefore,

$$\overline{\left(\frac{\partial v}{\partial y} \right)^2} = \frac{1}{H} \int_0^H \left(\frac{\partial v}{\partial y} \right)^2 dy = \left(\frac{u_{sh}^2}{12} + \frac{A^2}{720} \right) \frac{1}{\nu^2} \left(\frac{d\nu}{dx} \right)^2.$$

In this section, our objective is merely to analyze the flow in the straight region of the race track shear cell. Thus to evaluate our theory, we assume that conditions at the entrance and exit of the straight region are known from numerical simulations. Later, we will derive another theory for the curved regions, and thus be in a position to predict the flow in the entire race track apparatus without resorting to entrance and exit data from the simulations.

In particular, to solve Eqs. (5.14)-(5.16), we set the values of particle volume fraction and granular temperature at the entrance and exit of the straight channel, i.e., $\nu(x^* = 0)$, $\nu(x^* = 1)$, $T^*(x^* = 0)$, and $T^*(x^* = 1)$. We also borrow from simulations the dimensionless flow rate Q^* . An alternative approach would be to specify the average volume fraction $\bar{\nu}$ in the entire straight channel, and to iterate for the value of Q^* that yields correct $\bar{\nu}$.

Figure 5.2 compares our theoretical predictions for ν , \bar{u}^* and $\sqrt{T^*}$ with simulation data. Also shown in the figure are two simpler theories. The first assumes that the shear production balances the inelastic dissipation at any cross section, so the granular temperature can be determined by an algebraic equation that does not involve the working of the normal stresses or fluxes through the walls. The second simplifies the energy conservation in Eq. 5.16 by ignoring the working of the normal stress ($P + \tau_{xx}$) in the energy balance. Predictions of the two simpler theories deviate from computer simulations. In particular, because they ignore the working of normal stresses, they do not capture the temperature rise near the exit that is due to a rapid compression in the flow.

For additional insight into the balance of fluctuation energy, Figure 5.3 shows calculations of the relative magnitude of its terms for shear production, inelastic dissipation, working of the normal stress and total heat flux through bumpy boundaries. It is clear that the working of the normal stress plays an important role in the energy balance, especially in the regions with rapid expansion or compression. This explains why the two simpler theories mentioned earlier are not predicting correctly the evolution of the granular temperature.

5.1.1 Effects of flat side walls

Figure 5.4 compares the flow development in three different channels with identical spheres, the same length L and height H , but different channel width W , or different friction coefficients μ_{sw} .

With smooth side walls, the mean particle velocity is large, so that diffusion terms in the momentum and energy equations are relatively small except near the exit. Thus, the presence of the exit is not felt far upstream. In particular, the

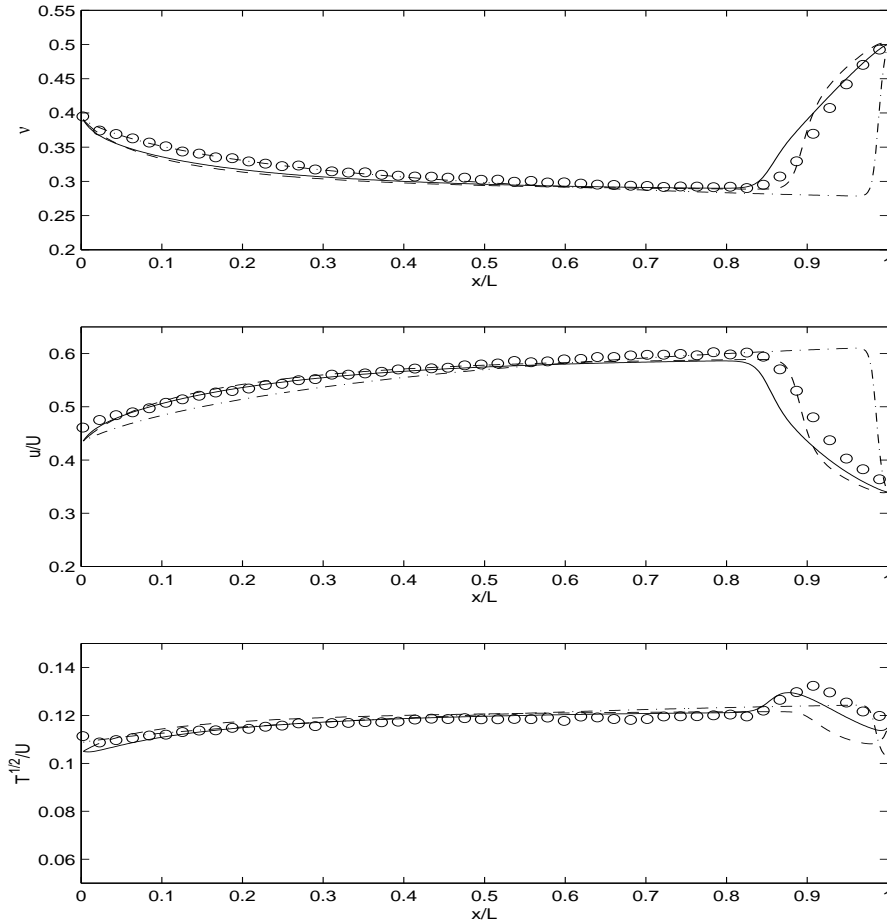


Figure 5.2: Flow development in the straight section; comparison of theory and simulations. Top plot: $\nu(x^*)$, middle plot: $\bar{u}^*(x^*)$, bottom plot: $\sqrt{T^*}(x^*)$. Circles are simulation results. Solid lines are theoretical predictions; dash-dotted lines are predictions of a simplified theory that assumes a balance between shear production and inelastic dissipation at each cross section; dashed lines are predictions that ignore the working of the normal stress in the energy balance. Geometric parameters: $L = 420$, $H = 11.74$, $W = 8.85$, $\sigma = d_i = 3$, $d_o = 2$, and $s_i = s_o = 0$. Impact properties of flow spheres: $e = 0.95$, $\mu = 0.1$, $\beta_0 = 0.4$; bumpy boundaries: $e_w = 0.85$, $\mu_w = 0.1$, $\beta_{0,w} = 0.4$; flat side walls: $e_{sw} = 0.95$, $\mu_{sw} = 0$, $\beta_{0,sw} = 0$.

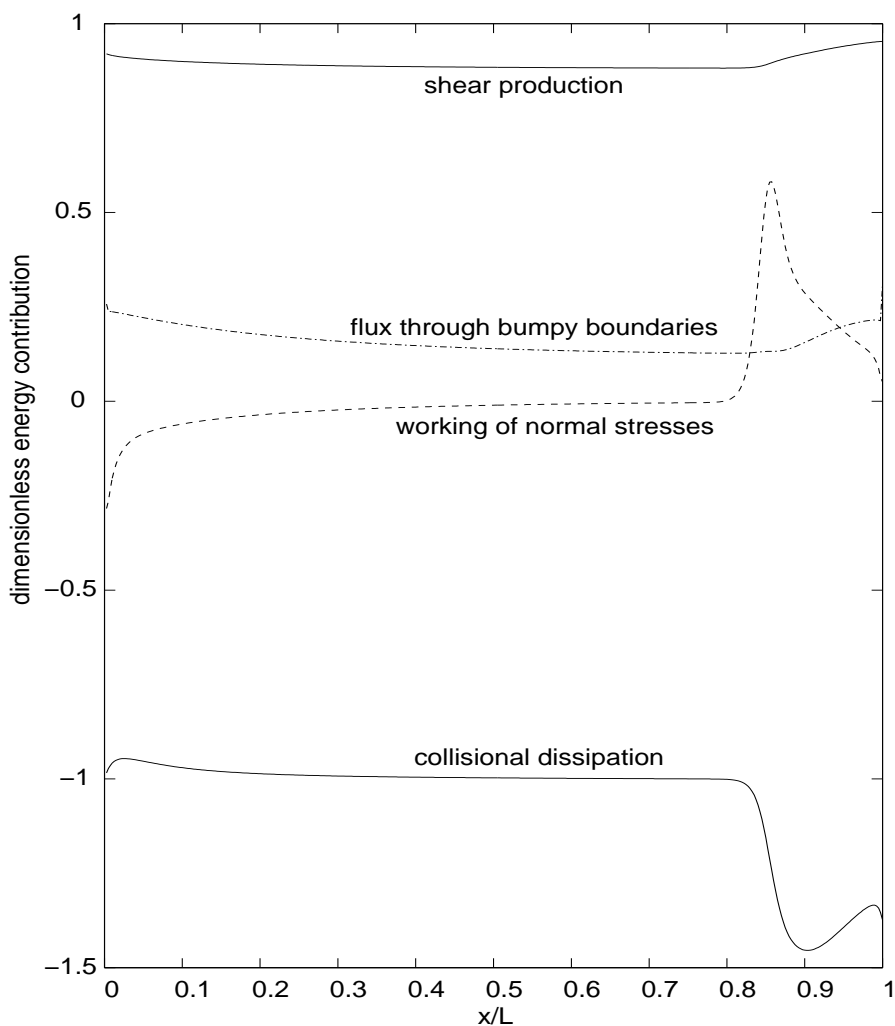


Figure 5.3: Relative magnitude of the terms in the energy balance along the straight section. Thin solid line: shear production; dash-dotted line: total heat flux through both bumpy boundaries; dashed line: working of the normal stress; thick solid line: inelastic dissipation. All terms are made dimensionless by the inelastic dissipation in the fully developed region. Other terms in energy balance, i.e., conduction, convection, and total heat flux through the flat side walls, are very small and are not shown. For parameters and impact properties, see Figure 5.2.

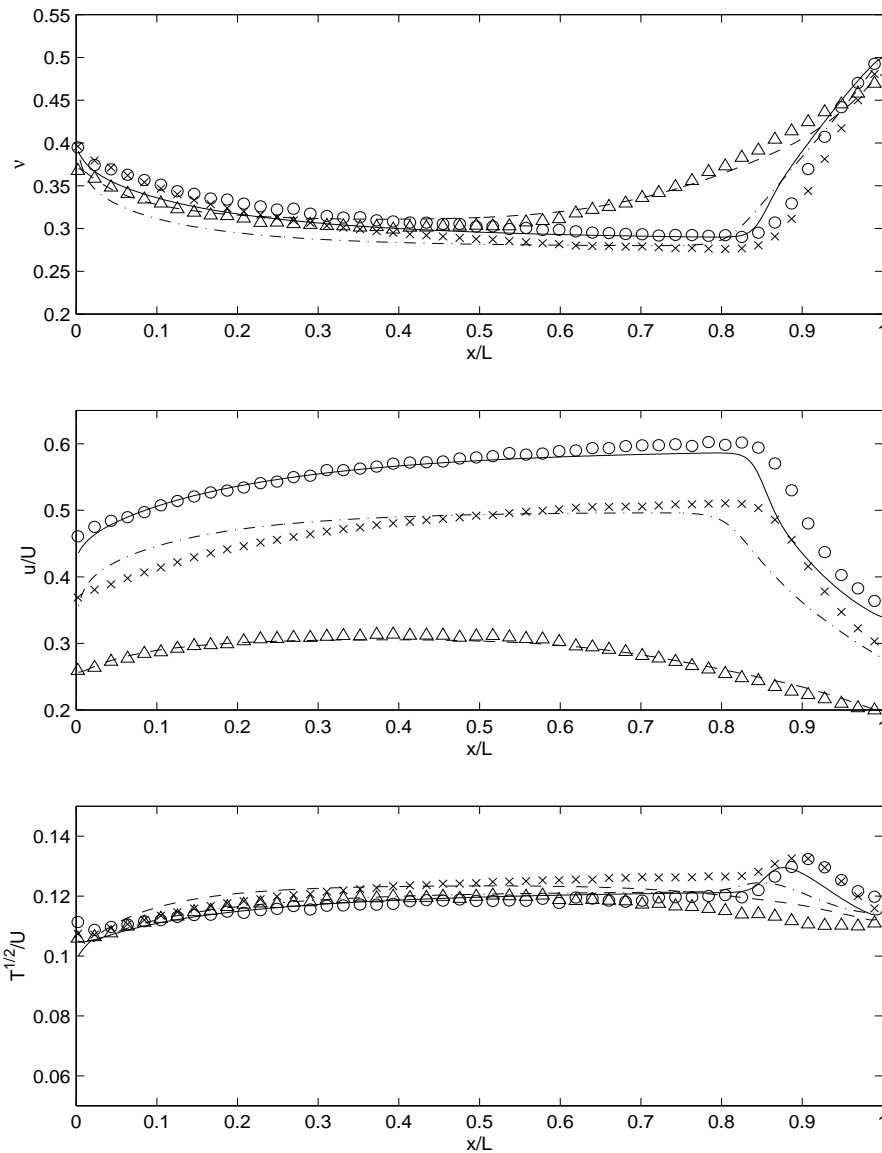


Figure 5.4: Effects of flat side walls on flow development. Top plot: $\nu(x^*)$, middle plot: $\bar{u}^*(x^*)$, bottom plot: $\sqrt{T^*}(x^*)$. Symbols are simulation results and lines are theoretical predictions. Circles and solid lines: smooth side walls, $\mu_{sw} = 0$ and $W = 8.85$. Triangles and dashed lines: frictional side walls, $\mu_{sw} = 0.1$ and $W = 8.85$. Crosses and dash-dotted lines: a wider cell with frictional side walls, $\mu_{sw} = 0.1$ and $W = 36.86$. All other parameters are found in Figure 5.2.

volume fraction, which gradually decreases from the entrance as the flow accelerates, rises sharply near the exit while the mean velocity drops abruptly. As a consequence of this rapid compression, the granular temperature rises from the working of the normal stress in a thin region ahead of the exit. The rapid increase of both the particle volume fraction and granular temperature near $x/L \approx 0.83$ resembles a normal shock in supersonic gas flows.

When the flat side walls are frictional, the mean velocity is smaller and diffusion is more significant. The higher exit volume fraction is felt farther upstream, thus producing a gradual increase of ν toward the exit. Under these conditions, there is no region of rapid compression, and thus the situation is analog to the subsonic flow of a molecular gas. From an experimental viewpoint, a fully developed region with $d\nu/dx \approx 0$ now migrates upstream to $x^* \approx 0.3 \sim 0.4$.

Because frictional side walls appear through the term $(2H/W)\mu_{sw}$ in the momentum balance Eq. (5.15), their role is diminished in wider cells or with flat walls of lesser friction. Thus as the cell widens, the flow resembles the smooth wall case just discussed, even if the wider cell has frictional walls. However, because frictional side walls provide greater shear production of fluctuation energy through τ_{xz} , the granular temperature is slightly higher compared to the smooth side wall case.

5.1.2 Effects of section length

Figure 5.5 illustrates the role of section length on flow development. As expected, longer straight sections produce longer fully developed regions. Surprisingly, in the conditions under study, it takes a fixed length for the flow to become fully developed. The theory captures these effects well.

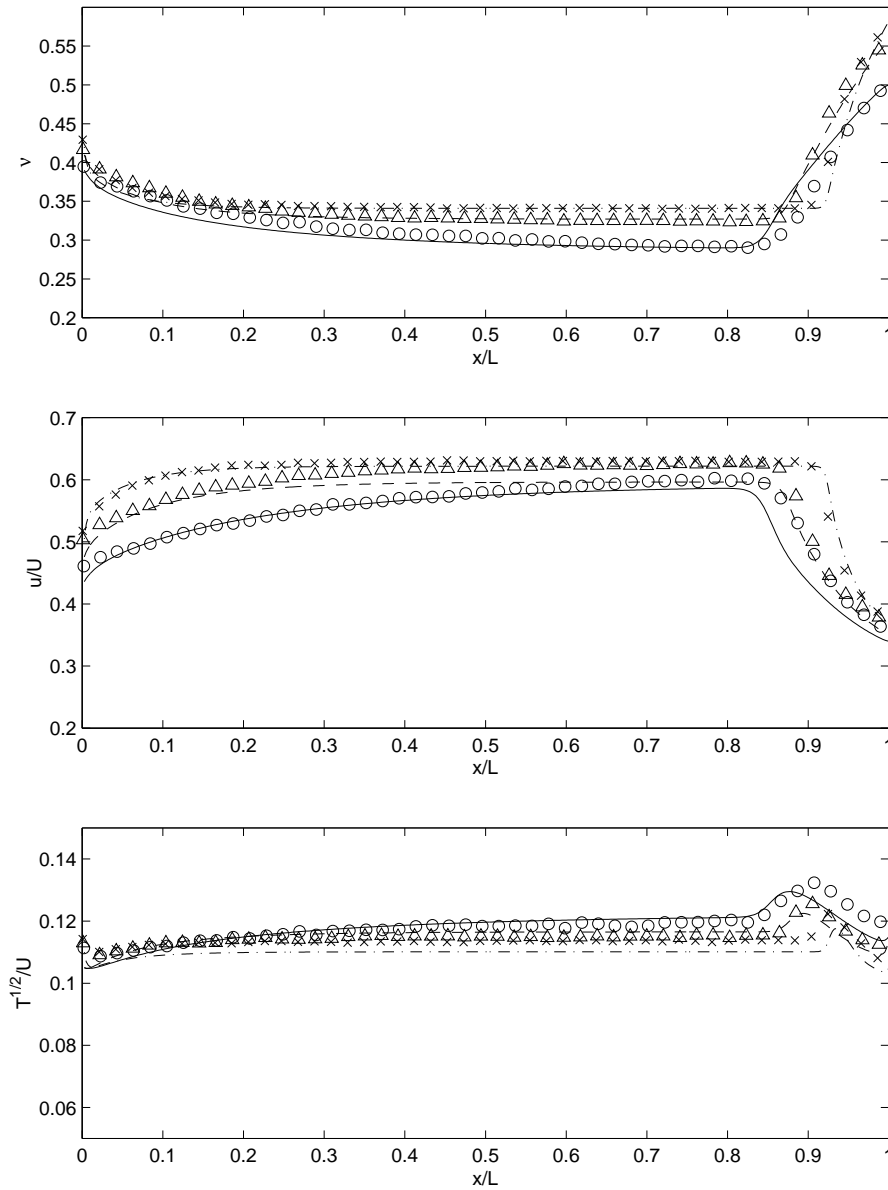


Figure 5.5: Effects of straight section length on flow development. Top plot: $\nu(x^*)$, middle plot: $\bar{u}^*(x^*)$, bottom plot: $\sqrt{T^*}(x^*)$. Symbols are simulation results and lines are theoretical predictions. Circles and solid lines, $L/\sigma = 140$; triangles and dashed lines, $L/\sigma = 280$; crosses and dash-dotted lines, $L/\sigma = 560$. Other parameters, see Figure 5.2.

5.2 Granular Flow in an Axisymmetric Shear Cell

Louge *et al* [83] recently proposed to study gas-particle interactions in an axisymmetric shear cell operating in microgravity. The cell features an inner and an outer bumpy boundary that can rotate independently, and two stationary flat side walls (Fig. 5.6). The cell is designed to allow gas injection and withdrawal through narrow distributors located on one of the flat side walls. When such gas circulation takes place, the inherent axisymmetry of the cell is lost. This causes cross-sectional average quantities such as the particle volume fraction, the mean gas and solid velocities, and the granular temperature, to vary along the cell. Two such cell arrangements are shown in Fig. 5.6. The first involves two gas distributors that form a “co-flow” and a “counter-flow” region, in which the gas travels, respectively, along with, and against, the solids. The second arrangement used a third gas distributor to create an “iso-kinetic” region, where the overall gas pressure gradient is kept as close to zero as possible.

Our objective is to evaluate flow development in the axisymmetric shear cell of Louge *et al* [83]. We achieve this with two analyses. First, we design a granular development theory similar to that presented earlier, and we compare its results with numerical simulations. For this comparison, instead of creating a gas-solid simulation as sophisticated as that of Verberg and Koch [123], we exploit our molecular dynamic simulations of the granular phase to replace the gas pressure gradients by equivalent streamwise body forces. This permits us to capture the principal force that the gas exerts on the granular medium, without the complexity of treating the gas phase explicitly. In turn, this artifice gives us confidence in the simulation data, and it allows us to test the essence of the development theory. In the second analysis, we design another development theory with a more realistic

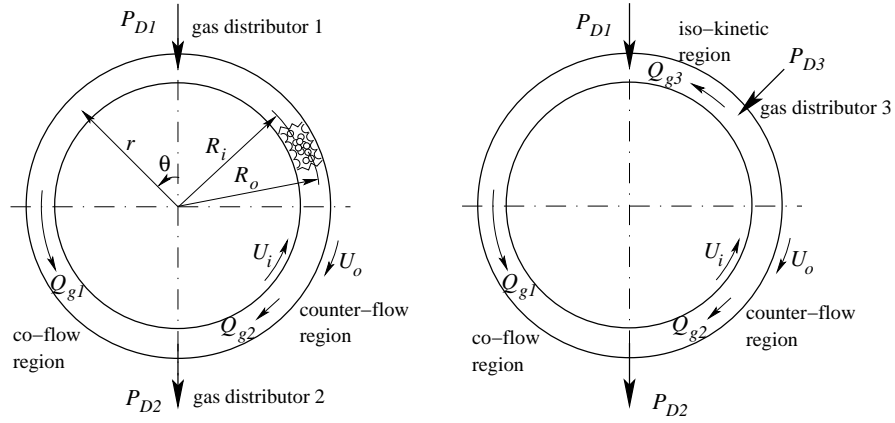


Figure 5.6: A sketch of the axisymmetric shear cell. Left: shear cell with two gas distributors separating the cell into a “co-flow” and a “counter-flow” region. Right: shear cell with three gas distributors. The third distributor creates an “iso-kinetic region” by maintaining $P_{D1} = P_{D3}$.

interaction between gas and solids. We begin with the formulation and results of the first, purely granular development analysis.

In the first analysis, the governing equations are similar to Eqs. (5.1)-(5.3), except that they are written in a cylindrical coordinate system. We choose the origin of the latter at the center of the cell, with the z axis perpendicular to the flat side walls. As in our analysis of the straight channel, we assume that the mean particle velocity in the z direction vanishes, and we denote the components of mean velocity in the streamwise θ -direction and the transverse r -direction as u

and v , respectively. Then, the conservation equations are

$$\frac{\partial \rho u}{r \partial \theta} + \frac{1}{r} \frac{\partial r \rho v}{\partial r} = 0, \quad (5.17)$$

$$\frac{\partial}{r \partial \theta} (\rho u u) + \frac{1}{r^2} \frac{\partial}{\partial r} (r^2 \rho u v) = - \frac{\partial P}{r \partial \theta} + \frac{\partial \tau_{\theta\theta}}{r \partial \theta} + \frac{1}{r^2} \frac{\partial}{\partial r} (r^2 \tau_{r\theta}) + \frac{\partial \tau_{\theta z}}{\partial z} + \rho f_{\theta}, \quad (5.18)$$

$$\begin{aligned} \frac{3}{2} \left[\frac{\partial}{r \partial \theta} (\rho u T) + \frac{1}{r} \frac{\partial}{\partial r} (r \rho v T) \right] &= - \frac{\partial q_{\theta}}{r \partial \theta} - \frac{1}{r} \frac{\partial r q_r}{\partial r} - \frac{\partial q_z}{\partial z} - P \left(\frac{\partial u}{r \partial \theta} + \frac{1}{r} \frac{\partial r v}{\partial r} \right) \\ &+ P_{prod} - \gamma_{inelas}, \end{aligned} \quad (5.19)$$

where f_{θ} is the streamwise body force and P_{prod} is the production of fluctuation energy due to viscous stresses.

We invoke the same assumptions as in our earlier treatment of straight channels, namely,

1. $v \ll u$ and $\partial/r \partial \theta \ll \partial/\partial r$;
2. $\nu = \nu(\theta)$ and $T = T(\theta)$;
3. $\tau_{\theta z} = \frac{2z}{W} \tau_{\theta z} \Big|_{z=W/2}$;
4. $u = u(r, \theta) = \bar{u}(\theta) - \bar{u}_{FD} + u_{FD}(r)$.

The fully developed velocity profile then derives from the momentum equation

$$\frac{1}{r^2} \frac{d}{dr} \left[r^3 \frac{d}{dr} \left(\frac{u_{FD}}{r} \right) \right] = \frac{1}{\eta} \left(\frac{2}{W} \frac{\tau_{\theta z}|_{z=W/2}}{P} - \rho f_x \right). \quad (5.20)$$

The boundary conditions are $u_{FD}(r = R_i) = u_{i,FD}$ and $u_{FD}(r = R_o) = u_{o,FD}$, where the inner and outer radii R_i and R_o are respectively defined as the distance from the cell center to the flow sphere center touching the crest of the half cylinders on the inner and outer boundaries (Fig. 5.6).

To characterize the axisymmetric geometry in a simple way, we define the parameter $\delta \equiv H/R$, where $H \equiv R_o - R_i$ is the channel height and $R \equiv (R_i + R_o)/2$

is the average channel radius. We then express the velocity profile in terms of δ , but ignore terms of order δ^2 or higher. Therefore, the velocity profile in the fully developed state is

$$u_{FD}(r) = \bar{u}_{FD} - \frac{1}{24}A + u_{sh}r^* + \frac{1}{2}Ar^{*2} \quad (5.21)$$

$$+ \delta \left[u_{sh} \left(\frac{1}{24} - \frac{1}{2}r^{*2} \right) + \frac{1}{6}A \left(\frac{1}{4}r^* - r^{*3} \right) \right], \quad (5.22)$$

where $r^* \equiv (r - R)/H$,

$$A = U \frac{5\sqrt{\pi}F}{2J} \frac{H}{\sigma} T_{FD}^{*1/2} \left(\frac{2H}{W} \frac{u_{i,FD} + u_{o,FD}}{|u_{i,FD}| + |u_{o,FD}|} \mu_{sw} - \frac{Fr_x \frac{H}{\sigma}}{4FGT_{FD}^{*1/2}} \right), \quad (5.23)$$

and the constant u_{sh} has the same meaning as in Section 5.1. To obtain Eq. (5.23), we extend Eq. (5.13) by allowing the two boundaries to move in opposite directions. In that case, to account for the effect of side walls on the mean velocity profiles, we integrate the shear stresses on these walls using the ‘‘all-sliding’’ boundary condition of Jenkins [50], and we enforce a sign on the frictional stresses that is opposite to the direction of the local mean velocity at the wall.

We then integrate the conservation equations in the z - and r -directions to find the evolution of any cross-sectional averaged flow variables along θ defined as

$$\bar{\psi}(\theta) \equiv \frac{1}{HW} \int_{R_i}^{R_o} \int_{-W/2}^{W/2} \psi(r, \theta, z) dz dr,$$

where ψ represents any flow variable of interest. We express the result in terms of R , H and keep only terms of order δ . We also use the fact that $v = 0$ at both $r = R_i$ and $r = R_o$, and we evaluate $\partial v / \partial r$ using the continuity equation.

The resulting mass conservation in dimensionless form is the same as for straight channels,

$$\nu \bar{u}^* = Q^* = \text{constant}. \quad (5.24)$$

The momentum conservation is slightly different,

$$\begin{aligned} \frac{d^2\nu}{dx^{*2}} + \frac{1}{K^*} \left\{ \frac{dK^*}{dx^*} - \frac{L}{H} \left[\left(\frac{Q^*}{\nu} \right)^2 - \left(\frac{u_{sh}^*}{12} + \frac{A^{*2}}{720} + \delta \frac{A^* u_{sh}^*}{180} \right) \right] \right\} \frac{d\nu}{dx^*} \\ - \nu \frac{Fr_\theta}{K^*} \frac{L^2}{H\sigma} + \frac{L}{H} \frac{1}{K^*} \frac{dP^*}{dx^*} \\ - \frac{L^2}{H^2} \frac{P^*}{K^*} \left[(1-\delta) \left(\frac{S}{N} \right)_i - (1+\delta) \left(\frac{S}{N} \right)_o - \frac{2H}{W} \mu_{sw} \right] = 0, \end{aligned} \quad (5.25)$$

where $x^* \equiv \theta/2\pi$, $L \equiv 2\pi R$, the velocity scale U is the relative velocity between the inner and outer boundary, $U \equiv U_i - U_o$, and

$$Fr_\theta \equiv \frac{f_\theta \sigma}{U^2},$$

is the Froude number defined earlier. Other variables are defined in Section 5.1.

The dimensionless energy conservation equation is

$$\begin{aligned} \frac{d^2T^*}{dx^{*2}} + \frac{1}{\kappa^*} \left(\frac{d\kappa^*}{dx^*} - \frac{3L}{2H} Q^* \right) \frac{dT^*}{dx^*} + \frac{L^2}{\sigma^2} \frac{1}{M} \left[\frac{5\pi F^2}{6J} \mu_{sw}^2 - 6(1 - e_{eff}) \right] T^* \\ + \frac{L^2}{H^2} \left[u_{sh}^{*2} + \frac{A^*}{12} + \delta \left(2\bar{u}^* + \frac{1}{6} A^* u_{sh}^* \right) \right] \frac{\eta^*}{\kappa^*} \\ + \frac{L^2}{H^2} \frac{P^* \sqrt{T^*}}{\kappa^*} \left[\frac{2H}{W} q_z^* + \left(1 - \frac{1}{2} \delta \right) q_{y,i}^* + \left(1 + \frac{1}{2} \delta \right) q_{y,o}^* \right] \\ + \frac{10 + 8J}{15M} \left(\frac{d\bar{u}^*}{dx^*} \right)^2 \left\{ 1 + \frac{1}{\bar{u}^*} \left[\frac{1}{12} u_{sh}^{*2} + \frac{1}{720} A^{*2} - \delta u_{sh}^* \left(\frac{1}{6} \bar{u}^* + \frac{1}{180} A^* \right) \right] \right\} \\ - \frac{L}{H} \frac{1}{\kappa^*} \frac{d\bar{u}^*}{dx^*} \left[P^* + \delta \frac{1}{12} \frac{u_{sh}^*}{\bar{u}^*} \nu \left(\bar{u}^{*2} + \frac{1}{20} u_{sh}^{*2} + \frac{1}{720} A^{*2} \right) \right] = 0. \end{aligned} \quad (5.26)$$

We use Eqs. (5.24)-(5.26) to determine the evolution of ν , \bar{u}^* and T^* in the axisymmetric cell. To that end, we specify the total number of particles in the cell or, equivalently, the average volume fraction $\bar{\nu}$ in the entire channel. The solution then fixes the dimensionless flow rate Q^* . At the gas injection and withdrawal, we prescribe that both the particle volume fraction and the granular temperature

vary smoothly around the gas distributors, i.e.,

$$\nu(\theta_{Di} +) = \nu(\theta_{Di} -), \quad (5.27a)$$

$$\frac{d\nu}{d\theta}(\theta_{Di} +) = \frac{d\nu}{d\theta}(\theta_{Di} -), \quad (5.27b)$$

$$T(\theta_{Di} +) = T(\theta_{Di} -), \quad (5.27c)$$

$$\frac{dT}{d\theta}(\theta_{Di} +) = \frac{dT}{d\theta}(\theta_{Di} -), \quad (5.27d)$$

where θ_{Di} is the angular position of gas distributor Di , $i = 1, 2, 3$.

Figure 5.7 compares the predictions of the theory with computer simulations in which a streamwise body force is imposed on flowing spheres. To simulate the continuously varying gas pressure with two gas distributors, the body force in the “counter-flow” region is chosen to match the body force in the “co-flow” region such that

$$f_{\theta,co} \int_0^{\theta_{D2}} \nu d\theta + f_{\theta,cf} \int_{\theta_{D2}}^{2\pi} \nu d\theta = 0, \quad (5.28)$$

where $f_{\theta,co}$ and $f_{\theta,cf}$ are the body forces in the co-flow and the counter-flow regions, respectively, $\theta_{D1} = 0$, and θ_{D2} is the angular position of the gas distributor $D2$. The restriction on the body force in Eq (5.28) mimics a drag force that is proportional to the solid volume fraction, and a corresponding gas pressure gradient that is continuous across the distributors.

As expected, a larger body force produces stronger variations of particle volume fraction along the channel and, on average, a larger mean velocity and granular temperature. For this cell, the flow becomes fully developed in both the co-flow and the counter-flow regions for body forces that are representative of the drag forces expected in the experiments of Louge *et al* [83].

As Fig. 5.7 shows, the theoretical predictions agree reasonably well with numerical simulations. However, there are two possible reasons why quantitative

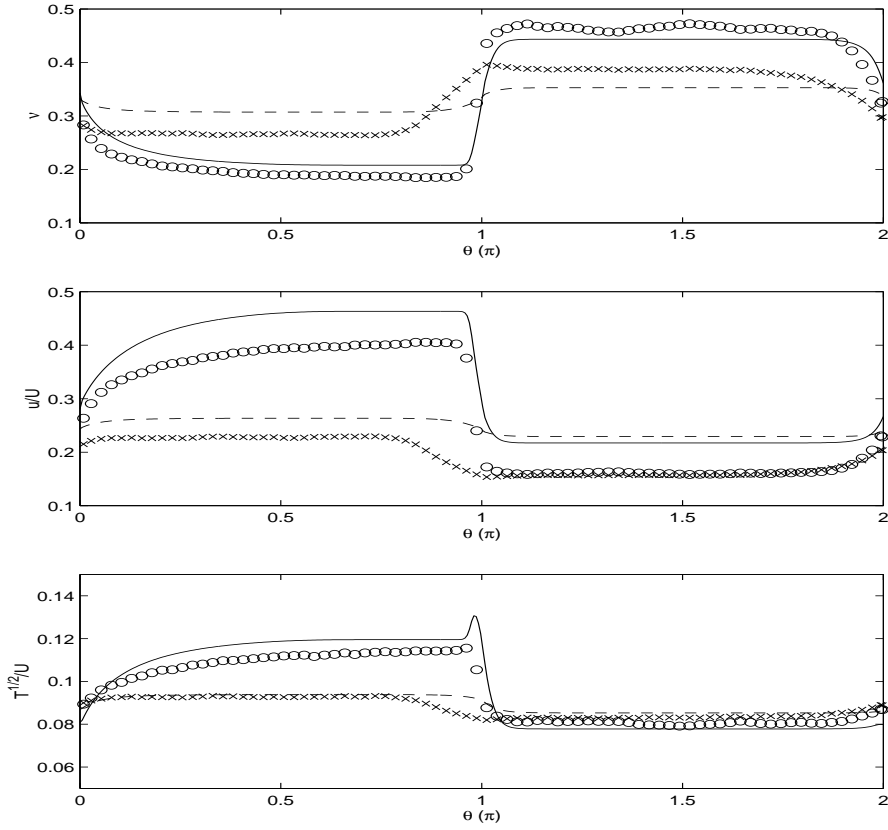


Figure 5.7: Theoretical predictions and simulation data for the flow development in an axisymmetric cell with two gas distributors. Top plot: $\nu(\theta)$, middle plot: $\bar{u}^*(\theta)$, bottom plot: $\sqrt{T^*}(\theta)$. The abscissa represents the angle θ defined in Fig. 5.6 in multiples of π . The “co-flow” region lies in the range $0 \leq \theta \leq \pi$. Symbols and lines represent simulations and theory. Circles and solid lines: $Fr_{\theta,co} = 0.00083$; crosses and dashed lines: $Fr_{\theta,co} = 0.00017$. Eq. (5.28) provides the corresponding values for $Fr_{\theta,cf}$ in the counter-flow region. Simulation parameters: $R_i = 211$, $R_o = 224$, $W = 17.4$, $\sigma = d_o = 2$, $d_i = 3$, $s_i = s_o = 0$, $U_i = U$, $U_o = 0$, and $\theta_{D2} = \pi$. The overall loading is $\bar{\nu} = 0.33$, Impact properties of flow spheres: $e = 0.95$, $\mu = 0.1$, $\beta_0 = 0.4$; bumpy boundaries and flat side walls: $e_w = e_{sw} = 0.85$, $\mu_w = \mu_{sw} = 0.1$, and $\beta_{0,w} = \beta_{0,sw} = 0.4$.

agreement is not as good as in the case of straight channels. First, the effects of centripetal accelerations are only treated to first order in δ . Second, while our analysis of straight channels borrows inlet and exit flow data from simulations, its counterpart for the axisymmetric cell only requires the average volume fraction in the entire cell and the speed of the inner boundary before predicting all other flow variables.

Figure 5.8 shows how the separation between the inlet and outlet distributors affects flow development. As the co-flow region narrows, the flow does not develop fully in this region, a feature that the theory captures well.

A practical design advantage of the axisymmetric cell over the race track is that both its inner and outer boundaries can move independently. However, because it is bounded by stationary side walls, flows in the axisymmetric cell are not only set by the relative velocity between the two moving boundaries, but they depend instead on the individual speed of each.

Figure 5.9 illustrates this point with one cell moving at $U_i = U$ and $U_o = 0$, and the other with $U_i = 0.75U$ and $U_o = -0.25U$. In the latter, the opposite motion of the two boundaries results in a smaller net average particle velocity. In this case, the diffusion becomes more important and the co-flow region experiences high volume fractions farther upstream, thus displacing the fully developed region in the same direction.

5.3 Granular Flow in a Shear Cell Shaped as a Race Track

In the previous two sections, we analyzed the development of collisional granular flows in straight, rectilinear channels and in axisymmetric cells. By combining the theory in Section 5.1 for straight regions and that in Section 5.2 for curved regions,

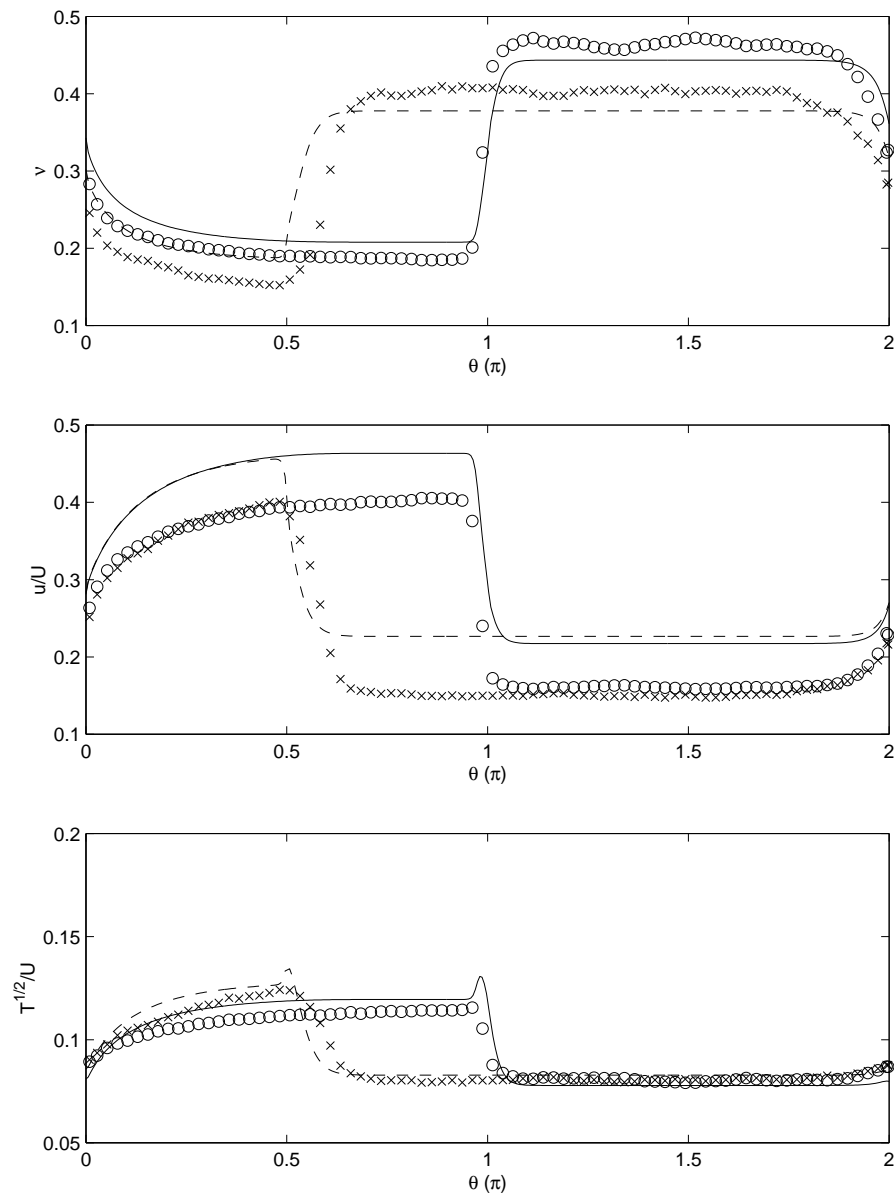


Figure 5.8: Effect of gas distributor separation on flow development in the axisymmetric cell for $Fr_{\theta,co} = 0.00083$. Circles and solid lines: gas distributor $D2$ at $\theta_{D2} = \pi$; crosses and dashed lines: $\theta_{D2} = \pi/2$. For other symbols and parameters, see Fig. 5.7.

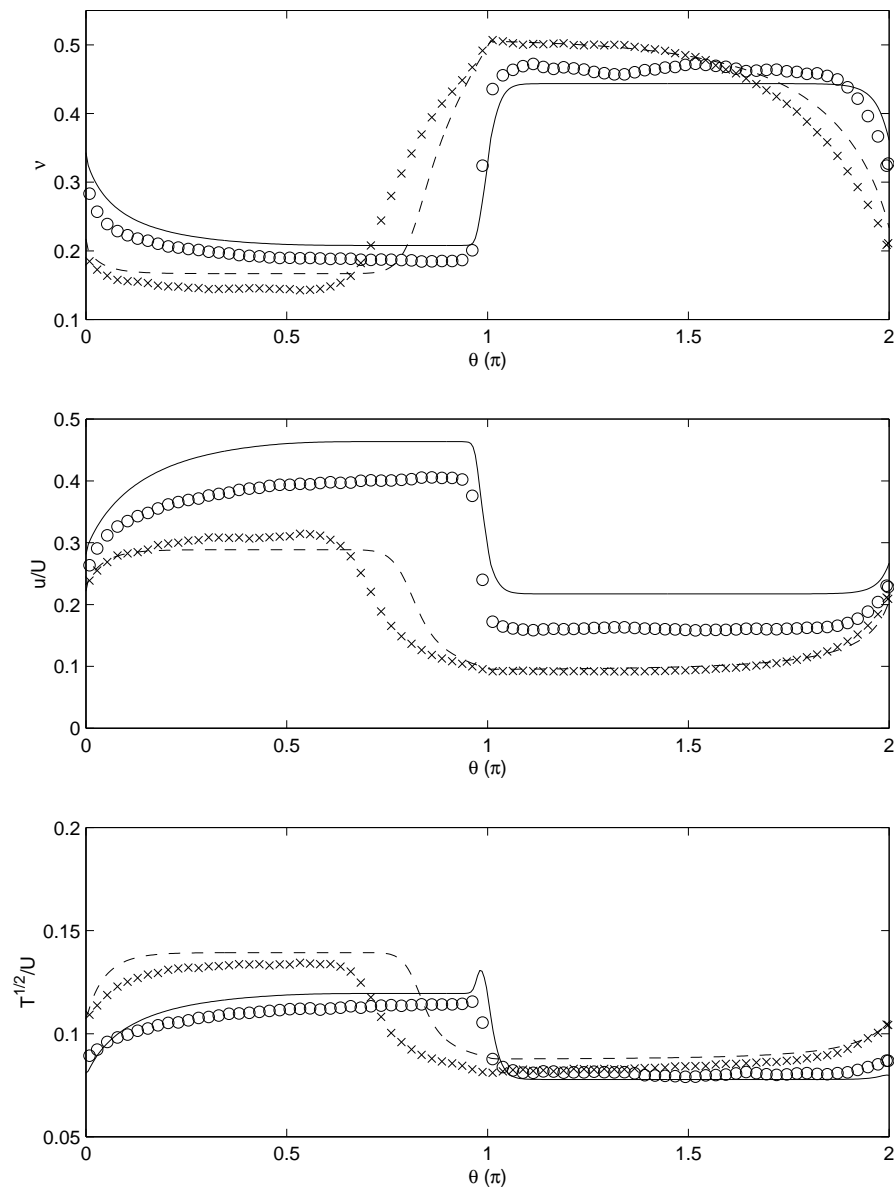


Figure 5.9: Effect of boundary velocities on flow development in an axisymmetric cell for $Fr_{\theta,co} = 0.00083$ and $\theta_{D2} = \pi$. Circles and solid lines: $U_i = U$ and $U_o = 0$; crosses and dashed lines: $U_i = 0.75U$ and $U_o = -0.25U$. For other symbols and parameters, see Fig. 5.7.

we can now predict the flow development in the entire race track shear cell.

Unlike the analysis for straight sections, we no longer require any input from the simulations. Instead, we assume continuity and smoothness of the particle volume fraction and granular temperature at junctions between straight and curved regions, Eq. (5.27). We only specify the overall loading $\bar{\nu}$ in the cell. In the absence of external forces, symmetry permits us to solve in only a half cell.

Figure 5.10 compares theoretical prediction and computer simulations for two different race tracks. In the first, the side walls are smooth. In the second, they are frictional. As discussed in Section 5.1, friction slows down the flow and increases the relative importance of diffusion. The theory captures the phenomena qualitatively. We attribute discrepancies to the relatively small radius $\delta \equiv H/R = 1/5.4$ of the curved regions, which exacerbates centripetal accelerations that the theory only treats to first order in δ .

5.4 Gas-particle Flow in an Axisymmetric Shear Cell

In previous sections, we analyzed the development of collisional granular flows in various geometries, with and without body forces. In Chapter 4, we also gained confidence in a theory for semi-infinite shear flows of solids in a viscous gas, albeit without a significant relative velocity between the two phases. The agreement between theory and simulations encourages us to extend our analysis of flow development to gas-solid suspensions. Our objective is to prescribe conditions for the microgravity experiments that Louge *et al* [83] proposed for an axisymmetric shear cell. Because numerical simulations involving gas and solids in the entire cell are not yet available to test the theory, our predictions are only meant to provide guidance for the design of experiments.

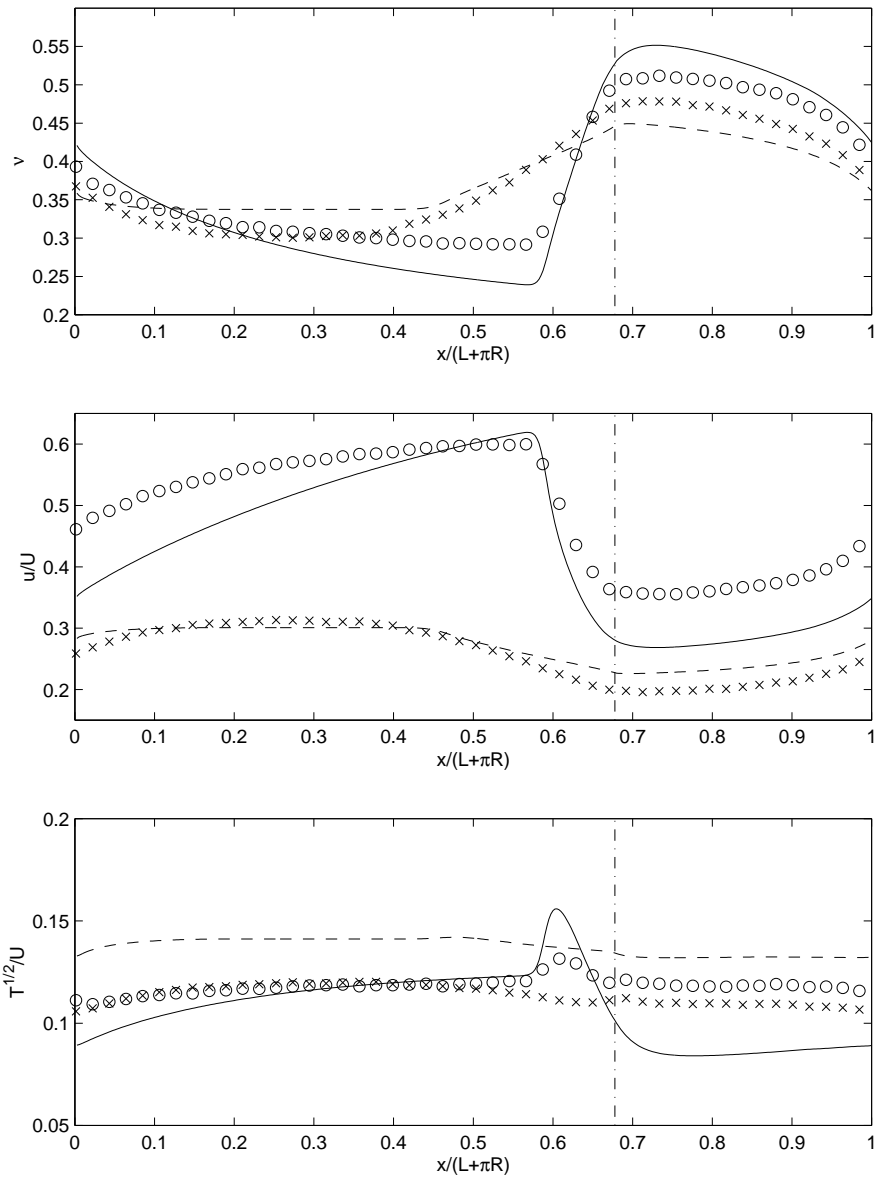


Figure 5.10: Flow development in a race track over half the cell. Circles and solid lines: smooth side walls; crosses and dashed lines: frictional side walls with $\mu_{sw} = 0.1$. The dash-dotted line indicates the junction of the straight and curved sections. The latter is located to the right of this vertical line. For other symbols and parameters, see Fig. 5.7.

We analyze the development of the gas-particle flow in axisymmetric shear cells sketched in Fig. 5.6. The imposed gas pressure gradient produces variation of particle volume fraction, mean velocity, and granular temperature along the cell. As in Chapter 4, we consider cases where the particle inertia is too large for the viscous forces to alter the granular velocity distribution significantly, so that all constitutive relations for the particle phase remain unchanged. Moreover, we assume that the gas pressure gradient is large enough for the drag force to dominate the viscous stresses due to velocity gradients in the gas phase. Therefore, the conservation equations for the granular phase are nearly identical to Eqs. (5.24)-(5.26). The only differences are that the Froude number Fr_θ in Eq. (5.25) is replaced by $(\sigma/H)^2 R_\tau/\nu$ and that the viscous dissipation γ_{vis} is added to Eq. (5.26) for the conservation of fluctuation energy.

The dimensionless pressure gradient is defined as

$$R_\tau \equiv \frac{-(dP_g/Rd\theta)}{\rho_s \sigma (U/H)^2}. \quad (5.29)$$

Note that this definition of R_τ is based on the local gas pressure gradient, which is not necessarily constant along the cell. In physical experiments, it is more convenient to define a dimensionless pressure gradient based on the overall pressure drop as

$$R_{\tau,\text{exp}} \equiv \frac{(P_{D2} - P_{D1})/R(\theta_{D2} - \theta_{D1})}{\rho_s \sigma (U/H)^2}. \quad (5.30)$$

Although R_τ differs numerically from $R_{\tau,\text{exp}}$, the two measures of the gas pressure gradient generally vary in tandem.

The mass conservation for the gas phase is

$$(1 - \nu)\bar{u}_g^* = Q_g^*, \quad (5.31)$$

where $\bar{u}_g^* \equiv \bar{u}_g/U$, and \bar{u}_g is the cross sectional average gas velocity. However,

in practical experiments, it is not straightforward to prevent gas from leaking through the four corners of the channel, where the rotating boundaries hover near the stationary walls of the cell. Such leaks can occur in thin channels of length L_l and thickness equal to the clearance gap δ_l between stator and rotor. A common situation is that the gas leaks from the flow channel to large voids of nearly constant pressure P_{ext} . In the presence of such leaks, the volume flow rate Q_g^* is not a constant. Because a typical leak occurs over a path $L_l \ll R$, the leak rate can be approximated by a simple one dimensional viscous flow in a thin channel, i.e.,

$$\frac{dQ_g^*}{dx^*} = \frac{\delta_l^3}{12L_l A_c} \frac{P_g - P_{ext}}{\mu_g U / 2\pi R}, \quad (5.32)$$

where $x^* \equiv \theta/2\pi$ and A_c is the cross-sectional area of the channel that is used to make the gas flow rate dimensionless, $Q_g^* \equiv Q_g/UA_c$. In our calculations, we assume that the void pressure equilibrates to the average pressure between inlet and outlet, $P_{ext} = (P_{D1} + P_{D2})/2$, unless specified otherwise.

Because in the relatively dense situations of interest the viscous stresses and inertia of the gas are smaller than the drag force or the gas pressure gradient, the gas momentum equation reduces to a balance between the latter two terms. In dimensionless form,

$$\frac{dP_g^*}{dx^*} = \frac{(2\pi R)^2 \beta}{(1 - \nu)\mu_g} (\bar{u}_s^* - \bar{u}_g^*), \quad (5.33)$$

where $P_g^* \equiv P_g / \frac{\mu U}{2\pi R}$ is the dimensionless gas pressure and \bar{u}_s^* is the dimensionless average solid velocity.

Following our treatment of granular flow in the axisymmetric cell, we assume that the particle volume fraction and the granular temperature are continuous and smooth at the gas distributors, see Eq. (5.27). In the gas phase, pressure is known at these locations.

Note that because the inertia and viscous stresses in the gas are ignored, the gas velocity changes abruptly as gas is added or withdrawn at the distributors. In our approach, this implies that the drag force is artificially discontinuous there. A more rigorous treatment would require to evaluate the three-dimensional gas and solid flow in the vicinity of the distributors. Because our interest resides where the flow is fully developed, and because these regions are far from the distributors, the discontinuities are not serious.

For given gas pressures at the inlet and outlet, for known velocities of the inner and outer boundaries, and for a specified overall solid volume fraction, Eqs. (5.24)-(5.26) are solved together with Eqs. (5.32) and (5.33) using initial guesses for the volume flow rate of solids in the entire cell and the corresponding quantity for the gas right after each distributor. The guesses are then adjusted until the total volume fraction of solids in the cell and the pressure difference across each region converge to the values imposed. Because of the nonlinearity of the problem, we use a modified Newton-chord method [99] to carry out the corresponding iterations. For given pressure differences across the distributors, the solution yields the solid mass flow rate and the gas flow rates in the co-flow, counter-flow and, if used, the iso-kinetic regions. As mentioned earlier, while the solid volume flow rate is unique along the cell, its counterpart in the gas changes abruptly at the distributors.

Figure 5.11 shows predictions of gas pressure, solid and gas velocities, solid volume fraction and granular temperature for two different Stokes number but the same dimensionless gas pressure gradient $R_{\tau,\text{exp}}$. Because $R_{\tau,\text{exp}}$ measures the gas pressure gradient relative to the solid phase shear stress, the same $R_{\tau,\text{exp}}$ implies that the particle motion remains unchanged, as illustrated in Fig. 5.11. However, because a larger Stokes number is associated with a larger solid phase stress, the

drag force exerted by the gas must be larger to maintain the same solid velocity, which in turn implies larger relative velocities between particles and gas.

As Fig. 5.12 illustrates, gas leaks along the channel modify the gas flow rate between distributors, and the gas velocity changes accordingly. In their presence, it is more difficult for the flow to become fully developed.

A significant experimental challenge is to measure the gas velocity in the presence of a concentrated suspension of large spheres. A method is to inject enough gas through a third distributor to equalize the mean gas and solid velocity over most of the channel cross-section in a short “isokinetic” region of the cell. Typically, the third gas distributor may be located near the injector $D1$. A sensitive control system then maintains the difference between the pressures at $D3$ and $D1$ as small as possible by injecting gas that is delivered by a servo-controlled valve.

To evaluate the effectiveness of the isokinetic region and its effect on flow development, Figure 5.13 compares two cells with two or three distributors. As this Fig. shows, the mean gas and particle velocities are nearly indistinguishable in the iso-kinetic region. Thus, if the volume fraction can be independently measured in the isokinetic region, it is possible to infer the gas volume flow rate there, and from the knowledge of the inlet and outlet volume flow rates, to calculate the corresponding quantities in all regions of the cell.

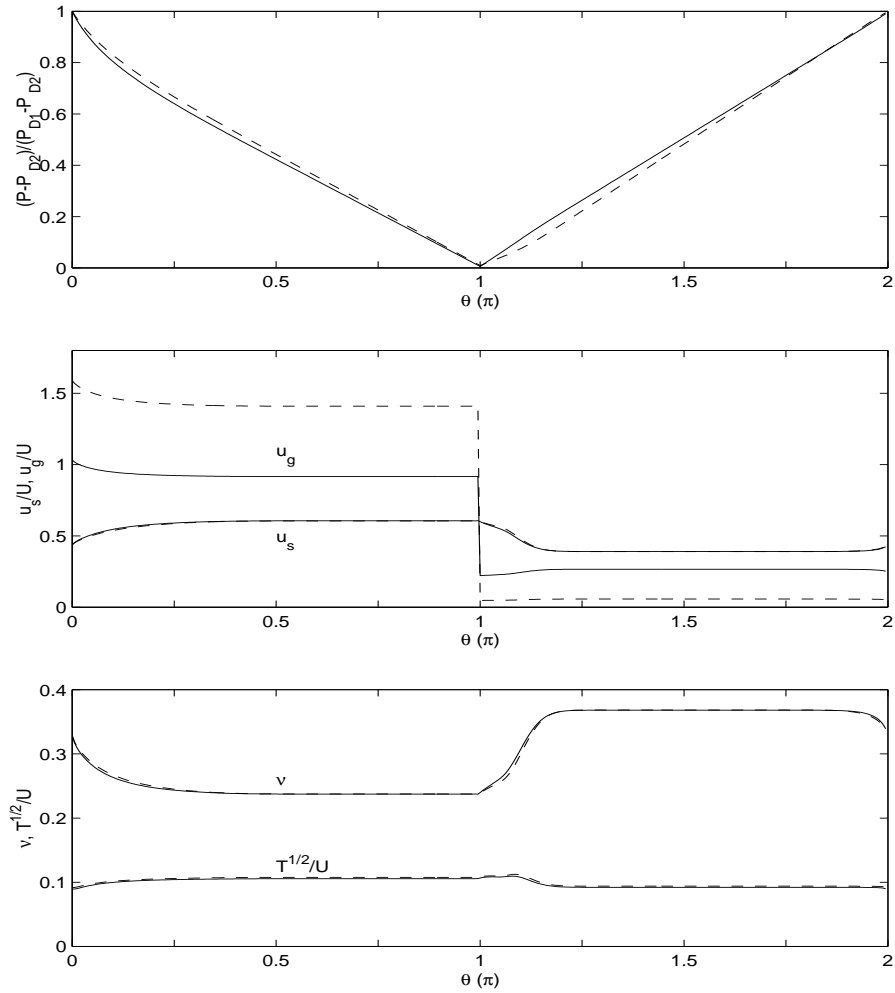


Figure 5.11: Predictions of gas-particle flows with different Stokes numbers in an axisymmetric cell with two distributors separated by π . Top plot: gas pressure $\frac{P_g - P_{D2}}{P_{D1} - P_{D2}}$, where P_{D1} and P_{D2} are the gas pressures at distributors $D1$ and $D2$, respectively. Middle plot: average solid velocity \bar{u}_s^* and gas velocity \bar{u}_g^* . Bottom plot: ν and $\sqrt{T^*}$. Solid lines: predictions for $St = 400$. Dashed lines: $St = 1000$. Simulation parameters: $R_i = 212$, $R_o = 226$, $W = 18$, $d = d_i = d_o = 2$, $s_i = 1$, $s_o = 0$, $\bar{\nu} = 0.3$, $R_{\tau, \text{exp}} = 0.008$. There are no leaks along the channel. Impact parameters for spheres: $e_{\text{eff}} = 0.85$; for all other impacts: $e = 0.85$, $\mu = 0.1$ and $\beta_0 = 0.4$.

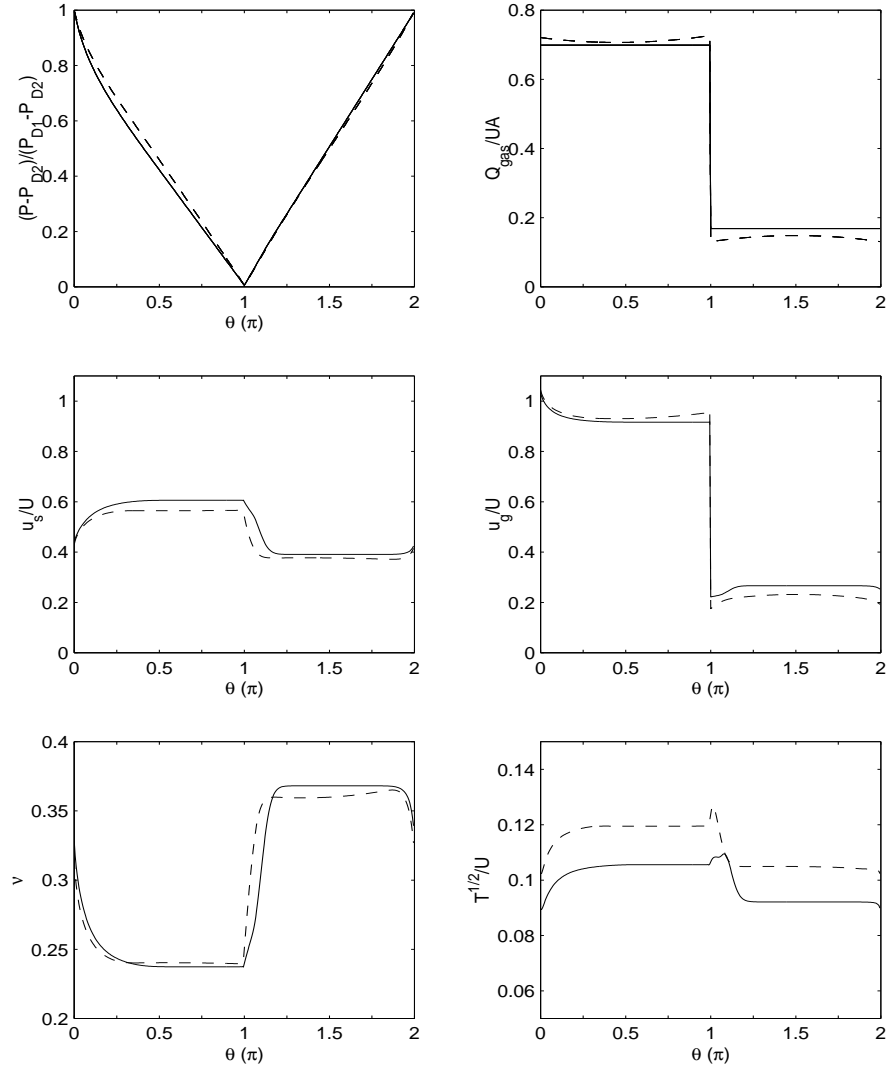


Figure 5.12: Predicted effects of gas leak on gas-particle flows in an axisymmetric cell with two distributors separated by π for a Stokes number $St = 400$. Top left: gas pressure $\frac{P_g - P_{D2}}{P_{D1} - P_{D2}}$, top right: dimensionless gas flow rate Q_g^* , middle left: \bar{u}_s^* , middle right: \bar{u}_g^* , bottom left: ν , bottom right: $\sqrt{T^*}$. Solid lines: predictions for a cell without leaks. Dashed lines: leak path length $L_l/R = 0.0688$ and clearance $\delta_l/L_l = 0.0133$. For all other parameters, see Fig. 5.11.

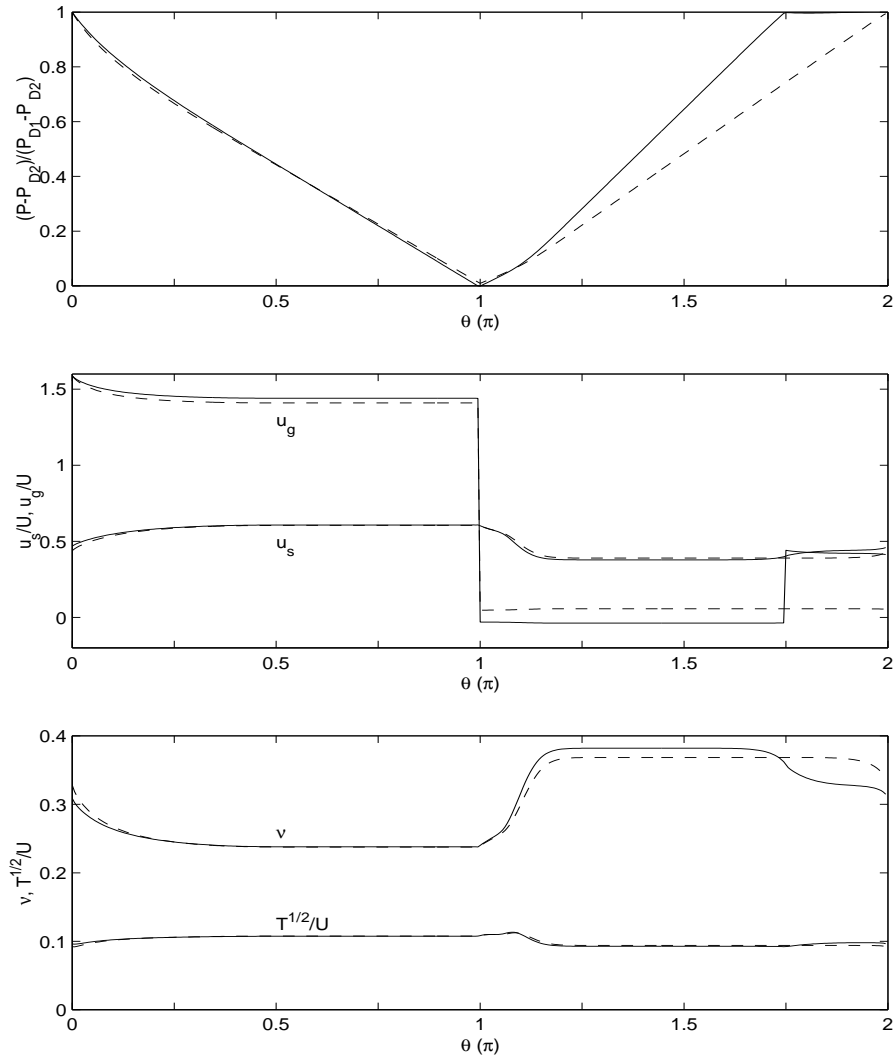


Figure 5.13: Predicted effects of the isokinetic region on the flow development in an axisymmetric cell with $St = 1000$. Top plot: gas pressure ratio $\frac{P_g - P_{D2}}{P_{D1} - P_{D2}}$, where P_{D1} and P_{D2} are pressures at the distributors for injection and withdrawal, respectively. Middle plot: average solid velocity \bar{u}_s^* and gas velocity \bar{u}_g^* . Bottom plot: particle volume fraction ν and fluctuation velocity $\sqrt{T^*}$. Solid lines: with three gas distributors, $D1$ at $\theta = 0$, $D2$ at π and $D3$ at $\frac{7}{4}\pi$. Dashed lines: with two distributors separated by π . For all other parameters, see Fig. 5.11.

Chapter 6

Measurement Errors in the Mean

Velocity and Granular Temperature

Flowing granular assemblies consist of a large number of discrete solid particles. Experimental measurements of particle velocity, density, and velocity fluctuation are crucial to the understanding of these flows and to the development of successful theories.

Several techniques are available to achieve such measurements. For example, positron emission particle tracking [100] and nuclear magnetic resonance [34] do not invade the flow and provide unique information in the interior of the granular material. However, these techniques are expensive and complex [71, 114, 96, 97, 136].

An alternative is to observe the flow through side walls with high-speed digital photography. This method is suitable for flows of spherical grains in which interior particles have similar velocity statistics than those near the observation windows [81, 10, 41]. It was also used in flows of a particle monolayer [132, 122] and in colloids [26]. In this technique, the camera captures successive digital images of the grains, thus yielding a series of instantaneous positions from which velocity statistics can be inferred.

Here, we focus on “rapid” granular flows, in which particles interact with one another through impulsive collisions rather than long-lasting contacts. Two parameters are of particular interest to the theoretical interpretation of such flows [81]. They are the average velocity u_k and the “granular temperature” $T_{kk} \equiv \langle u_k'^2 \rangle$ in the direction k , where $\langle \rangle$ means averaged quantities, $u_k \equiv \langle u_k^p \rangle$, $u_k' \equiv u_k^p - u_k$,

and u_k^p is the instantaneous particle velocity in direction k . Generally, observations through windows only permit the determination of the two components of u_k and T_{kk} in the plane of the window.

Because meaningful velocity statistics requires many images, the determination of particle positions and their tracking rely on automatic image processing. This paper describes an algorithm developed for this purpose. The accuracy of the software is predicated upon its ability to detect individual particles on a digital image, to track the detected spheres in two or more consecutive frames, and to measure the distance traveled.

This technique has four principal limitations. The first is associated with the size of image pixels. The second reflects the software's inability to track fast-moving spheres. The third has to do with the possible occurrence of collisions between two consecutive images. The last is associated with the finite size of the strips that partition images of the flow domain to evaluate profiles of the mean flow variables. We provide a statistical theory to calculate the corresponding errors in the time-average particle velocity and the granular temperature. We validate the theory against numerical simulations of typical granular flows, and we use it to prescribe ways to minimize such errors.

6.1 Vision Algorithm

We conducted microgravity experiments with solid spheres interacting in a series of short binary collisions [81]. The flow was sheared between a moving and a stationary boundary on which cylindrical bumps were attached. The rectangular channel was further bounded in its depth by two flat walls, one of which served as an observation window.

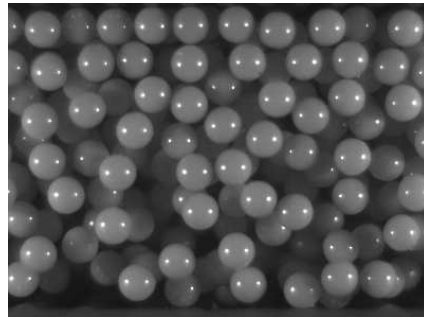
A Kodak EktaPro R0 camera recorded the motion of the spheres by collecting 1000 digital images per second consisting of 512×384 square pixels on a 0 – 255 greyscale. The scene was illuminated by two light sources that created small specular reflections on otherwise diffusively reflective monochrome, single-size spheres of acrylic devoid of identifying marks. Figure 6.1(a) shows a 400×296 region of interest containing spheres having a diameter of 34 pixels (2.0 mm).

The objective of the computer vision algorithm is to track as many unoccluded (fully visible) spheres as possible. As the image sequence progresses, some spheres become occluded, while others emerge to be completely visible. Consequently, certain trajectories terminate before reaching the edge of the imaging region while others spontaneously arise at any location.

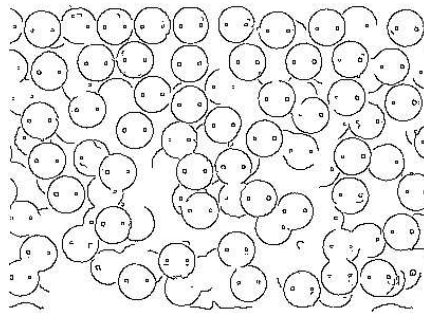
Our sphere tracking algorithm executes the following steps:

1. Compute a binary edge image containing all significant intensity transitions and consisting of lines of one-pixel width.
2. Partition the image into a set of non-overlapping circles by matching a binary sphere edge template to the result of step 1.
3. Record the locations of centers of spheres identified in step 2 as starting points for a set of trajectories.
4. Repeat steps 1 and 2 for the next image.
5. Reconcile the current set of trajectories with the sphere locations produced in step 4.

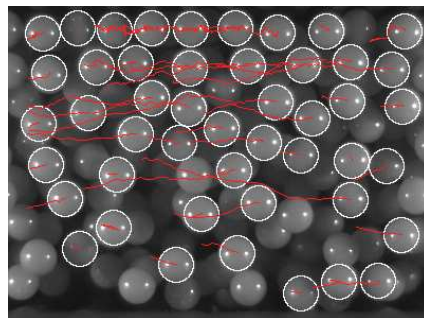
- (a) If a match is found between a sphere and a trajectory then the latter is extended by one step to the sphere center. If not, the trajectory is



(a) Original image



(b) Edge image



(c) Sphere trajectories

Figure 6.1: A typical image acquired in microgravity experiments with 2 mm acrylic spheres. The top stationary boundary and bottom moving boundary are barely distinguishable. Lighting on both sides produces specular spots on most spheres.

terminated.

- (c) If a sphere cannot be matched to an existing trajectory then its center becomes the starting point for a new trajectory.

6. Repeat steps 4-5 for all remaining images in the sequence.

The edge algorithm in step 1 is computed using gradient estimation followed by thresholding with hysteresis and non-maximum suppression [49]. The resulting edge image is shown in Figure 6.1(b). The image partitioning in step 2 involves the scanning of a binary template of a prototype circle over all possible pixel locations. A match requires that a given number of template pixels coincides with the edge image. If a conflict arises between two overlapping matches above the threshold, the match with the highest number of coincident pixels is selected. The result of step 1 are shown in Fig. 6.1(c). Because our spheres are indistinguishable, they are matched to a trajectory by proximity to their last known location. Thus, the algorithm of step 5 requires that the distance traveled from one image to the next be less than a maximum distance L_{tr} , which is generally smaller than, and proportional to, the radius of the sphere. This requirement places an upper bound on uF/d , where u is the projection of sphere velocity in the image plane, F is the camera frame rate and d is the sphere diameter. Equivalently, the algorithm loses track of spheres with speed larger than $U_{tr} = L_{tr}F$. Successful trajectories are shown by thin lines in Fig. 6.1(c).

If computation time is an issue, it is possible to achieve faster detection by limiting the processing to the immediate neighborhood of spheres having already been tracked in previous images. In this case, by ignoring the emergence of new spheres, the algorithm lets the population of detected objects shrink by gradual

occlusion. To avoid excessive corruption of the corresponding velocity statistics, the entire image is periodically reexamined for new spheres. Our experience is that a tradeoff can be found between the need for algorithmic speed and that of statistical accuracy.

6.2 Measurement Errors

In this section, we analyze errors that are intrinsic to the vision technique outlined earlier. We pay particular attention to errors in the granular temperature, which plays a crucial role in the dynamics of granular flows. Because granular temperature is a second moment of velocity fluctuations, its uncertainties can arise, for example, from correlated random velocity errors that would otherwise average to zero.

6.2.1 Imperfect Tracking

Because individual spheres are indistinguishable, the vision algorithm ignores large velocities in step 5, and thus it effectively truncates the velocity distribution function of the grains. Because the granular temperature is the second order central moment of the velocity distribution, the truncation modifies the granular temperature directly, as well as indirectly through errors in the mean velocity.

To predict the corresponding errors, we begin with general considerations of biased sampling. If the exact probability density function of a random variable x is $f(x)$ with

$$\int_{-\infty}^{\infty} f(x)dx = 1,$$

and if a measuring technique can only sample x within the interval $[a, b]$, the

probability density function of the sampled \tilde{x} is

$$\tilde{f}(\tilde{x}) = \begin{cases} \frac{1}{A}f & x \in [a, b] \\ 0 & \text{otherwise} \end{cases} \quad (6.1)$$

where

$$A \equiv \int_a^b f(x)dx$$

is a normalization constant for $\tilde{f}(\tilde{x})$, and the tilde represents the measured value of a variable. Then, the measured mean of x is

$$\tilde{\bar{x}} = \langle \tilde{x} \rangle = \int_{-\infty}^{\infty} \tilde{x} \tilde{f}(\tilde{x}) d\tilde{x} = \frac{1}{A} \int_a^b x f(x) dx = \bar{x} + \frac{1}{A} \int_{a-\bar{x}}^{b-\bar{x}} x' f dx' \quad (6.2)$$

where $\bar{x} \equiv \int_{-\infty}^{\infty} x f dx$ is the actual mean of x and $x' \equiv x - \bar{x}$ is the fluctuation.

Similarly, the measured variance of x is

$$\tilde{\sigma}_x^2 = \langle (\tilde{x} - \langle \tilde{x} \rangle)^2 \rangle = \langle (\tilde{x} - \bar{x})^2 \rangle - (\bar{x} - \tilde{\bar{x}})^2. \quad (6.3)$$

Substituting Eq. (6.2) into Eq. (6.3), we obtain

$$\tilde{\sigma}_x^2 = \frac{1}{A} \int_{a-\bar{x}}^{b-\bar{x}} (x')^2 f dx' - \left(\frac{1}{A} \int_{a-\bar{x}}^{b-\bar{x}} x' f dx' \right)^2. \quad (6.4)$$

We illustrate our analysis with steady, fully-developed granular flows in the rectangular channel mentioned earlier. For such flows, the mean velocity component normal to the moving boundary vanishes, and the observation technique only detects two components of particle velocity in the plane of the window. The limitations of particle tracking constrain detectable particle fluctuation velocities to lie within the circle in velocity space satisfying

$$C_y^2 + (u_x + C_x)^2 \leq U_{tr}^2, \quad (6.5)$$

where u_x is the mean granular velocity in the x -direction, and C_x and C_y are, respectively, particle fluctuation velocities in the x -direction of the mean flow and the y -direction perpendicular to the moving boundary.

Jenkins and Richman [59] derived the distribution of (C_x, C_y) for slightly inelastic spheres,

$$f(C_x, C_y) = \frac{1}{2\pi T} \left(1 - \sqrt{\frac{2}{\pi}} \frac{dB}{T^{3/2}} C_x \frac{\partial u_x}{\partial y} C_y \right) \exp \left(-\frac{C_x^2 + C_y^2}{2T} \right), \quad (6.6)$$

where $T = (\langle C_x^2 \rangle + \langle C_y^2 \rangle)/2$ is the granular temperature, d is the diameter of the spheres, $B = \pi(1 + 5/8G(\nu))/12\sqrt{2}$ is a correction to the Maxwellian distribution for dense flows, and $G(\nu) = \nu(2 - \nu)/2(1 - \nu)^3$ [22]. For simplicity, we assume that the granular temperature is isotropic, i.e.

$$T = \iint_{-\infty}^{\infty} C_x^2 f(C_x, C_y) dC_x dC_y = \iint_{-\infty}^{\infty} C_y^2 f(C_x, C_y) dC_x dC_y.$$

In principle, to calculate the measured mean velocity and granular temperature, we should substitute the velocity distribution into Eqs. (6.2) and (6.4). However, because the circular domain in Eq. (6.5) prohibits analytical integration, we approximate it by a square domain D ,

$$-(U_{tr} + u_x) \leq C_x \leq U_{tr} - u_x \quad \text{and} \quad -U_{tr} \leq C_y \leq U_{tr}. \quad (6.7)$$

to obtain analytical expressions for \tilde{u} and \tilde{T} . Because the square is larger than the circle, our analytical integrations underpredict the errors slightly. However, under typical conditions, we find negligible differences between the analytical results that follow and numerical integrations over the actual circular domain.

Using the square domain D , the measured mean velocity in the x -direction is

$$\tilde{u}_x = u_x + \frac{1}{A} \iint_D C_x f dC_x dC_y \quad (6.8)$$

where

$$A \equiv \iint_D f dC_x dC_y = \frac{1}{2} \operatorname{erf} \left(\frac{U_{tr}}{\sqrt{2T}} \right) \left[\operatorname{erf} \left(\frac{U_-}{\sqrt{2T}} \right) + \operatorname{erf} \left(\frac{U_+}{\sqrt{2T}} \right) \right]$$

with $U_+ \equiv U_{tr} + u_x$ and $U_- \equiv U_{tr} - u_x$. Upon evaluating the integral, we obtain

$$\tilde{u}_x = u_x - \sqrt{\frac{2T}{\pi}} \frac{\exp(-U_-^2/2T) - \exp(-U_+^2/2T)}{\operatorname{erf}(U_-/\sqrt{2T}) + \operatorname{erf}(U_+/\sqrt{2T})}. \quad (6.9)$$

Note that, because the correction term proportional to B in Eq. (6.6) is odd in C_y , it vanishes upon integrating over the domain D that is symmetric in C_y . Consequently, it does not affect \tilde{u}_x or, as we will later establish, the measured temperature in the x -direction. However, it does contribute to \tilde{u}_y , which only deviates from u_y if the velocity distribution is non-Maxwellian. With $u_y = 0$, we find

$$\tilde{u}_y = \frac{2B}{\pi} d \frac{\partial u_x}{\partial y} \left[1 - \frac{2}{\sqrt{\pi}} \frac{\frac{U_{tr}}{\sqrt{2T}} \exp(U_{tr}^2/2T)}{\operatorname{erf}(U_{tr}^2/2T)} \right] \left[\frac{\exp(-U_-^2/2T) - \exp(-U_+^2/2T)}{\operatorname{erf}(U_-/\sqrt{2T}) + \operatorname{erf}(U_+/\sqrt{2T})} \right]. \quad (6.10)$$

Upon carrying out the integrations in Eq. (6.4), we find

$$\begin{aligned} \frac{\tilde{T}_{xx}}{T} &= 1 - \frac{2}{\sqrt{\pi}} \frac{(U_-/\sqrt{2T}) \exp(-U_-^2/2T) + (U_+/\sqrt{2T}) \exp(-U_+^2/2T)}{\operatorname{erf}(U_-/\sqrt{2T}) + \operatorname{erf}(U_+/\sqrt{2T})} \\ &\quad - \frac{2}{\pi} \left[\frac{\exp(-U_-^2/2T) - \exp(-U_+^2/2T)}{\operatorname{erf}(U_-/\sqrt{2T}) + \operatorname{erf}(U_+/\sqrt{2T})} \right]^2, \end{aligned} \quad (6.11)$$

and

$$\frac{\tilde{T}_{yy}}{T} = 1 - \frac{2}{\sqrt{\pi}} \frac{(U_{tr}/\sqrt{2T}) \exp(-U_{tr}^2/2T)}{\operatorname{erf}(U_{tr}/\sqrt{2T})} - \frac{1}{T} (\tilde{u}_y)^2. \quad (6.12)$$

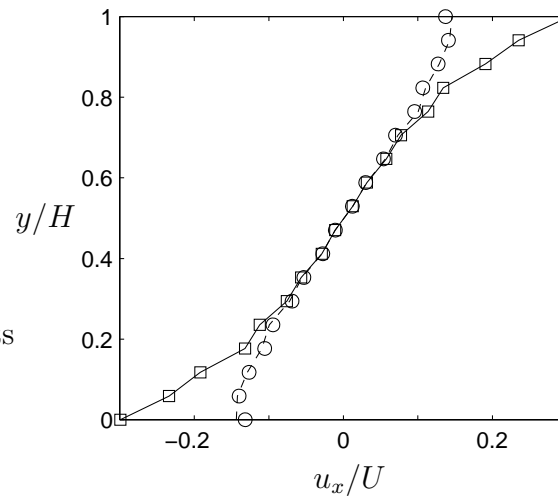
Molecular dynamic simulations provide a framework in which to isolate the contribution of imperfect tracking from other kinds of errors, and thus to test the predictions of Eqs. (6.9) to (6.12) with realistic velocity distributions. In these simulations [76], we shear spheres between two parallel bumpy boundaries moving at velocities U_t and U_b (as shown in Fig. 3.1), and apply a periodic boundary condition in the x -direction. We define the relative velocity between two boundaries as the characteristic velocity $U \equiv U_t - U_b$. The characteristic length H is the

distance in y -direction between two sphere centers touching the crest of bumps on top and bottom boundaries, respectively. The origin of the coordinates is chosen to be in the center plane between the two flat side walls and at a sphere radius above the crest of a bump on the bottom boundary.

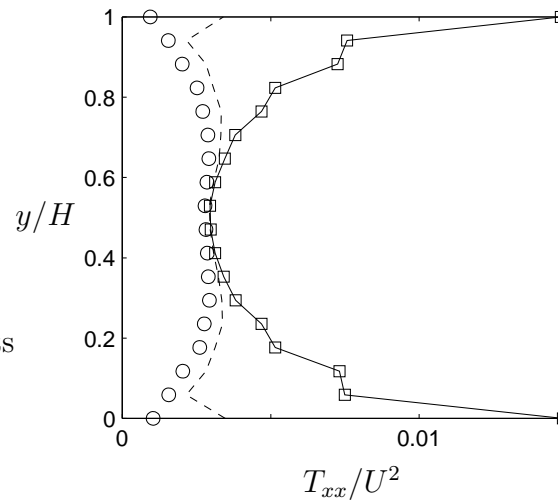
We focus on “visible” spheres within a diameter from the observation window and compute their velocity statistics. After reaching a steady state, we simulate imperfect tracking by computing another velocity statistics on only those spheres whose speed in the xy plane is smaller than a pre-selected value.

Figure 6.2 compare the theoretical prediction of the error on the mean velocity and granular agitation in x -direction due to imperfect tracking to the molecular dynamical simulation results. In simulations, the two boundaries move at the same speed but opposite directions, $U_t = U/2$ while $U_b = -U/2$. The ordinate is the distance in the y -direction made dimensionless by H (Fig. 3.1). The symbols are data from simulations in which granular speeds exceeding U_{tr} are ignored. The lines are predictions of the theory in Eqs. (6.9) and (6.11). Squares and solid lines: $U_{tr}/U = 1$; circles and dash-dotted lines: $U_{tr}/U = 0.2$. The distances between the line of centers of bumps on the two opposite bumpy boundaries and between the observation window and the far flat wall are $9d$. The cylindrical bumps have a diameter d . The overall volume fraction is 45%. The flow spheres have a coefficient of normal restitution $e = 0.93$, a coefficient of tangential restitution $\beta_0 = 0.4$, and a friction coefficient $\mu = 0.1$. The cylindrical bumps have $e_b = 0.85$, $\beta_{0,b} = 0.4$, and $\mu_b = 0.1$. The flat wall and observation window have $e_w = 0.8$, $\beta_{0,w} = 0.4$, and $\mu_w = 0.1$.

As Fig. 6.2 indicates, our predictions of \tilde{u}_x and \tilde{T}_{xx} agree well with simulations. However, while our theory also captures \tilde{u}_y and \tilde{T}_{yy} , it only does so qualitatively



(a) Mean velocity



(b) Granular temperature

Figure 6.2: Effects of tracking failure on measured mean velocity (a) and granular temperature profiles (b), all in the x -direction, made dimensionless with the relative speed U .

when $U_{tr}/U \lesssim 0.2$. We attribute this to the nature of the velocity distribution in the y -direction. In that direction, the boundaries produce a distribution that exhibits two distinct lobes resembling a “Weibull” distribution [130], rather than the Gaussian postulated by Jenkins and Richman [59] in Eq. (6.6). However, because the Weibull distribution remains symmetrical in C_y , this subtlety does not affect \tilde{u}_x or \tilde{T}_{xx} .

6.2.2 Finite Pixel Size

In our experiments, granular motion is recorded in a series of digital images consisting of an array of square pixels of size p . Because the vision algorithm detects several pixels on the circular outline of a sphere, it can generally fix the (x, y) position of the latter with sub-pixel accuracy. The corresponding uncertainties in sphere location produce random errors in the recorded velocity, which are interpreted as an artificial augmentation of the granular temperature.

The accuracy depends on practical factors that include illumination, contrast and completeness of the outline. Because it is generally no worse than a half pixel, we calculate the corresponding augmentation in T by considering that a sphere center lying with equal probability anywhere within a pixel is artificially relocated at the center of the pixel. Equivalently, the measured x -coordinate is

$$\tilde{x}_0 = x_0 + (1/2)p\xi_0, \quad (6.13)$$

where x_0 is the exact center coordinate and ξ_0 is a random variable that is uniformly distributed in the interval $[-1, 1]$. Similarly, the measured coordinate in the next image is

$$\tilde{x}_1 = x_1 + (1/2)p\xi_1, \quad (6.14)$$

where x_1 is the exact x -coordinate in that image and ξ_1 is a random variable distributed like ξ_0 .

At the camera frequency $F = 1/\Delta t$, the x -component of the measured sphere velocity measured from the two consecutive images is

$$\tilde{u} = \frac{\tilde{x}_1 - \tilde{x}_0}{\Delta t} = \frac{x_1 - x_0}{\Delta t} + \frac{(\xi_1 - \xi_0)p}{2\Delta t} = u + \eta \frac{1}{2}pF \quad (6.15)$$

where u is the actual velocity component, and $\eta \equiv \xi_1 - \xi_0$ is a new random variable.

Because ξ_1 and ξ_0 are independent random variables, η is distributed as

$$f_\eta(\eta) = \int_{-\infty}^{\infty} f(t)f(t-\eta)dt = \begin{cases} (1/2) + (1/4)\eta & \eta \in [-2, 0] \\ (1/2) - (1/4)\eta & \eta \in [0, 2] \\ 0 & \text{otherwise} \end{cases} \quad (6.16)$$

Using this distribution, we find the errors in velocity and temperature,

$$\tilde{u}_x = \langle \tilde{u} \rangle = \langle u + \eta(1/2)pF \rangle = \langle u \rangle + \langle \eta \rangle (1/2)pF, \quad (6.17)$$

and

$$\begin{aligned} \tilde{T}_{xx} &= \langle (\tilde{u} - \langle \tilde{u} \rangle)^2 \rangle \\ &= \langle (u - \langle \tilde{u} \rangle)^2 \rangle + \langle \eta^2 \rangle (1/4)(pF)^2 + \langle \eta(u - \langle \tilde{u} \rangle) \rangle (1/2)pF, \end{aligned} \quad (6.18)$$

where $\langle \rangle$ denotes the ensemble average, so that the mean particle velocity and temperature in the x -direction are $u_x = \langle u \rangle$ and $T_{xx} = \langle (u - u_x)^2 \rangle$. From Eq. (6.16) we calculate $\langle \eta \rangle = 0$ and $\langle \eta^2 \rangle = 2/3$. Assuming η and u to be independent so that $\langle \eta(u - \langle \tilde{u} \rangle) \rangle = \langle \eta \rangle \langle (u - \langle \tilde{u} \rangle) \rangle = 0$, we find the contributions of the finite pixel size to the errors in mean velocity and granular temperature,

$$\Delta u_x = \tilde{u}_x - u_x = 0, \quad (6.19)$$

and

$$\Delta T_{xx} = \tilde{T}_{xx} - T_{xx} = (1/6)(pF)^2. \quad (6.20)$$

By inspection, errors in the y -components of mean velocity and granular temperature can be obtained by substituting y for x in these expressions.

In our microgravity shear cell, experimental parameters combine to yield a characteristic frequency

$$F_0 \equiv U/(d/2), \quad (6.21)$$

in terms of which it is convenient to express the error in T that is attributed to the finite pixel size,

$$\Delta T_{xx}/U^2 = \frac{2}{3} \left(\frac{p}{d} \frac{F}{F_0} \right)^2. \quad (6.22)$$

We test our predictions by superimposing a pixel grid on the numerical simulations outlined earlier. The best resolution corresponds to $p = 0$. To simulate a finite pixel size, the simulations relocate the sphere center coordinates (x, y) to the center of the pixel that includes (x, y) . To evaluate the role of resolution alone, the simulations track all spheres regardless of speed, and the virtual camera frame rate is set much higher than the collision frequency. First, the simulations confirm that finite pixel size leads to no error in mean velocity. Then, as Fig. 6.3 shows, the simulations agree well with our analysis, except in the center of the flow, where the mean particle velocity vanishes. In this case, more samples are needed for the velocity statistics to converge.

Our analysis also reveals that errors due to finite pixel size are large if the camera frequency is high or the local speed is low i.e., if the distance traveled between two consecutive images is only on the order of a few pixels. This problem can be remedied if the spheres do not experience gravitational accelerations. In this case, their velocity can be inferred from more than two consecutive images, as long

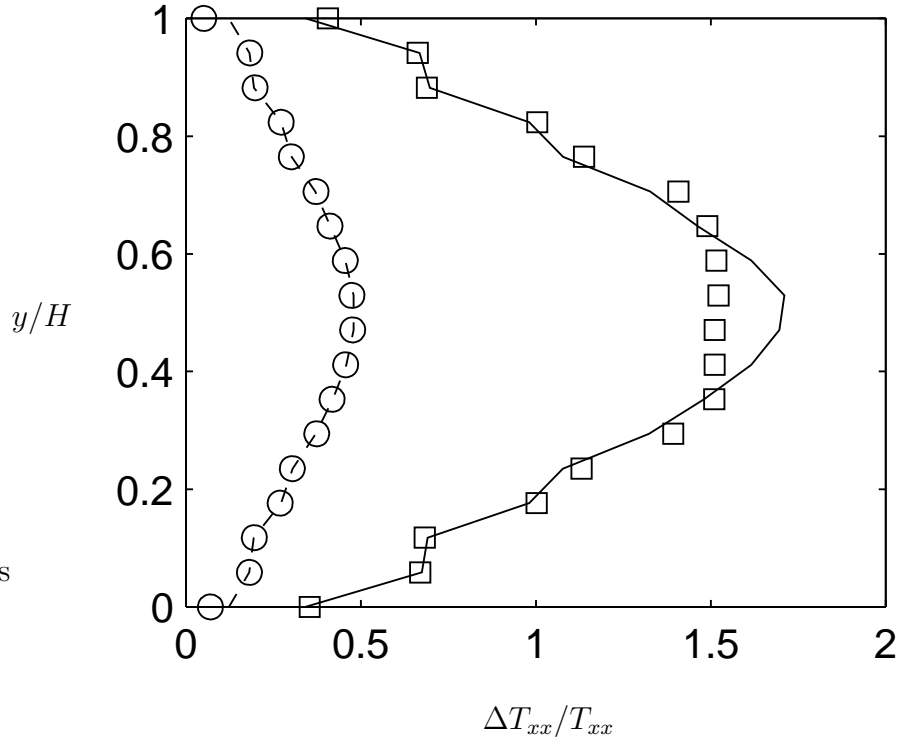


Figure 6.3: Effects of finite pixel size on measured profiles of granular temperature in the x -direction. The abscissa is the corresponding relative error in T_{xx} . For the ordinate, see Fig. 6.2. The symbols are data from simulations in which grain centers are artificially repositioned to the center of a pixel before calculating grain velocities between two consecutive frames. The lines are predictions of the theory in Eq. (6.20). Circles and dashed lines: $F/F_0 = 1.85$; squares and solid lines: $F/F_0 = 3.70$. There are 384 pixels between the lines of bump centers on the two moving boundaries, which corresponds a ratio $d/p \approx 43$. See Fig. 6.2 for other simulation parameters.

as they do not collide with other spheres. To implement this method, the vision algorithm inspects trajectories and, if the latter are straight, finds spheres that have not experienced any collision. The algorithm then infers their velocity from as many successive frames as possible using a linear regression of the trajectory, thus reducing p to a lower effective resolution p' and behaving as if the camera frequency F was smaller. Because the pixel error in Eq. (6.20) is proportional to $(pF)^2$, it can be substantially reduced. However, because the effective frame rate can be no lower than the collision frequency f_{coll} , a lower bound of the error in granular temperature is

$$\Delta T \geq (1/6)(p' f_{coll})^2, \quad (6.23)$$

where the collision frequency derives from the kinetic theory

$$f_{coll} = (24/\sqrt{\pi})G(\nu)\sqrt{T}/d. \quad (6.24)$$

6.2.3 Collisions

In agitated flows, some spheres can experience undetected collisions between two consecutive frames. In this section, we examine the resulting errors for an algorithm that infers velocity from the distance traveled between the two images, and that ignores whether collisions may have occurred. In the absence of gravity, and with sufficient frame rate, more elaborate algorithms could in principle interpolate prior and subsequent trajectories, infer the likelihood that a sphere has collided between the two frames, and reject the corrupted velocity sample. Our analysis of the simpler algorithm will therefore yield a worst case benchmark to justify whether more sophisticated methods are necessary.

The role of particle collisions in generating errors was also examined by Wildman and Huntley [132], who inferred granular temperature from the observed mean

displacement, rather than from the direct calculation of second moments that we use. In their method, assuming that a particle stops if it collides between two images, Wildman and Huntley showed that collisions contribute a second order correction to the mean displacement.

We begin our analysis by assuming that the velocity distribution is Maxwellian. Then, the most probable number of collisions a sphere may experience between two successive images is

$$\alpha = f_{coll}\Delta t, \quad (6.25)$$

where $\Delta t = 1/F$ is the time elapsed between the two images. For frame rates exceeding the collision frequency, we ignore the likelihood that one sphere collides more than once between two successive images. Then, on average, if N is the total number of particles sampled, αN spheres experience one collision during Δt and the other $(1 - \alpha)N$ spheres proceed with intact trajectories.

If a sphere i collides between two frames, the event occurs with uniform probability during Δt . Therefore, in the absence of gravity, the algorithm reports a velocity

$$\tilde{u}_i^c = \xi u_{a_i} + (1 - \xi)u_{b_i}, \quad (6.26)$$

where ξ is a random variable uniformly distributed between 0 and 1, u_{a_i} and u_{b_i} are the pre- and post-collision velocities of sphere i , respectively, and the superscript c denotes a velocity measurement corrupted by a collision. The measured mean velocity is then

$$\langle \tilde{u} \rangle = \frac{1}{N} \sum_{i=1}^N \tilde{u}_i = \frac{1}{N} \sum_{i=1}^{\alpha N} \tilde{u}_i^c + \frac{1}{N} \sum_{i=1}^{(1-\alpha)N} \tilde{u}_i^p = \alpha \langle \tilde{u}^c \rangle + (1 - \alpha) \langle \tilde{u}^p \rangle,$$

where the superscript p on the measured velocity denotes intact particles. The

average measured velocities of collided and intact spheres are

$$\langle \tilde{u}^c \rangle = \frac{1}{\alpha N} \sum_{i=1}^{\alpha N} \tilde{u}_i^c \quad \text{and} \quad \langle \tilde{u}^p \rangle = \frac{1}{(1-\alpha)N} \sum_{i=1}^{(1-\alpha)N} \tilde{u}_i^p$$

Similarly, the measured granular temperature can be expressed as

$$\tilde{T} = \alpha \tilde{T}^c + (1-\alpha) \tilde{T}^p \quad (6.27)$$

with

$$\tilde{T}^c = \frac{1}{\alpha N} \sum_{i=1}^{\alpha N} (\tilde{u}_i^c - \tilde{u})^2 \quad \text{and} \quad \tilde{T}^p = \frac{1}{(1-\alpha)N} \sum_{i=1}^{(1-\alpha)N} (\tilde{u}_i^p - \tilde{u})^2.$$

Assuming that the number of sampled particles is large, we replace the summation by an integral over the velocity distribution. For example,

$$\frac{1}{\alpha N} \sum_{i=1}^{\alpha N} \psi(\mathbf{u}_i) \implies \frac{1}{n} \int \psi(\mathbf{c}) f_M(\mathbf{c}) d\mathbf{c},$$

where ψ is any function of particle velocity, n is the particle number density, and f_M is the Maxwellian velocity distribution. For simplicity, we ignore correlations between the pre- and post-collision velocities, so that u_{a_i} and u_{b_i} behave as two independent random variables distributed as a Gaussian.

We find that collisions do not alter measurements of the mean velocity u ,

$$\langle \tilde{u} \rangle = \langle \tilde{u}^c \rangle = \langle \tilde{u}^p \rangle = u. \quad (6.28)$$

However, they affect measurements of the granular temperature since

$$\begin{aligned} \tilde{T}^p &= \int (\tilde{u}^p - u)^2 f(c) dc = T, \\ \tilde{T}^c &= \int (\tilde{u}^c - u)^2 f(c) dc = \int_{\xi} \int_{c_1} \int_{c_2} [\xi c_1 + (1-\xi)c_2 - u]^2 f(c_1) f(c_2) dc_1 dc_2 d\xi \\ &= 2 \int_0^1 \xi^2 d\xi \int_{-\infty}^{\infty} c^2 f(c) dc + 2 \int_0^1 \xi(1-\xi) d\xi \left[\int_{-\infty}^{\infty} c f(c) dc \right]^2 - u^2 \\ &= \frac{2}{3} \left(\langle u^2 \rangle - u^2 \right) = \frac{2}{3} T. \end{aligned} \quad (6.29)$$

Finally, combining Eqs. (6.27) and (6.29), the measured granular temperature is

$$\tilde{T} = (1 - \alpha/3)T. \quad (6.30)$$

Because $\alpha > 0$, collisions tend to reduce the measured granular temperature. Because our analysis assumes that spheres collide no more frequently than once on average during Δt , it is only valid when $\alpha < 1$. As Fig. 6.4 shows, the analysis agrees best with simulations at small α . Here, the simulations mimic actual measurements by inferring velocity from Eq. (6.15). To isolate errors attributed to collisions alone, they assume that the pixel size vanishes and that the tracking distance is infinite.

When $\alpha \gtrsim 1$, because it is more likely for spheres to collide more than once during Δt , our theoretical predictions begin to deviate from the simulations. However, because one sphere colliding twice during Δt has a smaller effect on the measured temperature than two spheres colliding once, our theory yields a higher, more conservative estimate of the actual error (Fig. 6.4).

6.2.4 Strip Statistics

In the previous sections, we assumed implicitly that an experiment could generate an infinite number of samples anywhere in the two-dimensional imaging region, so that errors in u_x and T_{xx} , for example, were independent of sample size or, equivalently, that spatial variations of these variables could be measured on a resolution of a pixel. In practice, because experiments last a finite time, the flow must be partitioned in coarser subregions, in which estimates of u_x and T_{xx} are derived from statistics of spheres having their mean position between two consecutive images in the subregion. If flow variables only change along one direction, then the subre-

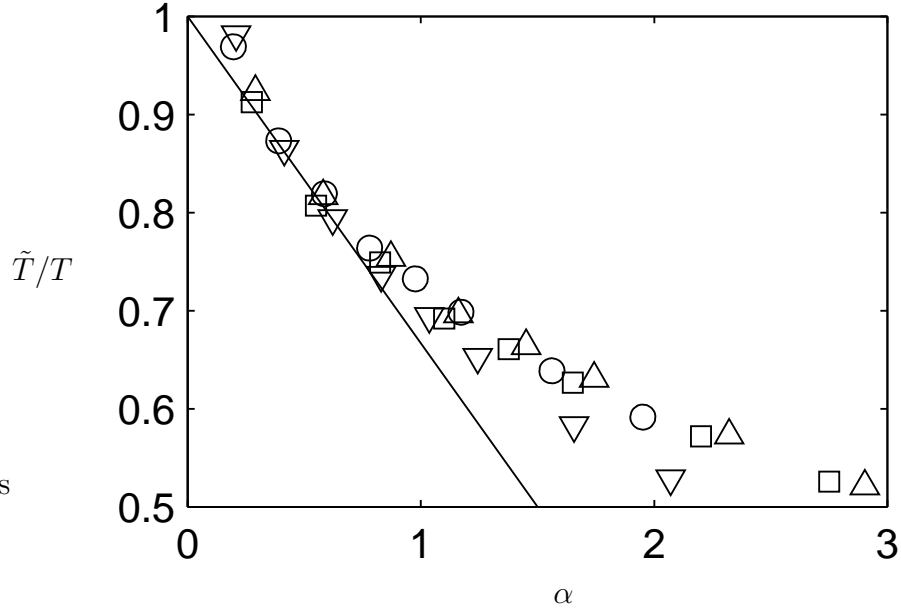


Figure 6.4: Effects of undetected collisions on the measured granular temperature in the x -direction. The abscissa is $\alpha \equiv f_{coll}\Delta t$. The ordinate is the measured granular temperature at the frame rate $F = 1/\Delta t$ relative to its actual value when $\Delta t \rightarrow 0$. The symbols are data derived from consecutive image realizations separated by Δt in simulations with $p = 0$ and $U_{tr} = \infty$. The solid line is the prediction of the theory in Eq. (6.30). Squares and circles: \tilde{T}_{xx}/T_{xx} ; triangles: \tilde{T}_{yy}/T_{yy} . Squares and up-triangles: at $y/H = 0.5$; circles and down-triangles: at $y/H = 0.8$. See Fig. 6.2 for other simulation parameters.

gion can be a narrow strip spanning the observation region in the perpendicular direction.

Even if the three errors considered earlier were absent ($p = 0$, $L_{tr} = \infty$, $F \gg f_{coll}$), the statistics of u_x and T_{xx} in a strip would be subject to uncertainties associated with the finite sample size. If we assume that sphere velocities are distributed as a Gaussian, then their actual mean u_x and standard deviation T_{xx} are derived from the corresponding sample mean $u_{s,x}$ and sample standard deviation $\sigma_{s,xx}$ using Student's t-distribution [13],

$$u_x = u_{s,x} \pm a(C, N)\sigma_{s,xx}/\sqrt{N} \quad (6.31)$$

and

$$b(C, N)\frac{\sigma_{s,xx}}{N-1} \leq T_{xx} \leq c(C, N)\frac{\sigma_{s,xx}}{N-1} \quad (6.32)$$

where $a(C, N)$, $b(C, N)$ and $c(C, N)$ are numbers that vary with the degree of confidence C at which u_x and T_{xx} are sought. For example, in the limit where N is large, $a(80\%, N) = 1.282$, $b(80\%, N) \approx (\sqrt{2N-3} - 1.282)^2/2$, and $c(80\%, N) \approx (\sqrt{2N-3} + 1.282)^2/2$. The uncertainty in T_{yy} can be obtained by replacing x in the equation above with y .

The width of a strip is chosen so that enough samples can be collected in the finite time of an experiment. Effectively, one trades off the ability to resolve profiles of u_x and T_{xx} with the certainty that one requires in knowing these variables.

There is yet another, more subtle source of error in granular temperature that arises from strip statistics when a gradient of mean velocity is present. To illustrate this, we consider a simple shear flow, in which the mean velocity u_x varies linearly with y , but the mean velocity u_y vanishes. For simplicity, we assume that the solid volume fraction and granular temperature are uniform within a strip. Then, the

measured mean velocity and the granular temperature are

$$\tilde{u}_x = u_x + \int_{-\frac{\delta}{2}}^{\frac{\delta}{2}} \gamma y dy = u_x, \quad (6.33)$$

$$\tilde{T}_{yy} = T_{yy}, \quad (6.34)$$

and

$$\tilde{T}_{xx} = T_{xx} + \int_{-\frac{\delta}{2}}^{\frac{\delta}{2}} \gamma^2 y^2 dy = T_{xx} + \frac{1}{12} \gamma^2 \delta^2, \quad (6.35)$$

where $\gamma \equiv \partial u_x / \partial y$ is the local shear rate and δ is the strip width. Note that this error is always positive, and only affects the streamwise component of granular temperature, thus exaggerating the temperature anisotropy.

6.3 Tradeoffs

In the previous section, we found that strip statistics could be made arbitrarily precise by reducing the strip width and increasing the number of image samples. However, the three errors associated with imperfect tracking (Eqs. (6.9), (6.10), (6.11), (6.12)), undetected collisions (Eqs. (6.19), (6.20)) and finite pixel size (Eqs. (6.28), (6.30)) cannot be minimized so easily. There are two reasons for this. First, while the measured granular temperature is *reduced* by imperfect tracking and undetected collisions, it is artificially *increased* by a finite pixel size. Thus, errors can compensate in subtle ways. Second, as Fig. 6.5 shows, there are conditions for which it is not possible, given a certain pixel resolution, to find a camera frequency that will simultaneously limit the relative errors in T_{xx} associated with each of the three errors. In the event, the only way to produce an acceptable error is to reduce the pixel size. To generate Fig. 6.5, we express relative errors in terms of F/F_0 , e.g., we substitute $U_+/\sqrt{2T}$ in Eq. (6.11) by

$$\frac{U_+}{\sqrt{2T}} = \frac{U_{tr} + u_x}{\sqrt{2T}} = \frac{(F/F_0)(2L_{tr}/d) + u_x^*}{\sqrt{2T^*}}, \quad (6.36)$$

where $u_x^* = u_x/U$ and $T^* = T/U^2$ are the dimensionless mean velocity and granular temperature, respectively.

In practical situations, errors due to imperfect tracking can be insidious. They are, however, captured by the theory that we have outlined. Consider microgravity experiments with 2 mm acrylic spheres similar to those in Fig. 6.1(a). Here, the top boundary moves at $U = 0.8$ m/s, the mean volume fraction is 30%, and images are acquired at 1000 frames per second on a resolution of 41 pixels per sphere diameter. In such situation, our experience is that numerical simulations faithfully reproduce actual profiles of mean velocity and granular temperature [80, 81] (see also Chapter 3). Thus, a comparison of measured and simulated profiles can highlight flow regions where the measurements fail. As Fig. 6.6 shows, our error theory captures the magnitude of the corresponding failure. Without such theoretical insight, the collapse of the velocity and temperature profiles near the moving boundary may have appeared to be real. In fact, our error theory clearly reveals that it is artificial.

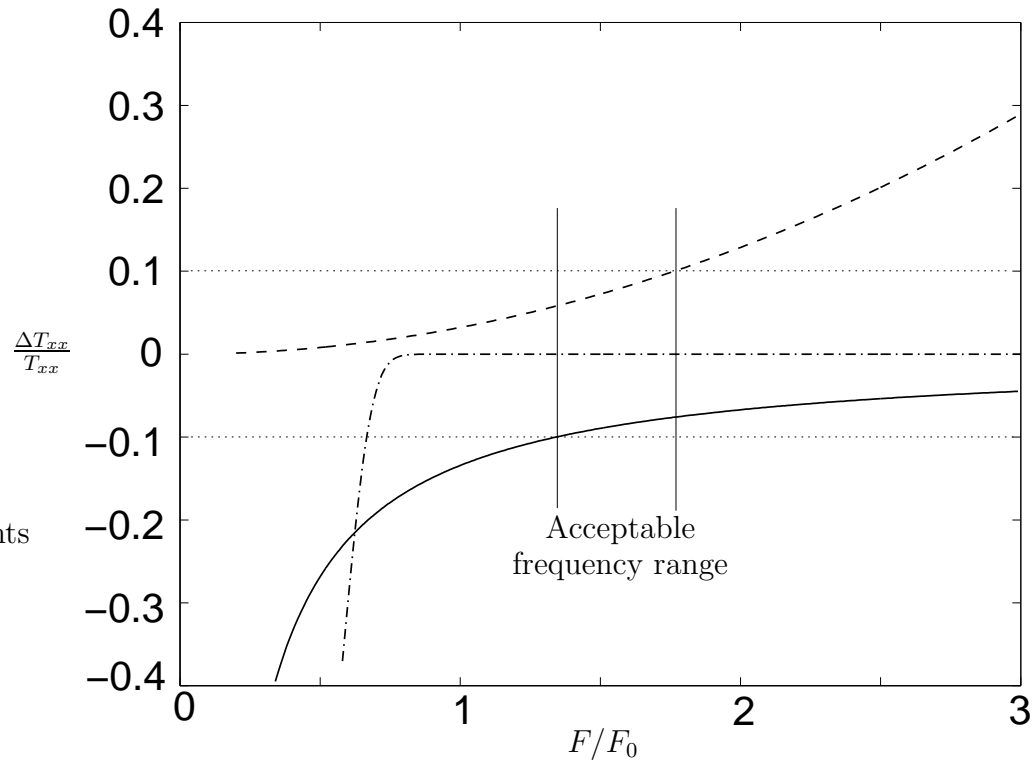


Figure 6.5: Theoretical prediction of the effects of camera frequency on the relative errors of granular temperature with $u_x/U = 0.5$, $T^{1/2}/U = 0.08$, and $\nu = 0.3$. The abscissa is the frame rate relative to F_0 in Eq. (6.21). The ordinate is the relative error in T_{xx} . The solid, dashed and dotted line represent the respective contributions of imperfect tracking, finite pixel resolution and collisions upon measurement errors. The horizontal dotted lines indicate $\pm 10\%$. Thus, if such an error level can be tolerated, one may adopt a frame rate in the range shown. In contrast, no camera frequency yields a relative error smaller than, for example, $\pm 5\%$.

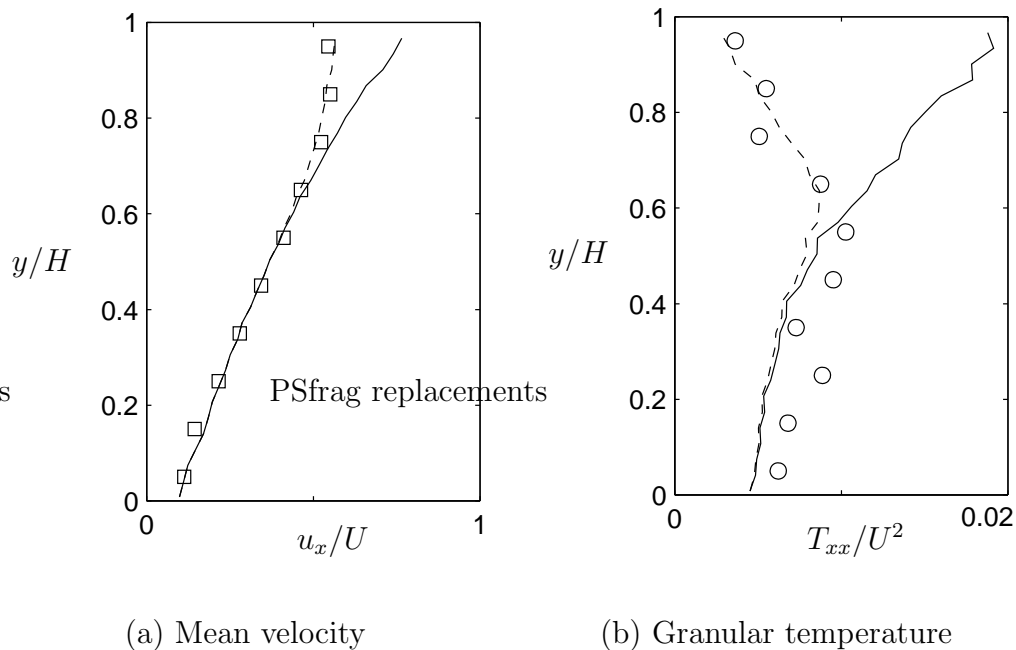


Figure 6.6: Profiles of mean velocity u_x (a) and granular temperature T_{xx} (b) in the shear flow of Fig. 6.1(a) made dimensionless with U . In this experiment, the top boundary is moving at speed U and the bottom boundary is stationary. The solid lines are predictions of the numerical simulations. The symbols are experimental measurements. The dashed lines are simulation results corrupted by errors predicted by the theory, in which we assume that tracking is lost for displacements beyond $L_{tr} = d/4$.

Chapter 7

Design of Experiments to Study

Gas-particle Interaction in Microgravity

The role of collisional interactions in gas-solid flows has received wide attention. In these flows, collisions can transfer a significant amount of momentum, which helps maintain homogeneity and may prevent the formation of clusters.

The crucial parameter to characterize particle agitation is the granular temperature T , which determines the effective viscosity and the “thermal” conductivity of the solid phase, i.e., the ability for the solid phase to transfer momentum and fluctuation energy. Particle agitation may be generated by shearing and is entirely dissipated by inelastic collisions when there is no interstitial gas between particles. In gas-particle flows, the interaction between gas and particles may contribute additional mechanisms to produce or to dissipate particle fluctuation energy.

Sangani, Mo, Tsao and Koch [107] have determined the dissipation of particle fluctuation energy due to the viscous gas when particle inertia is large and gas inertia is negligible. Koch and Sangani [67] showed that the relative mean velocity between the gas and solid phases can produce additional particle agitation. Recently, Verberg and Koch [123] extended the study of Sangani *et al* [107] to consider the effect of gas inertia on the dissipation of particle fluctuation energy.

Through their work, the understanding of the detailed physics of particle-particle interaction and particle-gas interaction have advanced to a point at which it is possible to design experiments that address fundamental questions of practical importance and to interpret them in the context of an appropriate theory.

In this light, we are designing a microgravity flow cell in which to study the

interaction of a flowing gas with relatively massive particles that collide with each other and with the boundaries of the cell. This axisymmetric Couette cell will permit suspensions to be studied over a range of laminar, steady, fully developed conditions where viscous forces dominate the gas flow. Unlike terrestrial flows, where the gas velocity must be set to a value large enough to support the weight of particles, the duration and quality of microgravity on the International Space Station will permit us to achieve suspensions in which the agitation of the particles and the gas flow can be controlled independently by adjusting the pressure gradient along the flow and the relative motion of the boundaries.

7.1 Experiment Objectives

We plan two series of experiments on a long-term microgravity platform. The goal of the first is to characterize the viscous dissipation of the energy of the particle fluctuations when there is no relative mean velocity between gas and solids. We call these tests “Viscous Dissipation Experiments”.

In the second series, we will impose a pressure gradient in the gas and record the corresponding drag on the agitated granular medium. We call these tests “Viscous Drag Experiments”. In this section, we briefly outline the principle of these two series.

7.1.1 Viscous dissipation experiments

In the case of steady, simple shear flow, the flux term vanishes and the shear production of particle fluctuation energy is balanced by the inelastic collisional

dissipation and the viscous dissipation,

$$\frac{8}{5\sqrt{\pi}}\rho_s\sigma T^{1/2}\nu GJ\Gamma^2 = \frac{54}{\sigma^2}\mu_g T\nu R_{diss} + \frac{24}{\sqrt{\pi}\sigma}(1 - e_{eff})\rho_s\nu GT^{3/2}, \quad (7.1)$$

where Γ is the shear rate.

Verberg and Koch [123] suggested that the viscous dissipation of particle fluctuation energy increases linearly with gas inertia,

$$R_{diss} = R_{diss,0}(\nu, \varepsilon_m) + K(\nu)Re_T \quad (7.2)$$

where $R_{diss,0}$ is the viscous dissipation coefficient at negligible gas inertia (Sangani *et al* [107]), $K(\nu)$ is a function of particle volume fraction ν , and

$$Re_T \equiv \frac{\rho_g\sigma T^{1/2}}{\mu_g} \quad (7.3)$$

is the Reynolds number based on particle diameter and gas density.

With Eq. (7.2), Eq. (7.1) can be solved for the dimensionless particle fluctuation velocity $T^{1/2}/\Gamma\sigma$ as

$$\frac{T^{1/2}}{\Gamma\sigma} = \frac{-\frac{3}{2}\frac{R_{diss,0}}{St} + \sqrt{\left(\frac{3}{2}\frac{R_{diss,0}}{St}\right)^2 + \frac{8}{5\sqrt{\pi}}GJ\left[\frac{24}{\sqrt{\pi}}(1 - e_{eff})G + 54K\frac{\rho_g}{\rho_s}\right]}}{\frac{24}{\sqrt{\pi}}(1 - e_{eff})G + 54K\frac{\rho_g}{\rho_s}} \quad (7.4)$$

where

$$St \equiv \Gamma\tau_v = \Gamma\frac{\rho_s\sigma^2}{18\mu_g}$$

is the Stokes number and τ_v is the viscous relaxation time.

In gas-particle flows, the density ratio ρ_g/ρ_s is of order 10^{-3} or smaller. The terms proportional to ρ_g/ρ_s in Eq. (7.4) can usually be neglected unless $e_{eff} \approx 1$, i.e., particles are nearly perfectly smooth and elastic. Because the spheres selected for our experiments have $e_{eff} \approx 0.8$, the viscous dissipation is negligible compared to the inelastic dissipation in the limit of large particle inertia (large St), and

the granular temperature is approximately determined by a balance between shear production and inelastic dissipation alone,

$$\frac{T^{1/2}}{\Gamma\sigma} = \left[\frac{\frac{8}{5\sqrt{\pi}}GJ}{\frac{24}{\sqrt{\pi}}(1 - e_{eff})G + 54K\frac{\rho_g}{\rho_s}} \right]^{1/2} \approx \sqrt{\frac{J}{15(1 - e_{eff})}}, \quad (7.5)$$

In this case, the dimensionless particle fluctuation velocity $T^{1/2}/\Gamma\sigma$ is independent of St when Stokes number is large.

The chief objective of our experiments is to create small enough particle Stokes number to let the gas affect the fluctuation energy balance appreciably. In the limit of large viscous dissipation and small inelastic dissipation, the granular temperature is

$$\frac{T^{1/2}}{\Gamma\sigma} = \frac{8}{15\sqrt{\pi}}GJ\frac{St}{R_{diss}} \approx \frac{8}{15\sqrt{\pi}}GJ\frac{St}{R_{diss,0}}, \quad (7.6)$$

i.e., $T^{1/2}/\Gamma\sigma$ is proportional to St when St is small.

Figure 7.1 plots the variations of $T^{1/2}/\Gamma\sigma$ with St given by Eq. (7.4) and the two limiting cases in Eq. (7.5) and Eq. (7.6). If the elasticity and friction of the spheres remain constant with relative impact velocity and, consequently, with Γ , then measurements of the granular temperature T at different Stokes numbers and particle volume fractions ν , make it possible to infer the viscous dissipation rate of particle fluctuation energy.

According to Sangani *et al* [107], the viscous dissipation coefficient R_{diss} depends on the lubrication cut-off ε_m , which, as Sundararajakumar and Koch [118] showed, is related to the mean free path of gas molecules. To check this theoretical prediction, we will reduce the gas pressure in the apparatus and thus vary the mean free path. The resulting variations in granular temperature will betray the corresponding variations in R_{diss} . We will also reduce the pressure to control the particle Reynolds number, which will make it possible to record the dependence of R_{diss} on Re_T .

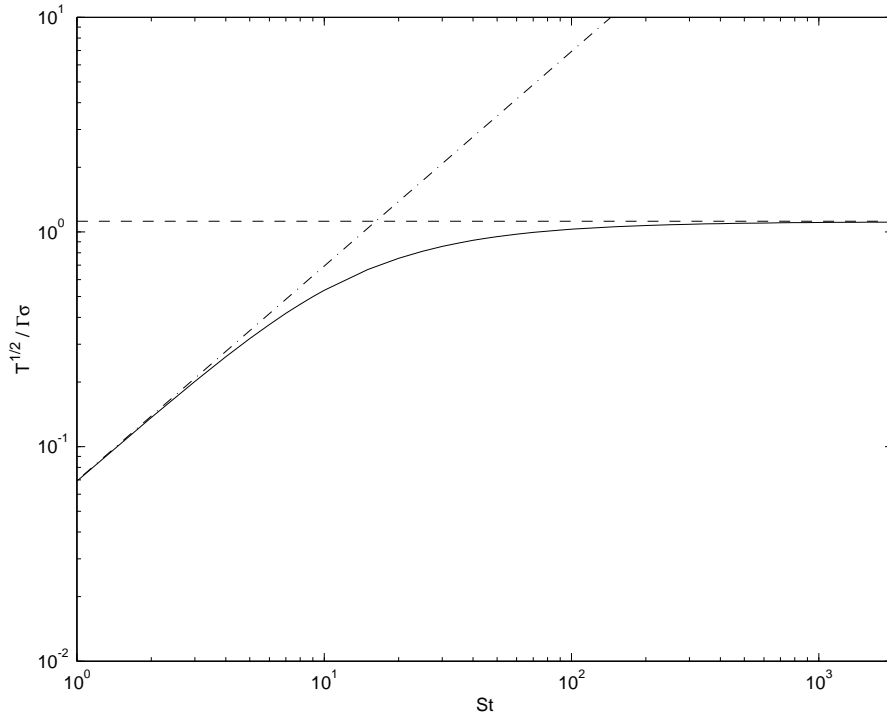


Figure 7.1: Variations of the dimensionless fluctuation velocity $T^{1/2}/\Gamma\sigma$ with Stokes number in the simple shear flow of a gas-particle suspension. Solid line: solution given by the energy balance Eq. (7.4). Dashed line: limit of $St \rightarrow \infty$. Dash-dotted line: limit of small St . Parameters: $\nu = 0.3$, $e_{eff} = 0.8$, $\rho_g = 1.29 \times 10^{-3}$, $\rho_s = 6.71$, and lubrication cutoff $\varepsilon_m = 0.01$.

The presence of solid boundaries complicates the simple energy balance of Eq. (7.1) by adding the flux of fluctuation energy and by changing the local shear rate. Consequently, the granular temperature in the cell is not uniform between bumpy boundaries. Although our experimental strategy remains that suggested by Figure 7.1, we will in fact measure transverse profiles of granular temperature and then compare these with theoretical predictions.

7.1.2 Viscous drag experiments

In the second series of experiments, we will impose a gas pressure gradient on the shear cell. The gradient will induce a relative velocity between the two phases, while the shearing will set independently the agitation of the solids. These “Viscous Drag Experiments” will be unique in exploring a regime where particle velocity fluctuations are determined by a mechanism other than interactions with the gas. In this regime, we will measure the dependence of R_{diss} and the drag coefficient R_{drag} on the volume fraction. In a steady, fully developed uniform flow, the drag is balanced by the gradient in gas pressure,

$$\frac{dP}{dx} = 18 \frac{\mu_g}{\sigma^2} \nu (1 - \nu) R_{drag}(\nu) (u_s - u_g). \quad (7.7)$$

Therefore, we can infer R_{drag} by measuring the mean solid velocity u_s , the mean gas velocity u_g and the gas pressure gradient. As in the first series of experiments, the solid boundaries add shear stresses to the force balance. Thus we will record transverse profiles of mean gas velocity, mean solid velocity, granular temperature and solid volume fraction and compare these with theoretical predictions. By reducing gas pressure in the cell, we will also record the effects of particle Reynolds number on R_{drag} .

7.2 Constraints on the design of experiments

Our desire is to explore as wide a range of Stokes and Reynolds numbers as possible in the experiments. However, the latter are constrained by instrument limitations or economical concerns, and the theories that they aim to check are only valid within a limited range of parameters. Therefore, we will design experiments that are relevant to the verification or extension of current theories, and that are feasible given the experimental apparatus and instruments available.

7.2.1 Particle inertia

The theories of Sangani *et al* [107], Koch and Sangani [67], and our work in Chapter 4 all assume that the particle inertia is large, so that viscous forces do not affect the particle motion significantly between collisions, that the particle velocity distribution is determined by inelastic collisions, and that is nearly Maxwellian. In this context, we define a Stokes number as

$$St_{local} = f_{coll}\tau_v, \quad (7.8)$$

where

$$f_{coll} = \frac{24}{\sqrt{\pi}}G(\nu)\frac{T^{1/2}}{\sigma} \quad (7.9)$$

is the collision frequency and τ_v is the viscous relaxation time. Note that, because the granular temperature is not uniform in our shear cell, St_{local} is based on the local granular temperature.

Recently, Wylie *et al* [135] showed that, for a sheared suspension without mean relative motion between the two phases, the isotropic Maxwellian theory [107] captures well the viscous dissipation of particle fluctuation energy in the computer

simulation of Wylie and Koch [134] if

$$St_{local} > 2R_{diss}. \quad (7.10)$$

By calculating the velocity distribution, Sangani *et al* [107] showed that for the normal stress to remain nearly isotropic, St_{local} must be larger than a critical Stokes number

$$St_{cr} = \frac{5}{2} \left(\frac{3}{\varepsilon_p} \frac{1 + \frac{8}{5}G(\nu)}{1 + 4G(\nu)} - 1 \right) R_{diss}, \quad (7.11)$$

where ε_p is the relative normal stress difference that one tolerates as a measure of the anisotropy. Thus, a criterion for observing a nearly isotropic Maxwellian velocity distribution is

$$St_{local} > St_{cr}. \quad (7.12)$$

The criterion given by Eq. (7.12) is much more stringent than Eq. (7.10) for any tolerance $\varepsilon_p \leq 20\%$. Thus, in our experiments we adopt $\varepsilon_p = 10\%$ and use Eq. (7.12) as the only criterion for St_{local} . We also adopt this criterion for viscous drag experiments. Because we plan tests with St_{local} both greater and less than St_{cr} , the interpretation of the latter should be done with caution when Eq. (7.12) is not satisfied.

7.2.2 Gas inertia

In the viscous dissipation experiments, the gas inertia is characterized by the Reynolds number in Eq. (7.3) that is based on the particle fluctuation velocity. The computer simulations of Verberg and Koch [123] show that R_{diss} increases with Re_T . In the experiments, if other conditions remain the same, Re_T increases with St . However, by partially evacuating the cell, we can maintain $Re_T \ll 1$, and

thus measure $R_{diss,0}$. By changing gas pressure in the cell, we can then infer the dependence of R_{diss} on Re_T .

In the viscous drag experiment, another Reynolds number can be defined using the relative velocity between gas and solids,

$$Re_{rel} \equiv \frac{\rho_g(u_g - u_s)\sigma}{\mu_g}. \quad (7.13)$$

In general, R_{drag} depends on both Re_{rel} and Re_T . By adjusting the boundary speed and the pressure gradient independently, we can control Re_{rel} and Re_T separately. Once again, we can also reduced the gas pressure to adjust the magnitudes of both Re_{rel} and Re_T .

7.2.3 Duration of microgravity

For each test, the required duration of microgravity is determined by the time for the flow to reach a steady state and the time to acquire enough number of images for the statistics of both particle and gas velocities. As described in Chapter 6, we measure the velocities of solid particles using a vision algorithm that tracks particles in successive images. However, the gas velocity is measured indirectly by adding small tracer particles that follow the local motion of the gas. These gas tracers produce streaks on the image from which we can infer their velocity. Different considerations apply to the tracking of flow spheres and gas tracers.

We employ computer simulation to determine the minimum number of images necessary for tracking the flow spheres. To evaluate the evolution of the velocity statistics with the number of images gathered, the simulation does not employ its knowledge of sphere velocities. Instead, it generates successive realizations of the observation region by collecting the longitudinal and transverse coordinates of

sphere centers at a frequency of $2U/\sigma$, where U is the relative velocity between the inner and the outer boundaries. As discussed in Chapter 6, the vision algorithm tracks the center of spheres with completely visible outline, but generally ignores spheres with partial circular outlines. Then, for all spheres with fully visible outline in two successive frames, the simulation infers the two components of the center velocity from the distance traveled and the time interval separating the two frames. The data is then used to build up a statistic of mean velocity and velocity fluctuations.

Our simulations show that the evolution of granular temperature statistics depends strongly on the mean solid volume fraction. For a transverse resolution of 20 strips, we find that the minimum number of images producing an error less than 2.5% in the measured granular fluctuation velocity is, approximately,

$$N_{\min} \approx \frac{700}{\bar{\nu}}, \quad (7.14)$$

where $\bar{\nu}$ is the mean solid volume fraction in simulation.

On the other hand, our experiments are guided by the analysis of measurement errors in the mean and fluctuation velocities from the vision algorithm, which usually requires a camera frequency $F \geq 2U/\sigma$. To ensure coverage of the same overall test duration, the actual number of images to be acquired is

$$N_{images} \geq N_{\min} \frac{F\sigma}{2U}. \quad (7.15)$$

We use statistical considerations to estimate the minimum number of images required for tracking the motion of the gas in the viscous drag experiments. For simplicity, we assume that estimates of the mean gas velocity are corrupted by Gaussian fluctuations of the tracer velocity with variance on the order of the granular temperature. We prescribe that the resulting uncertainties in the mean gas

velocity be less than 5% of the mean gas velocity u_g at 95% degree of confidence. In an experiment, the number of velocity samples is the product of N_{images} and n_{tracer} , where N_{image} is the number of images acquired and n_{tracer} is the number of tracers in the measurement volume. Then using Student's t -distribution, we obtain the criterion

$$N_{images} \geq \frac{(a_t/0.05)^2 T}{n_{tracer} u_g^2}, \quad (7.16)$$

where $a_t \approx 2$ is the 2.5 percentage point of Student's t -distribution for large samples. We plan to adjust the tracer number density to have approximately 5 tracers per visible strip. This calculation indicates that the requisite number of images does not exceed 70 for any of the experiments we propose. Therefore, the criterion given by Eq. (7.14) is far more stringent and thus is used to determine the number of images to be acquired in each experiment.

We estimate the time necessary to establish a steady flow t_{ss} by assuming that the shear cell is started from rest. As computer simulation results in Figure 7.2 show, t_{ss} is largely governed by the establishment and relaxation of granular temperature. In the early stages of the process, the production of fluctuation energy from the incipient shearing of the grains promotes a rapid increase in T , which in turn gives rise to collisional dissipation. Production and dissipation then quickly reach a balance. However, the corresponding temperature is higher than that in a steady balance that involves collisional fluxes of fluctuation energy. As these fluxes diffuse the excess energy through the boundaries, the grains slowly relax to a steady temperature according to

$$\frac{3}{2} \nu \rho_s \frac{\partial T}{\partial t} \approx -\frac{\partial q_y}{\partial y} \quad (7.17)$$

where q_y is the flux of granular fluctuation energy in the y -direction. When writing Eq. (7.17), we assumed that, locally, the shear production balances the collisional

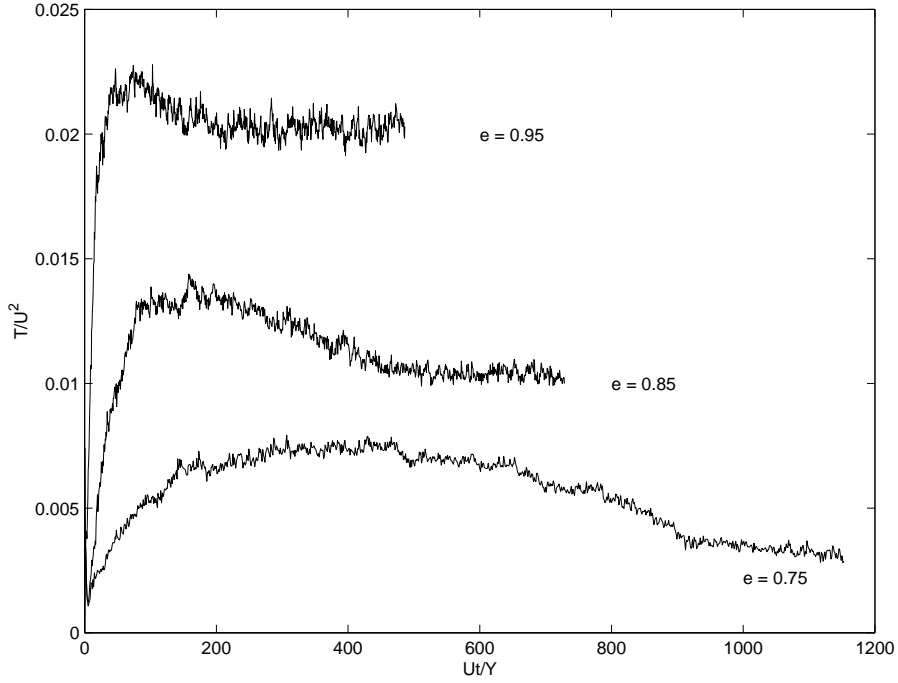


Figure 7.2: Simulated evolution of the granular temperature in a shear flow between parallel, bumpy boundaries. The granular temperature is averaged across the cell and made dimensionless with U^2 . Simulation parameters: $H/\sigma = 6.4$, $d_i = 3$, $d_o = \sigma = 2$, $s_i = s_o = 0$, $\bar{\nu} = 0.33$, $\mu = 0.1$, $\beta_0 = 0.4$, and the coefficients of normal restitution shown in the figure.

dissipation and we ignored the effects of flat side walls and the curvature of the cell.

Eq. (7.17) can be integrated from the inner bumpy boundary to the outer bumpy boundary to yield,

$$\frac{3}{2}\nu\rho_s\frac{\partial\bar{T}}{\partial t}\approx\frac{1}{H}(q_{y,i}+q_{y,o}), \quad (7.18)$$

where \bar{T} is the average granular temperature in the cell, $q_{y,i}$ and $q_{y,o}$ are the fluxes of fluctuation energy into the flow from the inner and outer bumpy boundaries,

respectively. As shown in Chapter 2, the boundary fluxes q_b are, in dimensionless form,

$$\frac{q_b}{N\sqrt{T}} = \frac{Sv - D}{N\sqrt{T}} = \left(\frac{S}{N}\right)\left(\frac{v}{\sqrt{T}}\right) - \frac{D}{N\sqrt{T}}, \quad (7.19)$$

where N and S are the normal and shear stresses at the boundary, respectively, v is the slip velocity, and D is the collisional dissipation at the boundary. To obtain the correct scaling of the time to reach a steady state in a simple way, we use the linear boundary condition derived by Richman [104], which can be written as

$$\frac{S}{N} = b\frac{v}{\sqrt{T}}, \quad (7.20)$$

where b is a constant that depends on boundary geometry. Substituting Eq. (7.20) into Eq. (7.19), we find

$$q_b = N\sqrt{T}\left[\frac{1}{b}\left(\frac{S}{N}\right)^2 - d_c\right], \quad (7.21)$$

where d_c is a constant that depends on boundary geometry and impact properties. Combining Eq. (7.21) with Eq. (7.18), we obtain an equation for the evolution of the granular temperature,

$$\frac{\partial \bar{T}}{\partial t} \approx \frac{2}{3} \frac{1 + 4G}{H} \bar{T}^{3/2} \left[\left(\frac{1}{b_i} + \frac{1}{b_o} \right) \left(\frac{S}{N} \right)^2 - d_{c,i} - d_{c,o} \right], \quad (7.22)$$

in which the subscripts i and o stand for the inner and outer boundaries, respectively. In writing Eq. (7.22), we have used the fact that the normal stress is continuous so that the normal stress N equals the pressure P in the interior and we have tacitly replaced the granular temperature T in the interior by its averaged value \bar{T} . Note that terms on the right hand side of Eq. (7.22) are constants except G and T . Hence we write it in dimensionless form as

$$\frac{\partial \ln \bar{T}^*}{\partial t^*} = A_b(1 + 4G)\sqrt{\bar{T}^*}, \quad (7.23)$$

where $\bar{T}^* \equiv \bar{T}/U^2$ is the dimensionless granular temperature, $t^* \equiv tU/H$ is the dimensionless time, and A_b is a constant.

As suggested by Eq. (7.23), we find that the relaxation time of the diffusion process is proportional to

$$\frac{t_{ss}U}{H} \approx 42 \left[(1 + 4G) \sqrt{\bar{T}_{ss}} \right]^{-1}, \quad (7.24)$$

where the granular temperature is evaluated at the steady state. We determine the constant of proportionality through numerical simulations with different levels of steady granular temperature and mean volume fraction (Figure 7.3). We expect that Eq. (7.24) is also valid in the presence of an interstitial gas. Because the relaxation process to a steady temperature does not, in general, begin with a granular flow at rest, the time given by Eq. (7.24) may be regarded as conservative.

Finally, by adding contributions from t_{ss} and the minimum number of images, we find that the minimum required time of microgravity is

$$t_{\mu g} > t_{ss} + \frac{N_{\min} \sigma}{2U}, \quad (7.25)$$

where t_{ss} is given by Eq. (7.24) and N_{\min} by Eq. (7.14).

7.2.4 Quality of microgravity

The quality of microgravity can be compromised by quasisteady residual accelerations, by vibrations and by occasional transients resulting from the firing of attitude thrusters.

Quasi-steady accelerations

We first contemplate quasisteady microgravity levels, such as those resulting from atmospheric drag or from tidal forces on experiments located away from the center

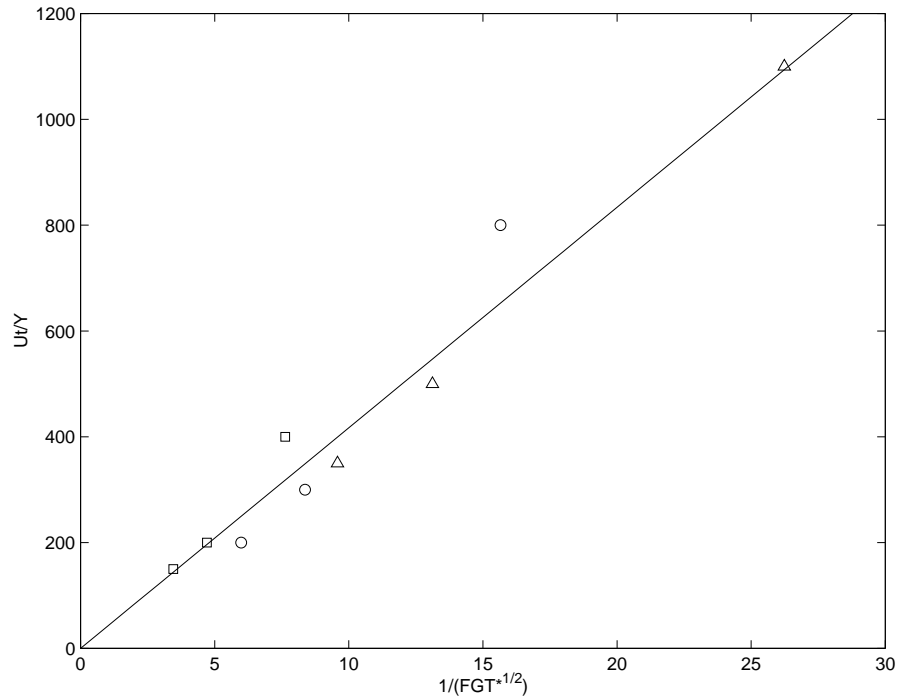


Figure 7.3: Dimensionless relaxation time versus $[(1 + 4G)\sqrt{T_{ss}^*}]^{-1}$ evaluated at steady state. The circles, triangles and squares represent numerical simulations with conditions of Figure 7.2 at $\bar{\nu} = 0.23, 0.33$ and 0.43 , respectively. For each volume fraction, the three data points correspond to $e = 0.75, 0.85$, and 0.95 .

of mass of the International Space Station. In the absence of a gas, the effects of small accelerations scale with a Froude number Fr involving the diameter of flow spheres and the relative velocities of the moving boundaries, $Fr = g_r \sigma / U^2$, where g_r is the quasisteady residual acceleration. Thus, reductions in boundary speeds make the flow more susceptible to residual microgravity. This sensitivity is exacerbated by the presence of a gas, which further reduces the fluctuation velocity of the spheres.

To derive an analytical expression for the corresponding requirements, we consider grains flowing along a single direction in a rectilinear, fully developed channel. As in Section 5.2, we treat the gas drag as an effective body force g_{eff} exerted on all grains in the flow direction. If we assume that the component of mean granular velocity in the x -direction is u_s and the components in the y - and z -directions vanish, the granular momentum balances are then

$$\frac{\partial \tau_{xy}}{\partial y} + \frac{\partial \tau_{xz}}{\partial z} + \nu \rho_s (g_{r,x} + g_{eff}) = 0, \quad (7.26)$$

$$-\frac{\partial P}{\partial y} + \nu \rho_s g_{r,y} = 0, \quad (7.27)$$

and

$$-\frac{\partial P}{\partial z} + \nu \rho_s g_{r,z} = 0, \quad (7.28)$$

where $g_{r,x}$, $g_{r,y}$ and $g_{r,z}$ are small residual accelerations in the x -, y - and z -directions, respectively, τ_{xy} and τ_{xz} are the granular shear stresses, and P is the granular pressure. Substituting Eqs. (7.27) and (7.28) into Eq. (7.26), we have, after some manipulation,

$$P \left[\frac{\partial}{\partial y} \left(\frac{\tau_{xy}}{P} \right) + \frac{\partial}{\partial z} \left(\frac{\tau_{xz}}{P} \right) \right] + \frac{\tau_{xy}}{P} \nu \rho_s g_{r,y} + \frac{\tau_{xz}}{P} \nu \rho_s g_{r,z} + \nu \rho_s g_{r,x} = 0. \quad (7.29)$$

Using the constitutive relations in Chapter 3 for the granular pressure and shear

stresses, the dimensionless x -momentum balance becomes,

$$\begin{aligned} \frac{\partial^2 u_s^*}{\partial y^{*2}} + \frac{\partial^2 u_s^*}{\partial z^{*2}} + \frac{F\sqrt{T^*}}{J} \frac{\partial}{\partial y^*} \left(\frac{J}{F\sqrt{T^*}} \right) \frac{\partial u_s^*}{\partial y^*} + \frac{F\sqrt{T^*}}{J} \frac{\partial}{\partial z^*} \left(\frac{J}{F\sqrt{T^*}} \right) \frac{\partial u_s^*}{\partial z^*} \\ + \frac{5\sqrt{\pi}}{8JG\sqrt{T^*}} \left(\frac{H}{\sigma} \right)^2 \left(Fr_x + Fr_{eff} + \frac{\tau_{xy}}{P} Fr_y + \frac{\tau_{xz}}{P} Fr_z \right) = 0, \end{aligned} \quad (7.30)$$

where $u_s^* \equiv u_s/U$, $y^* \equiv y/H$, $z^* \equiv z/H$, $T^* \equiv T/U^2$, J and F are analytical functions of ν given in Chapter 3, and the Froude numbers are based on the particle diameter σ and the relative boundary speed U .

From Eq. (7.30) it is clear that, because $\tau_{xz}/P < \tau_{xy}/P < 1$ in general, the residual microgravity in the flow direction produces the most severe effects. Thus, to derive a conservative criterion, we focus our analysis on residual accelerations in that direction. We then assume for simplicity that u_s only varies across the cell, and that ν and T are constant. Thus Eq. (7.30) is simplified to

$$\frac{d^2 u_s^*}{dy^{*2}} \approx -\frac{5\sqrt{\pi}}{8JG\sqrt{T^*}} \left(\frac{H}{\sigma} \right)^2 Fr_x. \quad (7.31)$$

Using Eq. (7.31), we then calculate the additional centerline velocity due to the extra curvature of the velocity profile,

$$\Delta u_{s,c}^* \approx \frac{5\sqrt{\pi}}{64JG\sqrt{T^*}} \left(\frac{H}{\sigma} \right)^2 Fr_x. \quad (7.32)$$

To calculate the additional velocity due to the extra slip at the bumpy walls, we first write the imbalance in the shear stress on the two boundaries by integrating Eq. (7.26) between these, and ignoring the presence of side walls,

$$S_1 - S_0 + \nu\rho_s(g_{r,x} + g_{eff})H = 0, \quad (7.33)$$

where S_1 and S_0 are, respectively, the shear stresses at the top and bottom bumpy boundaries. From Eq. (7.33), it is clear that the additional shear stresses at the boundaries due to the residual acceleration satisfy

$$\Delta S_1 - \Delta S_0 + \nu\rho_s g_{r,x} H = 0, \quad (7.34)$$

which gives, after dividing both sides by normal stress N and using the definition of Froude number,

$$\Delta\left(\frac{S}{N}\right)_1 - \Delta\left(\frac{S}{N}\right)_0 + \frac{(H/\sigma)Fr_x}{(1+4G)T^*} = 0. \quad (7.35)$$

Substituting the boundary condition (7.20), we calculate the average of the increase in the slip velocity at the wall,

$$\Delta u_{s,b}^* \approx \frac{(H/\sigma)Fr_x}{(b_1 + b_0)(1+4G)\sqrt{T^*}}, \quad (7.36)$$

where b_1 and b_0 are the constants depending on the geometry of the top and bottom boundaries, respectively. Finally, we take the resulting increase in the mean granular velocity at the centerline to be the sum of the contributions from Eq. (7.32) and Eq. (7.36). In this simple analysis, the sum may be written

$$\Delta u_s^* \approx c \frac{Fr_x}{\sqrt{T^*}}, \quad (7.37)$$

where the coefficient c is a function of ν , H/σ and, through b_1 and b_0 , the geometry of the boundaries. To evaluate this coefficient, we integrate Eqs. (7.26) through (7.28) numerically and find Δu_s^* for a variety of volume fractions and ratios $Fr_x/\sqrt{T^*}$. The resulting values of c compare well with the estimates from the simpler analysis of Eqs. (7.32) and (7.36). For the geometrical parameters of our apparatus, we fit $c(\nu)$ to the expression

$$c(\nu) = 10.69 + 80.39\nu - 183.4\nu^2, \quad (0.05 \leq \nu \leq 0.4). \quad (7.38)$$

Figure 7.4 shows the curve-fit of $c(\nu)$ and the comparison of the increase of granular velocity at the centerline with $Fr_x/\sqrt{T^*}$ from the numerical integration and the simpler analysis Eq. (7.37). We then specify that the change in the centerline mean granular velocity resulting from residual accelerations should be smaller than 5%

of U ,

$$Fr \equiv \frac{g_r \sigma}{U^2} < 5\% \frac{\sqrt{T^*}}{c(\nu)}. \quad (7.39)$$

Vibrations

On the International Space Station (ISS), vibrations may be caused by the use of the robot arm, by the resonance of the KU band antenna, or by the routine physical exercises carried out by the astronauts. The magnitude of such vibrations is generally specified as an rms acceleration. To evaluate their effects on our experiments, we assume that the vibrations are sinusoidal, and we calculate the corresponding rms velocity fluctuations. We then assume that vibrations play a negligible role in our tests if the rms velocity fluctuations that they impose on the cell are much smaller than their granular counterpart, \sqrt{T} , over the entire frequency spectrum. Thus, we require

$$\max(g_{rms}/2\pi f) \leq \sqrt{T} \quad (7.40)$$

where g_{rms} is the rms residual acceleration of the ISS at the frequency f and T is the mean granular temperature in the experiment. Because the rms acceleration spectrum grows at a rate no greater than the first power of f , this is equivalent to ensuring that g_{rms} at the collision frequency f_{coll} is less than

$$g_{rms}(f_{coll}) \leq 2\pi f_{coll} \sqrt{T}. \quad (7.41)$$

Thrusters

Another potentially disruptive source of acceleration arises from the occasional firing of thruster rockets. Data collected after these transient events are corrupted and should not be used. We use the time to steady state in Eq. (7.24) as an

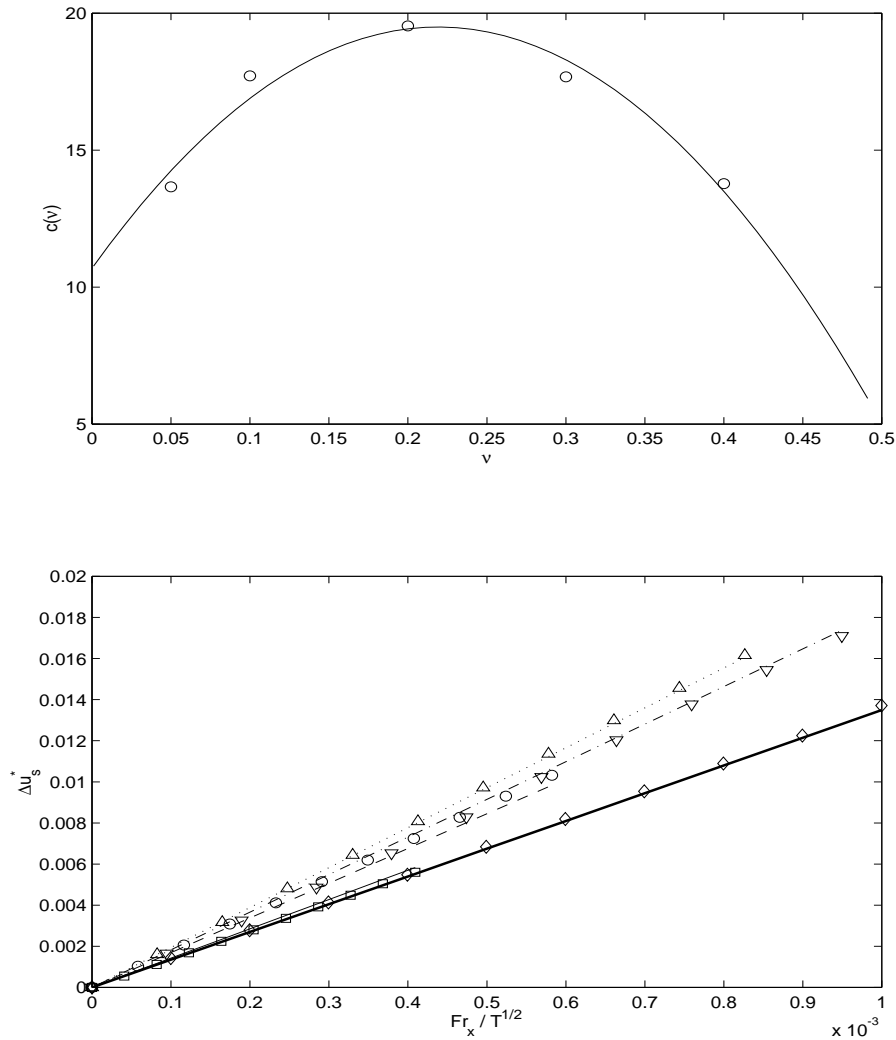


Figure 7.4: Increase in the mean granular velocity at the centerline with streamwise residual acceleration. Top plot: curve-fit of $c(\nu)$ in Eq. (7.37). Symbols are results from numerical integration of the conservation equations. The solid line is the least square fit Eq. (7.38). Bottom plot: variations of Δu_s^* with $Fr_x / \sqrt{T^*}$. Symbols are results from the numerical integration and lines are the simpler analysis Eq. (7.37) with $c(\nu)$ given by Eq. (7.38). Squares and thin solid line: $\nu = 0.05$, circles and dashed line: $\nu = 0.1$, up-triangles and dotted line: $\nu = 0.2$, down-triangles and dash-dotted line: $\nu = 0.3$, diamonds and thick solid line: $\nu = 0.4$.

estimate of the waiting time required after thruster firing. Because the grains are already agitated when a thruster is fired, we anticipate that this estimate is conservative.

7.2.5 Sphere properties

The material properties of the flow spheres influence experiments in many ways. We prescribe sphere materials in order to control experimental conditions.

In the derivation of kinetic theory, the coefficient of normal restitution e between flow particles is assumed to be a constant. Using the collision apparatus described by Foerster *et al* [33], we can measure these impact parameters before experiments. However, it is well known that even for collisions between perfect spheres, e depends on impact velocity [38, 43]. According to the elastic-plastic theory of Thornton and Ning [120], the normal restitution coefficient decreases with relative impact velocity of the order of $T^{1/2}$ only when the latter exceeds a critical value

$$u_{s,cr} = \left(\frac{\pi}{E^*} \right)^2 \left(\frac{\sigma_c^5}{160\rho_s} \right)^{1/2}, \quad (7.42)$$

where σ_c is the compressive yield strength of the sphere material and E^* is a parameter that combines the Poisson's ratio and Young's modulus as defined in Eq. (4.6). For the sphere materials we considered, the critical impact velocity is about $0.1 \sim 1$ m/s. Because the projected experiments do not reach a fluctuation velocity exceeding $u_{s,cr}$, we expect that the impact parameters of the flow spheres will remain the same as measured in our facility.

In our viscous dissipation experiments, we measure the granular temperature to infer the viscous dissipation coefficient R_{diss} . As Sangani *et al* [107] and Verberg & Koch [123] showed, R_{diss} depends on the lubrication cut-off ε_m , which characterizes

the non-continuum breakdown of the lubrication flow in the gap between two approaching particles [118].

With real spheres colliding in a gas, three other phenomena may affect the magnitude of R_{diss} . The first arises from the compressibility of the gas. It is significant when the gap separating two spheres is less than h_c in Eq. (4.5). The second phenomenon occurs when lubrication forces induce elastic deformations in the solid. It is relevant when the gap is smaller than h_d in Eq. (4.6). Because we plan to determine the dependence of R_{diss} on ε_m by changing λ_g through partial evacuation of the cell, we require that the lubrication breakdown be controlled by the non-continuum effect. Therefore, we choose sphere materials such that $h_c < 9.76\lambda_g$ and $h_d < 9.76\lambda_g$.

The third potential difficulty is associated with microscopic asperities on the particle surface. Following the analysis of Leighton [72], Davis [29] showed that the lubrication force due to small asperities is always much smaller than the corresponding force on the sphere as a whole. However, if asperities rising a distance δ above the smooth particle surface are larger than the cutoff distance $\varepsilon_m\sigma$, they can bring the grains into mechanical contact before the spheres can experience non-continuum lubrication flows. Although this suggests that the expression for R_{diss} may be modified by simply substituting the ratio δ/σ in place of ε_m in Eq. (7.2), it is unclear how the terms in R_{diss} that depend on ν alone and that are measured in the smooth particle simulations are affected by the new cut-off distance. Nonetheless, because these terms are collectively smaller than $G(\nu)\ln\varepsilon_m$ at sufficiently large ν , this objection is generally inconsequential. At any rate, because asperities are much more difficult to characterize than the mean free path of the gas, it is prudent to ensure that experimental spheres have typical asperities with $\delta < \varepsilon_m\sigma$,

which is achievable for material of high polish like ceramic or hard metals.

7.2.6 Continuum flow

To describe the entire gas flow through the particles as a continuum, it is necessary for the Knudsen number

$$Kn_g \equiv \frac{\lambda_g}{L_c}$$

to be small. In this expression, λ_g is the molecular mean free path of the gas and L_c is a characteristic length scale of the flow, which can either be the size of the particles or the gap between them, whichever is smaller. The gap between particles can be estimated as the product of the particle fluctuation velocity and the mean free time of particles. Hence the gas Knudsen number is

$$Kn_g \equiv \frac{\lambda_g}{\min\left(\sigma, \frac{\sqrt{\pi}\sigma}{24G(\nu)}\right)}. \quad (7.43)$$

In experiments involving partial evacuation of the cell, Kn_g should be kept much smaller than one to limit non-continuum gas flow to small regions between approaching spheres. We adopt the conservative criterion of $Kn_g \leq 0.01$, which is common practice in continuum flows of molecular gases.

We are also interested in interpreting our experimental data with a continuum description of the solid phase. For that to be valid, the particle Knudsen number must also be small. Here the particle Knudsen number is defined as

$$Kn_s \equiv \frac{\lambda_s}{H}, \quad (7.44)$$

in which

$$\lambda_s = \frac{\sigma}{6\sqrt{2}G(\nu)} \quad (7.45)$$

is the mean free path of particles. In a typical shearing flow, we find that the continuum theory agrees well with the results of numerical simulations for $Kn_s \leq 0.4$. We adopt this criterion for other granular flows as well.

7.2.7 Accuracy of gas flow rate

In the Viscous Drag experiments, we will infer the drag coefficient R_{drag} by measuring simultaneously the particle and gas velocities, or, at least, measure the gas volume flow rate. Thus the accuracy of R_{drag} is mainly predicated on the measurement accuracy of the gas flow rate. To estimate this accuracy, we vary R_{drag} in our numerical solutions and find the corresponding changes in the gas volume flow rate Q_g . We also estimate the gas flow rate as

$$Q_g^* \approx (1 - \bar{\nu})\bar{u}_s^* + \frac{1}{H/\sigma} \frac{R_\tau St}{\bar{\nu} R_{drag}}, \quad (7.46)$$

which is made dimensionless with the boundary velocity U and the cross sectional area of the channel. In this expression, \bar{u}_s^* and $\bar{\nu}$ are the average particle mean velocity and volume fraction, respectively. When writing Eq. (7.46), we ignored the effects of solid boundaries on the gas flow rate and balanced the pressure gradient with the drag. The first term in Eq. (7.46) represents the gas flow due to the entrainment by the particles. The second term in Eq. (7.46) represents the relative motion between the gas and the solids due to the gas pressure gradient in the flow direction.

From this expression, we calculate the change in gas flow rate due to a change in R_{drag} ,

$$\Delta Q_g^* = R_\tau St \frac{\sigma}{H} \frac{1}{\bar{\nu}} \left(\frac{1}{R_{drag} + \Delta R_{drag}} - \frac{1}{R_{drag}} \right). \quad (7.47)$$

To obtain Eq. (7.47), we noted that the mean solid velocity is determined almost

entirely by the gas pressure gradient and is independent of R_{drag} .

Eq. (7.47) leads to the relative change in gas flow rate,

$$\frac{\Delta Q_g^*}{Q_g^*} \approx \frac{\varepsilon_{drag} R_\tau St}{\bar{u}_s^* (H/\sigma) \bar{\nu} (1 - \bar{\nu}) R_{drag} + R_\tau St}, \quad (7.48)$$

in which

$$\varepsilon_{drag} \equiv \frac{\Delta R_{drag}}{R_{drag}}$$

is the relative change in R_{drag} and if the change in R_{drag} is not large, then

$$\frac{1}{R_{drag} + \Delta R_{drag}} - \frac{1}{R_{drag}} \approx \frac{\Delta R_{drag}}{R_{drag}} = \varepsilon_{drag}.$$

Because \bar{u}_s^* also varies with $\bar{\nu}$, we can write Eq. (7.48) as

$$\frac{\Delta Q_g^*}{Q_g^*} \approx \frac{\varepsilon_{drag} R_\tau St}{C_Q(\bar{\nu}) \bar{\nu} (1 - \bar{\nu}) R_{drag} + R_\tau St}, \quad (7.49)$$

where $C_Q(\bar{\nu})$ is a function of $\bar{\nu}$ that we approximate by curve fitting the results of the numerical calculations. Figure 7.5 shows the relative change in Q_g^* corresponding to a 20% change in R_{drag} , i.e., $\varepsilon_{drag} = 0.2$. For this particular cell, the coefficient $C_Q(\bar{\nu})$ is fitted to the expression

$$C_Q = 2.571 \bar{\nu}^{-0.2835}. \quad (7.50)$$

We plot in Figure 7.5 the variations of Eq. (7.49) using the expression of $C_Q(\bar{\nu})$ in Eq. (7.50).

With a specified uncertainty ε_{drag} , Eq. (7.49) then prescribes the minimum accuracy in Q_g^* for each experiment. Alternatively, if the accuracy in gas flow rate measurement is known, Eq. (7.49) then sets a limit on the combination of parameters $R_\tau St$ for meaningful experiments,

$$R_\tau St \geq \frac{C_Q \bar{\nu} (1 - \bar{\nu}) R_{drag} \varepsilon_Q}{\varepsilon_{drag} - \varepsilon_Q}, \quad (7.51)$$

where ε_Q is the accuracy that can be achieved in the measurement of gas volume flow rate.

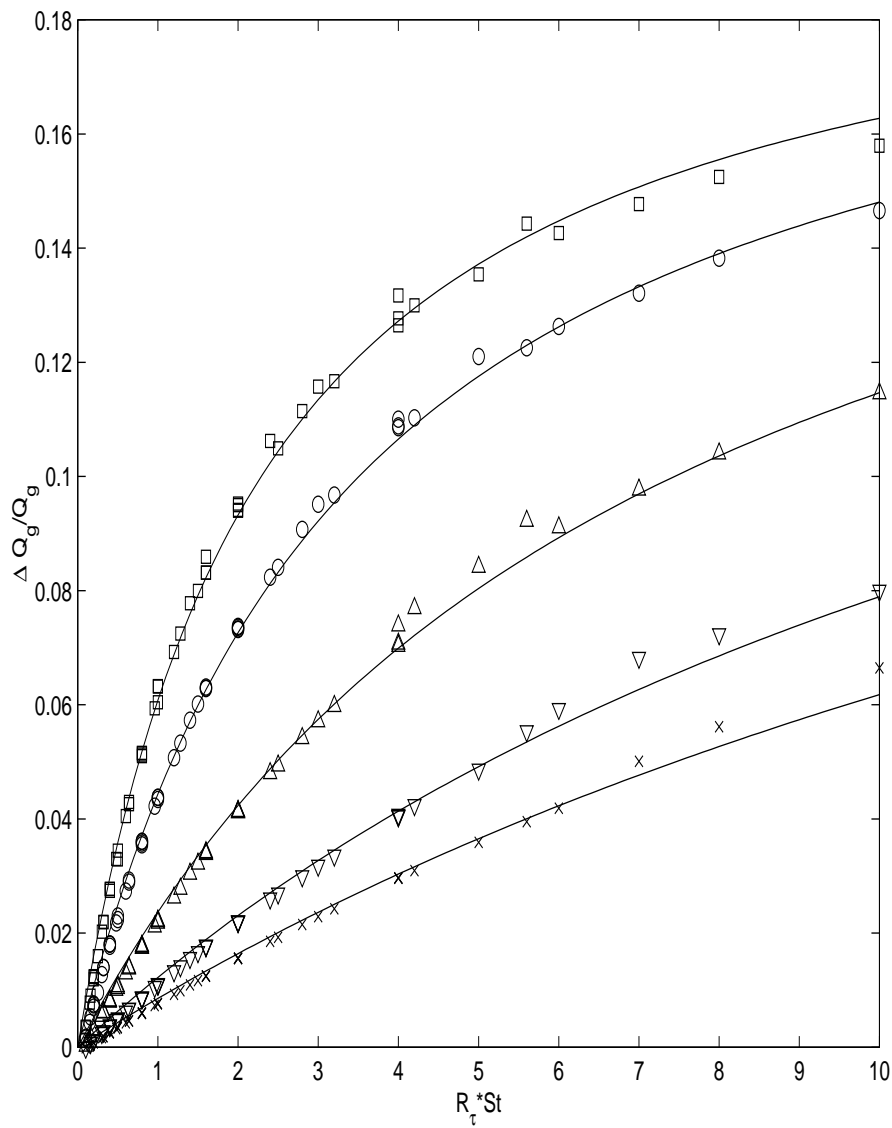


Figure 7.5: Variations of the gas volume flow rates due to a 20% change in R_{drag} . Symbols are numerical solutions of the 1 dimensional integral Eqs. (4.38), (4.40), and (4.41). Lines are the corresponding curve fits of Eq. (7.49). Squares: overall volume fraction $\bar{\nu} = 0.15$. Circles: $\bar{\nu} = 0.2$. Up-triangles: $\bar{\nu} = 0.3$. Down-triangles: $\bar{\nu} = 0.4$. Crosses: $\bar{\nu} = 0.45$. For other parameters, see Appendix E.

Chapter 8

Conclusions and Recommendations

In this work, we studied continuum descriptions of granular flows with negligible interstitial gas and gas-particle flows with large to moderate particle inertia. In both kinds of flows, particle collisions are the dominant mechanism for momentum transfer and the particle velocity distribution is determined by collisions rather than by hydrodynamic interactions.

We solved the governing equations for the granular and gas phases with appropriate boundary conditions and we compared the results with computer simulations and/or physical experiments in microgravity.

In particular, we derived new boundary conditions for granular flows interacting with bumpy frictional walls made of cylinders perpendicular to the mean flow, in the case where the wall slip may be large. We developed several numerical techniques to solve the governing equations for dry granular flows of a single species, for dry granular flows of a binary mixture, and for granular flows interacting with a viscous gas, with or without body forces present. We generally found good agreement between theory, simulations and experiments in the limits that the underlying theories were meant to capture e.g., nearly elastic spheres, nearly identical species, moderate to high Stokes numbers, etc.

We considered steady, fully-developed flows in rectangular channels, and we studied flow development along a shear cell shaped as a race track, and along an axisymmetric Couette cell into which gas is injected.

With the corresponding gas-solid theories, we designed future long-term microgravity experiments in the axisymmetric cell by prescribing test conditions, by

evaluating errors in the computer vision techniques used to record granular velocity statistics, and by providing requirements for carrying out the experiments in Space.

We now discuss salient problems remaining in this field, and suggest avenues for further research. Our analyses focused on steady granular flows. It would be natural to extend our work to unsteady flows in a way outlined by Babic [8]. For example, one may consider the unsteady segregation process in a Couette cell with a binary mixture of granular materials. One could also revisit the development of granular flows by solving the governing equations directly instead of using an integral treatment and an assumed shape of the velocity profile.

For greater relevance to practical problems, it is desirable to consider flows that do not involve nearly elastic, nearly frictionless grains. A difficulty with greater inelasticity or friction is that the fluctuation energy becomes strongly anisotropic and that it is not distributed equally among different granular species. Another is that strong collisional dissipation creates regions where grains condense into amorphous assemblies or clusters that experience long-term contacts. This situation is typical of most practical granular flows on Earth. In such regions, the stresses develop a component that is not rate-dependent [17]. A challenge for future research is to produce a theory that can successfully reconcile the collisional flows considered in this work and flows where rate-dependent and rate-independent stresses coexist.

Boundary conditions for collisional granular flows at a solid wall are derived by considering the transfer of momentum and fluctuation energy at the wall through collisions between flow particles and the wall. Wall stresses and flux of fluctuation energy are obtained by integrating over the particle velocity distribution. In current derivations, the particle velocity distribution at the wall is either taken

to be the same as in the bulk flow [104, 105], or it is assumed to have a simple form [61, 50]. In principle, the velocity distribution at the wall can be found by solving the Boltzmann equation with an appropriate collision operator that takes into account the effect of the solid wall. Another problem associated with the particle velocity distribution at the wall is that particle velocities before and after a collision are correlated. As Jenkins & Louge [56] showed, this correlation can change the flux of fluctuation energy at the wall. For boundary conditions at frictional walls, the effect of particle spin is only included in a crude way by relating the mean particle spin to the vorticity of the mean flow. However, computer simulations showed that this assumption is not valid at the boundary [19, 76], although it is approximately true for flows in the interior. Recently, Mitarai *et al* [88] proposed a “micropolar” theory to predict the transport of particle angular momentum near solid boundaries, which might be included in the derivation of boundary conditions.

Stability of granular flows is another important problem that we have ignored. Collisional shearing flows have been the subject of several stability analyses [7, 129, 128, 2, 98]. Nott *et al* [98] showed that boundaries play an important role in stabilizing the flow. However, these authors used heuristic boundary conditions for their analysis. Although we verified by computer simulations that the steady solutions in Chapter 3 are stable, it would be instructive to perform stability analyses of all solutions found in our study.

Lastly, the average equations for gas-particle flows in this work have not been rigorously derived. In particular, the constitutive equations for the particle phase are borrowed directly from the kinetic theory of granular flows. Moreover, the correct form of the term representing the stress due to gas-particle hydrodynamic

interactions is not yet clear. To extend existing theories to lower Stokes numbers, one may consider an approach similar to Sangani *et al* [107] to derive constitutive equations for gas-particle flows with both inelastic and viscous dissipations of fluctuation kinetic energy.

Appendix A

Collision Integrals

When calculating collisional contributions to the stresses and flux of fluctuation energy at solid boundaries, we need to evaluate integrals of the form

$$I(n, a) = \int_a^\infty x^n e^{-\frac{x^2}{2T}} dx,$$

where $n = 0, 1, 2, \dots$, is non-negative integers and $-\infty \leq a \leq \infty$.

For arbitrary a , the integrals can be written in compact form as if n is odd,

$$I(n, a) = \frac{1}{2} \Gamma\left(\frac{n+1}{2}\right) (2T)^{\frac{n+1}{2}} e^{-\frac{a^2}{2T}} \sum_{k=0}^{\frac{n-1}{2}} \frac{\left(\frac{a^2}{2T}\right)^k}{\Gamma(k+1)};$$

and if n is even,

$$I(n, a) = \frac{1}{2} \Gamma\left(\frac{n+1}{2}\right) (2T)^{\frac{n+1}{2}} \left[1 - \operatorname{erf}\left(\frac{a}{\sqrt{2T}}\right) + e^{-\frac{a^2}{2T}} \sum_{k=0}^{\frac{n}{2}-1} \frac{\left(\frac{a^2}{2T}\right)^{k+\frac{1}{2}}}{\Gamma\left(k+\frac{3}{2}\right)} \right];$$

where $\Gamma(x)$ is the Gamma-function, and

$$\operatorname{erf}(x) = \frac{2}{\sqrt{\pi}} \int_0^x e^{-t^2} dt, \quad (-\infty \leq x \leq \infty),$$

is the error function.

If $a = 0$, the two results can be combined as

$$I(n, 0) = \int_0^\infty x^n e^{-\frac{x^2}{2T}} dx = \frac{1}{2} \Gamma\left(\frac{n+1}{2}\right) (2T)^{\frac{n+1}{2}}, \quad (n = 0, 1, 2, \dots).$$

For convenience, some frequently used results with arbitrary a are listed below,

$$\begin{aligned}\int_a^\infty e^{-\frac{x^2}{2T}} dx &= \frac{1}{2}\sqrt{2\pi T} \left[1 - \operatorname{erf} \left(\frac{a}{\sqrt{2T}} \right) \right], \\ \int_a^\infty x e^{-\frac{x^2}{2T}} dx &= T e^{-\frac{a^2}{2T}}, \\ \int_a^\infty x^2 e^{-\frac{x^2}{2T}} dx &= \frac{1}{2}T\sqrt{2\pi T} \left[1 - \operatorname{erf} \left(\frac{a}{\sqrt{2T}} \right) \right] + aT e^{-\frac{a^2}{2T}}, \\ \int_a^\infty x^3 e^{-\frac{x^2}{2T}} dx &= (a^2 + 2T)T e^{-\frac{a^2}{2T}}, \\ \int_a^\infty x^4 e^{-\frac{x^2}{2T}} dx &= \frac{3}{2}T^2\sqrt{2\pi T} \left[1 - \operatorname{erf} \left(\frac{a}{\sqrt{2T}} \right) \right] + (a^3 + 3aT)T e^{-\frac{a^2}{2T}}.\end{aligned}$$

Appendix B

Approximations of Stresses and Heat

Flux at Flat, Frictional Walls

In section 2.2, we calculated the stress ratio and heat flux at flat frictional walls in two mutually exclusive cases, respectively called the “all-sticking” and “all-sliding” limits. On p. 36, we provided simplified expressions of S/N and Q assuming a distribution of normal velocity shaped as twin δ -functions. In this Appendix, we list the corresponding expressions for the Maxwellian and Weibull velocity distributions. These results can be used as approximations to Eqs. (2.48)-(2.51).

For a Maxwellian distribution, in the “small-slip/all-sliding” regime,

$$\frac{S}{N} = \sqrt{\frac{2}{\pi}} \frac{\mu}{\gamma} r, \quad (\text{B.1})$$

$$\begin{aligned} \frac{Q}{N\sqrt{T_{yy}}} &= \sqrt{\frac{2}{\pi}} \left\{ \frac{1}{2\gamma^2} \mu \bar{\mu}_0 (1 + \beta_0) r^2 - \frac{1}{4\gamma^2} \mu \bar{\mu}_0 (1 - \beta_0) - (1 - e) \right\} \\ &= \sqrt{\frac{2}{\pi}} \left\{ \frac{\mu}{\bar{\mu}_0} (1 + \beta_0) \frac{T_{xx}}{T_{yy}} \left(\frac{g_0^2}{2T_{xx}} \right) - \frac{1}{2} \frac{\mu}{\bar{\mu}_0} (1 - \beta_0) \frac{T_{xx}}{T_{yy}} - (1 - e) \right\} \end{aligned} \quad (\text{B.2})$$

and in the “all-sliding” regime,

$$\frac{S}{N} = \mu \operatorname{erf} \left(\frac{g_0}{\sqrt{2T_{xx}}} \right) \approx \mu, \quad (\text{B.3})$$

$$\frac{Q}{N\sqrt{T_{yy}}} \approx \sqrt{\frac{2}{\pi}} \left[\mu \bar{\mu}_0 (1 + \beta_0) - (1 - e) \right]. \quad (\text{B.4})$$

For a Weibull distribution, in the “small-slip/all-sliding” regime,

$$\frac{S}{N} = \frac{\sqrt{\pi}}{2} \frac{\mu}{\gamma} r, \quad (\text{B.5})$$

$$\begin{aligned} \frac{Q}{N\sqrt{T_{yy}}} &= \frac{\sqrt{\pi}}{2} \left\{ \frac{1}{2\gamma^2} \mu \bar{\mu}_0 (1 + \beta_0) r^2 - \frac{1}{4\gamma^2} \mu \bar{\mu}_0 (1 - \beta_0) - \frac{3}{4} (1 - e) \right\} \\ &= \frac{\sqrt{\pi}}{2} \left\{ \frac{\mu}{\bar{\mu}_0} (1 + \beta_0) \frac{T_{xx}}{T_{yy}} \left(\frac{g_0^2}{2T_{xx}} \right) - \frac{1}{2} \frac{\mu}{\bar{\mu}_0} (1 - \beta_0) \frac{T_{xx}}{T_{yy}} - \frac{3}{4} (1 - e) \right\} \end{aligned} \quad (\text{B.6})$$

and in the “all-sliding” regime,

$$\frac{S}{N} = \mu \operatorname{erf} \left(\frac{g_0}{\sqrt{2T_{xx}}} \right) \approx \mu, \quad (\text{B.7})$$

$$\frac{Q}{N\sqrt{T_{yy}}} \approx \frac{3\sqrt{\pi}}{8} \left[\mu\bar{\mu}_0(1 + \beta_0) - (1 - e) \right]. \quad (\text{B.8})$$

Figure B.1 and B.2 compare the stress ratio and heat flux from the two-limit approximation and the exact calculation for various impact parameters. As with the twin δ velocity distribution in the small-slip regime, the two-limit approximation agrees with the exact calculation only when γ is large.

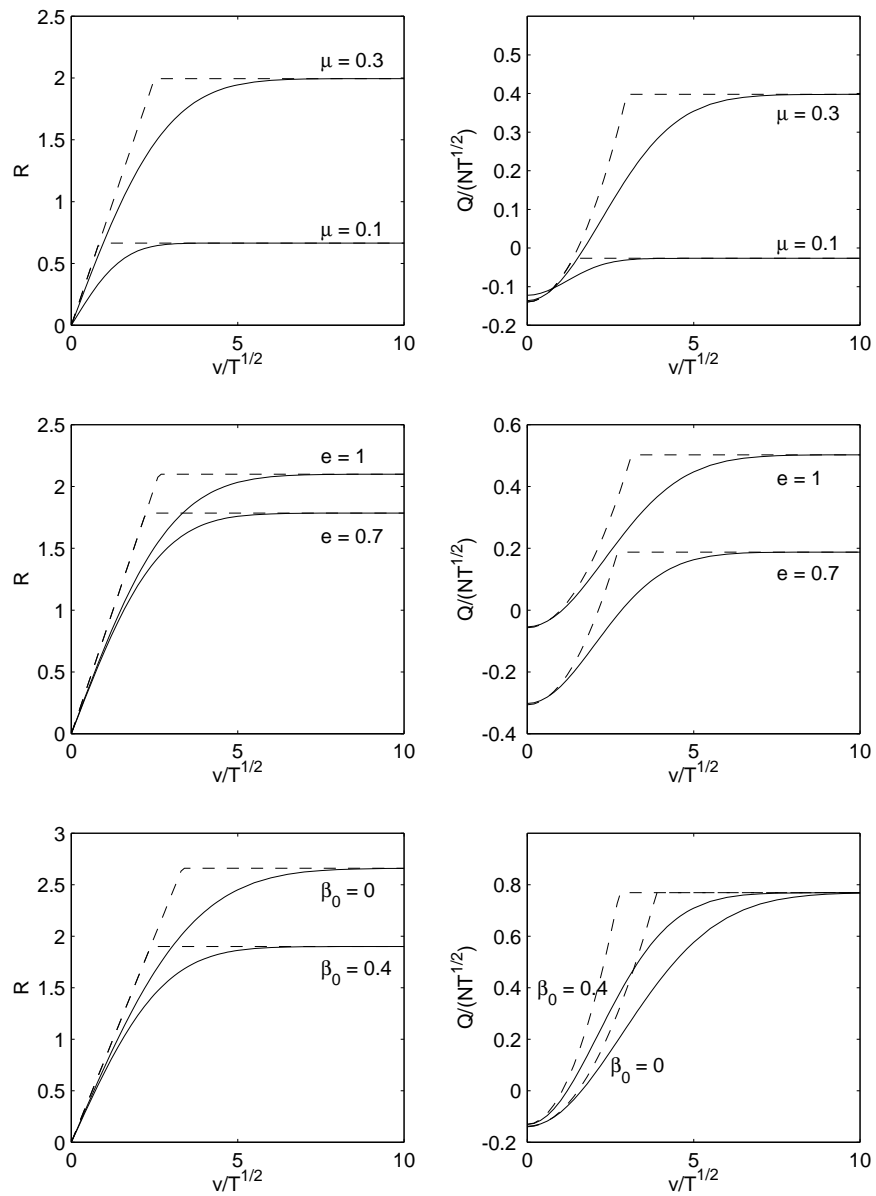


Figure B.1: Comparison of stress ratios and fluxes of fluctuation energy calculated in the two limits of “all-sticking” and “all-sliding” with the exact calculation assuming a Maxwellian distribution. For lines and parameters, see Fig. 2.6.

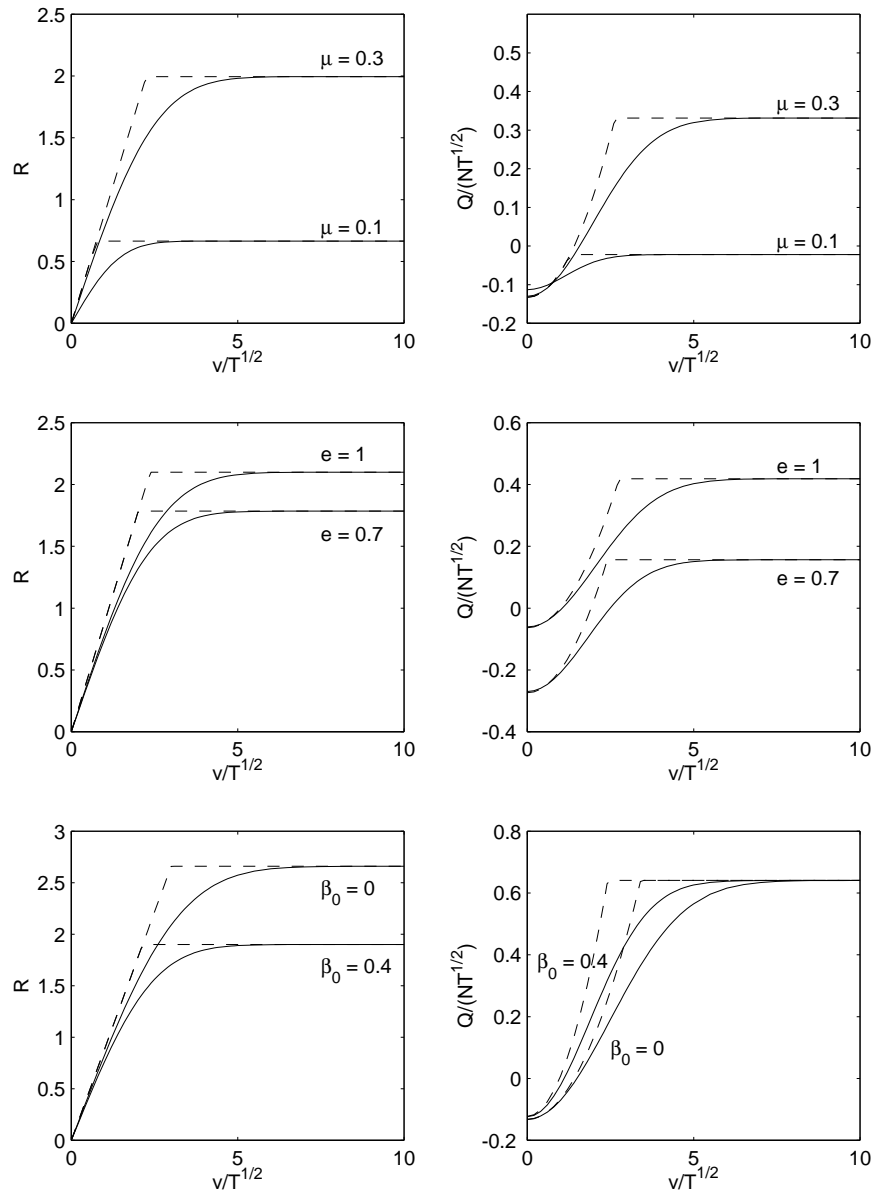


Figure B.2: Comparison of stress ratios and fluxes of fluctuation energy calculated in the two limits of “all-sticking” and “all-sliding” with the exact calculation assuming a Weibull distribution. For lines and parameters, see Fig. 2.6.

Appendix C

Determination of Granular Pressure

When solving the governing equations for granular flows, we often need to determine the granular pressure based on a known average particle volume fraction. The simplest case is when $P = \text{const}$, as in the rectilinear flow without transverse body forces. To that end, we find the solid volume fraction ν as a function of P^*/T^* , where $P^* \equiv P/\rho_s U^2$ is the dimensionless granular pressure and $T^* \equiv T/U^2$ is the dimensionless granular temperature. For convenience, we denote P^*/T^* as \tilde{P} . From the constitutive relation for granular pressure, $\tilde{P} = \nu(1 + 4G)$. The variations of ν with \tilde{P} are shown in Figure C.1. After observing the shape of this curve, we propose to fit it as

$$\nu = \frac{a_1 \tilde{P}^3 + b_1 \tilde{P}^2 + c_1 \tilde{P} + d_1}{a_2 \tilde{P}^3 + b_2 \tilde{P}^2 + c_2 \tilde{P} + d_2}, \quad (\text{C.1})$$

where a_1, b_1, \dots, d_2 , are constants.

We require that the curve fit preserve some important properties of the original function, namely,

$$\nu(\tilde{P} = 0) = 0, \quad (\text{C.2})$$

$$\nu(\tilde{P} \rightarrow \infty) \rightarrow \nu_c, \quad (\text{C.3})$$

and

$$\left. \frac{d\nu}{d\tilde{P}} \right|_{\tilde{P}=0} = 1, \quad (\text{C.4})$$

where ν_c is the random close-packing volume fraction. Following Torquato [121], we choose $\nu_c = 0.64$. It is straightforward to show that these requirements lead to

$$d_1 = 0, \quad (\text{C.5})$$

$$a_1 = \nu_c a_2, \quad (\text{C.6})$$

and

$$c_1 = d_2. \quad (\text{C.7})$$

Therefore, the functional form C.1 can be written as

$$\nu = \frac{\tilde{P}(\nu_c \tilde{P}^2 + a\tilde{P} + b)}{\tilde{P}^3 + c\tilde{P}^2 + d\tilde{P} + b}, \quad (\text{C.8})$$

where a , b , c , and d are constants and can be derived from least square error conditions,

$$\begin{pmatrix} a \\ b \\ c \\ d \end{pmatrix} = \begin{bmatrix} \int x^2 & \int xy & \int xz & \int xs \\ \int xy & \int y^2 & \int yz & \int ys \\ \int xz & \int yz & \int z^2 & \int zs \\ \int xs & \int ys & \int zs & \int s^2 \end{bmatrix}^{-1} \begin{pmatrix} \int xt \\ \int yt \\ \int zt \\ \int st \end{pmatrix}, \quad (\text{C.9})$$

where $\int()$ is a short-hand notation for $\int()d\tilde{P}$, and x , y , z , s , and t are functions of ν and \tilde{P} ,

$$\begin{aligned} x &\equiv \tilde{P}^2, \\ y &\equiv \tilde{P} - \nu, \\ z &\equiv -\nu\tilde{P}^2, \\ s &\equiv -\nu\tilde{P}, \\ t &\equiv (\nu_c - \nu)\tilde{P}^3. \end{aligned}$$

For convenience, we choose to fit between $0 \leq \nu \leq 0.3$. Then, we have

$$a = 1.53650,$$

$$b = 0.39083,$$

$$c = 4.70196,$$

$$d = 3.08592.$$

The curve fit is shown in Figure C.1 together with the original function. The relative error between the original function and Eq. (C.8) is less than 1.5% over the range $0 \leq \nu \leq 0.6$.

We use the curve fit in an iteration to determine P^* once the granular temperature is known from the energy equation. Starting with an initial guess P^* , we calculate the local particle volume fraction ν and then compare the cross-sectional average volume fraction with the known mean value. We then modify our initial guess of P^* until the error in average volume fractions is less than a specified tolerance.

C.1 Iteration Scheme

We provide details of the iteration procedure for solving the governing equations appearing in this thesis. We begin with a procedure for ordinary differential equations associated with a single dimension. We then extend the procedure to partial differential equations in two dimensions.

C.2 One Dimension

The one dimensional case applies to the integral equations of single species flows in rectilinear (Sections 3.1.2 and 3.1.2) and axisymmetric geometries (Sec. 3.1.2). It also pertains to governing equations for rectilinear flows of binary mixtures (Sections 3.2.1 and 3.2.2). In this Appendix, we illustrate the method with rectilinear flows of a single species. The corresponding ordinary differential equations (3.25), (3.26) and (3.30) for the mean granular velocity u , the fluctuation velocity $w \equiv \sqrt{T}$ and the “volume fraction integral” I are given in Sec. 3.1.2. Here, we write them

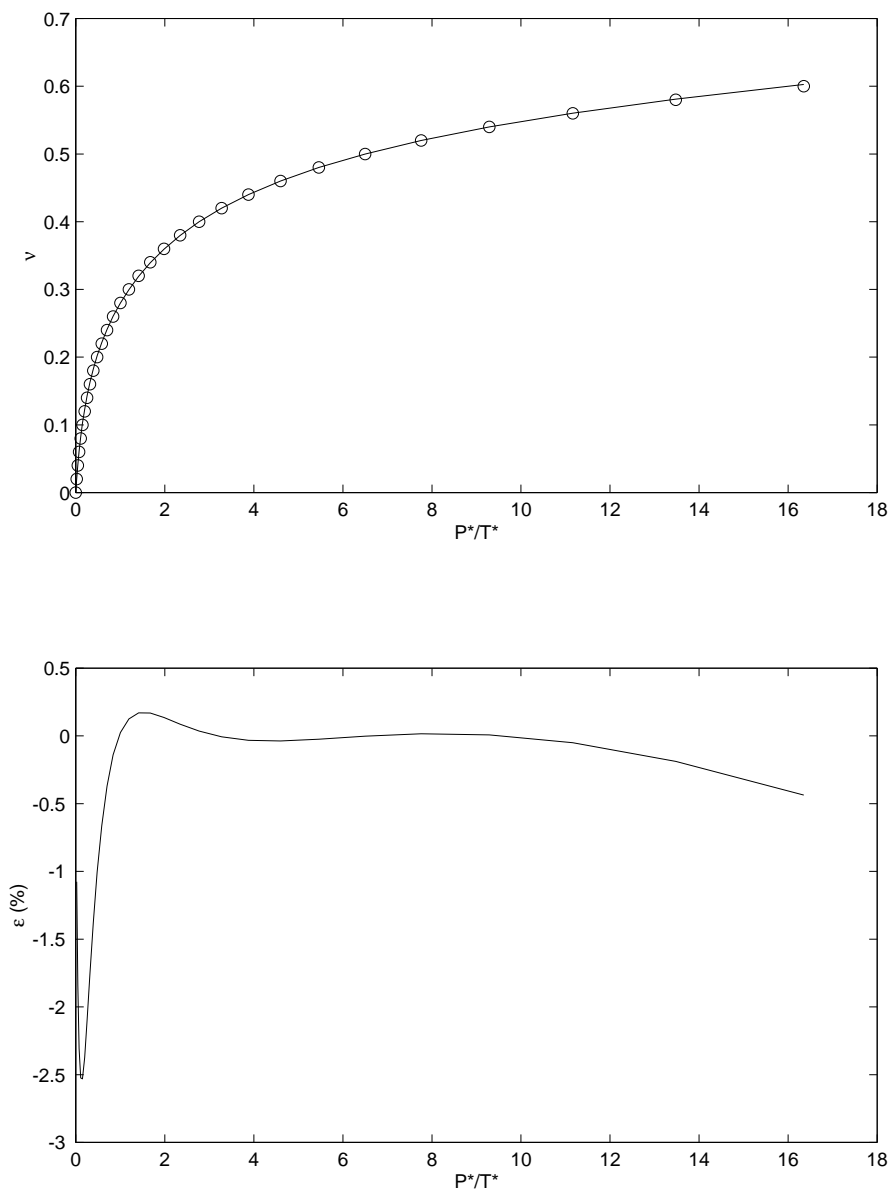


Figure C.1: Curve fit of ν as a function of P^*/T^* . Top plot: ν vs. P^*/T^* ; symbols represent the exact function; the solid line is the curve fit of Eq. C.8. Bottom plot: relative error in the curve fit.

in generic form,

$$\frac{d^2u}{dy^2} + p_u(y; u, w, \nu) \frac{du}{dy} + r_u(y; u, w, \nu)u = s_u(y; u, w, \nu), \quad (\text{C.10})$$

$$\frac{d^2w}{dy^2} + p_w(y; u, w, \nu) \frac{dw}{dy} + r_w(y; u, w, \nu)w = s_w(y; u, w, \nu), \quad (\text{C.11})$$

and

$$\frac{d^2I}{dy^2} + p_\nu(y; u, w, \nu) \frac{dI}{dy} + r_\nu(y; u, w, \nu)I = s_\nu(y; u, w, \nu), \quad (\text{C.12})$$

with the boundary conditions:

at $y=0$,

$$\frac{du}{dy} = a_u(u, w, \nu)u + b_u(u, w, \nu), \quad (\text{C.13a})$$

$$\frac{dw}{dy} = a_w(u, w, \nu)w + b_w(u, w, \nu), \quad (\text{C.13b})$$

$$I(0) = I_0, \quad (\text{C.13c})$$

and at $y=H$,

$$\frac{du}{dy} = c_u(u, w, \nu)u + d_u(u, w, \nu), \quad (\text{C.14a})$$

$$\frac{dw}{dy} = c_w(u, w, \nu)w + d_w(u, w, \nu), \quad (\text{C.14b})$$

$$I(H) = I_n. \quad (\text{C.14c})$$

We solve the coupled equations numerically on a set of equally-spaced points y_j , $j = 0, 1, \dots, n$, with $y_{j+1} - y_j = h$. For convenience, we introduce the short-hand notations $u_j \equiv u(y_j)$, $p_{u,j} \equiv p_u(y_j; u_j, w_j, \nu_j)$, etc.

We replace the differentials with finite differences, e.g.

$$\frac{du}{dy} \approx \frac{u_{j+1} - u_{j-1}}{2h}, \quad \frac{d^2u}{dy^2} \approx \frac{u_{j+1} - 2u_j + u_{j-1}}{h^2} \quad \text{and} \quad \nu_j \approx H \frac{I_{j+1} - I_{j-1}}{2h}. \quad (\text{C.15})$$

and the functions a , b , c , and d in the boundary conditions (C.13), (C.14) are not known without finding u , w and ν first. To handle this difficulty, we solve the difference equation iteratively. At a given iteration step, we use the u , w , and ν calculated in previous step to evaluate the unknown functions. Effectively, this technique allows us to decouple and linearize the problem at each step. The procedure thus consists of the following steps

- [1] At step $k = 0$, set $\mathbf{u}^{(k)}$, $\mathbf{w}^{(k)}$, and $\mathbf{I}^{(k)}$ to the initial guesses $\mathbf{u}^{(0)}$, $\mathbf{w}^{(0)}$, and $\mathbf{I}^{(0)}$.
- [2] Calculate $\nu_j^{(k)}$ from differences of $I_j^{(k)}$, $j = 0, 1, \dots, n$.
- [3] Calculate $A_u^{(k)}$, $A_w^{(k)}$, $A_\nu^{(k)}$, $\mathbf{b}_u^{(k)}$, $\mathbf{b}_w^{(k)}$ and $\mathbf{b}_\nu^{(k)}$ by evaluating $p_{u,j}^{(k)}$, $r_{u,j}^{(k)}$, \dots and using $u_j^{(k)}$, $w_j^{(k)}$, and $\nu_j^{(k)}$, $j = 0, 1, \dots, n$.
- [4] Use TDMA to solve for $\mathbf{u}^{(k+1)} = (A_u^{(k)})^{-1}\mathbf{b}_u^{(k)}$, $\mathbf{w}^{(k+1)} = (A_w^{(k)})^{-1}\mathbf{b}_w^{(k)}$, and $\mathbf{I}^{(k+1)} = (A_\nu^{(k)})^{-1}\mathbf{b}_\nu^{(k)}$.
- [5] Repeat from step 2 with $k \rightarrow k+1$ if not converged; otherwise, stop iterating.

For simplicity, our convergence criteria are

$$\begin{aligned} \max_{j=0,1,\dots,n} |u_j^{(k+1)} - u_j^{(k)}| &\leq \varepsilon_u, \\ \max_{j=0,1,\dots,n} |w_j^{(k+1)} - w_j^{(k)}| &\leq \varepsilon_w, \\ \text{and } \max_{j=0,1,\dots,n} |\nu_j^{(k+1)} - \nu_j^{(k)}| &\leq \varepsilon_\nu, \end{aligned}$$

where ε_u , ε_w and ε_ν are pre-selected error tolerances.

For the equations governing axisymmetric flows in Sec. 3.1.2 and for the equations of the simplified mixture theory in Sec. 3.2.2, the iteration procedure is as shown above, except that y is replaced by r and that all functions p_u , p_w , etc., have

different forms. For the equations (3.36), (3.38), and (3.55) of the exact theory for binary mixtures, we seek four dependent variables u , w , I_A , and I_B . Here, the mixture velocity u and the fluctuation velocity w are treated the same way as in the single species case. The integrals I_A and I_B are obtained in a similar way than the volume fraction integral I in the single species case with Dirichlet boundary conditions, see (C.13) and (C.14).

C.3 Two Dimensions

We extend the procedure above to the partial differential equations (3.18) and (3.21) given in Sec. 3.1.2. The idea is to solve along either the y - or the z -directions at each step, while treating quantities in the other direction as known from the previous iteration. This method allows us to use the efficient TDMA algorithm at each iteration.

Because it is no longer possible to evaluate the solid volume fraction from a one-dimensional integral, we derive ν instead by adjusting the constant pressure imposed by equation (3.19) until the average volume fraction in the cross-section is equal to the prescribed value for $\bar{\nu}$. In each cell, we calculate ν from P and T by inverting the equation of state (3.6), $\nu = \nu(P/w^2)$, where $w \equiv \sqrt{T}$. The pressure adjustment is carried out with the procedure described in Appendix C.

We write the partial differential equations for u and w in a generic form,

$$\frac{\partial^2 u}{\partial y^2} + \frac{\partial^2 u}{\partial z^2} + p_u \frac{\partial u}{\partial y} + q_u \frac{\partial u}{\partial z} + r_u u = s_u, \quad (\text{C.21})$$

and

$$\frac{\partial^2 w}{\partial y^2} + \frac{\partial^2 w}{\partial z^2} + p_w \frac{\partial w}{\partial y} + q_w \frac{\partial w}{\partial z} + r_w w = s_w, \quad (\text{C.22})$$

subject to the boundary conditions

$$\text{at } y = 0 \quad \frac{\partial u}{\partial y} = a_{yu}u + b_{yu}, \quad \frac{\partial w}{\partial y} = a_{yw}w + b_{yw}, \quad (\text{C.23})$$

$$\text{at } y = H \quad \frac{\partial u}{\partial y} = c_{yu}u + d_{yu}, \quad \frac{\partial w}{\partial y} = c_{yw}w + d_{yw}, \quad (\text{C.24})$$

$$\text{at } z = 0 \quad \frac{\partial u}{\partial z} = a_{zu}u + b_{zu}, \quad \frac{\partial w}{\partial z} = a_{zw}w + b_{zw}, \quad (\text{C.25})$$

$$\text{at } z = H \quad \frac{\partial u}{\partial z} = c_{zu}u + d_{zu}, \quad \frac{\partial w}{\partial z} = c_{zw}w + d_{zw}, \quad (\text{C.26})$$

where p_u, q_u, \dots, d_{zw} depend on u, w and ν in general.

On a rectangular mesh (y_j, z_i) with $y_{j+1} - y_j = h_y$ and $z_{i+1} - z_i = h_z$, ($j = 0, 1, \dots, n; i = 0, 1, \dots, m$), we replace the partial differentials by finite differences, e.g.,

$$\frac{\partial u}{\partial y} \approx \frac{u_{j+1,i} - u_{j,i}}{2h_y}, \quad (\text{C.27})$$

$$\frac{\partial u}{\partial z} \approx \frac{u_{j,i+1} - u_{j,i}}{2h_z}, \quad (\text{C.28})$$

$$\frac{\partial^2 u}{\partial y^2} \approx \frac{u_{j+1,i} - 2u_{j,i} + u_{j-1,i}}{h_y^2}, \quad (\text{C.29})$$

and

$$\frac{\partial^2 u}{\partial z^2} \approx \frac{u_{j,i+1} - 2u_{j,i} + u_{j,i-1}}{h_z^2}. \quad (\text{C.30})$$

For example, the difference equations for u are

$$\begin{aligned} & \left(1 - \frac{h_y}{2}p_{u,j,i}\right)u_{j-1,i} + \left(1 - \frac{h_z}{2}q_{u,j,i}\right)\frac{h_y^2}{h_z^2}u_{j,i-1} + \left(1 + \frac{h_y}{2}p_{u,j,i}\right)u_{j+1,i} \\ & + \left(1 + \frac{h_z}{2}q_{u,j,i}\right)\frac{h_y^2}{h_z^2}u_{j,i+1} + \left[-2\left(1 + \frac{h_y^2}{h_z^2}\right) + h_y^2r_{u,j,i}\right]u_{j,i} = h_y^2s_{u,j,i}. \end{aligned} \quad (\text{C.31})$$

Equation (C.31) can be used directly on interior nodes ($j = 1, 2, \dots, n-1; i = 1, 2, \dots, m-1$). However, on boundary nodes, the equations involve values of u at “virtual nodes”, $u_{j,-1}$, $u_{j,m+1}$, $u_{-1,i}$, and $u_{n+1,i}$, which are determined using

boundary conditions in a way similar to the derivation of Eq. (C.17) in Sec. C.2. For example, the difference equations at $(0, z_i)$, $i = 1, 2, \dots, m - 1$ are

$$\begin{aligned} & \left[-2 \left(1 + \frac{h_y^2}{h_z^2} \right) + h_y^2 r_{u,0,i} - 2h_y a_{yu,i} \left(1 - \frac{h_y}{2} p_{u,0,i} \right) \right] u_{0,i} + 2u_{1,i} \\ & + \frac{h_y^2}{h_z^2} \left[\left(1 - \frac{h_z}{2} q_{u,0,i} \right) u_{0,i-1} + \left(1 + \frac{h_z}{2} q_{u,0,i} \right) u_{0,i+1} \right] = h_y^2 s_{u,0,i} + 2h_y \left(1 - \frac{h_y}{2} p_{u,0,i} \right) b_{yu,i}. \end{aligned} \quad (\text{C.32})$$

At corner nodes, two boundary conditions must be invoked to eliminate the two “virtual nodes”. For example, the difference equation at $(0, 0)$ is

$$\begin{aligned} & \left[-2 \left(1 + \frac{h_y^2}{h_z^2} \right) + h_y^2 r_{u,0,0} - 2h_y a_{yu,0} \left(1 - \frac{h_y}{2} p_{u,0,0} \right) - 2 \frac{h_y^2}{h_z} a_{zu,0} \left(1 - \frac{h_z}{2} q_{u,0,0} \right) \right] u_{0,0} \\ & + 2u_{1,0} + 2 \frac{h_y^2}{h_z^2} u_{0,1} = h_y^2 s_{u,0,0} + 2h_y \left(1 - \frac{h_y}{2} p_{u,0,0} \right) b_{yu,0} + 2 \frac{h_y^2}{h_z} \left(1 - \frac{h_z}{2} q_{u,0,0} \right) b_{zu,0}. \end{aligned} \quad (\text{C.33})$$

Equations (C.31), (C.32), and (C.33) form a set of algebraic equations for $u_{j,i}$, ($j = 0, 1, \dots, n$; $i = 0, 1, \dots, m$). Unfortunately, because the resulting coefficient matrix is no longer tri-diagonal, a direct solver is not as efficient as in the one-dimensional case. Furthermore, because Eqs. (C.21) and (C.22) are non-linear and coupled, a numerical iteration method is inevitable. However, at each iteration step, it is not necessary to determine u and w simultaneously in the entire domain.

Instead, as suggested by Peaceman and Rachford [103] for multi-dimensional heat transfer problems, we accelerate convergence by computing u and w line-by-line in alternating directions, *viz* we perform an ordered sweep of the domain on lines at constant y , followed by a similar orthogonal sweep on lines at constant z . When solving along each line, the “off-line” unknowns are replaced by their known values from the previous step and, thus, they are moved to the right side of the linear system of equations. In this way, the resulting coefficient matrices

where

$$\begin{aligned}
A_{00} &= -2 + h_y^2 r_{u,0,i} - 2h_y a_{yu,i} \left(1 - \frac{h_y}{2} p_{u,0,i}\right), \\
A_{nm} &= -2 + h_y^2 r_{u,n,i} + 2h_y c_{yu,i} \left(1 + \frac{h_y}{2} p_{u,n,i}\right), \\
b_0 &= h_y^2 s_{u,0,i} + 2h_y \left(1 - \frac{h_y}{2} p_{u,0,i}\right) b_{yu,i} \\
&\quad - \frac{h_y^2}{h_z^2} \left[\left(1 - \frac{h_z}{2} q_{u,0,i}\right) u_{0,i-1} + \left(1 + \frac{h_z}{2} q_{u,0,i}\right) u_{0,i+1} \right],
\end{aligned}$$

and

$$b_n = h_y^2 s_{u,n,i} - 2h_y \left(1 + \frac{h_y}{2} p_{u,n,i}\right) d_{yu,i} - \frac{h_y^2}{h_z^2} \left[\left(1 - \frac{h_z}{2} q_{u,n,i}\right) u_{n,i-1} + \left(1 + \frac{h_z}{2} q_{u,n,i}\right) u_{n,i+1} \right].$$

The functions in $A_{u,i}^{(k-1)}$ and $\mathbf{b}_{u,i}^{(k-1)}$ are evaluated using $u_{j,i}^{(k-1)}$, $w_{j,i}^{(k-1)}$, and $\nu_{j,i}^{(k-1)}$.

Similarly, when solving along $j = \text{const}$, we have

$$A_{u,j}^{(k-1)} \mathbf{u}_j^{(k)} = \mathbf{b}_{u,j}^{(k-1)}, \quad (\text{C.35})$$

with tri-diagonal matrices $A_{u,j}^{(k-1)}$. For the border lines ($j = 0, n$ or $i = 0, m$), the coefficient matrices and the vector \mathbf{b} have different forms, but the matrices remain tri-diagonal. The algebraic equations for w are similar to those for u and, for conciseness, they are not shown here.

The iteration procedure then becomes

- [1] At step $k = 0$, set $u_{j,i}^{(k)}$, $w_{j,i}^{(k)}$, and $\nu_{j,i}^{(k)}$ to the initial guesses $u_{j,i}^{(0)}$, $w_{j,i}^{(0)}$, and $\nu_{j,i}^{(0)}$, ($j = 0, 1, \dots, n$, and $i = 0, 1, \dots, m$).
- [2] For each $i = 0, 1, \dots, m$, do steps 3 and 4.
- [3] Calculate $A_{u,i}^{(k)}$, $A_{w,i}^{(k)}$, $\mathbf{b}_{u,i}^{(k)}$ and $\mathbf{b}_{w,i}^{(k)}$ by evaluating functions in the PDE's using $u_{j,i}^{(k)}$, $w_{j,i}^{(k)}$, and $\nu_{j,i}^{(k)}$, ($j = 0, 1, \dots, n$, $i \in [i-1, i, i+1]$).
- [4] Solve for $u_{j,i}^{(k+1)} = (A_{u,i}^{(k)})^{-1} \mathbf{b}_{u,i}^{(k)}$, and $w_{j,i}^{(k+1)} = (A_{w,i}^{(k)})^{-1} \mathbf{b}_{w,i}^{(k)}$, ($j = 0, 1, \dots, n$), using the TDMA.

- [5] Find the volume fractions $\nu_{j,i}^{(k+1)}$ by inverting the equation of state $\nu = \nu(P/w^2)$ and adjusting the constant pressure P iteratively by the Newton-Raphson method until the domain-average volume fraction is $\bar{\nu}$.
- [6] Set $k \rightarrow k + 1$; for each $j = 0, 1, \dots, n$, do steps 7 and 8.
- [7] Calculate $A_{u,j}^{(k)}$, $A_{w,j}^{(k)}$, $\mathbf{b}_{u,j}^{(k)}$ and $\mathbf{b}_{w,j}^{(k)}$ by evaluating functions in the PDE's using $u_{j,i}^{(k)}$, $w_{j,i}^{(k)}$, and $\nu_{j,i}^{(k)}$, ($i = 0, 1, \dots, m$, $j \in [j - 1, j, j + 1]$).
- [8] Solve for $u_{j,i}^{(k+1)} = (A_{u,j}^{(k)})^{-1} \mathbf{b}_{u,j}^{(k)}$, and $w_{j,i}^{(k+1)} = (A_{w,j}^{(k)})^{-1} \mathbf{b}_{w,j}^{(k)}$, ($i = 0, 1, \dots, m$), using the TDMA.
- [9] Find the volume fraction $\nu_{j,i}^{(k+1)}$ as in step 5.
- [10] Repeat from step 2 with $k \rightarrow k + 1$ if not converged; otherwise, stop iterating.

The convergence criteria are identical to those in one dimension.

Appendix D

Expressions in the Exact Mixture

Theory

The elements of the determinant D in Eqs. (3.51) and (3.52) are

$$\begin{aligned}
\frac{1}{T} \frac{\partial P}{\partial n_A} &= 1 + \frac{1}{R_{AA}^3} \nu_A g_{AA} + \frac{1}{R_{BA}^3} \nu_B g_{AB} \\
&+ \left[10\nu_A^2 + 4 \frac{R_{AB}^2}{R_{BA}^2} \left(\frac{R_{AB}}{R_{BA}} + \frac{3}{2} \right) \nu_B^2 + \frac{1}{R_{BA}^3} (1 + 3R_{BA}) \nu_A \nu_B \right] \frac{1}{(1-\nu)^2} \\
&+ \left[16\nu_A^2 + 4 \frac{R_{AB}}{R_{BA}} \left(3 \frac{R_{AB}}{R_{BA}} + 1 \right) \nu_B^2 + \frac{1}{R_{BA}^2} (6 + 4R_{BA}) \nu_A \nu_B \right] \frac{r_A \xi_2}{(1-\nu)^3} \\
&+ \left[\nu_A^2 + \frac{R_{AB}}{R_{BA}} \nu_B^2 + \frac{1}{R_{BA}} \nu_A \nu_B \right] \frac{6r_A^2 \xi_2^2}{(1-\nu)^4}, \tag{D.1}
\end{aligned}$$

$$\begin{aligned}
\frac{1}{T} \frac{\partial P}{\partial n_B} &= 1 + \frac{1}{R_{BB}^3} \nu_B g_{BB} + \frac{1}{R_{AB}^3} \nu_A g_{AB} \\
&+ \left[10\nu_B^2 + 4 \frac{R_{BA}^2}{R_{AB}^2} \left(\frac{R_{BA}}{R_{AB}} + \frac{3}{2} \right) \nu_A^2 + \frac{1}{R_{AB}^3} (1 + 3R_{AB}) \nu_A \nu_B \right] \frac{1}{(1-\nu)^2} \\
&+ \left[16\nu_B^2 + 4 \frac{R_{BA}}{R_{AB}} \left(3 \frac{R_{BA}}{R_{AB}} + 1 \right) \nu_A^2 + \frac{1}{R_{AB}^2} (6 + 4R_{AB}) \nu_A \nu_B \right] \frac{r_B \xi_2}{(1-\nu)^3} \\
&+ \left[\nu_B^2 + \frac{R_{BA}}{R_{AB}} \nu_A^2 + \frac{1}{R_{AB}} \nu_A \nu_B \right] \frac{6r_B^2 \xi_2^2}{(1-\nu)^4}, \tag{D.2}
\end{aligned}$$

$$\begin{aligned}
\frac{1}{T} \frac{\partial \mu_A}{\partial n_A} &= \frac{4}{3} \pi r_A^3 \frac{1}{T} \frac{\partial P}{\partial n_A} + \frac{1}{n_A} + \frac{4}{3} \pi r_A^3 \left\{ \frac{7}{1-\nu} + \frac{3r_A^2 \xi_1}{(1-\nu)^2} \right. \\
&+ \left[\frac{3}{(1-\nu)^2} + \frac{2}{\nu(1-\nu)} + \frac{2 \ln(1-\nu)}{\nu^2} \right] 3r_A \xi_2 \\
&+ \left[\frac{1+\nu}{\nu(1-\nu)^3} - \frac{4-\nu}{\nu^2(1-\nu)} - \frac{4 \ln(1-\nu)}{\nu^3} \right] 3r_A^2 \xi_2^2 \\
&\left. + \left[\frac{6-2\nu}{\nu^3(1-\nu)} + \frac{6 \ln(1-\nu)}{\nu^4} + \frac{1}{\nu^2(1-\nu)^2} \right] r_A^3 \xi_2^3 \right\}, \tag{D.3}
\end{aligned}$$

and

$$\begin{aligned}
\frac{1}{T} \frac{\partial \mu_A}{\partial n_B} &= \frac{4}{3} \pi r_A^3 \frac{1}{T} \frac{\partial P}{\partial n_B} + \frac{4}{3} \pi r_B^3 \left\{ \left(1 + 3 \frac{R_{AB}}{R_{BA}} + 3 \frac{R_{AB}^2}{R_{BA}^2} \right) \frac{1}{1-\nu} + \frac{3r_A^2 \xi_1}{(1-\nu)^2} \right. \\
&+ \left[\left(1 + 2 \frac{R_{AB}}{R_{BA}} \right) \frac{1}{(1-\nu)^2} + \frac{R_{AB}}{R_{BA}} \left(\frac{2}{\nu(1-\nu)} + \frac{2 \ln(1-\nu)}{\nu^2} \right) \right] 3r_A \xi_2 \\
&+ \left[\frac{1+\nu}{\nu(1-\nu)^3} - \left(2 + \frac{R_{AB}}{R_{BA}} \right) (2-\nu) \right] \frac{1}{\nu^2(1-\nu)} \\
&- \left. \left(1 + \frac{R_{AB}}{R_{BA}} \right) \frac{2 \ln(1-\nu)}{\nu^3} \right] 3r_A^2 \xi_2^2 \\
&+ \left. \left[\frac{6-2\nu}{\nu^3(1-\nu)} + \frac{6 \ln(1-\nu)}{\nu^4} + \frac{1}{\nu^2(1-\nu)^2} \right] r_A^3 \xi_2^3 \right\}, \tag{D.4}
\end{aligned}$$

where

$$R_{ij} \equiv \frac{r_i}{r_i + r_j}, \quad i, j = A \text{ or } B.$$

Appendix E

Tentative Test Matrices

We list here tentative test matrices for the Viscous Dissipation and the Viscous Drag experiments. The experiment apparatus is the axisymmetric shear cell sketched in Figure 5.6 with an inner radius $R_i = 210$ mm and an outer radius $R_o = 228$ mm. The two radii are defined at the centers of the boundary cylinders. The diameters of the boundary cylinders are $d_i = d_o = 2$ mm. Separations between cylinders are $s_i = 1$ mm and $s_o = 0$. The distance between flat side walls are $Z = 20$ mm. Test matrices are for Nitinol spheres with $\rho_s = 6.71$ g/cm³ and $\sigma = 2$ mm.

E.1 Viscous Dissipation Experiments

In the viscous dissipation experiments, we vary the rotation speeds of the inner and outer boundaries systematically to investigate the effect of viscous gas on particle fluctuation velocity. Some selected parameters are listed in the test matrix:

$\bar{\nu}$ The overall particle volume fraction in the cell. By default, flows in the viscous dissipation experiments are axisymmetric.

St Stokes number

$$St \equiv \frac{\rho_s \sigma^2 U}{18\mu_g H}$$

where $U \equiv U_i - U_o$ is the relative velocity between the inner and outer boundary and $H \equiv R_o - R_i - \sigma - (d_i + d_o)/2$ is the distance between the flow spheres touching the crests of the inner and outer boundary bumps, respectively.

P_g Average gas pressure in the cell, which determines the molecular mean free path of the gas and hence the viscous dissipation through the lubrication cut-off in Eq. (4.4). We also vary P_g to control gas inertia effect by change its density, see below.

U_i The velocity of the inner boundary. In the viscous dissipation experiments, the outer boundary rotates at the same speed as the inner boundary but in the opposite direction, i.e., $U_o = -U_i$.

$\bar{T}^{1/2}$ Average particle fluctuation velocity in any cross section of the cell.

Re_T Reynolds number based on the particle fluctuation velocity

$$Re_T \equiv \frac{\rho_g \sigma \bar{T}^{1/2}}{\mu_g}$$

where ρ_g and μ_g are the gas density and molecular viscosity, respectively. We control Re_T by changing ρ_g through P_g .

St_{local} Stokes number defined in Eq. (7.8).

St_{cr} Critical Stokes number defined in Eq. (7.11). If $St_{local} \leq St_{cr}$, then the measured particle fluctuation velocity may be different from predictions derived from the isotropic theory of Sangani *et al* [107].

F_{min} The required minimum camera frame rate, which is determined from our analysis of measurement errors, i.e., Eqs. (6.11), (6.12), and (6.30).

N_{min} Required minimum number of images from Eq. (7.15).

Table 1: Viscous Dissipation Experiments.

Control Parameters				Flow Parameters				Image System	
$\bar{\nu}$	St	P_g (atm)	U_i (cm/s)	$\bar{T}^{1/2}$ (cm/s)	Re_T	St_{local}	St_{cr}	F_{min} (fps)	N_{min}
0.05	5	1	0.04	0.01	0.01	2	131	0.6	9776
0.05	10	1	0.08	0.02	0.02	4	131	1.2	10161
0.05	20	1	0.17	0.05	0.07	14	131	2.8	11690
0.05	20	0.1	0.17	0.05	0.01	15	123	2.9	11960
0.05	20	0.01	0.17	0.05	0.00	16	115	2.9	12230
0.05	40	1	0.34	0.12	0.18	39	131	6.4	13243
0.05	40	0.1	0.34	0.13	0.02	40	123	6.4	13394
0.05	40	0.01	0.34	0.13	0.00	41	115	6.5	13546
0.05	50	1	0.42	0.16	0.23	51	131	8.2	13594
0.05	50	0.1	0.42	0.16	0.02	52	123	8.2	13718
0.05	50	0.01	0.42	0.17	0.00	53	115	8.3	13841
0.05	80	1	0.67	0.28	0.40	89	131	13.6	14140
0.05	100	1	0.84	0.36	0.52	115	131	17.2	14325
0.05	200	1	1.68	0.76	1.09	242	131	35.3	14694
0.05	500	1	4.20	1.94	2.80	623	131	89.5	14912
0.05	1000	1	8.40	3.92	5.65	1257	131	179.9	14984
0.10	5	1	0.04	0.00	0.01	3	167	0.5	4372
0.10	10	1	0.08	0.01	0.02	7	167	1.1	4589
0.10	20	1	0.17	0.03	0.05	23	167	2.5	5158
0.10	20	0.1	0.17	0.04	0.01	26	150	2.6	5339

Table 1 (Continued)

Control Parameters				Flow Parameters				Image System	
$\bar{\nu}$	St	P_g (atm)	U_i (cm/s)	$\bar{T}^{1/2}$ (cm/s)	Re_T	St_{local}	St_{cr}	F_{min} (fps)	N_{min}
0.10	20	0.01	0.17	0.04	0.00	29	133	2.6	5515
0.10	40	1	0.34	0.09	0.13	65	167	5.5	5758
0.10	40	0.1	0.34	0.09	0.01	68	150	5.6	5858
0.10	40	0.01	0.34	0.10	0.00	70	133	5.7	5957
0.10	50	1	0.42	0.12	0.17	86	167	7.1	5895
0.10	50	0.1	0.42	0.12	0.02	89	150	7.2	5976
0.10	50	0.01	0.42	0.13	0.00	92	133	7.4	6153
0.10	80	1	0.67	0.21	0.30	150	167	12.1	6281
0.10	80	0.1	0.67	0.21	0.03	153	150	12.3	6405
0.10	80	0.01	0.67	0.21	0.00	156	133	12.5	6530
0.10	100	1	0.84	0.26	0.38	193	167	15.5	6458
0.10	200	1	1.68	0.56	0.80	409	167	32.8	6822
0.10	500	1	4.20	1.44	2.07	1056	167	84.6	7044
0.10	1000	1	8.40	2.91	4.19	2135	167	170.9	7118
0.20	25	1	0.21	0.03	0.05	63	237	5.1	4237
0.20	25	0.1	0.21	0.04	0.01	71	200	5.7	4762
0.20	25	0.01	0.21	0.04	0.00	79	162	6.3	5277
0.20	50	1	0.42	0.08	0.11	157	237	12.6	5245
0.20	50	0.1	0.42	0.08	0.01	165	200	13.3	5525
0.20	50	0.01	0.42	0.09	0.00	174	162	13.9	5803

Table 1 (Continued)

Control Parameters				Flow Parameters				Image System	
$\bar{\nu}$	St	P_g (atm)	U_i (cm/s)	$\bar{T}^{1/2}$ (cm/s)	Re_T	St_{local}	St_{cr}	F_{min} (fps)	N_{min}
0.20	60	1	0.50	0.10	0.14	195	237	15.6	5428
0.20	60	0.1	0.50	0.10	0.01	203	200	16.3	5663
0.20	60	0.01	0.50	0.11	0.00	212	162	17.0	5896
0.20	80	1	0.67	0.14	0.20	271	237	21.7	5660
0.20	80	0.1	0.67	0.14	0.02	280	200	22.4	5837
0.20	80	0.01	0.67	0.15	0.00	288	162	23.1	6015
0.20	100	1	0.84	0.18	0.25	348	237	27.9	5801
0.20	200	1	1.68	0.37	0.53	730	237	58.5	6090
0.20	500	1	4.20	0.95	1.37	1879	237	150.4	6267
0.20	1000	1	8.40	1.91	2.76	3795	237	303.7	6326
0.30	25	1	0.21	0.03	0.04	114	334	9.2	5085
0.30	25	0.1	0.21	0.03	0.00	132	268	10.6	5909
0.30	25	0.01	0.21	0.04	0.00	150	201	12.1	6701
0.30	50	1	0.42	0.07	0.10	278	334	22.3	6193
0.30	50	0.1	0.42	0.07	0.01	297	268	23.8	6614
0.30	50	0.01	0.42	0.08	0.00	316	201	25.3	7030
0.30	60	1	0.50	0.08	0.12	344	334	27.6	6386
0.30	60	0.1	0.50	0.09	0.01	363	268	29.1	6738
0.30	60	0.01	0.50	0.09	0.00	382	201	30.6	7086
0.30	80	1	0.67	0.11	0.16	477	334	38.2	6629

Table 1 (Continued)

Control Parameters				Flow Parameters				Image System	
$\bar{\nu}$	St	P_g (atm)	U_i (cm/s)	$\bar{T}^{1/2}$ (cm/s)	Re_T	St_{local}	St_{cr}	F_{min} (fps)	N_{min}
0.30	80	0.1	0.67	0.12	0.02	496	268	39.7	6894
0.30	80	0.01	0.67	0.12	0.00	515	201	41.2	7158
0.30	100	1	0.84	0.15	0.21	609	334	48.8	6776
0.30	200	1	1.68	0.30	0.44	1273	334	101.9	7075
0.30	500	1	4.20	0.78	1.12	3265	334	261.3	7256
0.30	1000	1	8.40	1.57	2.26	6584	334	526.9	7316
0.40	25	1	0.21	0.03	0.04	217	490	17.4	7252
0.40	50	1	0.42	0.06	0.09	515	490	41.3	8592
0.40	50	0.1	0.42	0.07	0.01	555	374	44.5	9261
0.40	50	0.01	0.42	0.07	0.00	594	258	47.6	9917
0.40	60	1	0.50	0.08	0.11	634	490	50.8	8818
0.40	60	0.1	0.50	0.08	0.01	674	374	54.0	9375
0.40	60	0.01	0.50	0.09	0.00	714	258	57.2	9924
0.40	80	1	0.67	0.10	0.15	873	490	69.9	9101
0.40	80	0.1	0.67	0.11	0.02	913	374	73.1	9520
0.40	80	0.01	0.67	0.11	0.00	953	258	76.3	9933
0.40	100	1	0.84	0.13	0.19	1112	490	89.0	9272
0.40	200	1	1.68	0.28	0.40	2307	490	184.7	9615
0.40	500	1	4.20	0.71	1.02	5892	490	471.5	9821
0.40	1000	1	8.40	1.42	2.05	11866	490	949.7	9890

E.2 Viscous Drag Experiments

The Viscous Drag experiments will be carried out in the same apparatus and will use the same Nitinol spheres as the Viscous Dissipation experiments. Two versions of the test matrices for the Viscous Drag experiments exist. The first assumes the presence of two gas distributors separated by an angle 180° for gas injection and withdrawal, respectively. The second adds a third distributor to create an isokinetic section, in which the mean gas volume flow rate can be evaluated, see Chapter refchap:FD. For conciseness, we only provide here the test matrices for two distributors. In these experiments, we allow only the inner boundary to rotate. Consequently, the cell is divided into a co-flow region and a counter flow region. The parameters in the test matrices are:

St Stokes number

$$St \equiv \frac{\rho_s \sigma^2 U_i}{18 \mu_g H}$$

where U_i is the velocity of the inner boundary. Note that in the viscous drag experiments, the outer boundary is stationary, $U_o = 0$.

R_τ Dimensionless pressure gradient

$$R_\tau \equiv \frac{\Delta P_g / \pi R}{\rho_s \sigma (U_i / H)^2}$$

where ΔP_g is the pressure difference between gas injection and withdrawal and $R \equiv (R_i + R_o)/2$ is the average radius of the cell.

P_g Average gas pressure in the cell, see comments on the Viscous Dissipation experiments.

U_i The velocity of the inner boundary.

$\bar{\nu}_{FD}$ Average particle volume fraction in the fully developed regions of the co- or counter-flow sections.

$\bar{T}_{FD}^{1/2}$ Average particle fluctuation velocity in the fully developed regions.

\bar{u}_g Average gas velocity in the fully developed regions.

In these parameters, St , R_τ , and P_g are control parameters, while $\bar{\nu}_{FD}$, $\bar{T}_{FD}^{1/2}$ and \bar{u}_g are theoretical predictions. They are listed here to guide the design of experiments, and in particular to choose appropriate instruments.

Table 2: Viscous Drag Experiments ($\bar{\nu} = 0.15$).

Control Parameters				Co-flow Region			Counter-flow		
St	R_τ	P_g (atm)	U_i (cm/s)	$\bar{\nu}_{FD}$	$\bar{T}_{FD}^{1/2}$ (cm/s)	\bar{u}_g (cm/s)	$\bar{\nu}_{FD}$	$\bar{T}_{FD}^{1/2}$ (cm/s)	\bar{u}_g (cm/s)
50	0.002	1	0.84	0.13	0.12	0.47	0.17	0.10	0.32
50	0.002	0.1	0.84	0.13	0.13	0.47	0.17	0.10	0.32
50	0.002	0.01	0.84	0.13	0.13	0.47	0.17	0.11	0.32
80	0.002	1	1.34	0.13	0.21	0.77	0.17	0.18	0.50
80	0.002	0.1	1.34	0.13	0.21	0.77	0.17	0.18	0.50
80	0.002	0.01	1.34	0.13	0.22	0.77	0.17	0.19	0.50
100	0.002	1	1.68	0.13	0.27	0.98	0.17	0.23	0.61
100	0.002	0.1	1.68	0.13	0.27	0.98	0.17	0.23	0.61
100	0.002	0.01	1.68	0.13	0.28	0.99	0.17	0.24	0.61
160	0.002	1	2.69	0.13	0.45	1.68	0.17	0.38	0.89
160	0.002	0.1	2.69	0.13	0.46	1.68	0.17	0.39	0.89
160	0.002	0.01	2.69	0.13	0.46	1.68	0.17	0.39	0.89
400	0.002	1	6.72	0.13	1.17	5.36	0.17	1.01	1.35
400	0.002	0.1	6.72	0.13	1.18	5.36	0.17	1.01	1.35
400	0.002	0.01	6.72	0.13	1.18	5.36	0.17	1.01	1.36
700	0.002	1	11.76	0.13	2.08	11.95	0.17	1.78	0.48
700	0.002	0.1	11.76	0.13	2.08	11.95	0.17	1.79	0.48
700	0.002	0.01	11.76	0.13	2.09	11.96	0.17	1.79	0.49
1000	0.002	1	16.81	0.13	2.98	20.77	0.17	2.56	-2.00
1000	0.002	0.1	16.81	0.13	2.99	20.77	0.17	2.56	-2.00
1000	0.002	0.01	16.81	0.13	2.99	20.78	0.17	2.57	-2.00

Table 2 (Continued)

Control Parameters				Co-flow Region			Counter-flow		
St	R_τ	P_g (atm)	U_i (cm/s)	$\bar{\nu}_{FD}$	$\bar{T}_{FD}^{1/2}$ (cm/s)	\bar{u}_g (cm/s)	$\bar{\nu}_{FD}$	$\bar{T}_{FD}^{1/2}$ (cm/s)	\bar{u}_g (cm/s)
50	0.004	1	0.84	0.12	0.13	0.54	0.18	0.10	0.27
50	0.004	0.1	0.84	0.12	0.13	0.54	0.18	0.10	0.28
50	0.004	0.01	0.84	0.12	0.13	0.54	0.18	0.10	0.28
80	0.004	1	1.34	0.12	0.22	0.91	0.18	0.17	0.41
80	0.004	0.1	1.34	0.12	0.22	0.91	0.18	0.18	0.41
80	0.004	0.01	1.34	0.12	0.23	0.91	0.18	0.18	0.42
100	0.004	1	1.68	0.12	0.28	1.18	0.18	0.22	0.49
100	0.004	0.1	1.68	0.12	0.28	1.18	0.18	0.23	0.49
100	0.004	0.01	1.68	0.12	0.29	1.18	0.18	0.23	0.49
160	0.004	1	2.69	0.12	0.47	2.13	0.18	0.37	0.63
160	0.004	0.1	2.69	0.12	0.47	2.13	0.18	0.38	0.63
160	0.004	0.01	2.69	0.12	0.47	2.13	0.18	0.38	0.63
400	0.004	1	6.72	0.12	1.21	7.89	0.18	0.97	-0.01
400	0.004	0.1	6.72	0.12	1.21	7.89	0.18	0.98	0.00
400	0.004	0.01	6.72	0.12	1.22	7.89	0.18	0.98	0.00
700	0.004	1	11.76	0.13	2.14	19.46	0.18	1.73	-3.48
700	0.004	0.1	11.76	0.13	2.14	19.46	0.18	1.73	-3.48
700	0.004	0.01	11.76	0.13	2.15	19.46	0.18	1.74	-3.48
1000	0.004	1	16.81	0.13	3.07	35.89	0.18	2.48	-9.93
1000	0.004	0.1	16.81	0.13	3.07	35.89	0.18	2.49	-9.93
1000	0.004	0.01	16.81	0.13	3.08	35.89	0.18	2.49	-9.93

Table 2 (Continued)

Control Parameters				Co-flow Region			Counter-flow		
St	R_τ	P_g (atm)	U_i (cm/s)	$\bar{\nu}_{FD}$	$\bar{T}_{FD}^{1/2}$ (cm/s)	\bar{u}_g (cm/s)	$\bar{\nu}_{FD}$	$\bar{T}_{FD}^{1/2}$ (cm/s)	\bar{u}_g (cm/s)
50	0.008	1	0.84	0.10	0.14	0.70	0.20	0.09	0.22
50	0.008	0.1	0.84	0.11	0.14	0.69	0.20	0.09	0.22
50	0.008	0.01	0.84	0.11	0.14	0.69	0.20	0.10	0.22
80	0.008	1	1.34	0.11	0.23	1.24	0.20	0.16	0.29
80	0.008	0.1	1.34	0.11	0.23	1.24	0.20	0.16	0.29
80	0.008	0.01	1.34	0.11	0.24	1.23	0.19	0.17	0.30
100	0.008	1	1.68	0.11	0.30	1.67	0.19	0.21	0.31
100	0.008	0.1	1.68	0.11	0.30	1.67	0.19	0.21	0.31
100	0.008	0.01	1.68	0.11	0.30	1.66	0.19	0.22	0.31
160	0.008	1	2.69	0.11	0.49	3.27	0.19	0.35	0.23
160	0.008	0.1	2.69	0.11	0.49	3.26	0.19	0.35	0.23
160	0.008	0.01	2.69	0.11	0.49	3.25	0.19	0.36	0.23
400	0.008	1	6.72	0.11	1.26	14.20	0.19	0.92	-2.19
400	0.008	0.1	6.72	0.11	1.27	14.19	0.19	0.92	-2.19
400	0.008	0.01	6.72	0.11	1.27	14.18	0.19	0.93	-2.19
700	0.008	1	11.76	0.11	2.23	38.14	0.19	1.63	-9.93
700	0.008	0.1	11.76	0.11	2.24	38.12	0.19	1.64	-9.93
700	0.008	0.01	11.76	0.11	2.24	38.10	0.19	1.64	-9.94
1000	0.008	1	16.81	0.11	3.20	73.49	0.19	2.34	-22.90
1000	0.008	0.1	16.81	0.11	3.21	73.46	0.19	2.35	-22.91
1000	0.008	0.01	16.81	0.11	3.21	73.43	0.19	2.35	-22.92

Table 2 (Continued)

Control Parameters				Co-flow Region			Counter-flow		
St	R_τ	P_g (atm)	U_i (cm/s)	$\bar{\nu}_{FD}$	$\bar{T}_{FD}^{1/2}$ (cm/s)	\bar{u}_g (cm/s)	$\bar{\nu}_{FD}$	$\bar{T}_{FD}^{1/2}$ (cm/s)	\bar{u}_g (cm/s)
50	0.01	1	0.84	0.10	0.14	0.78	0.20	0.09	0.20
50	0.01	0.1	0.84	0.10	0.14	0.77	0.20	0.09	0.20
50	0.01	0.01	0.84	0.10	0.14	0.77	0.20	0.10	0.20
80	0.01	1	1.34	0.10	0.23	1.43	0.20	0.16	0.25
80	0.01	0.1	1.34	0.10	0.24	1.42	0.20	0.16	0.25
80	0.01	0.01	1.34	0.10	0.24	1.42	0.20	0.17	0.25
100	0.01	1	1.68	0.10	0.30	1.95	0.20	0.20	0.24
100	0.01	0.1	1.68	0.10	0.30	1.94	0.20	0.21	0.24
100	0.01	0.01	1.68	0.11	0.30	1.93	0.20	0.21	0.24
160	0.01	1	2.69	0.11	0.49	3.91	0.20	0.34	0.07
160	0.01	0.1	2.69	0.11	0.50	3.90	0.20	0.35	0.07
160	0.01	0.01	2.69	0.11	0.50	3.89	0.20	0.35	0.07
400	0.01	1	6.72	0.11	1.28	17.89	0.20	0.90	-3.12
400	0.01	0.1	6.72	0.11	1.28	17.87	0.20	0.90	-3.13
400	0.01	0.01	6.72	0.11	1.28	17.85	0.20	0.91	-3.13
700	0.01	1	11.76	0.11	2.26	49.12	0.20	1.60	-12.71
700	0.01	0.1	11.76	0.11	2.26	49.09	0.20	1.60	-12.72
700	0.01	0.01	11.76	0.11	2.26	49.06	0.20	1.61	-12.72
1000	0.01	1	16.81	0.11	3.24	95.64	0.20	2.29	-28.51
1000	0.01	0.1	16.81	0.11	3.24	95.60	0.20	2.30	-28.52
1000	0.01	0.01	16.81	0.11	3.24	95.56	0.20	2.30	-28.53

Table 3: Viscous Drag Experiments ($\bar{\nu} = 0.2$).

Control Parameters				Co-flow Region			Counter-flow		
St	R_τ	P_g (atm)	U_i (cm/s)	$\bar{\nu}_{FD}$	$\bar{T}_{FD}^{1/2}$ (cm/s)	\bar{u}_g (cm/s)	$\bar{\nu}_{FD}$	$\bar{T}_{FD}^{1/2}$ (cm/s)	\bar{u}_g (cm/s)
50	0.002	1	0.84	0.17	0.10	0.46	0.23	0.08	0.33
50	0.002	0.1	0.84	0.17	0.10	0.46	0.23	0.09	0.33
50	0.002	0.01	0.84	0.17	0.11	0.46	0.23	0.09	0.33
80	0.002	1	1.34	0.17	0.17	0.74	0.23	0.15	0.52
80	0.002	0.1	1.34	0.18	0.18	0.74	0.23	0.15	0.52
80	0.002	0.01	1.34	0.18	0.18	0.74	0.23	0.16	0.53
100	0.002	1	1.68	0.18	0.22	0.93	0.23	0.19	0.64
100	0.002	0.1	1.68	0.18	0.23	0.93	0.22	0.20	0.65
100	0.002	0.01	1.68	0.18	0.23	0.93	0.22	0.20	0.65
160	0.002	1	2.69	0.18	0.37	1.55	0.22	0.33	0.99
160	0.002	0.1	2.69	0.18	0.38	1.55	0.22	0.33	0.99
160	0.002	0.01	2.69	0.18	0.38	1.55	0.22	0.34	0.99
400	0.002	1	6.72	0.18	0.97	4.54	0.22	0.86	1.98
400	0.002	0.1	6.72	0.18	0.97	4.54	0.22	0.86	1.98
400	0.002	0.01	6.72	0.18	0.98	4.54	0.22	0.87	1.98
700	0.002	1	11.76	0.18	1.71	9.45	0.22	1.53	2.35
700	0.002	0.1	11.76	0.18	1.72	9.45	0.22	1.53	2.36
700	0.002	0.01	11.76	0.18	1.72	9.45	0.22	1.54	2.36
1000	0.002	1	16.81	0.18	2.46	15.67	0.22	2.19	1.79
1000	0.002	0.1	16.81	0.18	2.46	15.67	0.22	2.20	1.79
1000	0.002	0.01	16.81	0.18	2.47	15.67	0.22	2.20	1.79

Table 3 (Continued)

Control Parameters				Co-flow Region			Counter-flow		
St	R_τ	P_g (atm)	U_i (cm/s)	$\bar{\nu}_{FD}$	$\bar{T}_{FD}^{1/2}$ (cm/s)	\bar{u}_g (cm/s)	$\bar{\nu}_{FD}$	$\bar{T}_{FD}^{1/2}$ (cm/s)	\bar{u}_g (cm/s)
50	0.004	1	0.84	0.16	0.10	0.51	0.24	0.08	0.29
50	0.004	0.1	0.84	0.16	0.11	0.50	0.24	0.09	0.30
50	0.004	0.01	0.84	0.16	0.11	0.50	0.24	0.09	0.30
80	0.004	1	1.34	0.16	0.18	0.83	0.24	0.15	0.46
80	0.004	0.1	1.34	0.16	0.18	0.83	0.24	0.15	0.47
80	0.004	0.01	1.34	0.17	0.19	0.83	0.24	0.16	0.47
100	0.004	1	1.68	0.17	0.23	1.06	0.24	0.19	0.56
100	0.004	0.1	1.68	0.17	0.23	1.06	0.24	0.19	0.57
100	0.004	0.01	1.68	0.17	0.24	1.06	0.23	0.20	0.57
160	0.004	1	2.69	0.17	0.38	1.84	0.23	0.32	0.82
160	0.004	0.1	2.69	0.17	0.38	1.84	0.23	0.33	0.82
160	0.004	0.01	2.69	0.17	0.39	1.83	0.23	0.33	0.82
400	0.004	1	6.72	0.17	0.99	6.06	0.23	0.84	1.14
400	0.004	0.1	6.72	0.17	0.99	6.06	0.23	0.85	1.14
400	0.004	0.01	6.72	0.17	1.00	6.06	0.23	0.85	1.14
700	0.004	1	11.76	0.17	1.75	13.91	0.23	1.50	-0.06
700	0.004	0.1	11.76	0.17	1.75	13.90	0.23	1.50	-0.06
700	0.004	0.01	11.76	0.17	1.76	13.90	0.23	1.51	-0.06
1000	0.004	1	16.81	0.17	2.51	24.57	0.23	2.15	-3.00
1000	0.004	0.1	16.81	0.17	2.51	24.57	0.23	2.16	-3.00
1000	0.004	0.01	16.81	0.17	2.52	24.57	0.23	2.16	-3.00

Table 3 (Continued)

Control Parameters				Co-flow Region			Counter-flow		
St	R_τ	P_g (atm)	U_i (cm/s)	$\bar{\nu}_{FD}$	$\bar{T}_{FD}^{1/2}$ (cm/s)	\bar{u}_g (cm/s)	$\bar{\nu}_{FD}$	$\bar{T}_{FD}^{1/2}$ (cm/s)	\bar{u}_g (cm/s)
50	0.008	1	0.84	0.14	0.11	0.62	0.26	0.08	0.25
50	0.008	0.1	0.84	0.14	0.11	0.61	0.26	0.08	0.25
50	0.008	0.01	0.84	0.14	0.11	0.61	0.26	0.09	0.26
80	0.008	1	1.34	0.15	0.19	1.06	0.26	0.14	0.38
80	0.008	0.1	1.34	0.15	0.19	1.05	0.26	0.14	0.38
80	0.008	0.01	1.34	0.15	0.19	1.05	0.25	0.15	0.38
100	0.008	1	1.68	0.15	0.24	1.39	0.26	0.18	0.44
100	0.008	0.1	1.68	0.15	0.24	1.38	0.25	0.18	0.44
100	0.008	0.01	1.68	0.15	0.25	1.37	0.25	0.19	0.45
160	0.008	1	2.69	0.15	0.40	2.55	0.25	0.30	0.56
160	0.008	0.1	2.69	0.15	0.40	2.54	0.25	0.31	0.56
160	0.008	0.01	2.69	0.15	0.40	2.54	0.25	0.31	0.56
400	0.008	1	6.72	0.15	1.03	9.88	0.25	0.80	-0.20
400	0.008	0.1	6.72	0.15	1.04	9.87	0.25	0.81	-0.20
400	0.008	0.01	6.72	0.15	1.04	9.86	0.25	0.81	-0.20
700	0.008	1	11.76	0.15	1.82	25.06	0.25	1.42	-3.90
700	0.008	0.1	11.76	0.15	1.83	25.04	0.25	1.43	-3.91
700	0.008	0.01	11.76	0.15	1.83	25.01	0.25	1.44	-3.91
1000	0.008	1	16.81	0.15	2.62	46.90	0.25	2.05	-10.66
1000	0.008	0.1	16.81	0.15	2.62	46.87	0.25	2.05	-10.67
1000	0.008	0.01	16.81	0.15	2.62	46.84	0.25	2.06	-10.68

Table 3 (Continued)

Control Parameters				Co-flow Region			Counter-flow		
St	R_τ	P_g (atm)	U_i (cm/s)	$\bar{\nu}_{FD}$	$\bar{T}_{FD}^{1/2}$ (cm/s)	\bar{u}_g (cm/s)	$\bar{\nu}_{FD}$	$\bar{T}_{FD}^{1/2}$ (cm/s)	\bar{u}_g (cm/s)
50	0.01	1	0.84	0.14	0.11	0.68	0.27	0.08	0.24
50	0.01	0.1	0.84	0.14	0.11	0.67	0.27	0.08	0.24
50	0.01	0.01	0.84	0.14	0.11	0.66	0.26	0.09	0.24
80	0.01	1	1.34	0.14	0.19	1.18	0.26	0.14	0.35
80	0.01	0.1	1.34	0.14	0.19	1.17	0.26	0.14	0.35
80	0.01	0.01	1.34	0.14	0.19	1.17	0.26	0.15	0.35
100	0.01	1	1.68	0.14	0.24	1.56	0.26	0.18	0.40
100	0.01	0.1	1.68	0.14	0.24	1.56	0.26	0.18	0.40
100	0.01	0.01	1.68	0.14	0.25	1.55	0.26	0.19	0.40
160	0.01	1	2.69	0.14	0.40	2.96	0.26	0.30	0.46
160	0.01	0.1	2.69	0.15	0.40	2.95	0.26	0.30	0.46
160	0.01	0.01	2.69	0.15	0.41	2.94	0.26	0.31	0.46
400	0.01	1	6.72	0.15	1.04	12.10	0.26	0.79	-0.75
400	0.01	0.1	6.72	0.15	1.04	12.08	0.26	0.79	-0.75
400	0.01	0.01	6.72	0.15	1.05	12.07	0.26	0.80	-0.75
700	0.01	1	11.76	0.15	1.84	31.55	0.26	1.40	-5.51
700	0.01	0.1	11.76	0.15	1.85	31.53	0.26	1.40	-5.52
700	0.01	0.01	11.76	0.15	1.85	31.50	0.26	1.41	-5.52
1000	0.01	1	16.81	0.15	2.64	59.77	0.26	2.01	-13.85
1000	0.01	0.1	16.81	0.15	2.65	59.73	0.26	2.02	-13.86
1000	0.01	0.01	16.81	0.15	2.65	59.70	0.26	2.02	-13.87

Table 4: Viscous Drag Experiments ($\bar{\nu} = 0.3$).

Control Parameters				Co-flow Region			Counter-flow		
St	R_τ	P_g (atm)	U_i (cm/s)	$\bar{\nu}_{FD}$	$\bar{T}_{FD}^{1/2}$ (cm/s)	\bar{u}_g (cm/s)	$\bar{\nu}_{FD}$	$\bar{T}_{FD}^{1/2}$ (cm/s)	\bar{u}_g (cm/s)
50	0.002	1	0.84	0.25	0.08	0.45	0.35	0.07	0.32
50	0.002	0.1	0.84	0.25	0.08	0.45	0.35	0.08	0.33
50	0.002	0.01	0.84	0.26	0.09	0.45	0.34	0.08	0.33
80	0.002	1	1.34	0.26	0.14	0.72	0.34	0.13	0.52
80	0.002	0.1	1.34	0.26	0.14	0.72	0.34	0.13	0.53
80	0.002	0.01	1.34	0.26	0.15	0.72	0.34	0.14	0.53
100	0.002	1	1.68	0.26	0.18	0.91	0.34	0.16	0.66
100	0.002	0.1	1.68	0.26	0.18	0.91	0.34	0.17	0.66
100	0.002	0.01	1.68	0.26	0.19	0.90	0.34	0.17	0.67
160	0.002	1	2.69	0.26	0.30	1.47	0.34	0.27	1.04
160	0.002	0.1	2.69	0.26	0.30	1.47	0.34	0.28	1.05
160	0.002	0.01	2.69	0.26	0.31	1.47	0.34	0.28	1.05
400	0.002	1	6.72	0.26	0.78	3.92	0.34	0.72	2.45
400	0.002	0.1	6.72	0.26	0.79	3.93	0.34	0.73	2.45
400	0.002	0.01	6.72	0.26	0.79	3.93	0.34	0.73	2.46
700	0.002	1	11.76	0.27	1.39	7.52	0.33	1.28	3.88
700	0.002	0.1	11.76	0.27	1.39	7.52	0.33	1.29	3.88
700	0.002	0.01	11.76	0.27	1.40	7.52	0.33	1.29	3.88
1000	0.002	1	16.81	0.27	1.99	11.69	0.33	1.84	4.92
1000	0.002	0.1	16.81	0.27	2.00	11.69	0.33	1.85	4.93
1000	0.002	0.01	16.81	0.27	2.00	11.70	0.33	1.85	4.93

Table 4 (Continued)

Control Parameters				Co-flow Region			Counter-flow		
St	R_τ	P_g (atm)	U_i (cm/s)	$\bar{\nu}_{FD}$	$\bar{T}_{FD}^{1/2}$ (cm/s)	\bar{u}_g (cm/s)	$\bar{\nu}_{FD}$	$\bar{T}_{FD}^{1/2}$ (cm/s)	\bar{u}_g (cm/s)
50	0.004	1	0.84	0.24	0.08	0.49	0.36	0.07	0.30
50	0.004	0.1	0.84	0.24	0.08	0.49	0.36	0.07	0.31
50	0.004	0.01	0.84	0.24	0.09	0.48	0.36	0.08	0.32
80	0.004	1	1.34	0.24	0.14	0.78	0.36	0.12	0.50
80	0.004	0.1	1.34	0.25	0.15	0.78	0.35	0.13	0.50
80	0.004	0.01	1.34	0.25	0.15	0.78	0.35	0.13	0.51
100	0.004	1	1.68	0.25	0.18	0.98	0.35	0.16	0.62
100	0.004	0.1	1.68	0.25	0.19	0.98	0.35	0.17	0.62
100	0.004	0.01	1.68	0.25	0.19	0.98	0.35	0.17	0.63
160	0.004	1	2.69	0.25	0.30	1.61	0.35	0.27	0.97
160	0.004	0.1	2.69	0.25	0.31	1.61	0.35	0.28	0.98
160	0.004	0.01	2.69	0.25	0.31	1.61	0.35	0.28	0.98
400	0.004	1	6.72	0.26	0.79	4.64	0.34	0.72	2.10
400	0.004	0.1	6.72	0.26	0.79	4.64	0.34	0.72	2.10
400	0.004	0.01	6.72	0.26	0.80	4.64	0.34	0.73	2.10
700	0.004	1	11.76	0.26	1.40	9.53	0.34	1.27	2.88
700	0.004	0.1	11.76	0.26	1.40	9.53	0.34	1.28	2.88
700	0.004	0.01	11.76	0.26	1.41	9.54	0.34	1.28	2.88
1000	0.004	1	16.81	0.26	2.01	15.67	0.34	1.83	2.96
1000	0.004	0.1	16.81	0.26	2.01	15.67	0.34	1.83	2.96
1000	0.004	0.01	16.81	0.26	2.02	15.68	0.34	1.84	2.97

Table 4 (Continued)

Control Parameters				Co-flow Region			Counter-flow		
St	R_τ	P_g (atm)	U_i (cm/s)	$\bar{\nu}_{FD}$	$\bar{T}_{FD}^{1/2}$ (cm/s)	\bar{u}_g (cm/s)	$\bar{\nu}_{FD}$	$\bar{T}_{FD}^{1/2}$ (cm/s)	\bar{u}_g (cm/s)
50	0.008	1	0.84	0.22	0.08	0.55	0.38	0.07	0.28
50	0.008	0.1	0.84	0.22	0.09	0.54	0.38	0.07	0.29
50	0.008	0.01	0.84	0.23	0.09	0.54	0.37	0.08	0.30
80	0.008	1	1.34	0.23	0.14	0.89	0.37	0.12	0.46
80	0.008	0.1	1.34	0.23	0.15	0.89	0.37	0.13	0.46
80	0.008	0.01	1.34	0.23	0.15	0.89	0.37	0.13	0.47
100	0.008	1	1.68	0.23	0.18	1.14	0.37	0.16	0.56
100	0.008	0.1	1.68	0.23	0.19	1.13	0.37	0.16	0.57
100	0.008	0.01	1.68	0.24	0.19	1.13	0.36	0.17	0.57
160	0.008	1	2.69	0.24	0.31	1.95	0.36	0.27	0.86
160	0.008	0.1	2.69	0.24	0.31	1.94	0.36	0.27	0.86
160	0.008	0.01	2.69	0.24	0.32	1.94	0.36	0.28	0.86
400	0.008	1	6.72	0.24	0.80	6.29	0.36	0.71	1.52
400	0.008	0.1	6.72	0.24	0.81	6.29	0.36	0.71	1.53
400	0.008	0.01	6.72	0.24	0.81	6.28	0.36	0.72	1.53
700	0.008	1	11.76	0.24	1.42	14.25	0.36	1.25	1.24
700	0.008	0.1	11.76	0.24	1.42	14.24	0.36	1.26	1.24
700	0.008	0.01	11.76	0.24	1.43	14.24	0.36	1.26	1.24
1000	0.008	0.1	16.81	0.24	2.04	25.00	0.36	1.80	-0.28
1000	0.008	0.01	16.81	0.24	2.04	24.99	0.36	1.81	-0.28

Table 4 (Continued)

Control Parameters				Co-flow Region			Counter-flow		
St	R_τ	P_g (atm)	U_i (cm/s)	$\bar{\nu}_{FD}$	$\bar{T}_{FD}^{1/2}$ (cm/s)	\bar{u}_g (cm/s)	$\bar{\nu}_{FD}$	$\bar{T}_{FD}^{1/2}$ (cm/s)	\bar{u}_g (cm/s)
50	0.01	1	0.84	0.21	0.08	0.58	0.39	0.07	0.27
50	0.01	0.1	0.84	0.22	0.09	0.57	0.38	0.07	0.28
50	0.01	0.01	0.84	0.22	0.09	0.57	0.38	0.08	0.29
80	0.01	1	1.34	0.22	0.14	0.95	0.38	0.12	0.44
80	0.01	0.1	1.34	0.22	0.15	0.95	0.38	0.13	0.45
80	0.01	0.01	1.34	0.23	0.15	0.94	0.37	0.13	0.45
100	0.01	1	1.68	0.22	0.19	1.22	0.38	0.16	0.54
100	0.01	0.1	1.68	0.23	0.19	1.22	0.37	0.16	0.55
100	0.01	0.01	1.68	0.23	0.19	1.21	0.37	0.17	0.55
160	0.01	1	2.69	0.23	0.31	2.13	0.37	0.27	0.81
160	0.01	0.1	2.69	0.23	0.31	2.12	0.37	0.27	0.81
160	0.01	0.01	2.69	0.23	0.32	2.12	0.37	0.28	0.82
400	0.01	1	6.72	0.23	0.81	7.24	0.37	0.70	1.29
400	0.01	0.1	6.72	0.23	0.81	7.23	0.37	0.71	1.29
400	0.01	0.01	6.72	0.24	0.81	7.21	0.37	0.71	1.29
700	0.01	1	11.76	0.24	1.43	16.95	0.37	1.24	0.56
700	0.01	0.1	11.76	0.24	1.43	16.94	0.37	1.25	0.56
700	0.01	0.01	11.76	0.24	1.43	16.92	0.37	1.25	0.55
1000	0.01	1	16.81	0.24	2.05	30.38	0.37	1.79	-1.64
1000	0.01	0.1	16.81	0.24	2.05	30.36	0.37	1.79	-1.64
1000	0.01	0.01	16.81	0.24	2.06	30.34	0.37	1.80	-1.65

Table 5: Viscous Drag Experiments ($\bar{\nu} = 0.4$).

Control Parameters				Co-flow Region			Counter-flow		
St	R_τ	P_g (atm)	U_i (cm/s)	$\bar{\nu}_{FD}$	$\bar{T}_{FD}^{1/2}$ (cm/s)	\bar{u}_g (cm/s)	$\bar{\nu}_{FD}$	$\bar{T}_{FD}^{1/2}$ (cm/s)	\bar{u}_g (cm/s)
50	0.002	1	0.84	0.33	0.07	0.44	0.47	0.07	0.32
50	0.002	0.1	0.84	0.34	0.08	0.44	0.46	0.07	0.33
50	0.002	0.01	0.84	0.35	0.08	0.43	0.45	0.08	0.34
80	0.002	1	1.34	0.34	0.13	0.70	0.46	0.12	0.52
80	0.002	0.1	1.34	0.35	0.13	0.70	0.45	0.12	0.53
80	0.002	0.01	1.34	0.35	0.13	0.69	0.45	0.13	0.54
100	0.002	1	1.68	0.35	0.16	0.88	0.45	0.15	0.66
100	0.002	0.1	1.68	0.35	0.16	0.87	0.45	0.16	0.67
100	0.002	0.01	1.68	0.35	0.17	0.87	0.45	0.16	0.68
160	0.002	1	2.69	0.35	0.27	1.40	0.45	0.26	1.07
160	0.002	0.1	2.69	0.35	0.27	1.40	0.45	0.26	1.08
160	0.002	0.01	2.69	0.36	0.28	1.39	0.44	0.27	1.09
400	0.002	1	6.72	0.36	0.70	3.60	0.44	0.67	2.64
400	0.002	0.1	6.72	0.36	0.71	3.59	0.44	0.68	2.65
400	0.002	0.01	6.72	0.36	0.71	3.58	0.44	0.68	2.66
700	0.002	1	11.76	0.36	1.24	6.58	0.44	1.19	4.45
700	0.002	0.1	11.76	0.36	1.25	6.57	0.44	1.19	4.46
700	0.002	0.01	11.76	0.36	1.25	6.56	0.44	1.20	4.47
1000	0.002	1	16.81	0.36	1.79	9.83	0.44	1.71	6.10
1000	0.002	0.1	16.81	0.36	1.79	9.82	0.44	1.71	6.11
1000	0.002	0.01	16.81	0.36	1.79	9.81	0.44	1.72	6.12

Table 5 (Continued)

Control Parameters				Co-flow Region			Counter-flow		
St	R_τ	P_g (atm)	U_i (cm/s)	$\bar{\nu}_{FD}$	$\bar{T}_{FD}^{1/2}$ (cm/s)	\bar{u}_g (cm/s)	$\bar{\nu}_{FD}$	$\bar{T}_{FD}^{1/2}$ (cm/s)	\bar{u}_g (cm/s)
50	0.004	1	0.84	0.32	0.07	0.47	0.48	0.07	0.31
50	0.004	0.1	0.84	0.33	0.08	0.47	0.47	0.07	0.32
50	0.004	0.01	0.84	0.34	0.08	0.46	0.46	0.08	0.33
80	0.004	1	1.34	0.33	0.13	0.75	0.47	0.12	0.51
80	0.004	0.1	1.34	0.34	0.13	0.74	0.46	0.12	0.52
80	0.004	0.01	1.34	0.34	0.13	0.73	0.46	0.13	0.53
100	0.004	1	1.68	0.33	0.16	0.94	0.47	0.15	0.64
100	0.004	0.1	1.68	0.34	0.17	0.92	0.46	0.16	0.65
100	0.004	0.01	1.68	0.34	0.17	0.91	0.46	0.16	0.66
160	0.004	1	2.69	0.34	0.27	1.50	0.46	0.25	1.03
160	0.004	0.1	2.69	0.34	0.27	1.49	0.46	0.26	1.04
160	0.004	0.01	2.69	0.35	0.28	1.48	0.45	0.26	1.05
400	0.004	1	6.72	0.35	0.70	3.99	0.45	0.67	2.47
400	0.004	0.1	6.72	0.35	0.71	3.97	0.45	0.67	2.48
400	0.004	0.01	6.72	0.35	0.71	3.96	0.45	0.68	2.49
700	0.004	1	11.76	0.35	1.25	7.62	0.45	1.18	4.00
700	0.004	0.1	11.76	0.35	1.25	7.60	0.45	1.19	4.00
700	0.004	0.01	11.76	0.35	1.26	7.59	0.45	1.19	4.01
1000	0.004	1	16.81	0.35	1.79	11.83	0.45	1.70	5.22
1000	0.004	0.1	16.81	0.35	1.80	11.81	0.45	1.70	5.22
1000	0.004	0.01	16.81	0.35	1.80	11.80	0.45	1.71	5.22

Table 5 (Continued)

Control Parameters				Co-flow Region			Counter-flow		
St	R_τ	P_g (atm)	U_i (cm/s)	$\bar{\nu}_{FD}$	$\bar{T}_{FD}^{1/2}$ (cm/s)	\bar{u}_g (cm/s)	$\bar{\nu}_{FD}$	$\bar{T}_{FD}^{1/2}$ (cm/s)	\bar{u}_g (cm/s)
50	0.008	1	0.84	0.30	0.07	0.52	0.50	0.07	0.30
50	0.008	0.1	0.84	0.31	0.07	0.51	0.49	0.07	0.31
50	0.008	0.01	0.84	0.32	0.08	0.50	0.48	0.08	0.32
80	0.008	1	1.34	0.31	0.13	0.83	0.49	0.12	0.49
80	0.008	0.1	1.34	0.32	0.13	0.82	0.48	0.12	0.50
80	0.008	0.01	1.34	0.32	0.13	0.81	0.48	0.13	0.51
100	0.008	1	1.68	0.31	0.16	1.04	0.48	0.15	0.61
100	0.008	0.1	1.68	0.32	0.17	1.03	0.48	0.16	0.62
100	0.008	0.01	1.68	0.33	0.17	1.01	0.47	0.16	0.63
160	0.008	1	2.69	0.32	0.27	1.71	0.48	0.25	0.97
160	0.008	0.1	2.69	0.33	0.27	1.69	0.47	0.26	0.98
160	0.008	0.01	2.69	0.33	0.28	1.67	0.47	0.26	0.99
400	0.008	1	6.72	0.33	0.71	4.86	0.47	0.66	2.20
400	0.008	0.1	6.72	0.33	0.71	4.84	0.47	0.67	2.21
400	0.008	0.01	6.72	0.33	0.72	4.82	0.47	0.67	2.21
700	0.008	1	11.76	0.33	1.25	9.97	0.47	1.17	3.26
700	0.008	0.1	11.76	0.33	1.26	9.95	0.47	1.18	3.26
700	0.008	0.01	11.76	0.33	1.26	9.92	0.47	1.18	3.26
1000	0.008	1	16.81	0.33	1.80	16.40	0.47	1.68	3.77
1000	0.008	0.1	16.81	0.33	1.80	16.36	0.47	1.69	3.77
1000	0.008	0.01	16.81	0.33	1.81	16.33	0.47	1.69	3.76

Table 5 (Continued)

Control Parameters				Co-flow Region			Counter-flow		
St	R_τ	P_g (atm)	U_i (cm/s)	$\bar{\nu}_{FD}$	$\bar{T}_{FD}^{1/2}$ (cm/s)	\bar{u}_g (cm/s)	$\bar{\nu}_{FD}$	$\bar{T}_{FD}^{1/2}$ (cm/s)	\bar{u}_g (cm/s)
50	0.01	1	0.84	0.30	0.07	0.53	0.50	0.07	0.30
50	0.01	0.1	0.84	0.30	0.07	0.53	0.50	0.07	0.31
50	0.01	0.01	0.84	0.31	0.08	0.52	0.49	0.08	0.31
80	0.01	1	1.34	0.30	0.13	0.87	0.49	0.12	0.48
80	0.01	0.1	1.34	0.31	0.13	0.86	0.49	0.12	0.49
80	0.01	0.01	1.34	0.32	0.13	0.84	0.48	0.13	0.50
100	0.01	1	1.68	0.31	0.16	1.09	0.49	0.15	0.60
100	0.01	0.1	1.68	0.31	0.17	1.08	0.49	0.16	0.61
100	0.01	0.01	1.68	0.32	0.17	1.06	0.48	0.16	0.62
160	0.01	1	2.69	0.32	0.27	1.80	0.48	0.25	0.95
160	0.01	0.1	2.69	0.32	0.27	1.78	0.48	0.26	0.96
160	0.01	0.01	2.69	0.32	0.28	1.77	0.48	0.26	0.97
400	0.01	1	6.72	0.32	0.71	5.31	0.48	0.66	2.09
400	0.01	0.1	6.72	0.33	0.71	5.28	0.47	0.66	2.10
400	0.01	0.01	6.72	0.33	0.72	5.26	0.47	0.67	2.10
700	0.01	1	11.76	0.33	1.26	11.22	0.47	1.17	2.94
700	0.01	0.1	11.76	0.33	1.26	11.18	0.47	1.17	2.94
700	0.01	0.01	11.76	0.33	1.26	11.15	0.47	1.18	2.94
1000	0.01	1	16.81	0.33	1.80	18.83	0.47	1.68	3.14
1000	0.01	0.1	16.81	0.33	1.81	18.79	0.47	1.68	3.14
1000	0.01	0.01	16.81	0.33	1.81	18.75	0.47	1.69	3.13

Table 6: Viscous Drag Experiments ($\bar{\nu} = 0.45$).

Control Parameters				Co-flow Region			Counter-flow		
St	R_τ	P_g (atm)	U_i (cm/s)	$\bar{\nu}_{FD}$	$\bar{T}_{FD}^{1/2}$ (cm/s)	\bar{u}_g (cm/s)	$\bar{\nu}_{FD}$	$\bar{T}_{FD}^{1/2}$ (cm/s)	\bar{u}_g (cm/s)
50	0.002	1	0.84	0.39	0.07	0.41	0.51	0.07	0.32
50	0.002	0.1	0.84	0.40	0.07	0.42	0.50	0.07	0.33
50	0.002	0.01	0.84	0.40	0.08	0.42	0.50	0.08	0.34
80	0.002	1	1.34	0.40	0.12	0.67	0.50	0.12	0.53
80	0.002	0.1	1.34	0.40	0.13	0.67	0.50	0.12	0.54
80	0.002	0.01	1.34	0.41	0.13	0.67	0.49	0.13	0.55
100	0.002	1	1.68	0.40	0.16	0.84	0.50	0.15	0.67
100	0.002	0.1	1.68	0.40	0.16	0.83	0.50	0.16	0.68
100	0.002	0.01	1.68	0.41	0.16	0.83	0.49	0.16	0.69
160	0.002	1	2.69	0.41	0.26	1.33	0.49	0.25	1.09
160	0.002	0.1	2.69	0.41	0.26	1.33	0.49	0.26	1.10
160	0.002	0.01	2.69	0.41	0.27	1.33	0.49	0.26	1.11
400	0.002	1	6.72	0.41	0.68	3.37	0.49	0.66	2.73
400	0.002	0.1	6.72	0.41	0.68	3.37	0.49	0.66	2.74
400	0.002	0.01	6.72	0.41	0.69	3.37	0.48	0.67	2.75
700	0.002	1	11.76	0.41	1.20	6.14	0.49	1.16	4.65
700	0.002	0.1	11.76	0.41	1.21	6.14	0.49	1.17	4.66
700	0.002	0.01	11.76	0.41	1.21	6.13	0.49	1.17	4.67
1000	0.002	1	16.81	0.41	1.73	9.09	0.49	1.67	6.46
1000	0.002	0.1	16.81	0.41	1.73	9.09	0.49	1.67	6.47
1000	0.002	0.01	16.81	0.41	1.74	9.08	0.49	1.68	6.48

Table 6 (Continued)

Control Parameters				Co-flow Region			Counter-flow		
St	R_τ	P_g (atm)	U_i (cm/s)	$\bar{\nu}_{FD}$	$\bar{T}_{FD}^{1/2}$ (cm/s)	\bar{u}_g (cm/s)	$\bar{\nu}_{FD}$	$\bar{T}_{FD}^{1/2}$ (cm/s)	\bar{u}_g (cm/s)
50	0.004	1	0.84	0.37	0.07	0.45	0.53	0.07	0.31
50	0.004	0.1	0.84	0.38	0.07	0.44	0.52	0.07	0.32
50	0.004	0.01	0.84	0.39	0.08	0.44	0.51	0.08	0.33
80	0.004	1	1.34	0.38	0.12	0.71	0.52	0.12	0.52
80	0.004	0.1	1.34	0.39	0.13	0.70	0.51	0.12	0.53
80	0.004	0.01	1.34	0.40	0.13	0.69	0.50	0.13	0.54
100	0.004	1	1.68	0.39	0.16	0.88	0.51	0.15	0.66
100	0.004	0.1	1.68	0.39	0.16	0.87	0.50	0.15	0.67
100	0.004	0.01	1.68	0.40	0.16	0.86	0.50	0.16	0.68
160	0.004	1	2.69	0.40	0.26	1.40	0.50	0.25	1.07
160	0.004	0.1	2.69	0.40	0.26	1.39	0.50	0.26	1.08
160	0.004	0.01	2.69	0.40	0.27	1.39	0.50	0.26	1.09
400	0.004	1	6.72	0.40	0.68	3.61	0.49	0.66	2.61
400	0.004	0.1	6.72	0.41	0.68	3.61	0.49	0.66	2.62
400	0.004	0.01	6.72	0.41	0.69	3.60	0.49	0.67	2.63
700	0.004	1	11.76	0.40	1.20	6.77	0.50	1.16	4.34
700	0.004	0.1	11.76	0.40	1.21	6.77	0.50	1.17	4.34
700	0.004	0.01	11.76	0.40	1.21	6.76	0.50	1.17	4.35
1000	0.004	1	16.81	0.40	1.73	10.34	0.50	1.66	5.86
1000	0.004	0.1	16.81	0.40	1.73	10.33	0.50	1.67	5.86
1000	0.004	0.01	16.81	0.40	1.74	10.32	0.50	1.68	5.87

Table 6 (Continued)

Control Parameters				Co-flow Region			Counter-flow		
St	R_τ	P_g (atm)	U_i (cm/s)	$\bar{\nu}_{FD}$	$\bar{T}_{FD}^{1/2}$ (cm/s)	\bar{u}_g (cm/s)	$\bar{\nu}_{FD}$	$\bar{T}_{FD}^{1/2}$ (cm/s)	\bar{u}_g (cm/s)
50	0.008	1	0.84	0.35	0.07	0.50	0.55	0.07	0.31
50	0.008	0.1	0.84	0.36	0.07	0.48	0.54	0.07	0.32
50	0.008	0.01	0.84	0.37	0.08	0.47	0.53	0.08	0.33
80	0.008	1	1.34	0.36	0.12	0.77	0.53	0.12	0.51
80	0.008	0.1	1.34	0.37	0.12	0.76	0.53	0.12	0.52
80	0.008	0.01	1.34	0.38	0.13	0.75	0.52	0.13	0.53
100	0.008	1	1.68	0.37	0.16	0.96	0.53	0.15	0.64
100	0.008	0.1	1.68	0.38	0.16	0.95	0.52	0.15	0.65
100	0.008	0.01	1.68	0.38	0.16	0.93	0.52	0.16	0.66
160	0.008	1	2.69	0.38	0.26	1.54	0.52	0.25	1.02
160	0.008	0.1	2.69	0.38	0.27	1.53	0.52	0.25	1.03
160	0.008	0.01	2.69	0.39	0.27	1.51	0.51	0.26	1.04
400	0.008	1	6.72	0.39	0.68	4.16	0.51	0.65	2.41
400	0.008	0.1	6.72	0.39	0.69	4.14	0.51	0.66	2.42
400	0.008	0.01	6.72	0.39	0.69	4.12	0.51	0.66	2.42
700	0.008	1	11.76	0.39	1.21	8.12	0.51	1.16	3.79
700	0.008	0.1	11.76	0.39	1.21	8.10	0.51	1.16	3.80
700	0.008	0.01	11.76	0.39	1.22	8.09	0.51	1.17	3.80
1000	0.008	1	16.81	0.39	1.73	12.96	0.51	1.66	4.79
1000	0.008	0.1	16.81	0.39	1.74	12.95	0.51	1.66	4.80
1000	0.008	0.01	16.81	0.39	1.74	12.92	0.51	1.67	4.79

Table 6 (Continued)

Control Parameters				Co-flow Region			Counter-flow		
St	R_τ	P_g (atm)	U_i (cm/s)	$\bar{\nu}_{FD}$	$\bar{T}_{FD}^{1/2}$ (cm/s)	\bar{u}_g (cm/s)	$\bar{\nu}_{FD}$	$\bar{T}_{FD}^{1/2}$ (cm/s)	\bar{u}_g (cm/s)
50	0.01	1	0.84	0.34	0.07	0.51	0.56	0.07	0.31
50	0.01	0.01	0.84	0.37	0.08	0.49	0.53	0.08	0.32
80	0.01	1	1.34	0.36	0.12	0.81	0.54	0.12	0.50
80	0.01	0.1	1.34	0.37	0.12	0.79	0.53	0.12	0.51
80	0.01	0.01	1.34	0.37	0.13	0.77	0.52	0.13	0.52
100	0.01	1	1.68	0.36	0.16	1.00	0.54	0.15	0.63
100	0.01	0.1	1.68	0.37	0.16	0.99	0.53	0.15	0.64
100	0.01	0.01	1.68	0.38	0.16	0.97	0.52	0.16	0.65
160	0.01	1	2.69	0.37	0.26	1.62	0.53	0.25	1.01
160	0.01	0.1	2.69	0.38	0.26	1.60	0.52	0.25	1.01
160	0.01	0.01	2.69	0.38	0.27	1.58	0.52	0.26	1.02
400	0.01	1	6.72	0.38	0.68	4.46	0.52	0.65	2.33
400	0.01	0.1	6.72	0.38	0.69	4.44	0.52	0.66	2.33
400	0.01	0.01	6.72	0.38	0.69	4.42	0.52	0.66	2.34
700	0.01	1	11.76	0.38	1.21	8.92	0.52	1.15	3.56
700	0.01	0.1	11.76	0.39	1.21	8.90	0.51	1.16	3.56
700	0.01	0.01	11.76	0.39	1.22	8.87	0.51	1.16	3.56
1000	0.01	1	16.81	0.38	1.73	14.43	0.51	1.65	4.33
1000	0.01	0.1	16.81	0.39	1.74	14.40	0.51	1.66	4.33
1000	0.01	0.01	16.81	0.39	1.74	14.38	0.51	1.67	4.33

BIBLIOGRAPHY

- [1] M. Alam and S. Luding. How good is the equipartition assumption for the transport properties of a granular mixture? *Granular Matter*, 4(3):139–142, 2002.
- [2] M. Alam and P. R. Nott. Stability of plane Couette flow of a granular material. *J. Fluid Mech.*, 377:99–136, 1998.
- [3] M. Alam, J. T. Willits, B. Ö. Arnarson, and S. Luding. Kinetic theory of binary mixture of nearly elastic disks with size and mass disparity. *Phys. Fluids*, 14:4085–4087, 2002.
- [4] B. Ö. Arnarson and J. T. Jenkins. Binary mixtures of inelastic spheres: Simplified constitutive theory. *under review*, 2002.
- [5] B. Ö. Arnarson, J. T. Jenkins, M. Y. Louge, and H. Xu. Binary mixtures of inelastic spheres: A boundary value problem. *under review*, 2002.
- [6] B. Ö. Arnarson and J. T. Willits. Thermal diffusion in binary mixtures of smooth, nearly elastic spheres with and without gravity. *Phys. Fluids*, 10:1324–1328, 1998.
- [7] M. Babic. On the stability of rapid granular flows. *J. Fluid Mech.*, 254:127–150, 1993.
- [8] M. Babic. Unsteady Couette granular flows. *Phys. Fluids*, 9:2486–2505, 1997.
- [9] R. A. Bagnold. Experiments on a gravity-free dispersion of large solid spheres in a Newtonian fluid under shear. *Proc. R. Soc. Lond. A*, 225:49–63, 1954.
- [10] L. Bocquet, W. Losert, D. Schalk, T. C. Lubensky, and J. P. Gollub. Shocks in vertically oscillated granular layers. *Phys. Rev. E*, 66:051301, 2002.
- [11] E. J. Bolio, J. A. Yasuna, and J. L. Sinclair. Dilute, turbulent gas-solid flow in risers with particle-particle interactions. *AIChE J.*, 41:1375–1388, 1995.
- [12] J. Bougie, S. J. Moon, J. B. Swift, and H. L. Swinney. Granular shear flow dynamics and forces: Experiment and continuum theory. *Phys. Rev. E*, 65:011307, 2002.
- [13] A. H. Bowker and G. J. Lieberman. *Engineering Statistics*. Prentice-Hall, 1972.
- [14] J. F. Brady and G. Bossis. Stokesian dynamics. *Annu. Rev. Fluid Mech.*, 20:111–157, 1998.

- [15] J. Calsamiglia, A. W. Kennedy, A. Chatterjee, A. Ruina, and J. T. Jenkins. Anomalous frictional behavior in collisions of thin disks. *J. Appl. Mech.*, 66:146–152, 1999.
- [16] C. S. Campbell. Rapid granular flows. *Annu. Rev. Fluid Mech.*, 22:57–92, 1990.
- [17] C. S. Campbell. Granular shear flows at the elastic limit. *J. Fluid Mech.*, 465:261–291, 2002.
- [18] C. S. Campbell and C. E. Brennen. Computer simulation of granular shear flows. *J. Fluid Mech.*, 151:167–188, 1985.
- [19] C. S. Campbell and A. Gong. The stress tensor in a two-dimensional granular shear flow. *J. Fluid Mech.*, 164:107–125, 1986.
- [20] J. Cao, G. Ahmadi, and M. Massoudi. Gravity granular flows of slightly frictional particles down an inclined bumpy chute. *J. Fluid Mech.*, 316:197–221, 1996.
- [21] P. C. Carman. The determination of the specific surface area of powder i. *J. Soc. Chem. Ind.*, 57:225–236, 1937.
- [22] N. F. Carnahan and K. E. Starling. Equation of state for nonattracting rigid spheres. *J. Chem. Phys.*, 51:635–636, 1969.
- [23] S. Chen and G. D. Doolen. Lattice Boltzmann method for fluid flows. *Annu. Rev. Fluid Mech.*, 30:329–364, 1998.
- [24] E. G. D. Cohen. Fifty years of kinetic theory. *Physica A*, 194:229–257, 1993.
- [25] K. Craig, R. H. Buckholz, and G. Domoto. Effect of shear surface boundaries on stress for shearing flow of dry cohesionless metal powders – An experimental study. *J. Tribology*, 109:232–237, 1987.
- [26] J. C. Crocker and D. G. Grier. Methods of digital video microscopy for colloidal studies. *J. Colloid and Interface Sci.*, 179:298–310, 1996.
- [27] P. A. Cundall and O. D. L. Strack. Discrete numerical model for granular assemblies. *Geotechnique*, 29(1):47–65, 1979.
- [28] S. Dasgupta, R. Jackson, and S. Sundaresan. Turbulent gas-particle flow in verticle risers. *AIChE J.*, 40:215–228, 1994.
- [29] R. H. Davis. Elastohydrodynamic collisions of particles. *Physicochemical Hydrodynamics: PCH*, 9:41–52, 1987.
- [30] R. H. Davis, J.-M. Serayssol, and E. J. Hinch. The elastohydrodynamic collision of two spheres. *J. Fluid Mech.*, 163:479–497, 1986.

- [31] A. Einstein. Calculation of the viscosity-coefficient of a liquid in which a large number of small spheres are suspended in irregular distribution. *Ann. Physik*, 19:286–306, 1906.
- [32] S. Ergun. Pressure drop through granular beds. *Chem. Eng. Prog.*, 48:84–88, 1952.
- [33] S. F. Foerster, M. Y. Louge, Hongder Chang, and K. Allia. Measurements of the collision properties of small spheres. *Phys. Fluids A*, 6:1108–1115, 1994.
- [34] E. Fukushima. Nuclear magnetic resonance as a tool to study flow. *Annu. Rev. Fluid Mech.*, 31:95–123, 1999.
- [35] V. Garzó and J. Dufty. Homogeneous cooling state for a granular mixture. *Phys. Rev. E*, 60:5706–5713, 1999.
- [36] I. Goldhirsch. Rapid granular flows. *Annu. Rev. Fluid Mech.*, 35:267–293, 2003.
- [37] A. Goldshtein and M. Shapiro. Mechanics of collisional motion of granular materials. part 1. General hydrodynamic equations. *J. Fluid Mech.*, 282:75–114, 1995.
- [38] W. Goldsmith. *Impact: the theory and physical behaviour of colliding solids*. Edward Arnold Publication, 1960.
- [39] A. Gopinath, S. B. Chen, and D. L. Koch. Lubrication flows between spherical particles colliding in a compressible non-continuum gas. *J. Fluid Mech.*, 344:245–269, 1997.
- [40] D. M. Hanes and D. L. Inman. Observations of rapidly flowing granular-fluid materials. *Phys. Fluids*, 150:357–380, 1985.
- [41] D. M. Hanes and O. R. Walton. Simulations and physical measurements of glass spheres flowing down a bumpy incline. *Powder Tech.*, 109:133–144, 2000.
- [42] J. Happel and H. Brenner. *Low Reynolds number hydrodynamics*. Prentice-Hall, 1965.
- [43] H. Hayakawa and H. Kuninaka. Simulation and theory of the impact of two-dimensional elastic disks. *Chem. Eng. Sci.*, 57:239–252, 2002.
- [44] M. A. Hopkins and M. Y. Louge. Inelastic microstructure in rapid granular flows of smooth disks. *Phys. Fluids A*, 3:47–57, 1991.
- [45] M. A. Hopkins and H. H. Shen. A Monte Carlo solution for rapidly shearing granular flows based on the kinetic theory of dense gases. *J. Fluid Mech.*, 244:477–491, 1992.

- [46] K. Hui, P. K. Haff, J. E. Ungar, and R. Jackson. Boundary conditions for high-shear grain flows. *J. Fluid Mech.*, 145:223–233, 1984.
- [47] M. L. Hunt, R. Zenit, C. S. Campbell, and C. E. Brennen. Revisiting the 1954 suspension experiments by R. A. Bagnold. *J. Fluid Mech.*, 452:1–24, 2002.
- [48] G. J. Hwang and H. H. Shen. Modeling the phase interaction in the momentum equations of a fluid-solid mixture. *Int. J. Multiphase Flow*, 17:45–57, 1991.
- [49] R. Jain, R. Kasturi, and B. G. Schunk. *Machine Vision*. McGraw-Hill, NY, 1970.
- [50] J. T. Jenkins. Boundary conditions for rapid granular flows: Flat, frictional walls. *J. Appl. Mech.*, 59:120–127, 1992.
- [51] J. T. Jenkins. Boundary conditions for collisional granular flows at bumpy, frictional walls. In T. Pöschel and S. Luding, editors, *Granular gases*, pages 125–139. Springer, 2001.
- [52] J. T. Jenkins and B. Ö Arnarson. Average equations for granular flows in a rectilinear channel. Private communication, 2002.
- [53] J. T. Jenkins and E. Askari. Boundary conditions for rapid granular flow: Phase interfaces. *J. Fluid Mech.*, 223:497–508, 1990.
- [54] J. T. Jenkins and C. Chang. Kinetic theory for identical, frictional, nearly inelastic spheres. *Phys. Fluids*, 14:1228–1235, 2002.
- [55] J. T. Jenkins and D. M. Hanes. The balance of momentum and energy at an interface between colliding and freely flying grains in a rapid granular flow. *Phys. Fluids A*, 5:781–783, 1993.
- [56] J. T. Jenkins and M. Y. Louge. On the flux of fluctuation energy in a collisional grain flow at a flat, frictional wall. *Phys. Fluids*, 9:2835–2840, 1997.
- [57] J. T. Jenkins and F. Mancini. Balance laws and constitutive relations for plane flows of a dense, binary mixture of smooth, nearly elastic, circular disks. *J. Appl. Mech.*, 54:27–34, 1987.
- [58] J. T. Jenkins and F. Mancini. Kinetic theory for binary mixtures of smooth, nearly elastic spheres. *Phys. Fluids A*, 1:2050–2057, 1989.
- [59] J. T. Jenkins and M. W. Richman. Grad’s 13-moment system for a dense gas of inelastic spheres. *Arch. Rat. Mech. Anal.*, 87:355–377, 1985.

- [60] J. T. Jenkins and M. W. Richman. Kinetic theory for plane shear flows of a dense gas of identical, rough, inelastic, circular disks. *Phys. Fluids*, 28:3485–3494, 1985.
- [61] J. T. Jenkins and M. W. Richman. Boundary conditions for plane flows of smooth, nearly elastic, circular disks. *J. Fluid Mech.*, 171:313–328, 1986.
- [62] J. T. Jenkins and M. W. Richman. Plane simple shear of smooth inelastic circular disks: The anisotropy of the second moment in the dilute and dense limits. *J. Fluid Mech.*, 192:53–69, 1988.
- [63] P. C. Johnson and R. Jackson. Frictional-collisional constitutive relations for granular materials and their applications to plane shearing. *J. Fluid Mech.*, 176:67–93, 1987.
- [64] J. M. Kincaid, E. G. D. Cohen, and M. López de Haro. The Enskog theory for multicomponent mixtures. IV. Thermal diffusion. *J. Chem. Phys.*, 86:963–975, 1987.
- [65] J. M. Kincaid, M. López de Haro, and E. G. D. Cohen. The Enskog theory for multicomponent mixtures. II. Mutual diffusion. *J. Chem. Phys.*, 79:4509–4521, 1983.
- [66] D. L. Koch and R. J. Hill. Inertial effects in suspension and porous media flows. *Annu. Rev. Fluid Mech.*, 33:619–647, 2001.
- [67] D. L. Koch and A. S. Sangani. Particle pressure and marginal stability limits for a homogeneous monodisperse gas fluidized bed: kinetic theory and numerical simulations. *J. Fluid Mech.*, 400:229–263, 1999.
- [68] V. Kumaran. Asymptotic solution of the Boltzmann equation for the shear flow of smooth inelastic disks. *Physica A*, 275:483–504, 2000.
- [69] A. J. C. Ladd. Numerical simulations of particulate suspension via a discretized Boltzmann equation. Part 1. Theoretical foundation. *J. Fluid Mech.*, 271:285–309, 1994.
- [70] A. J. C. Ladd. Numerical simulations of particulate suspension via a discretized Boltzmann equation. Part 2. Numerical results. *J. Fluid Mech.*, 271:311–339, 1994.
- [71] B. F. C. Laurent, J. Bridgewater, and D. J. Parker. Motion in a particle bed agitated by a single blade. *AIChE J.*, 46:1723–1734, 1995.
- [72] D. T. Leighton. Measurement of the hydrodynamic surface roughness of non-colloidal spheres. *Bull. Am. Phys. Soc.*, 31:1713, 1986.

- [73] M. López de Haro and E. G. D. Cohen. The Enskog theory for multicomponent mixtures. I. Linear transport theory. *J. Chem. Phys.*, 78:2746–2759, 1983.
- [74] M. Louge and M. Adams. Anomalous behavior of normal kinetic restitution in the oblique impacts of hard spheres on an elasto-plastic plates. *Phys. Rev. E*, 65:021303, 2002.
- [75] M. Louge and S. Keast. On dense granular flows down flat frictional inclines. *Phys. Fluids*, 13:1213–1233, 2001.
- [76] M. Y. Louge. Computer simulations of rapid granular flows of spheres interacting with a flat, frictional boundary. *Phys. Fluids*, 6:2253–2269, 1994.
- [77] M. Y. Louge. A model for dense granular flows down bumpy inclines. *Phys. Rev. E*, 66:under review, 2003.
- [78] M. Y. Louge, J. T. Jenkins, and M. A. Hopkins. Computer simulations of rapid granular shear flows between parallel bumpy boundaries. *Phys. Fluids A*, 2:1042–1044, 1990.
- [79] M. Y. Louge, J. T. Jenkins, and M. A. Hopkins. The relaxation of the second moments in rapid shear flows of smooth disks. *Mech. Materials*, 16:199–203, 1993.
- [80] M. Y. Louge, J. T. Jenkins, A. Reeves, and S. Keast. Microgravity segregation in collisional granular shearing flows. In A. D. Rosato and D. L. Blackmore, editors, *Proceedings of the IUTAM Symposium on Segregation in Granular Materials*, pages 103–112. Kluwer Academic Publishers, 2000.
- [81] M. Y. Louge, J. T. Jenkins, H. Xu, and B. Ö. Arnarson. Granular segregation in collisional shearing flows. In H. Aref and J. Phillips, editors, *Mechanics for a New Millennium*, pages 239–252. Kluwer Academic Publishers, 2001.
- [82] M. Y. Louge, M. Mastorakos, and J. T. Jenkins. The role of particle collisions in pneumatic transport. *J. Fluid Mech.*, 231:345–359, 1991.
- [83] M. Y. Louge, H. Xu, and J. T. Jenkins. Studies of gas-particle interactions in a microgravity flow cell. In Y. Kishino, editor, *Powders and Grains 2001*, pages 557–560. Kluwer Academic Publishers, 2001.
- [84] S. Luding, M. Huthmann, S. McNamara, and A. Zippelius. Homogeneous cooling of rough, dissipative particles: Theory and simulations. *Phys. Rev. E*, 58:3416–3425, 1998.
- [85] S. Luding and S. McNamara. How to handle the inelastic collapse of a dissipative hard-sphere gas with the TC model. *Granular Matter*, 1:113–128, 1998.

- [86] C. K. K. Lun. Kinetic theory for granular flow of dense, slightly inelastic, slightly rough spheres. *J. Fluid Mech.*, 233:539–559, 1991.
- [87] C. K. K. Lun, S. B. Savage, D. J. Jeffrey, and N. Chepurniy. Kinetic theories for granular flow: Inelastic particles in Couette flow and slightly inelastic particles in a general flowfield. *J. Fluid Mech.*, 140:223–256, 1984.
- [88] N. Mitarai, H. Hayakawa, and H. Nakanishi. Collisional granular flow as a micropolar fluid. *Phys. Rev. Lett.*, 88:174301, 2002.
- [89] G. Mo and A. S. Sangani. A method for computing Stokes flow interactions among spherical objects and its application to suspensions of drops and porous particles. *Phys. Fluids*, 6:1637–1652, 1994.
- [90] P. Moin and K. Mahesh. Direct numerical simulation: a tool in turbulent research. *Annu. Rev. Fluid Mech.*, 30:539–578, 1998.
- [91] J. M. Montanero and V. Garzó. Monte Carlo simulation of the homogeneous cooling state for a granular mixture. *Granular Matter*, 4:17–24, 2002.
- [92] J. M. Montanero, V. Garzó, A. Santos, and J. J. Brey. Kinetic theory of simple granular shear flows of smooth hard spheres. *J. Fluid Mech.*, 389:391–411, 1999.
- [93] J. M. Montanero and A. Santos. Monte Carlo simulation method for the Enskog equation. *Phys. Rev. E*, 54:438–444, 1996.
- [94] J. M. Montanero and A. Santos. Simulation of the Enskog equation *à la* Bird. *Phys. Fluids*, 9:2057–2060, 1997.
- [95] J. J. Moreau. Some numerical methods in multibody dynamics: Application to granular materials. *Euro. J. Mech. A*, 13(4(Suppl.)):93–114, 1994.
- [96] D. M. Mueth, G. F. Debregeas, G. S. Karczmar, P. J. Eng, S. R. Nagel, and H.M. Jaeger. Signatures of granular microstructure in dense shear flows. *Nature*, 406:385–389, 2000.
- [97] M. Nakagawa, S. A. Altobelli, A. Caprihan, E. Fukushima, and E.-K. Jeong. Noninvasive measurements of granular flows by magnetic resonance imaging. *Exp. Fluids*, 12:54, 1993.
- [98] P. R. Nott, M. Alam, K. Agrawal, R. Jackson, and S. Sundaresan. The effect of boundaries on the plane Couette flow of granular materials: a bifurcation analysis. *J. Fluid Mech.*, 397:203–229, 1999.
- [99] J. M. Ortega and W. C. Rheinboldt. *Iterative solution of nonlinear equations in several variables*. Academic Press, 1970.

- [100] D. J. Parker, A. E. Dijkstra, T. W. Martin, and J. P. K. Seville. Positron emission particle tracking studies of spherical particle motion in rotating drums. *Chem. Eng. Sci.*, 52:2011–2022, 1997.
- [101] G. C. Pasquarell. Granular flows: Boundary conditions for slightly bumpy walls. *ASCE J. Eng. Mech.*, 117:312–325, 1991.
- [102] G. C. Pasquarell and N. L. Ackermann. Boundary conditions for planar granular flows. *ASCE J. Eng. Mech.*, 115:1283–1302, 1989.
- [103] D. W. Peaceman and H. H. Rachford. The numerical solution of parabolic and elliptic differential equations. *J. SIAM*, 3:28–41, 1955.
- [104] M. W. Richman. Boundary conditions based upon a modified Maxwellian velocity distribution function for flows of identical, smooth, nearly elastic spheres. *Acta Mech.*, 75:227–240, 1988.
- [105] M. W. Richman and C. S. Chou. Boundary effects on granular flows of smooth disks. *J. Appl. Mech. Phys.(ZAMP)*, 39:885–901, 1988.
- [106] A. S. Sangani and G. Mo. Inclusion of lubrication forces in dynamic simulations. *Phys. Fluids*, 6:1653–1662, 1994.
- [107] A. S. Sangani, G. Mo, H.-K. Tsao, and D. L. Koch. Simple shear flows of dense gas-solid suspensions at finite Stokes numbers. *J. Fluid Mech.*, 313:309–341, 1996.
- [108] S. B. Savage. Analyses of slow high-concentration flows of granular materials. *J. Fluid Mech.*, 377:1–26, 1998.
- [109] S. B. Savage and M. Sayed. Stresses developed by dry cohesionless granular materials sheared in an annular shear cell. *J. Fluid Mech.*, 142:391–430, 1984.
- [110] N. Sela and I. Goldhirsch. Hydrodynamic equations for rapid flows of smooth inelastic spheres, to Burnett order. *J. Fluid Mech.*, 361:41–74, 1998.
- [111] N. Sela, I. Goldhirsch, and S. H. Noskowitz. Kinetic theoretical study of a simply sheared two-dimensional granular gas to Burnett order. *Phys. Fluids*, 8:2337–2353, 1996.
- [112] S. Shih. *Numerical Heat Transfer*. Hemisphere, 1984.
- [113] J. L. Sinclair and R. Jackson. Gas-particle flow in a vertical pipe with particle-particle interactions. *AIChE J.*, 39:1473–1486, 1989.
- [114] M. Stein, J. P. K. Seville, and D. J. Parker. Attrition of porous glass particles in a fluidised bed. *Powder Tech.*, 100:242–250, 1998.

- [115] P. Strating. The stress tensor in colloidal suspensions. *J. Chem. Phys.*, 103:10226–10237, 1995.
- [116] S. Sundaram and L. R. Collins. Collision statistics in an isotropic particle-laden turbulent suspension. I. Direct numerical simulations. *J. Fluid Mech.*, 335:75–109, 1997.
- [117] S. Sundaram and L. R. Collins. A numerical study of the modulation of isotropic turbulence by suspended particles. *J. Fluid Mech.*, 379:105–143, 1999.
- [118] R. R. Sundararakumar and D. L. Koch. Non-continuum lubrication flows between particles colliding in a gas. *J. Fluid Mech.*, 313:283–308, 1996.
- [119] S. Sundaresan. Instabilities in fluidized beds. *Annu. Rev. Fluid Mech.*, 35:63–88, 2003.
- [120] C. Thornton and Z. Ning. A theoretical model for the stick-bounce behaviour of adhesive, elastic-plastic spheres. *Powder Tech.*, 99:154–162, 1998.
- [121] S. Torquato. Nearest-neighbor statistics for packings of hard spheres and disks. *Phys. Rev. E*, 51(4):3170–3182, 1995.
- [122] J.-C. Tsai, W. Losert, G. A. Voth, and J.P. Gollub. Two-dimensional granular Poiseuille flow on an incline: Multiple dynamical regimes. *Phys. Rev. E*, 65(011306), 2002.
- [123] R. Verberg and D. L. Koch. Viscous dissipation of granular fluctuation energy at finite Reynold number. Private communication, 2003.
- [124] O. R. Walton. Numerical simulations of inclined chute flows of monodisperse, inelastic, frictional spheres. *Mech. Materials*, 16:239–253, 1993.
- [125] O. R. Walton. Numerical simulations of inelastic, frictional particle-particle interactions. In M. C. Roco, editor, *Particulate Two-Phase Flow*, pages 884–911. Butterworth-Heinemann, 1993.
- [126] O. R. Walton and R. L. Braun. Stress calculations for assemblies of inelastic spheres in uniform shear. *Acta Mech.*, 63:73–86, 1986.
- [127] O. R. Walton and R. L. Braun. Viscosity, granular temperature and stress calculations for shearing assemblies of inelastic, frictional disks. *J. Rheol.*, 30:949–980, 1986.
- [128] C.-H. Wang, R. Jackson, and S. Sundaresan. Instability of fully developed rapid flow of a granular material in a channel. *J. Fluid Mech.*, 342:179–197, 1996.

- [129] C.-H. Wang, R. Jackson, and S. Sundaresan. Stability of bounded rapid shear flows of a granular material. *J. Fluid Mech.*, 308:31–62, 1996.
- [130] W. Weibull. A statistical distribution function with wide applicability. *J. Appl. Mech.*, 73:293–297, 1951.
- [131] K. Wieghardt. Experiments in granular flow. *Annu. Rev. Fluid Mech.*, 7:89–114, 1975.
- [132] R. D. Wildman and J. M. Huntley. Novel method for measurement of granular temperature distributions in two-dimensional vibro-fluidised beds. *Powder Tech.*, 113:14–22, 2000.
- [133] J. T. Willits and B. O. Arnarson. Kinetic theory of a binary mixture of nearly elastic disks. *Phys. Fluids*, 11:3116–3122, 1999.
- [134] J. J. Wylie and D. L. Koch. Particle clustering due to hydrodynamic interactions. *Phys. Fluids*, 12:964–970, 2000.
- [135] J. J. Wylie, D. L. Koch, and A. J. C. Ladd. Rheology of suspensions with high particle inertia and moderate fluid inertia. *J. Fluid Mech.*, 480:95–118, 2003.
- [136] K. Yamane, M. Nakagawa, S. A. Altobelli T. Tanaka, and Y. Tsuji. Steady particulate flows in a horizontal rotating cylinder. *Phys. Fluids*, 10:1419–1427, 1998.
- [137] C. Zener. The intrinsic inelasticity of large plates. *Phys. Rev.*, 59:669, 1941.